TECHNISCHE UNIVERSITÄT MÜNCHEN

Fachgebiet Hydromechanik

Direct Numerical Simulation of Turbulent Drag Reduction by Rigid Fiber Additives

Amin Moosaie

Vollständiger Abdruck der von der Fakultät für Bauingenieur- und Vermessungswesen der Technischen Universität München zur Erlangung des akademischen Grades eines

Doktor-Ingenieurs

genehmigten Dissertation.

Vorsitzender: Univ.-Prof. Dr. rer. nat. E. Rank

Prüfer der Dissertation:

1. Univ.-Prof. Dr.-Ing. habil. M. Manhart
2. Univ.-Prof. Dr. rer. nat. B. Simeon
   Technische Universität Kaiserslautern
3. Prof. Dr. E. S. G. Shaqfeh
   Stanford University, USA
   (nur schriftliche Beurteilung)

Die Dissertation wurde am 08.03.2011 bei der Technischen Universität München eingereicht und durch die Fakultät für Bauingenieur- und Vermessungswesen am 12.08.2011 angenommen.

Abstract

A two-way coupled simulation technique for a dilute suspension of rigid fibers in turbulent flows is developed. It is based on an Eulerian direct numerical simulation of the incompressible Navier-Stokes equations and a Lagrangian direct Monte-Carlo simulation of the fiber conformation. The numerical methods are explained in detail and are implemented in an existing flow solver. A simple benchmark, for which an analytical solution exists, is designed. It is used to validate the two-way coupled solver. The developed simulation tool is employed to study the turbulent drag reduction by rigid fibers in a channel flow at a nominal shear Reynolds number $\mathrm{Re}_\tau = 180$. We use 128^3 grid cells to resolve the Eulerian field and 65 536 000 Lagrangian particle clusters each of which containing 100 fibers. This results in a total number of 6 553 600 000 fibers. All known features of a fibrous drag-reduced channel flow are reproduced in the reported simulation. We present the mean flow quantities. Especially, turbulence intensities are investigated by considering the probability density function of the fluctuating velocities. In order to explain the modification in the anisotropy of the Reynolds stress tensor, we study the pressure-strain correlation and analyze it by the use of a Green's function solution of the underlying Poisson equation. It turns out that the reduction in pressure fluctuations is partly and the reduction in strain fluctuations is mainly responsible for the reduction in the pressure-strain correlation. The budget of the strain fluctuations is also presented. The decrease in the strain fluctuations is mainly due to the reduction in contributions from the self-interaction and local vorticity effects. Ultimately, we study the vorticity field of the drag-reduced flow by presenting the vorticity fluctuations, the distribution of the tilting angle and the budget of the near-wall enstrophy.

Zusammenfassung

In vorliegender Dissertation wurde ein voll gekoppeltes Verfahren zur Simulation verdünnter Suspensionen starrer Faser in turbulenten Strömungen entwickelt. Es basiert auf einer direkten numerischen Simulation der inkompressiblen Navier-Stokes-Gleichungen für das Trägerfluid im Euler-Kontext und einer direkten Monte-Carlo-Simulation der stochastischen Faserorientierungen im Lagrange-Kontext. Die numerischen Methoden werden im Detail erläutert, in einen bestehendes Strömungslöser umgesetzt und in einem eigens entwickelten einfachen Strömungsfall für den eine analytische Lösung existiert validiert. Das entwickelte Simulationswerkzeug wird eingesetzt, um die Widerstandsverringerung durch starre Fasern in einer turbulenten Kanalströmung bei einer Scher-Reynoldszahl von $\mathrm{Re}_\tau = 180$ zu studieren. Das Eulersche Strömungsfeld wird dabei mit 128^3 Gitterzellen aufgelöst während der nicht-Newtonische Faseranteil am Spannungstensor auf 65 536 000 Lagrangen Bahnen, die jeweils über 100 Fasern repräsentieren, dargestellt wird. Daraus ergibt sich eine Gesamtzahl von 6 553 600 000 Fasern. Alle bekannten Eigenschaften einer widerstandsreduzierten verdünnten Fasersuspension werden durch die hier vorgestellten Simulationen reproduziert und bestätigt. Wir dokumentieren statistische Größen des Geschwindigkeitsfeldes, insbesondere die Wahrscheinlichkeitsdichtefunktionen der fluktuierenden Geschwindigkeitskomponenten. Die Anisotropie der Schwankungsgrößen steigt durch die Änderung der Druck-Scherkorrelationen an. Um dies zu erklären werden diese mit Hilfe einer Lösung basierend auf Greenschen Funktionen der zu Grunde liegenden Poisson analysiert. Es zeigt sich, dass die Verringerung der Druck-Scherkorrelationen zu einem kleinen Teil auf reduzierte Druckschwankungen, zu einem wesentlichen Teil jedoch auf eine Reduktion der Fluktuationen des Deformationstensors zurückzuführen ist. Die Analyse der Fluktuationen des Deformationstensors zeigt, dass diese hauptsächlich durch Beiträge der Selbstinteraktion sowie durch lokale Interaktionen mit dem Wirbelstärkefeld reduziert werden. Letztendlich untersuchen wir das Wirbelstärkefeld der widerstandsreduzierten Strömung an Hand der Wirbelstärkefluktuationen, der Häufigkeitsverteilung der Inklinationswinkel der Wirbel und den Haushalt der wandnahen Enstrophie.

Acknowledgments

The research presented in this dissertation has been accomplished during my time as a PhD candidate at Fachgebiet Hydromechanik, Technische Universität München.

I gratefully thank my advisor Prof. Dr.-Ing. habil. Michael Manhart for his support, encouragement, interest in my work, and giving me the opportunity to work on this topic and finish this thesis. I have always benefited from his broad and deep knowledge in the field during our long discussions.

This work has been funded by the International Graduate School of Science and Engineering (IGSSE) at Technische Universität München, Project 3.02, particle dynamics in turbulent flows. This support is gratefully acknowledged. I especially thank Prof. Dr. rer. nat. Ernst Rank, the founding director of IGSSE, for establishing IGSSE and especially for the stimulating annual forums at Raitenhaslach.

I am grateful to Prof. Dr. Bernd Simeon not only for being my PhD reviewer, but also for being the second mentor of my project. I am indebted to Prof. Dr. Eric S. G. Shaqfeh for acting as the reviewer of my thesis.

I acknowledge our project team leader Dr. A. Le Duc and my project partner Dipl. Tech. Math. E. Zharovsky. I thank my former colleague Dr.-Ing. A. Hokpunna for the interesting discussions that we had. I am also grateful to my colleague Sh. Kooshapur, MSc for proofreading a draft of this thesis. I thank all my colleagues at Fachgebiet Hydromechanik.

I acknowledge the high performance computational resources provided by the Leibniz Supercomputing Center (LRZ) of the Bavarian Academy of Sciences and Humanities.

Last but not least, I would like to especially thank my parents and family for their support, love and encouragement in all periods of my life.

Contents

List of Tables

List of Figures

Nomenclature

Roman letters

$\mathbf{a}$	Lumley anisotropy tensor
CFL	Courant-Friedrichs-Lewy (CFL) number
$\mathbf{D}$	strain-rate tensor
D_r	Brownian diffusivity
$\mathrm{d}m$	mass element
$\mathrm{d}p$	pressure correction
$\mathrm{d}\mathbf{W}$	increment of Wiener process
F_D	drag force
G	Green's function
H	shape factor of boundary-layer velocity profile
h	channel half-width
$\mathbf{1}$	identity tensor
$\mathbf{k}$	wavenumber vector in 3D
k	wavenumber
k_B	Boltzmann constant
m	mass
N_f	number of sampling fibers per cluster
N_p	number of Lagrangian particle clusters
N_{pc}	number of Lagrangian particle clusters per cell
$\mathbf{n}$	orientation vector of spheroidal particle
$\langle \mathbf{nn} \rangle_\Psi$	second moment of the orientation distribution function
$\langle \mathbf{nnnn} \rangle_\Psi$	fourth moment of the orientation distribution function
n	number density of suspended fibers
Pe_r	rotary Péclet number

p	pressure
p'	fluctuating pressure
Q_i	material constants
R	correlation coefficient
R_{ij}	two-point velocity correlation
R_{ij}	pressure-strain correlation
Re	Reynolds number
Re_c	Reynolds number based on centerline velocity
Re_τ	shear Reynolds number
$\mathbf{r}$	position vector
r	fiber aspect ratio
s'_{ij}	fluctuating strain-rate tensor
T	absolute temperature
TKE	turbulent kinetic energy
t	time
t_{FT}	flow-through time unit
$\mathbf{U}$	velocity vector
U	velocity in x-direction
U_b	bulk velocity in channel
U_c	centerline velocity in channel
u	fluctuating velocity in x-direction
u_τ	shear velocity
V	velocity in y-direction
v	fluctuating velocity in y-direction
$\mathbf{W}$	Wiener process
W	velocity in z-direction
w	fluctuating velocity in z-direction
$\mathbf{x}$	position vector
$\mathbf{x}_p$	position vector of Lagrangian particle

Greek letters

β_i	coefficients of IBOF closure
γ	Stokes' drag coefficient
$\dot{\gamma}$	characteristic shear rate
δ^*	displacement thickness of boundary layer
ϵ	dissipation rate
η	Kolmogorov's lengthscale
ζ	bulk viscosity of carrier fluid
θ	momentum thickness of boundary layer
θ	tilting angle of vorticity
ϑ	zenith angle of spherical coordinate
κ	fiber shape factor
$\boldsymbol{\mu}$	drift term in Langevin equation
μ	dynamic viscosity of carrier fluid
μ_i	material constants
ν	kinematic viscosity of carrier fluid
Ψ	orientation distribution function
ρ	mass density of carrier fluid
σ	diffusion term in Langevin equation
$\boldsymbol{\tau}$	stress tensor
$\boldsymbol{\tau}^{\mathrm{N}}$	Newtonian stress tensor
$\boldsymbol{\tau}^{\mathrm{NN}}$	non-Newtonian stress tensor
τ_w	wall shear stress
ϕ	volume fraction of fibers
φ	azimuth angle of spherical coordinate
$\boldsymbol{\Omega}$	rotation-rate tensor
$\boldsymbol{\omega}$	vorticity vector
ω_x	vorticity in x-direction
ω_y	vorticity in y-direction

ω_z	vorticity in z-direction

Symbols

II_a	second invariant of Lumley anisotropy map
III_a	third invariant of Lumley anisotropy map
$\langle \cdots \rangle$	ensemble-averaging operator
$\partial / \partial \cdot$	partial derivative with respect to $\cdot$
$\mathrm{D}/\mathrm{D}t$	material time derivative
$\widehat{\cdots}$	Fourier transform of $\cdots$
$\boldsymbol{\nabla}$	Nabla operator in physical space
$\boldsymbol{\nabla}_{\mathbf{n}}$	Nabla operator in conformation space
$\boldsymbol{\nabla}^2$	Laplacian operator

1. Introduction

1.1. Motivation and Literature Review

Hydro(aero)dynamic drag is often a parasitic effect that decreases the technical and/or economical efficiency of engineering devices and vehicles involving fluid flows. Therefore, drag reduction, even at small amounts, will result in a considerable reduction in the operating costs of the machinery. One can classify the drag in different categories. The shape drag is due to the pressure distribution around the body. The wave drag is associated with the wave phenomena that occur in fluid flows, e.g. surface waves in free-surface flows and sound waves in supersonic/hypersonic flows. Frictional drag is a result of viscous friction of the fluid at the wall. Due to the no-slip boundary condition, the velocity is zero at the wall and grows continuously by distance from it. Such a velocity distribution imposes a velocity gradient at the wall which, in turn, introduces a wall shear stress τ_w, according to the Newton's law of viscosity

$$\tau_w = \mu \left. \frac{\partial U}{\partial n} \right|_w , \tag{1.1}$$

in which μ, U and n are the dynamic viscosity of fluid, the velocity component tangential to the wall and the direction normal to the wall, respectively. The integral of the wall shear stress over the surface of a plain wall yields a net drag force

$$F_D = \iint_{\partial\Omega_w} \tau_w \, \mathrm{d}S, \tag{1.2}$$

where $\partial\Omega_w$ is the wall-bounded part of the flow boundary.

Momentum transfer is stronger in turbulent flows due to the fluctuations in flow quantities. As a consequence, the tangential velocity tends to the free-stream value at a closer distance to the wall, i.e. the mean velocity gradient is greater at the wall. This results in a higher wall shear stress and hence a dramatic increase in the frictional drag as compared to the laminar counterpart. Near-wall coherent structures are considered responsible for this effect. One can achieve turbulent drag reduction by controlling the near-wall vortical structures. Such a modulation of turbulence can be obtained by a variety of methods; polymer additives [67, 131], microbubbles [133], surfactants [135], riblets [13], active control techniques [14], etc. Recently, Zhao *et al.* [137] have investigated the possibility of turbulent drag reduction by a suspension of spherical particles.

Skin friction drag reduction in turbulent wall-bounded flows induced by polymer additives has been known for over half a century, since the discovery of Toms in 1948 [127]. Flexible polymers typically lead to higher drag reduction than rigid rod-like polymers (fibers) at a certain concentration. However, flexible polymers are sensitive to shear degradation, as pointed out by Paschkewitz [102] and as seen in the experiments of den Toonder *et al.* [20]. It is also known that a mixture of both flexible polymers and fibers lead to higher drag reduction than each of them alone (see [102] and references therein). The drag reducing behavior of flexible polymers has been more extensively studied than that of fibers. For a review of experimental studies refer to the recent publications of Mungal's group [52, 119] and the references therein. Numerical simulations can be also browsed in the literature, e.g. the works of the Beris' group ([123, 22, 10], etc.), De Angelis *et al.* [18], the works of the Stanford group ([25, 125, 126, 21], etc.), Benzi *et al.* [9]. In the following we review the previous experimental and numerical researches on fiber-induced turbulent drag reduction.

Frattini and Fuller [33] have experimentally investigated the orientation of small Brownian rod-like and disk-like particles in simple shear flow. Sasaki [114, 115] has performed experiments on the drag reducing effect of rod-like additives using xanthan polysaccharide and schizophyllum polysaccharide in a turbulent pipe flow. Experimental study of drag reduction by rigid fibers in a turbulent boundary-layer flow has been performed by the Stanford group [103]. More recently, Amarouchene *et al.* [4] have performed experimental and theoretical studies on the effect of the Reynolds number on the drag reducing behavior of rod-like particles.

Den Toonder *et al.* [20] have performed numerical investigation of drag reduction by rod-like additives in a turbulent pipe flow using a simplified model due to the computational limitations at that time. They have assumed that the fibers are oriented in the direction of the local velocity vector of the background flow. Despite this simplified model, they were able to reproduce the basic features of the drag-reduced flow. They have also performed experiments on drag reduction caused by a dilute polymer solution (Superfloc A110) in a turbulent pipe flow at $\mathrm{Re}_\tau = 1035$. One of the most important goals of their work was to investigate the effect of elasticity (due to Brownian motion) on drag reduction. They have concluded that increasing the elasticity has an adverse effect on drag reduction.

Manhart [71] has developed a direct Monte-Carlo solver for the fiber conformation, and used it to study the rheology of a dilute suspension of fibers in a turbulent channel flow through one-way coupled simulations. Fibers were treated in a Lagrangian framework. He has especially studied the effect of the fiber aspect ratio and Brownian motion on the mean fiber stress and the root-mean-square of fiber stress fluctuations. He has found that increasing the elasticity, increases the non-Newtonian shear stress level, which explains the decrease in the drag-reducing effectiveness of fibers by increasing the elasticity. He has also investigated the viscoelastic energy transfer in such a suspension [72]. Manhart [74] has also performed a two-way coupled simulation with the Monte-Carlo method. It was partly successful. However, due to computational limitations, no conclusion could be drawn.

The first fully successful two-way coupled simulations have been performed by Shaqfeh's group at Stanford [102, 104]. They have employed an Eulerian moment approximation method with two closure models, i.e. hybrid and invariant-based optimal fitted (IBOF) closures. The effects of the fibers' concentration, aspect ratio, Brownian motion, closure model, etc. on the drag reduction have been studied. They have also presented the joint probability density of fiber stresses with various flow quantities. Later, they have performed one-way coupled Lagrangian simulations and studied the drag-reduced flow by means of conditional statistics [105]. The flow field in the Lagrangian simulations was the one obtained by Eulerian two-way coupled simulations. They have proposed a mechanism of fiber-induced drag reduction that was supported by their simulations and Lagrangian conditional statistics. They have postulated that the fibers align in the intervortex regions and produce non-Newtonian stress fluctuations that oppose the vortical motion and eventually dampens out the vortex. This process continues to the next vortex and so fourth. Fiber-induced drag reduction in a turbulent boundary-layer flow has been also investigated by the same group [103].

Eulerian two-way coupled and Lagrangian one-way coupled methods have been also developed by the TU-Delft and NTNU groups; Gillissen *et al.* [38] have investigated the performance of the eigenvalue-based optimal fitted (EBOF) closure by comparison with a direct Fokker-Planck solver. The direct Fokker-Planck solver uses a spectral method based on the spherical harmonics. Due to the computational limitations, the simulation was restricted to relatively low Péclet numbers (strong Brownian motion). They also studied the non-Newtonian stresses generated by non-Brownian fibers in a turbulent channel flow [39]. Gillissen *et al.* [40] have numerically investigated the drag reduction in turbulent channel flow at various Reynolds numbers. Gillissen [37] has compared the drag reducing behavior of rigid fibers and flexible polymers in a channel flow, and concluded that the polymer elasticity plays a marginal role in the drag reduction.

Recently, Procaccia *et al.* [107] have developed a theory of drag reduction by flexible and rod-like polymers. Benzi *et al.* [8] have performed numerical simulation of drag reduction by rod-like particles and compared it with the theoretical predictions in [107]. All the simulations have been done using the moment approximation approach in an Eulerian framework.

In all the simulations reported above, authors assumed neutrally buoyant fibers, i.e. fibers with the same density as the carrier fluid. To the best knowledge of the author, there exists no two-way coupled simulation of inertial fibers in turbulent flows to date. However, a number of one-way coupled simulations can be found in the literature, e.g. Fan and Ahmadi [29], Zhang *et al.* [136], Mortensen *et al.* [91, 92, 93], and Marchioli *et al.* [77].

Significant advances have been made in stochastic simulation of polymers in the recent years, see for example the excellent monograph authored by Öttinger [100]. Since then, the Brownian dynamics have become a standard simulation technique. Here, we mention a few relevant publications. Somasi *et al.* [120] have developed a Brownian dynamics simulator for

bead-rod and bead-spring chains. Zhou and Akhavan [138] have performed one-way coupled simulation of the FENE and FENE-P dumbbell and chain models in a turbulent channel flow. Manhart has developed a stochastic solver for fiber orientation dynamics and have performed one-way coupled simulation in a turbulent channel flow. Terrapon *et al.* [126] have performed one-way coupled Brownian dynamics simulation of polymer stretch in a turbulent channel flow. More recently, Cyron and Wall [17] have developed a Brownian dynamics solver for polymers in the context of the finite element methods.

All the two-way coupled simulations reported so far were fully Eulerian. The only two exceptions are the following two works; the simulation of Manhart [74] using a Lagrangian Monte-Carlo simulation of fibers, which was partly successful due to the computational limitations, and the simulation of Terrapon [125], where he used a Lagrangian treatment of polymers using the FENE-P model, i.e. the FENE model with the Peterlin closure. Furthermore, all the reported two-way coupled simulations so far were using closure models with the exception of the work of Gillissen *et al.* [38]. They developed a direct Fokker-Planck solver, but it was restricted to relatively low Péclet numbers.

On the authors knowledge, to date, there is no fully successful two-way coupled direct simulation of turbulent drag reduction by fibrous (at high Péclet numbers) or flexible polymers that requires no closure. In this thesis, we study the turbulent drag reduction in a channel induced by rigid fiber additives by means of a direct numerical simulation technique without needing a closure model. The flow field is obtained by a direct solution of the Navier-Stokes equations in an Eulerian framework. The fibers are treated in a Lagrangian framework using a particle tracking scheme. The conformation of the suspended fibers is computed by a direct Monte-Carlo method developed by Manhart [71]. Such a direct approach is required as the performance of closures in complex turbulent flows is questionable.

A so-called minimal channel [55] has been used in the Paschkewitz *et al.* work to study the drag reduction. They have checked the domain size effect and concluded that such effects are modest. However, it is well known that the minimal channel leads to reliable statistics only in the near-wall region [55]. Another aim of this work is to use a larger channel to make sure that there is no artifact concerning the use of a small domain. We report results of a turbulent channel flow at $\mathrm{Re}_\tau = 180$. Of course, one could gain more insight by simulating flows at higher Reynolds numbers, as for example done by Paschkewitz *et al.* [104] (flow at $\mathrm{Re}_\tau = 300$). However, due to the selection of a large domain, and the expense of directly computing fiber conformation, we were able to afford a relatively low Reynolds number channel flow ($\mathrm{Re}_\tau = 180$).

Another issue in the previous two-coupled simulations was that they were all done in an Eulerian framework. Resolution of the non-Newtonian stresses in a fully Eulerian simulation is questionable, as the governing equation is of a pure convective nature. Theoretically, this cannot be resolved on any Eulerian grid. In this work, we chose to use a Lagrangian approach for the suspended microstructure.

Paschkewitz *et al.* [104] have reported that the streamwise vorticity fluctuations are de-

creased in a fibrous drag-reduced flow as compared to the Newtonian flow counterpart. In the present thesis, we perform a detailed analysis of the vorticity dynamics, especially in the near-wall region, by looking at the velocity-gradient fluctuations, the partial enstrophy, the correlation coefficients and the distribution of the vorticity inclination angle across the channel.

Recently, Frohnapfel *et al.* [35] have investigated the anisotropy of the Reynolds stress tensor in different kinds of drag-reduced flows, e.g. polymeric, fibrous, supersonic, etc., and concluded that the modifications in the Lumley anisotropy map in all these flows are similar. They concluded that it is a universal feature of these drag-reduced flows. In this work, we study the anisotropy in more details by looking at the pressure-strain correlation. This analysis shows us that there are some differences in the underlying physics of the modification in the anisotropy of the fibrous flow as compared to the supersonic flow.

We especially investigate the following open questions. How is the turbulence anisotropy modified in the drag-reduced flow? And how is the vorticity structure changed in the drag-reduced flow?

1.2. Contributions

The aim of this thesis is to answer some of the problems and issues explained in the above paragraphs. In particular, the contributions of this work to the field of turbulent drag reduction by rigid fibers are as follows.

1. Development of a Lagrangian simulation strategy for fiber suspensions combined with an Eulerian DNS solver.

2. Implementation of the developed method as a computer code that can be run on massively parallelized supercomputers.

3. Design of a benchmark problem with an analytical solution that can be used to validate two-way coupled simulations of fiber suspensions.

4. The first successful two-way coupled direct Monte-Carlo simulation of turbulent drag reduction by rigid fibers in a channel flow at $\mathrm{Re}_\tau = 180$.

5. Direct simulation of fiber conformation in turbulent channel flow at high rotary Péclet numbers (weak rotary Brownian motion) for the first time. This is important because Paschkewitz *et al.* [104] have shown that the drag reduction is maximum at the non-Brownian limit. The rotary Péclet number in the reported simulation is $\mathrm{Pe}_r = U_b/hD_r = 1000$. It is equivalent to a rotary Péclet number based on the mean wall shear stress $\mathrm{Pe}_r = u_\tau^2/\nu_{\mathrm{eff}} D_r \approx 10000$, which is relatively very high as compared to $\mathrm{Pe}_r = u_\tau^2/\nu_{\mathrm{eff}} D_r = 50$ achieved by Gillissen *et al.* [38] using a direct Fokker-Planck solver. ν_{eff} is the effective kinematic viscosity at the wall, i.e. the kinematic viscosity by taking the fiber

non-Newtonian shear stress into account:

$$\nu_{\text{eff}} = \nu + \frac{\left\langle \tau_{13}^{\text{NN}} \right\rangle|_w}{\mathrm{d}\left\langle U \right\rangle/\mathrm{d}z|_w}. \tag{1.3}$$

The developed method has been also used to simulate the drag reduction by non-Brownian fibers successfully. However, the results are not presented in this thesis.

6. Presentation of turbulence statistics of the drag-reduced flow at high Pe_r obtained by a direct method.

7. Detailed analysis of the modification in turbulence intensities by studying the probability density function (PDF) of the fluctuating velocity components.

8. Quadrant analysis of the Reynolds shear stress.

9. Analysis of the pressure-strain correlation using a Green's function solution of the corresponding Poisson equation to explain the modifications in turbulence intensities.

10. Detailed analysis of the vorticity field.

11. Finding the reduction in strain fluctuations as the reason for the reduction in the pressure-strain correlation and the streamwise vorticity fluctuations.

12. Presenting the budget of the strain fluctuations.

1.3. Outline

This thesis is organized as follows.

Chapter 2 briefly presents the basic concepts and underlying equations of turbulent incompressible flows. The incompressible Navier-Stokes equations and their dimensionless form are mentioned. The scales of turbulent motion and the spectral representation of turbulence are presented. This is followed by the Kolmogorov's statistical theory of turbulence. The numerical techniques that are nowadays in use for the simulation of turbulent flows are reviewed. Ultimately, the fully-developed turbulent channel flow is discussed in more detail, because it is the testcase used throughout this thesis.

The rheology of a dilute suspension of rigid, Brownian, neutrally buoyant fibers is presented in chapter 3. First, the basic assumptions and definitions of the theory are given. It is followed by a discussion on the role of Brownian motion in dilute fiber suspensions. The orientation dynamics of the suspended fibers is reviewed. The Fokker-Planck equation which governs the orientation distribution function and the moment approximation equation are discussed. The vastly used moment closure models are then presented. Brenner's rheological theory that provides the basis to compute the non-Newtonian fiber stress tensor is presented. The limit of zero rotary Péclet number is investigated, which provides a benchmark problem

with an analytical solution in the case of a channel flow. Finally, we compare Brenner's theory with Hinch and Leal's theory.

Chapter 4 contains the numerical methods. First, the principles of the DNS solver used in this work are explained. Then, the numerical algorithms developed for the fiber suspension flows are presented. The coupling of the developed schemes with the existing finite-volume-based DNS solver (called `MGLET`) is discussed. The parallelization strategy is also described. The last section of this chapter is the validation of the numerical tools, which is done in three subsections. First, the validation of the DNS solver for a Newtonian channel flow is performed by comparison with the reference DNS data of Kim *et al.* [58] and Moser *et al.* [94]. Second, the validation of the fiber conformation solver is presented by comparison with the existing analytical solution of Okagawa *et al.* [98]. Third, the two-way coupled fiber suspension solver is validated by simulating a channel flow at the limit of zero rotary Péclet number (very strong rotary Brownian motion).

In chapter 5, we present the results of the direct Monte-Carlo simulation of fiber-induced drag reduction in a turbulent channel flow. It starts with the numerical and physical parameters used in the reported simulation. The results are presented in the following subsections; mean velocity profile, turbulence intensities and the Reynolds shear stress, total shear stress balance, quadrant analysis, probability density function (PDF) of the fluctuating velocities, Lumley anisotropy map, pressure-strain correlation and its analysis by means of a Green's function solution of the corresponding Poisson equation, vorticity field, the near-wall partial enstrophy and the budget of the strain fluctuations.

The conclusions and outlook for further extention of this work are presented in chapter 6.

This thesis has three appendices. Appendix A gives the fitting coefficients of the IBOF closure. The transport equations of the Reynolds stress tensor and the turbulent kinetic energy of a turbulent non-Newtonian flow are derived in appendix B. The pressure-strain term is also shown in appendix B. Derivation of the Poisson equation for the fluctuating pressure in turbulent flow of a non-Newtonian fluid is presented in appendix C.

The thesis ends with a bibliography of the used literature.

2. Basics of Turbulent Flows

"I am an old man now, and when I die and go to heaven there are two matters on which I hope for enlightenment. One is quantum electrodynamics, and the other is the turbulent motion of fluids. And about the former I am rather optimistic."

Sir Horace Lamb, 1932

Fluid motions are encountered in nature and technology as well as in our bodies. Flows with low velocities are smooth and regular. They are called laminar flows. At higher velocities, irregularities in the flow field appear and the flow reaches a state of chaotic motion. This is a turbulent flow. Turbulent flows are characterized by their unsteadiness, random fluctuations, three-dimensional vortical structures, fast mixing, broad range of spatial and temporal scales, etc. Most of the flows appearing in natural and technological processes are turbulent.

Over a century of studying the turbulent motion of fluids starts with the experimental observations of O. Reynolds in 1883 [109]. Since then, there has been a numerous amount of theoretical, experimental and later numerical research on turbulence. The theoretical approach is extremely difficult as reflected by the famous quotation of Lamb, written above. The difficulty is due to the complexity of the governing equations of fluid dynamics. A theoretical breakthrough has been achieved by Kolmogorov [60, 61] in 1941, by postulating the statistical analysis of turbulence. Experimental studies have been the core of turbulence research before the invention of modern digital computers. Since this invention in mid-twenties, computational fluid dynamics (CFD) has been increasingly employed in turbulence research hand in hand with laboratory experiments. However, it was only after the introduction of powerful supercomputers that detailed investigations of turbulent flows became feasible [85]. Owing to the fast growth of computational power and improvements in numerical algorithms, detailed turbulence simulations are more frequently used, in both fundamental and applied research.

Turbulent flows are in some cases favorable. For example, they enhance the mixing of fuel and oxidizer in internal combustion engines. In some other cases, turbulent flows are not desirable. For example, turbulence in a boundary layer increases the drag dramatically. This is of paramount importance in air and water transportation, where the increase in drag results in more fuel consumption and hence less economical efficiency and more environmental pollution.

In this chapter, the basic concepts and underlying equations of turbulent flows are briefly reviewed. The chapter is organized as follows. Section 2.1 explains the continuum description of fluid motion. In section 2.2 the incompressible Navier-Stokes equations and their dimensionless form are presented. Section 2.3 is devoted to the scales of turbulent motion and is followed by section 2.4 on Kolmogorov's theory of turbulence. Statistical quantities of turbulence are presented in section 2.5. Section 2.6 contains the turbulence simulation strategies. The turbulent channel flow is introduced in section 2.7 as it is the benchmark used throughout this thesis.

2.1. Continuum Description of Fluid Flow

Fluids are composed of atoms/molecules which interact with each other as well as with atoms/molecules of other surrounding materials. They are also affected by external fields such as gravitational and electromagnetic forces. The microscopic particles move as a result of all these interactions and forces. The fluid motion can be simulated by considering these microscopic details [3, 42]. But in order to obtain meaningful macroscopic averaged quantities like temperature and pressure, one needs to simulate a huge number of microscopic particles. Hence, molecular dynamics (MD) simulations are prohibitively expensive and can only be afforded in very small domains and within very short time intervals. However, such a detailed information is not often required in engineering applications. Therefore, engineers try their best to refrain from such a computational burden unless it is well justified for a specific purpose.

Instead of the molecular description, the continuum approach has been traditionally chosen by engineers to analyze problems of classical physics, e.g. fluid dynamics. In this way, the macroscopic quantities are averaged over a sufficient number of microscopic particles. To clarify the concept, the averaging of velocity is presented here. Consider the fluid element dm as shown in figure 2.1. The element is sufficiently small to be the subject of infinitesimal

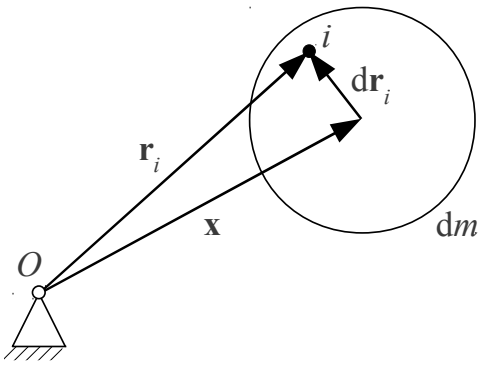

Figure 2.1: Schematic of a fluid element dm composed of many microscopic particles.

calculus, and yet, it is sufficiently large to contain enough microscopic particles. The number of particles N is enough if it allows for the calculation of meaningful macroscopic averages within the element. The i-th particle has the position vector $\mathbf{r}_i$ with respect to the origin O. The center of mass $\mathbf{x}$ of the element is given by

$$\mathbf{x} = \frac{\sum_{i=1}^{N} m_i \mathbf{r}_i}{\sum_{i=1}^{N} m_i}, \tag{2.1}$$

where m_i is the mass of the i-th particle, and $\mathrm{d}m = \sum_{i=1}^{N} m_i$ is the mass of the element. Differentiating equation (2.1) with respect to time yields

$$\dot{\mathbf{x}} = \frac{\sum_{i=1}^{N} m_i \dot{\mathbf{r}}_i}{\sum_{i=1}^{N} m_i}, \tag{2.2}$$

or

$$\mathbf{U}\mathrm{d}m = \sum_{i=1}^{N} m_i \mathbf{v}_i, \tag{2.3}$$

in which $\mathbf{v}_i$ is the velocity of the i-th particle. The above discussion can be summarized as follows. The continuum velocity $\mathbf{U}$ at a point $\mathbf{x}$ is obtained by equating the continuum momentum $\mathbf{U}\mathrm{d}m$ to the total microscopic momentum $\sum_{i=1}^{N} m_i \mathbf{v}_i$ of all particles located in an infinitesimal neighborhood of $\mathbf{x}$.

The continuum motion of a fluid can be observed in two different manners. In the first viewpoint, the observer $\mathbb{E}$ has a fixed position $\mathbf{x}_{\mathbb{E}}$ in space. $\mathbb{E}$ describes the flow quantities, e.g. velocity, as continuous fields over space and time. This means that $\mathbb{E}$ assigns a velocity $\mathbf{U}(\mathbf{x}, t)$ to every and each point $\mathbf{x}$ at the time instant t. In other words, the fluid element which passes through the point $\mathbf{x}$ at time t possesses the velocity $\mathbf{U}(\mathbf{x}, t)$. This is the Eulerian framework of describing flow kinematics. In the second point of view, the observer $\mathbb{L}$ follows a fluid particle P which has passed through some point $\mathbf{x}_0$ at some former time t_0. For $\mathbb{L}$, the flow quantities are functions of the initial conditions $\mathbf{x}_0$ and t_0, and the current time t. This particle tracking view is referred to as the Lagrangian framework. In the present work, both Eulerian and Lagrangian frameworks are used.

2.2. Navier-Stokes Equations

The dynamics of fluids are mathematically described by a set of partial differential equations, derived independently more than 150 years ago by the French engineer Claude Navier and the Irish mathematician George Stokes. These equations, known as the Navier-Stokes equations, are the mathematical formulation of the conservation laws of physics for an infinitesimal element of fluid. For example, the conservation laws of mass and linear momentum respectively

read

$$\frac{\mathrm{D}\rho}{\mathrm{D}t} + \boldsymbol{\nabla}\cdot\left(\rho\mathbf{U}\right) = 0, \tag{2.4}$$

$$\rho\frac{\mathrm{D}\mathbf{U}}{\mathrm{D}t} = -\boldsymbol{\nabla}p + \boldsymbol{\nabla}\cdot\boldsymbol{\tau}, \tag{2.5}$$

where $\rho(\mathbf{x},t)$, $p(\mathbf{x},t)$, $\mathbf{U}(\mathbf{x},t)$ and $\boldsymbol{\tau}(\mathbf{x},t)$ are the fluid density, pressure, velocity and total stress, respectively. $\mathrm{D}/\mathrm{D}t = \partial/\partial t + \mathbf{U}\cdot\boldsymbol{\nabla}$ is the material time derivative.

Due to the lack of a link to the microscopic details of the material, the obtained PDE's are not mathematically closed. This necessitates the use of a constitutive model relating the stress tensor $\boldsymbol{\tau}$ to the flow kinematics (and perhaps some other physical phenomena). For the simplest fluids, this is a linear relation referred to as the Newton's law of viscosity. Such fluids are called Newtonian fluids. However, there exist more complex fluids which behave differently and possess more complicated constitutive equations. For such complex fluids, the total stress tensor $\boldsymbol{\tau}$ can be written as the sum of a Newtonian part $\boldsymbol{\tau}^{\mathrm{N}}$ and a non-Newtonian part $\boldsymbol{\tau}^{\mathrm{NN}}$:

$$\boldsymbol{\tau} = \boldsymbol{\tau}^{\mathrm{N}} + \boldsymbol{\tau}^{\mathrm{NN}}. \tag{2.6}$$

The modification of turbulence by such non-Newtonian effects is the subject of the present thesis. However, the determination of the non-Newtonian stress $\boldsymbol{\tau}^{\mathrm{NN}}$ is discussed in the next chapter, and in this chapter we restrict ourselves to Newtonian fluids with $\boldsymbol{\tau} = \boldsymbol{\tau}^{\mathrm{N}}$. The Newtonian stress $\boldsymbol{\tau}^{\mathrm{N}}$ is linearly related to the flow kinematics via the generalized Newton's law of viscosity:

$$\boldsymbol{\tau}^{\mathrm{N}} = 2\mu\mathbf{D} + \zeta\left(\boldsymbol{\nabla}\cdot\mathbf{U}\right)\mathbf{1}, \tag{2.7}$$

in which μ and $\mathbf{1}$ are the dynamic viscosity of fluid and the identity tensor, respectively. ζ is the bulk viscosity of the fluid, which is immaterial in incompressible flows as $\boldsymbol{\nabla}\cdot\mathbf{U} = 0$ due to the continuity equation (2.9). In compressible flows, the bulk viscosity is often related to the dynamic viscosity using the Stokes' hypothesis $2\mu + 3\zeta = 0$ which expresses local thermodynamic equilibrium. The strain-rate tensor $\mathbf{D}$ is defined as

$$\mathbf{D} = \frac{1}{2}\left(\boldsymbol{\nabla}\mathbf{U} + \boldsymbol{\nabla}\mathbf{U}^{\mathrm{T}}\right), \tag{2.8}$$

where $\boldsymbol{\nabla}\mathbf{U}$ is the velocity gradient tensor.

Under the assumption of incompressible (ρ = constant) flow of a Newtonian fluid, the conservation laws of mass (2.4) and linear momentum (2.5) combined with the constitutive law (2.7) and the kinematic relation (2.8) reduce to

$$\boldsymbol{\nabla}\cdot\mathbf{U} = 0, \tag{2.9}$$

$$\rho \frac{\mathrm{D}\mathbf{U}}{\mathrm{D}t} = \rho \frac{\partial \mathbf{U}}{\partial t} + \rho \left(\mathbf{U} \cdot \boldsymbol{\nabla}\right) \mathbf{U} = -\boldsymbol{\nabla} p + \mu \boldsymbol{\nabla}^2 \mathbf{U}, \tag{2.10}$$

where $\boldsymbol{\nabla}^2 = \boldsymbol{\nabla} \cdot \boldsymbol{\nabla} = \partial^2 / \partial x_i \partial x_i$ is the Laplacian operator. Moreover, the constitutive law (2.7) reduces to

$$\boldsymbol{\tau}^{\mathrm{N}} = 2\mu \mathbf{D}, \tag{2.11}$$

for incompressible flows by taking into account the continuity equation (2.9).

Equations (2.9) and (2.10) are a system of four coupled nonlinear differential equations for four flow unknowns, i.e. the pressure and three components of the velocity vector. These equations are referred to as the incompressible Navier-Stokes equations.

2.2.1. Dimensionless Form of the Navier-Stokes Equations

The Navier-Stokes equations (2.9) and (2.10) are often written in the dimensionless form. The parameters are non-dimensionalized as follows:

$$\mathbf{x}^* = \frac{\mathbf{x}}{h}, \quad \mathbf{U}^* = \frac{\mathbf{U}}{U_b}, \quad t^* = \frac{t U_b}{h}, \tag{2.12}$$

where h is a characteristic length, e.g. the channel half-width and U_b is a characteristic velocity, e.g. the bulk velocity in the channel. Inserting these dimensionless parameters into the Navier-Stokes equations yields

$$\boldsymbol{\nabla}^* \cdot \mathbf{U}^* = 0, \tag{2.13}$$

$$\frac{\mathrm{D}\mathbf{U}^*}{\mathrm{D}t^*} = \frac{\partial \mathbf{U}^*}{\partial t^*} + \left(\mathbf{U}^* \cdot \boldsymbol{\nabla}^*\right) \mathbf{U}^* = -\boldsymbol{\nabla}^* p^* + \frac{1}{\mathrm{Re}} \boldsymbol{\nabla}^{2*} \mathbf{U}^*, \tag{2.14}$$

where $\boldsymbol{\nabla}^* = h\boldsymbol{\nabla}$, $\boldsymbol{\nabla}^{2*} = h^2 \boldsymbol{\nabla}^2$, $p^* = p / \rho U_b^2$ and

$$\mathrm{Re} = \frac{\rho U_b h}{\mu} = \frac{U_b h}{\nu}, \tag{2.15}$$

is the Reynolds number (with $\nu = \mu/\rho$ being the kinematic viscosity). The Reynolds number is the ratio of the inertial force to the viscous force in the fluid flow. A large value of Re implies that the inertial effects are dominant, and inversely, a small value of Re implies that the viscous effects are dominant. Turbulent flows occur at high Reynolds numbers. For every and each flow configuration, there exists a critical Reynolds number above which the disturbances are amplified and the flow becomes turbulent. Below this critical Reynolds number the disturbances are dampened out via viscous dissipation.

By looking at equation (2.14) one deduces that the viscous term vanishes in flows with

high Re and hence, the viscosity is ineffective in turbulent flows. This argument does not really hold. Because turbulence is a multiscale problem and there are scales at which the fluid viscosity is indeed effective. In order to understand this, the scales of turbulent motion are explained in the following section.

2.3. Scales of Turbulent Motion

Turbulent flows contain a broad range of spatial and temporal scales. The largest flow structures scale with the integral length of the problem, e.g. the channel width. The smallest scales can be several orders of magnitude smaller than the largest scales. The ratio of the largest length scales to the smallest ones is a function of the Reynolds number. This relation is given in subsection 2.6.1.

There is a continuous range of scales between the smallest and the largest scales in a fully-developed turbulent flow. In order to explain the production of various scales, we examine the nonlinear term in the Navier-Stokes equations, namely the advective term $(\mathbf{U}\cdot\boldsymbol{\nabla})\mathbf{U}$. For the sake of simplicity, we consider the x-component of the advective term in a two-dimensional flow:

$$U\frac{\partial U}{\partial x}+V\frac{\partial U}{\partial y}. \tag{2.16}$$

Furthermore, the velocity components U and V are assumed to be harmonic functions of x and y with wavenumbers k_u^x, k_u^y, k_v^x and k_v^y:

$$U=e^{i\left(k_u^x x+k_u^y y\right)},\quad V=e^{i\left(k_v^x x+k_v^y y\right)}. \tag{2.17}$$

Substituting (2.17) into (2.16) yields

$$ik_u^x e^{i\left(2k_u^x x+2k_u^y y\right)}+ik_u^y e^{i\left[\left(k_u^x+k_v^x\right)x+\left(k_u^y+k_v^y\right)y\right]}. \tag{2.18}$$

Expression (2.18) implies that smaller scales (greater wavenumbers), e.g. $\left(k_u^x+k_v^x\right)$, are created by the nonlinear term, and that all these scales are interacting with each other. On the other hand, introducing U and V in equation (2.17) to the viscous term $\boldsymbol{\nabla}^2U$ does not produce any new scale. The process of producing smaller scales by the advective term is essentially an inviscid process.

Now the question is: when does the viscosity come into play? In order to answer this question, it is worthwhile to assign a Reynolds number to the flow structures based on their length scale. For large structures, we observed that the viscosity is ineffective. The process of structure breakdown produces smaller and smaller scales until the structure Reynolds number becomes very small. At such small scales, the viscosity becomes effective. It dissipates the kinetic energy of the small structures into the heat. Therefore, the structure breakdown process stops here and the dissipation scales are the smallest flow structures that are energetically significant. This process is referred to as the Richardson's energy cascade [111]: kinetic energy

is transferred from the large scales to the small scales and it is dissipated at the smallest scales due to viscosity.

In practice, the scales of turbulence are studied by using the Fourier transform of the velocity field

$$\hat{\mathbf{U}}(\mathbf{k},t) = \iiint_{\Omega} \mathbf{U}(\mathbf{x},t)\, e^{2\pi i(\mathbf{k}\cdot\mathbf{x})} \mathrm{d}^3\mathbf{x}, \tag{2.19}$$

where $\mathbf{k} = \left[k_x, k_y, k_z\right]^{\mathrm{T}}$ is the three-dimensional wavenumber and Ω is the flow domain. $\hat{\mathbf{U}}(\mathbf{k},t)$ is the velocity as a function of the size of the flow structures L that is related to the magnitude of the wavenumber via $L = 2\pi/k$ in which $k = \|\mathbf{k}\|$. The spectrum of the turbulent kinetic energy is defined as

$$E(k,t) = \iiint_{|\mathbf{k}'|=k} \hat{\mathbf{U}}\left(\mathbf{k}',t\right) \cdot \hat{\mathbf{U}}\left(\mathbf{k}',t\right) \mathrm{d}^3\mathbf{k}'. \tag{2.20}$$

Instead of this three-dimensional spectrum, a one-dimensional spectrum is usually considered. The one-dimensional spectrum is defined using one component of the velocity vector measured in one direction. Moreover, in flows with homogeneous direction(s), e.g. the channel flow, the spectrum can be averaged over the homogeneous direction(s). Figure 2.2 shows the one-dimensional energy spectrum E_{uu} in the near-wall region of a turbulent channel flow in the streamwise direction x versus the wavenumber k_x. It can be seen that the energy density of large scales (small wavenumbers) is several decades higher than that of the small scales.

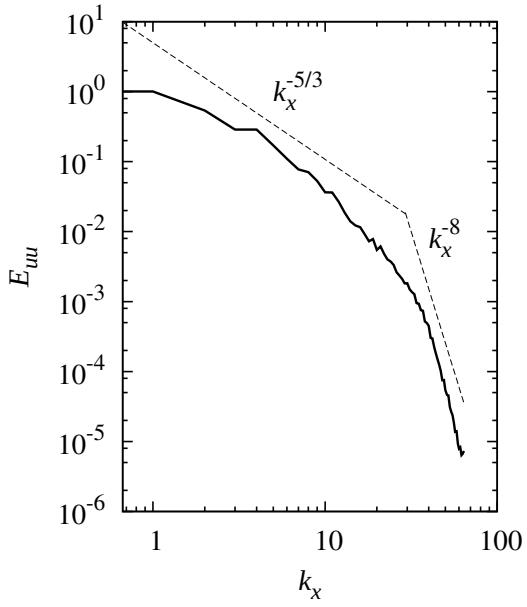

Figure 2.2: A typical one-dimensional energy spectrum E_{uu}.

These large scales contain most of the kinetic energy in a turbulent flow. Therefore, they are called energy-containing scales. The part of the spectrum proportional to $k_x^{-5/3}$ is called the inertial subrange. This proportionality is discussed in the following section. In this subrange, the kinetic energy is transferred from larger scales to the smaller ones with negligible dissipation. This region hardly exists in figure 2.2 which is typical for low Reynolds number turbulent flows. The part of the spectrum that is proportional to k_x^{-8} is called the dissipation range. The spectrum drops off very fast in this region which indicates the dissipation of kinetic energy into heat.

It is notable that the scales of turbulence are frequently related to the term "eddy". Eddy is somewhat difficult to define. It can be explained as a coherent patch of fluid that possesses distinct length, velocity and time scales. Eddies are assumed to be the construction blocks of turbulence.

2.4. Kolmogorov's Theory of Turbulence

Kolmogorov [60, 61] has made an ingenious contribution to the theory of turbulence. He postulated that, at sufficiently high Reynolds numbers, the small scales of turbulence are statistically isotropic [106]. Furthermore, he has made the following two hypotheses that are of paramount importance in the development of modern turbulence theory. The first hypothesis addresses the small scales of turbulence at which the dissipation takes place. The second hypothesis considers the inertial subrange, i.e. the scales at which the dissipation is negligible and inertial effects are dominant. In the following, we briefly present the Kolmogorov's hypotheses and their implications.

Kolmogorov's first hypothesis: *At sufficiently high Reynolds number turbulent flows, the small scales statistics are determined by the dissipation rate ϵ and the viscosity ν.*
Using this postulate and dimensional arguments, Kolmogorov obtained the length scale η, the velocity scale u_η and the time scale τ_η of the smallest eddies in turbulence:

$$\eta = \left(\frac{\nu^3}{\epsilon}\right)^{1/4}, \quad u_\eta = (\nu\epsilon)^{1/4}, \quad \tau_\eta = \left(\frac{\nu}{\epsilon}\right)^{1/2}, \tag{2.21}$$

where η is called the Kolmogorov length scale. Based on η and u_η one can define the Reynolds number of the smallest eddies:

$$\mathrm{Re}_\eta = \frac{\eta u_\eta}{\nu} = 1. \tag{2.22}$$

This explains why the viscosity is dominant at small scales and hence the name dissipation scale.

Kolmogorov's second hypothesis: *At sufficiently high Reynolds number turbulent flows, the statistics of the scales much smaller than the energy-containing scales and much larger than the Kolmogorov scale (i.e. inertial subrange) are solely determined by the dissipation rate ϵ.*

This hypothesis along with dimensional analysis leads to a universal energy spectrum model for the inertial subrange by additionally introducing a length scale ($l \sim 1/k$), where k is the wavenumber:

$$E(k) = C\epsilon^{2/3}k^{-5/3}. \tag{2.23}$$

The proportionality of the energy spectrum to $k^{-5/3}$ in the inertial subrange can be seen in figure 2.2, though it is not very clear due to the low Reynolds number considered.

2.5. Turbulence Statistics

An instantaneous turbulent flow field is irregular and random. Therefore, it is useful to introduce statistical quantities that can be reproduced in experiments and simulations. The random velocity field can be described by a probability density function (PDF) $f(\mathbf{U};\mathbf{x},t)$. The first and second statistical moments of the PDF are defined by

$$\langle \mathbf{U} \rangle (\mathbf{x},t) = \iiint \mathbf{U}(\mathbf{x},t) f(\mathbf{U};\mathbf{x},t)\, \mathrm{d}^3\mathbf{U}, \tag{2.24}$$

$$\langle \mathbf{UU} \rangle (\mathbf{x},t) = \iiint \mathbf{U}(\mathbf{x},t)\mathbf{U}(\mathbf{x},t) f(\mathbf{U};\mathbf{x},t)\, \mathrm{d}^3\mathbf{U}. \tag{2.25}$$

The higher-order moments are defined similarly. The first moment of the PDF (2.24) is the mean velocity. The velocity field is then decomposed as

$$\mathbf{U} = \langle \mathbf{U} \rangle + \mathbf{u}, \tag{2.26}$$

in which $\mathbf{u}$ is the fluctuating velocity with $\langle \mathbf{u} \rangle = \mathbf{0}$. Equation (2.26) is often called the Reynolds decomposition.

An important statistical quantity is the Reynolds stress tensor $\langle \mathbf{uu} \rangle$ defined as

$$\langle \mathbf{uu} \rangle (\mathbf{x},t) = \iiint \mathbf{u}(\mathbf{x},t)\mathbf{u}(\mathbf{x},t) f(\mathbf{U};\mathbf{x},t)\, \mathrm{d}^3\mathbf{U} = \langle \mathbf{UU} \rangle - \langle \mathbf{U} \rangle \langle \mathbf{U} \rangle . \tag{2.27}$$

$\langle \mathbf{uu} \rangle$ appears in the Reynolds equation for the mean flow [106], and is a measure for the intensity and anisotropy of turbulent fluctuations. The diagonal components of $\langle \mathbf{uu} \rangle$ are called turbulence intensities. The square roots of the turbulence intensities are the root-mean-square (r.m.s.) values of the velocity fluctuations, i.e. u_{rms}, v_{rms} and w_{rms}. The turbulence intensities and anisotropy are discussed in more details in section 2.7.

The definition of statistical moments, e.g. equation (2.24), based on the PDF of the velocity field is useful to derive relations between the moments such as relation (2.27). In simulation practice however, different strategies are used to compute the turbulence statistics. These strategies are discussed in the following section.

2.6. Turbulence Simulation

Analytical solution of the Navier-Stokes equations is extremely difficult due to their nonlinearity, and a general analytical solution for turbulent flows does not yet exist. On the other hand, the experimental study of turbulent flows is expensive and time consuming. Therefore, numerical solutions of the Navier-Stokes equations are of great importance to theoretical and industrial researchers in turbulence community. There are mainly three numerical approaches to turbulence [106, 34]:

1. Direct Numerical Simulation (DNS),
2. Large-Eddy Simulation (LES),
3. Statistical Turbulence Modeling (STM).

The principles of each method are discussed in the following. The DNS is explained in more details as it is the approach we take in this thesis.

2.6.1. Direct Numerical Simulation

We have seen in section 2.3 that a turbulent flow contains a broad and continuous range of spatial and temporal scales. A direct numerical simulation (DNS) is a numerical experiment in which all the spatiotemporal scales of turbulence are resolved. This means that the computational box must be large enough to accommodate the largest scales of the turbulent motion. On the other hand, the numerical grid and the time step must be sufficiently fine to resolve the smallest scales of turbulence at which the dissipation of the turbulent kinetic energy takes place. These two requirements impose a great demand on the computational resources. This is the main difficulty in performing DNS. On the other hand, DNS provides invaluable data regarding the detailed structure of turbulent flows. This information has been used to study the physics of turbulence, statistical turbulence models, mechanisms of transition from laminar to turbulent flow, turbulent combustion, compressible turbulence, etc. See for example the reviews in [86, 34, 66, 129] and references therein.

The resolution requirement of the DNS can be explained as follows. The ratio of the integral to the Kolmogorov length scale in a turbulent flow depends on the Reynolds number [106]:

$$\frac{L}{\eta} \sim \mathrm{Re}^{3/4}. \tag{2.28}$$

By taking the three spatial dimensions and the time steps into account, the computational cost of a DNS roughly scales with Re^3. However in practice, the Kolmogorov scale η does not need to be resolved. The spatial resolution has to be $O(\eta)$. The required grid spacing depends on the spectral resolution of the numerical scheme. Generally, a grid spacing of 15η to 20η would be sufficient [96]. This explains why DNS has been so far restricted to relatively low Reynolds number flows, and there is no hope for the application of DNS to industrial problems

in the near future. Therefore, DNS must be seen as a research tool rather than a brute force solution of the Navier-Stokes equations [86].

In addition to the resolution requirements, high fidelity numerical methods are needed for the DNS. For example, methods with significant numerical diffusion are not appropriate for DNS as the dynamics of small scales might be modified by the numerical diffusion. Spectral and pseudospectral methods have been traditionally employed, e.g. [99, 58, 94]. Despite their high order of accuracy, they are limited to relatively simple domains and boundary conditions. Therefore, other numerical methods, mainly based on finite differences and finite volumes, have been successfully applied to DNS of the Navier-Stokes equations, e.g. second-order [43] and compact high-order finite differences [65], second-order [75] and compact fourth-order finite volumes [51], to name a few.

A careful treatment of the boundary conditions is also important. At a smooth wall, no-slip boundary condition can be applied without difficulty. The problem arising here is the resolution of the wall layer which imposes restrictions on the grid spacing in the vicinity of the wall and thus on the time step size. Simulation of a rough wall requires modeling. If the flow possesses homogeneous direction(s) then periodic boundary condition can be applied. In this case, the length of the computational box in the periodic direction(s) must be large enough to contain a sufficient number of coherent structures. A good criterion to verify the appropriateness of the domain length is the decay of the velocity two-point correlation function [58, 34]. The main difficulty lies in the application of in- and outflow conditions [34]. In this thesis however, we simulate a turbulent channel flow that only involves no-slip and periodic boundary conditions. Therefore, we do not go into the details of in- and outflow conditions.

2.6.2. Large-Eddy Simulation

The large-eddy simulation (LES) technique is based on two assumptions. First, the large scales of turbulence that contain virtually all of the turbulent kinetic energy, highly depend on the problem. Secondly, the small scales of turbulence reveal universal behavior and are independent of the dynamics of the large scales. These postulates are supported by experiment and also by the success of LES to predict complex flows [83, 113, 69].

In the LES approach, the large, energy-containing scales are resolved while the effect of the unresolved small scales is modeled by the so-called subgrid scale (SGS) model. This is done by solving the filtered Navier-Stokes equations

$$\boldsymbol{\nabla} \cdot \widetilde{\mathbf{U}} = 0, \tag{2.29}$$

$$\frac{\partial \widetilde{\mathbf{U}}}{\partial t} + \left(\widetilde{\mathbf{U}} \cdot \boldsymbol{\nabla}\right) \widetilde{\mathbf{U}} = -\frac{1}{\rho} \boldsymbol{\nabla} \widetilde{p} + \nu \boldsymbol{\nabla}^2 \widetilde{\mathbf{U}} - \boldsymbol{\nabla} \cdot \boldsymbol{\tau}^{\mathrm{SGS}}, \tag{2.30}$$

using a low-pass filter, i.e. a filter that passes small wavenumbers (large scales) and attenuates large wavenumbers (small scales). An over-tilde in equations (2.29) and (2.30) denotes a filtered quantity. The subgrid scale stress tensor $\boldsymbol{\tau}^{\mathrm{SGS}}$ is to be modeled. The Smagorinsky

model [118] is usually used for this purpose:

$$\boldsymbol{\tau}^{\mathrm{SGS}} = -2\nu_{\mathrm{T}}\widetilde{\mathbf{D}}, \tag{2.31}$$

in which

$$\widetilde{\mathbf{D}} = \frac{1}{2}\left(\boldsymbol{\nabla}\widetilde{\mathbf{U}} + \boldsymbol{\nabla}\widetilde{\mathbf{U}}^{\mathrm{T}}\right), \tag{2.32}$$

is the filtered strain-rate tensor and

$$\nu_{\mathrm{T}} = \left(C_s\Delta_g\right)^2\sqrt{2\,\widetilde{\mathbf{D}} : \widetilde{\mathbf{D}}}, \tag{2.33}$$

is the turbulent viscosity. C_s and Δ_g are the model constant and the grid spacing, respectively. The computational grid acts as the filter in the Smagorinsky model.

Due to the lack of a full resolution, the complete energy spectrum cannot be recovered in LES. One-dimensional spectra obtained from DNS and LES of turbulent channel flow are shown in figure 2.3. It is seen that the LES spectrum follows the DNS one up to some wavenumber and then, deviates and drops off faster. However, by improving the resolution, the contribution of the SGS model reduces and the quality of the solution eventually increases.

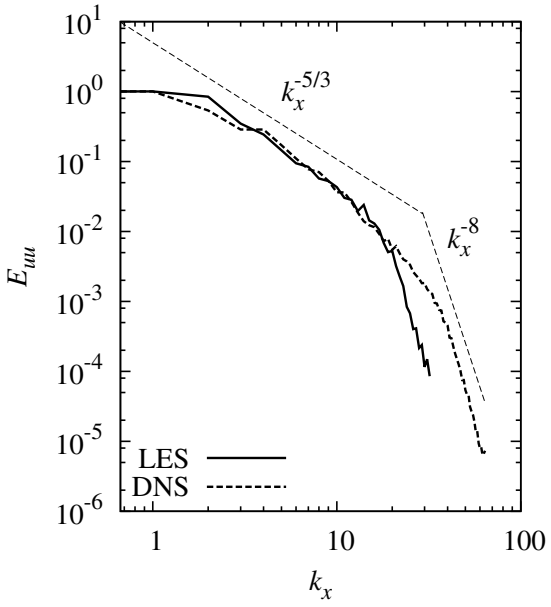

Figure 2.3: Typical one-dimensional energy spectra E_{uu} obtained by DNS and LES. The spectra are normalized by the energy of the first mode.

2.6.3. Statistical Turbulence Modeling

In this approach, which is also known as the Reynolds-averaged Navier-Stokes simulations (RANS), only the mean quantities are computed. Hence, the most loss of information on turbulence is associated with this approach. Application of the averaging operator on the nonlinear Navier-Stokes equations results in a closure problem. Therefore, turbulence modeling plays a vital role in the RANS context. However, due to its inexpensive computations as compared to LES and DNS, RANS is still the preferred simulation strategy in industrial applications of CFD. There has been an increasing tendency in recent years to use LES and coupled RANS/LES methods in industries [12].

2.7. Turbulent Channel Flow

The flow between two parallel plates of infinite span due to a constant pressure gradient is called the plane channel flow. Simulation of such an infinitely large domain is difficult, if not impossible. In practice, the simulation is conducted inside a box of finite size. The wall-normal direction z is bounded by the two walls with distance $2h$. Periodicity is assumed in the other two directions, i.e. the streamwise (x) and spanwise (y) directions. It is important that the box size in periodic directions be large enough to contain a representative of the flow structures. Jiménez and Moin [55] have investigated the minimal box that is required to sustain the turbulence. For example, they have found out that it is not possible to sustain turbulence in domains with a spanwise length of less than 100 wall units. The wall units are to be explained later in this section. The flow is driven by a constant (negative) mean pressure gradient $\mathrm{d}\langle p \rangle / \mathrm{d}x$. This flow configuration is schematically sketched in figure 2.4.

The turbulent channel flow was the first wall-bounded turbulent flow studied by DNS [86]. Surprisingly, DNS of turbulent flow in a channel with curved walls [96] preceded that of a plane channel [58]. Since then, the turbulent channel flow has been a standard benchmark

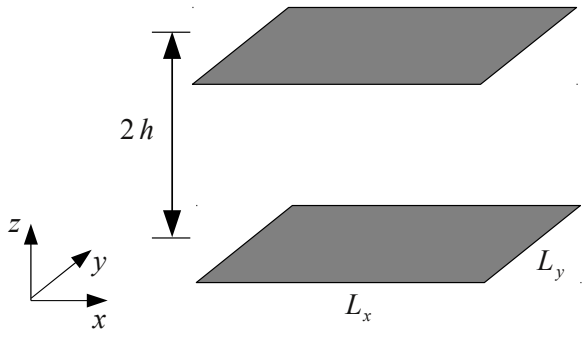

Figure 2.4: Schematic sketch of plane channel flow with dimensions L_x, L_y and $2h$ in streamwise, spanwise and wall-normal directions, respectively.

to study the physics of turbulent wall-bounded flows. In this thesis, we present the dynamics of elongated spheroidal particles in a turbulent channel flow using DNS.

In the following we introduce some basic concepts and non-dimensional parameters used to describe and characterize the channel flow statistics. For a more comprehensive discussion, the reader is referred to [106].

The bulk Reynolds number is defined as

$$\mathrm{Re}_b = \frac{U_b h}{\nu}, \tag{2.34}$$

with U_b, h and ν being the bulk velocity, channel half-width and the kinematic viscosity, respectively. The bulk velocity is computed from the mean velocity profile:

$$U_b = \frac{1}{2h}\int_0^{2h} \langle U \rangle (z)\, \mathrm{d}z. \tag{2.35}$$

The mean shear stress exerted by the flow on the wall reads

$$\tau_w = \mu \left.\frac{\mathrm{d}\langle U \rangle}{\mathrm{d}z}\right|_w, \tag{2.36}$$

in which the velocity gradient is calculated at the wall. The mean shear stress relates to the mean pressure gradient via

$$\tau_w = -h \frac{\mathrm{d}\langle p \rangle}{\mathrm{d}x}. \tag{2.37}$$

The friction velocity is defined as

$$u_\tau = \sqrt{\frac{\tau_w}{\rho}}. \tag{2.38}$$

The wall distance and the velocity are non-dimensionalized using the kinematic viscosity and the friction velocity:

$$z^+ = \frac{z u_\tau}{\nu}, \quad \langle U \rangle^+ = \frac{\langle U \rangle}{u_\tau}, \tag{2.39}$$

in which z^+ is called wall (viscous) coordinate. Such a non-dimensionalization is referred to as inner scaling. The friction Reynolds number is defined based on the friction velocity and the channel half-width:

$$\mathrm{Re}_\tau = \frac{u_\tau h}{\nu}. \tag{2.40}$$

For example, the first DNS of a plane channel flow [58] was performed at $\mathrm{Re}_\tau = 180$. The Kolmogorov length scale η in a turbulent channel flow can be estimated by knowing u_τ

[113]:

$$\eta = \left(\frac{\nu^3}{\epsilon}\right)^{1/4}, \quad \epsilon = \frac{u_\tau^2 U_b}{h}. \tag{2.41}$$

The mean velocity profile in the channel can be divided in various regions. The region $z^+ < 5$, the viscous sublayer, where the viscosity is dominant and the Reynolds shear stress is negligible. The mean velocity profile is well approximated by the linear law in the viscous sublayer:

$$\langle U \rangle^+ = z^+. \tag{2.42}$$

The viscous sublayer has to be well resolved in a DNS. The thickness of the viscous sublayer decreases with increasing the Reynolds number. Thus, the resolution of the wall layer in high Reynolds number flows is a computational challenge.

For $z^+ > 30$ and $z/h < 0.3$, the following logarithmic law holds as a good approximation to the mean velocity profile:

$$\langle U \rangle^+ = \frac{1}{\kappa} \ln z^+ + B, \tag{2.43}$$

where the von Kármán constant $\kappa = 0.4$, and $B = 5.5$. The mean velocity profile $\langle U \rangle^+$ of the turbulent channel flow at $\mathrm{Re}_\tau = 180$ is plotted versus z^+ in figure 2.5 along with the guidelines (2.42) and (2.43). It is generally accepted that the linear law is valid for $z^+ < 5$, and that the logarithmic law holds between $z^+ > 30$ and $z/h < 0.3$ [106].

The mean velocity $\langle \mathbf{U} \rangle$ is a first-order statistical quantity. Beside the first-order statistics, it is useful to look at the second-order statistics. The Reynolds stress tensor $\langle \mathbf{uu} \rangle$ is an important

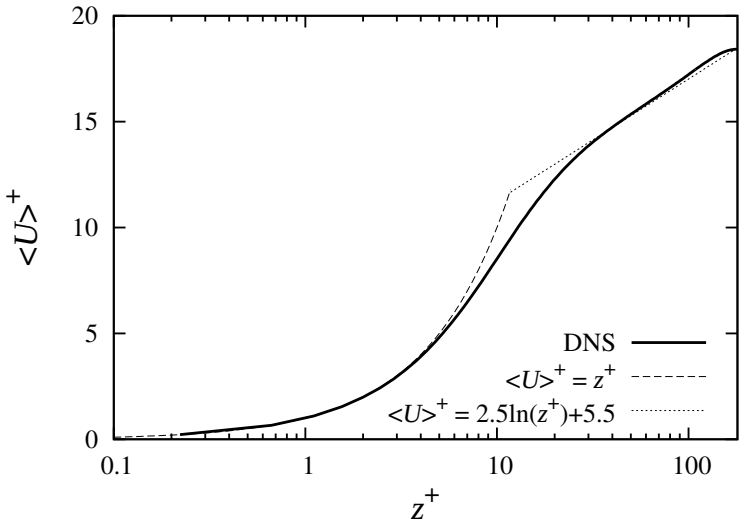

Figure 2.5: Mean velocity profile $\langle U \rangle^+$ versus z^+ of turbulent channel flow at $\mathrm{Re}_\tau = 180$.

second-order quantity. It is the unclosed term in the RANS approach. Furthermore, $\langle \mathbf{uu} \rangle$ is a measure of the intensity and anisotropy of turbulence. The diagonal components of $\langle \mathbf{uu} \rangle$, i.e. the Reynolds normal stresses $\langle uu \rangle$, $\langle vv \rangle$ and $\langle ww \rangle$ are called turbulence intensities. The square root of the turbulence intensities is the root-mean-square (r.m.s.) or standard deviation of velocity fluctuations. Figure 2.6 shows the r.m.s. of velocity fluctuations as a function of the wall distance z^+. The r.m.s. values are normalized by the shear velocity u_τ:

$$u^+_{\mathrm{rms}} = \frac{\sqrt{\langle uu \rangle}}{u_\tau}, \quad v^+_{\mathrm{rms}} = \frac{\sqrt{\langle vv \rangle}}{u_\tau}, \quad w^+_{\mathrm{rms}} = \frac{\sqrt{\langle ww \rangle}}{u_\tau}. \tag{2.44}$$

Half of the trace of $\langle \mathbf{uu} \rangle$, i.e.

$$\mathrm{TKE} = \frac{1}{2}\mathrm{tr}\left\{\langle \mathbf{uu} \rangle\right\} = \frac{1}{2}\langle \mathbf{uu} \rangle : \mathbf{1} = \frac{1}{2}\left(\langle uu \rangle + \langle vv \rangle + \langle ww \rangle\right) \tag{2.45}$$

is the turbulent kinetic energy (TKE), which is plotted in figure 2.7 for a turbulent channel flow at $\mathrm{Re}_\tau = 180$ as a function of the wall distance z^+. The turbulent kinetic energy vanishes at the wall and is maximum in the buffer layer.

Together with turbulence intensities, the anisotropy of turbulence is also reflected by the Reynolds stress tensor $\langle \mathbf{uu} \rangle$. The anisotropy is often represented by the Lumley anisotropy map [68]. In this approach, the anisotropic part of the Reynolds stress tensor $\langle \mathbf{uu} \rangle$ is defined in the following manner:

$$\mathbf{a} = \frac{\langle \mathbf{uu} \rangle}{\langle \mathbf{uu} \rangle : \mathbf{1}} - \frac{1}{3}\mathbf{1} = \frac{\langle \mathbf{uu} \rangle}{2\,\mathrm{TKE}} - \frac{1}{3}\mathbf{1}. \tag{2.46}$$

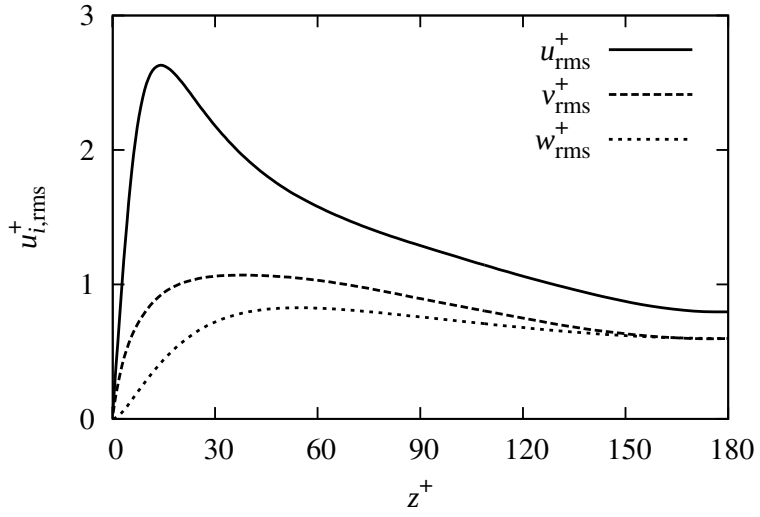

Figure 2.6: Root-mean-square (r.m.s.) of velocity fluctuations $u^+_{i,\mathrm{rms}}$ versus z^+ in turbulent channel flow at $\mathrm{Re}_\tau = 180$.

a is a symmetric tensor similar to $\langle \mathbf{uu} \rangle$. The two scalar invariants of the anisotropy tensor **a** are given by

$$\mathrm{II}_a = \mathbf{a} : \mathbf{a}, \tag{2.47}$$

$$\mathrm{III}_a = (\mathbf{a} \cdot \mathbf{a}) : \mathbf{a}. \tag{2.48}$$

In figure 2.8, II_a is plotted versus III_a for a turbulent channel flow at $\mathrm{Re}_\tau = 180$. The Lumley triangle is sketched by the dashed line. All possible realizations lie within this triangle. The upper line defined by

$$\mathrm{II}_a = \frac{2}{9} + 2\,\mathrm{III}_a, \tag{2.49}$$

describes the two-component turbulence state. The right and left lines are defined by the following nonlinear function:

$$\mathrm{II}_a = \frac{3}{2}\left(\frac{4}{3}\left|\mathrm{III}_a\right|\right)^{2/3}. \tag{2.50}$$

They describe the axisymmetric turbulence state, i.e. when two values of the turbulence intensities are equal and the third component is different. In more details, the left curve represents a state in which the different intensity is smaller than the two equal intensities, the so-called oblate spheroidal state of turbulence. Conversely, the right curve stands for the state in which the different turbulence intensity is greater than the other two equal intensities, the so-called prolate spheroidal state of turbulence. In the center of the channel, u_{rms} is greater than v_{rms} and w_{rms}, and the curve falls on the right guideline. The limiting cases reside on the corners of the Lumley triangle. The intersection of the two-component and the oblate

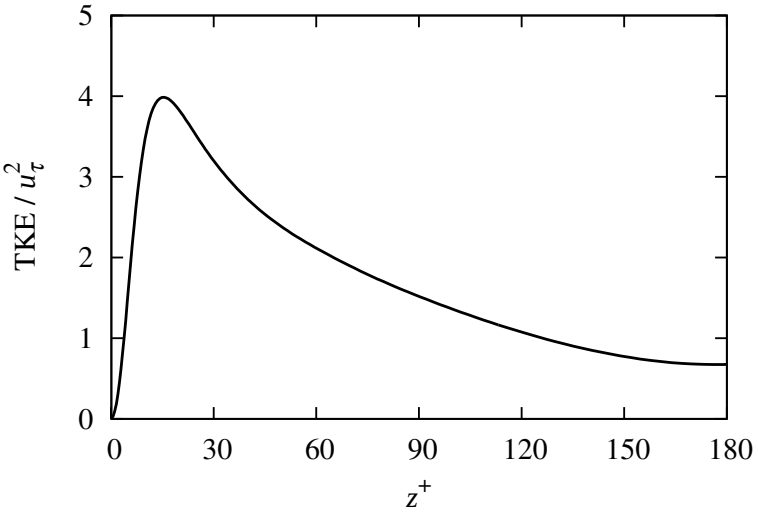

Figure 2.7: Turbulent kinetic energy (TKE) versus z^+ in turbulent channel flow at $\mathrm{Re}_\tau = 180$. TKE is normalized by u_τ^2.

spheroidal curves represents the two-component isotropic turbulence. The one-component turbulence state is located at the intersection of the two-component and the prolate spheroidal curves. Finally, the intersection of the two axisymmetric turbulence curves describes the three-component isotropic turbulence.

The continuous curve in figure 2.8 shows the anisotropy of turbulent channel flow at $\mathrm{Re}_\tau = 180$. Point A is at the wall ($z^+ = 0$), point B is in the buffer layer (at about $z^+ = 8$) and point C is at the center plane of the channel ($z^+ = 180$). A two-component turbulence state is found in the viscous sublayer. In the buffer layer, turbulence tends towards a one-component state, and after that, a nearly prolate spheroidal state of turbulence can be seen. This tends towards an isotropic turbulence state in the center plane of the channel.

By integrating the streamwise mean momentum equation we find out that the sum of the viscous and Reynolds shear stresses is balanced on a straight line:

$$\mu \frac{\mathrm{d}\langle U \rangle}{\mathrm{d}z} - \rho \langle uw \rangle = \tau_w \left(1 - \frac{z}{h}\right), \tag{2.51}$$

or alternatively

$$\nu \frac{\mathrm{d}\langle U \rangle}{\mathrm{d}z} - \langle uw \rangle = u_\tau^2 \left(1 - \frac{z}{h}\right). \tag{2.52}$$

The contribution of the viscous and Reynolds stresses to the total shear stress along the wall-normal direction is shown in figure 2.9. The stresses in figure 2.9 are normalized by the wall shear stress τ_w, and the wall distance z is normalized by the channel half-width h. At

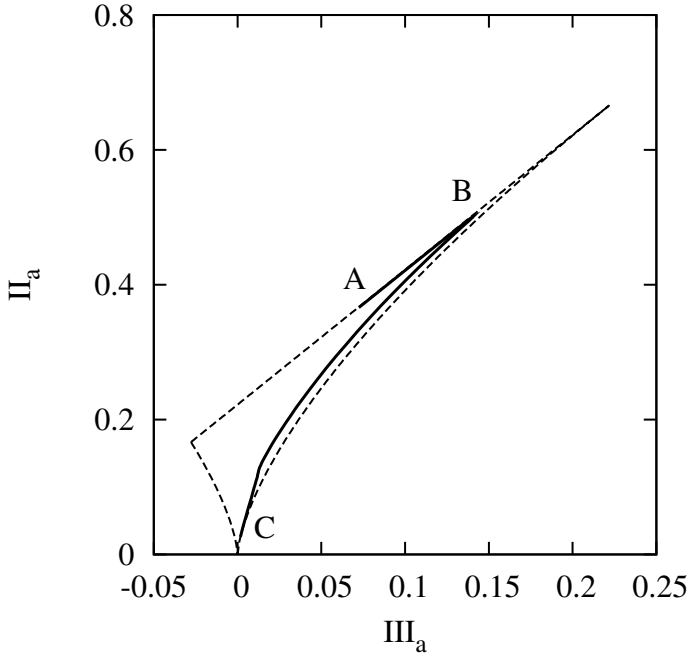

Figure 2.8: Lumley anisotropy map obtained by DNS of turbulent channel flow at $\mathrm{Re}_\tau = 180$.

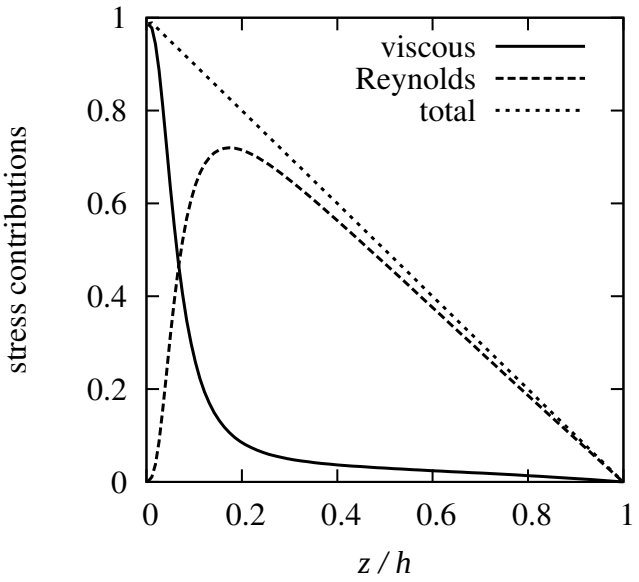

Figure 2.9: The viscous and Reynolds contributions to the total shear stress obtained by a DNS of turbulent channel flow at $\mathrm{Re}_\tau = 180$.

the wall, the viscous stress is maximum while the Reynolds stress vanishes. Farther from the wall, the viscous stress reduces monotonically. The Reynolds stress reaches a maximum at a wall distance of about $z/h = 0.2$, at the considered Re_τ, and drops off afterwards. Both contributions vanish at the channel center plane $z/h = 1$.

3. Rheology of a Dilute Suspension of Brownian Spheroidal Particles

"τα παντα ρει (everything flows)"

Heraclitus of Ephesus, 535-475 BC

A piece of rubber extends considerably under the application of a moderate tensile force while a piece of steel only shows an infinitesimal extension under the same loading. Stir a glass of water and a bowl of yoghurt for a while. No change is seen in the water viscosity while the yoghurt flows more easily with a reduced viscosity. Materials behave differently under loading of external forces. Based on these differences, we can classify the engineering materials in categories such as elastic solids, Newtonian fluids, viscoelastic materials, etc. The science of rheology studies the flow of matter. The name rheology comes from the famous quotation of Heraclitus written above: *ta panta rhei*. The Greek word *rhei* means to flow.

In this chapter, the rheology of a dilute suspension of Brownian spheroidal particles is presented. A suspension consists of small solid particles suspended in a liquid. Thus, a suspension flow is an example of a two-phase flow. In simulation practice however, the two-phase flow of the fluid-particle system is exchanged with a single-phase flow in which the effect of the suspended particles is modeled by additional forces and stresses. This process is called homogenization. Einstein's work [27, 28] is regarded as a pioneering theoretical breakthrough in the mechanics of suspension flows. He studied the dilute suspension of small spherical particles in a Newtonian fluid and concluded that the effect of the suspended particles can be described by an increase in the viscosity:

$$\mu_{\text{eff}} = \mu \left(1 + \frac{5}{2}\phi \right), \tag{3.1}$$

where ϕ is the volume fraction of the suspended particles and μ_{eff} is the effective viscosity of the homogenized single-phase fluid. This means that the homogenized system behaves similar to a Newtonian fluid with an increased viscosity. If the shape of the suspended particles deviates from a sphere, then the fluid reveals anisotropic behavior and is classified as a non-Newtonian fluid. Calculation of the non-Newtonian stress due to the presence of spheroidal particles is the main subject of this chapter.

The chapter is organized as follows. The underlying assumptions and definitions of the rheological theory that is used throughout this thesis are presented in section 3.1. Brownian motion is briefly noted in section 3.2. Then, we turn to the orientation dynamics of rigid fibers in section 3.3 by explaining Jeffery's theory, Fokker-Planck equation for the orientation distribution function and the moment approximation approach. Some moment closure models are also presented. Brenner's rheological theory of dilute Brownian fiber suspensions is detailed in section 3.6. This theory enables us to compute the non-Newtonian stress tensor from the orientation distribution of fibers. The behavior of the non-Newtonian stress in the limit of very strong Brownian motion is investigated in subsection 3.6.1 using Brenner's theory. This, in the case of a channel flow, provides us with an analytical benchmark that will be used later to validate the numerical methods and their computer implementation. Finally, we denote Hinch and Leal's rheological theory in section 3.7 and present its link to Brenner's theory.

3.1. Basic Assumptions and Definitions

Throughout this thesis, the terms carrier fluid and solvent refer to the Newtonian fluid in which the particles are suspended. The spheroidal particles are assumed to be rigid and neutrally buoyant. The latter means that the suspended particles have the same density as the carrier fluid. This assumption implies that the suspended particles affect the flow field only via an extra non-Newtonian stress [11]. Moreover, the particles are assumed to be smaller than the smallest flow structures, i.e. the Kolmogorov's scale in a turbulent flow. This means that every individual particle experiences a linear creeping flow and hence, the particle orientation is described by the Jeffery's theory. These assumptions imply that all the inertial effects are neglected in this work.

The term inertial effects needs to be clarified. It can be referred to the carrier fluid and/or to the suspended particles. The inertial effect of the carrier fluid means that whether a creeping flow is assumed around the particles. If a creeping flow is assumed, the inertial term (i.e. the convective term) of the Navier-Stokes equation is neglected, and the particle orientation is described by solving the Stokes equation. This is the basic assumption of Jeffery's [54] and Brenner's [11] theories. Subramanian and Koch [122] have studied the fiber motion in a simple shear flow by taking into account the fluid inertia. On the other hand, the particle inertial effects are due to the translational and rotational inertia of the particle. Of course, a real fiber possesses both. According to the author's knowledge, only one-way coupled simulations of inertial fibers in turbulent flows have been available to date [29, 136, 91, 92, 93, 77].

The particles considered in this work have a spheroidal shape. A spheroid is a special case of an ellipsoid. An ellipsoid is a quadratic surface (as shown in figure 3.1a) defined by the following quadratic equation:

$$\frac{\left(x - x_C\right)^2}{a^2} + \frac{\left(y - y_C\right)^2}{b^2} + \frac{\left(z - z_C\right)^2}{c^2} = 1, \tag{3.2}$$

where (x_C, y_C, z_C) is the Cartesian coordinate of the centroid of the ellipsoid. a, b and c are the equatorial radii of the ellipsoid in x, y and z directions, respectively. The case $a = b = c = R$ defines a sphere of radius R as depicted in figure 3.1b, while the case $a = b \neq c$ gives a spheroid with the aspect ratio $r = L/a$ in which $L = c$. The spheroids are twofold. First, prolate spheroids with $a = b < L$, i.e. $1 < r < \infty$, as sketched in figure 3.1c. The case $r \to \infty$ defines a slender rod-like particle, i.e. a rigid fiber. Second, the oblate spheroids with $a = b > L$ or $0 < r < 1$, as shown in figure 3.1d. The case $r \to 0$ defines a thin disk-like particle.

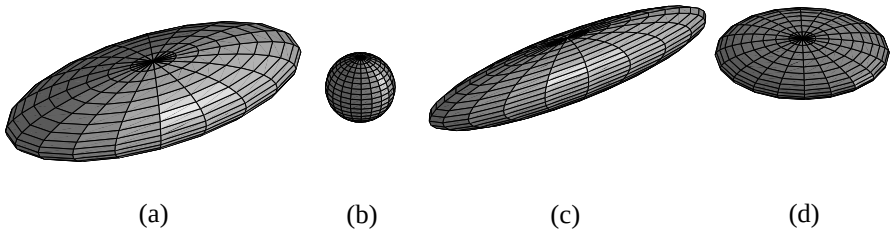

Figure 3.1: Sketch of (a) ellipsoid (b) sphere (c) prolate spheroid and (d) oblate spheroid.

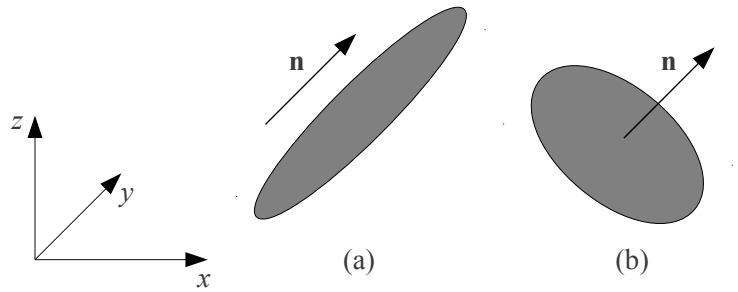

Figure 3.2: Schematic sketch of (a) prolate and (b) oblate spheroidal particle and their orientation vector **n**.

The spheroidal particles are identified by their orientation unit vector **n**. The definition of **n** is different for prolate and oblate spheroids. **n** is parallel to the rod major axis for the former while it is perpendicular to the disk plane for the latter. The definition of **n** for both prolate and oblate spheroids is schematically shown in figure 3.2. Since **n** is a unit vector, the space of all possible orientations is the surface of the unit sphere **S**. At any position **x** within the flow field and at any time instant t, the probability density of finding a particle with orientation **n** is given by the orientation distribution function $\Psi(\mathbf{n}; \mathbf{x}, t)$. We shall come back to the orientation distribution function in more details in section 3.3.

Furthermore, we assume that the suspension is dilute. In order to define a dilute suspension, one needs to define a measure of particle concentration. One typical measure is the

particle number density:

$$n = \frac{N_P}{V_t}, \tag{3.3}$$

where N_P is the number of particles and V_t is the total volume occupied by the particles and the carrier fluid. Another measure which is frequently used in rheological theories of particle suspensions is the volume fraction:

$$\phi = \frac{N_P V_P}{V_t} = n V_P, \tag{3.4}$$

in which V_P is the volume of a single particle. Thus, the volume fraction ϕ is the ratio of the total volume of particles $N_P V_P$ to the total volume of particles and carrier fluid V_t. The volume of a spheroidal object reads

$$V_P = \frac{4}{3}\pi a^2 L. \tag{3.5}$$

For a prolate spheroidal particle (fiber), the following relation between the volume fraction ϕ and the number density n can be derived:

$$\phi = \frac{4\pi n L^3}{3r^2}, \tag{3.6}$$

where $a = L/r$ is used. nL^3 is called the concentration parameter.

Based on the volume fraction ϕ and the aspect ratio r, three distinct concentration regimes can be realized in a fiber suspension flow (see for example [23]). A fiber suspension is considered dilute if $\phi r^2 < 1$. In a dilute suspension, both hydrodynamic and mechanical interactions between particles are negligible. Hydrodynamic interaction is the remote mutual influence of particles through the hydrodynamic field of the carrier fluid. The mechanical interaction is due to the mechanical contact of individual particles. In case where $\phi r < 1 < \phi r^2$ the suspension is in a semi-dilute regime. In this case, the mechanical interactions are still negligible while the hydrodynamic interactions are to be considered. Finally, when $\phi r > 1$ we have a concentrated suspension in which both hydrodynamic and mechanical interactions are significant. These regimes can also be expressed in terms of the concentration parameter nL^3 in the following way. The suspension is dilute if $nL^3 < 1$, semi-dilute if $1 < nL^3 < r$ and concentrated if $nL^3 > r$. The concentration regimes are schematically sketched in figure 3.3, in which an ellipse represents a fiber and a hatched circle stands for the hydrodynamic interaction zone.

Due to the above-mentioned assumptions, the rheological theory of a dilute suspension of Brownian spheroidal particles in a Newtonian carrier fluid is employed in the present study. This theory is explained in the following sections.

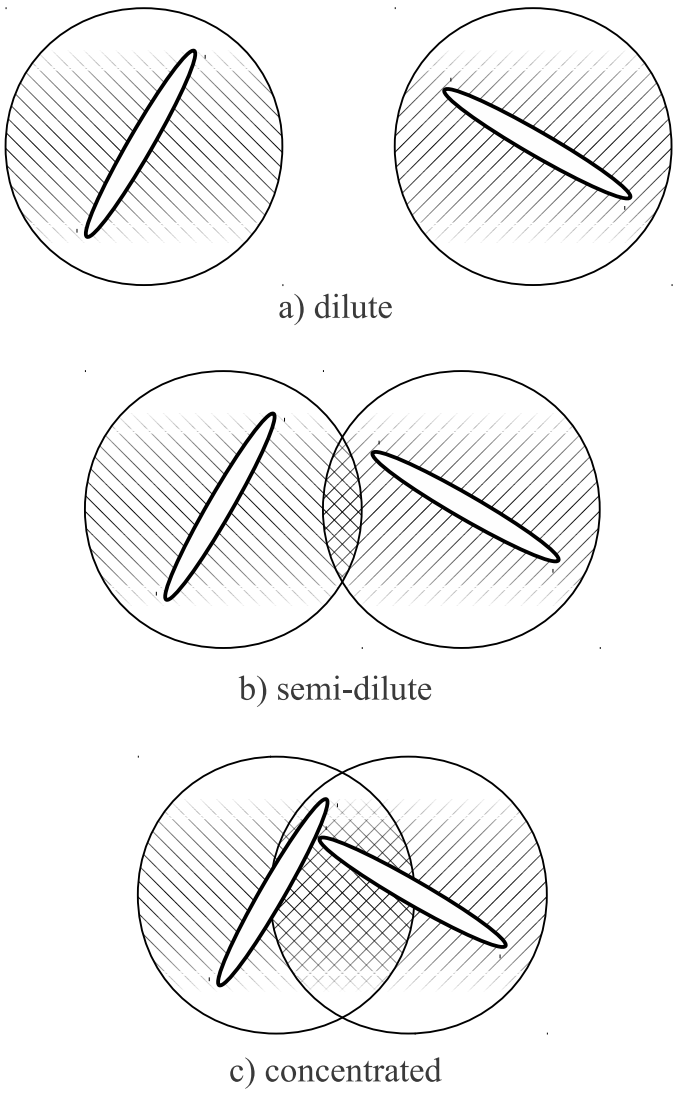

Figure 3.3: Schematic of three concentration regimes: a) dilute regime without hydrodynamic and mechanical interactions, b) semi-dilute regime with hydrodynamic and without mechanical interactions, c) concentrated regime with hydrodynamic and mechanical interactions. An ellipse represents a fiber and a hatched circle represents the hydrodynamic interaction zone.

3.2. Brownian Motion

A tiny particle that is suspended in a quiescent fluid moves in a seemingly random manner. A good example is the motion of dust particles suspended in the air when seen in the light ray inside a dark room. The reason is the collision with a huge number of fluid atoms/molecules that are typically much smaller and lighter than the suspended particles. A typical simulated Brownian path of a particle is shown in figure 3.4. The random and fluctuating nature of the motion can be observed.

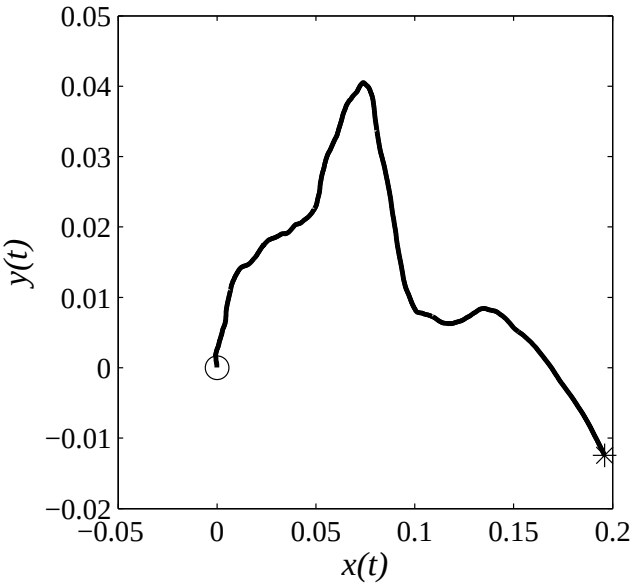

Figure 3.4: A typical simulated Brownian path of a particle, ∘ start point, ∗ end point.

Einstein [26] has formulated that the intensity of the Brownian motion experienced by a spherical particle is characterized by the Brownian diffusivity

$$D = \frac{k_B T}{\gamma}, \tag{3.7}$$

where $k_B \approx 1.381 \times 10^{-23} J/K$, T and γ are the Boltzmann constant, the absolute temperature of the fluid and the Stokes' drag coefficient of the suspended particle, respectively. The orientation of spherical particles is indefinite and hence immaterial. For elongated particles however, the orientation is important. Therefore, we should distinguish between their spatial and rotary Brownian motions. The former takes place in the physical space and exists for both spherical and elongated particles. The latter is a random motion in the orientation space of the elongated particles. The spatial and rotary Brownian diffusivities of fibers scale

as

$$D_s \propto \frac{k_B T}{\mu l}, \tag{3.8}$$

$$D_r \propto \frac{k_B T}{\mu l^3}, \tag{3.9}$$

respectively. In equations (3.8) and (3.9), $l = 2L$ is the fiber length. The ratio of the spatial to the rotary Brownian diffusivities reads

$$\frac{D_s}{D_r} \propto l^2. \tag{3.10}$$

Since we consider microfibers (with $l \ll 1$) in the present work, D_s is negligible as compared to D_r. Thus, the spatial Brownian motion is neglected throughout this thesis.

The intensity of the rotary Brownian motion is quantified by a dimensionless group, the rotary Péclet number:

$$\mathrm{Pe}_r = \frac{\dot{\gamma}}{D_r}, \tag{3.11}$$

where $\dot{\gamma}$ is a characteristic shear rate of the flow. Table 3.1 shows the rotary Péclet number of rigid fibers suspended in a turbulent channel flow at $\mathrm{Re}_\tau = 180$ and temperature $T = 300K$, as a function of the fiber length l. The rotary and spatial Brownian diffusivities are shown as well. The bulk velocity and the channel half-width are $U_b = 1m/s$ and $h = 1m$, respectively. It is seen that depending on the fiber length, the Péclet number ranges from relatively small to very large numbers. A shorter fiber leads to a smaller Pe_r and vice versa.

Table 3.1: Rotary Péclet number Pe_r of rigid fibers in turbulent channel flow at $\mathrm{Re}_\tau = 180$ and temperature $T = 300K$ with $U_b = 1m/s$ and $h = 1m$, as a function of the fiber length l. The rotary and spatial Brownian diffusivities are also shown.

$l\ [m]$	1×10^{-3}	1×10^{-4}	1×10^{-5}	1×10^{-6}
Pe_r	8.6×10^{9}	8.6×10^{6}	8.6×10^{3}	8.6
D_r	1.16×10^{-10}	1.16×10^{-7}	1.16×10^{-4}	1.16×10^{-1}
D_s	1.16×10^{-16}	1.16×10^{-15}	1.16×10^{-14}	1.16×10^{-13}

3.3. Orientation Dynamics of Rigid Fibers

In this section, we present the differential equations that govern the orientation dynamics of rigid fibers within a given flow field. The orientation of a rigid fiber is solely described by its unit axial vector $\mathbf{n}$. Therefore, one needs an evolution equation for $\mathbf{n}$. Jeffery [54] has analytically studied the Stokes flow around a neutrally buoyant non-Brownian ellipsoidal particle. This means that the inertial effects of the fluid and the particle were both neglected. He derived a differential equation for the time evolution of the orientation vector $\mathbf{n}$ of a non-Brownian ellipsoid:

$$\frac{\mathrm{D}\mathbf{n}}{\mathrm{D}t} = \boldsymbol{\Omega}\cdot\mathbf{n} + \kappa\left[\mathbf{D}\cdot\mathbf{n} - (\mathbf{n}\cdot\mathbf{D}\cdot\mathbf{n})\,\mathbf{n}\right], \tag{3.12}$$

where $\boldsymbol{\Omega}$ and $\mathbf{D}$ are the rotation-rate and strain-rate tensors, respectively. κ is the particle shape factor:

$$\kappa = \frac{r^2-1}{r^2+1}. \tag{3.13}$$

The term $\boldsymbol{\Omega}\cdot\mathbf{n}$ is a rigid body rotation of the orientation vector $\mathbf{n}$. Therefore, it preserves the length of $\mathbf{n}$. The term $\mathbf{D}\cdot\mathbf{n}$ is a straining of $\mathbf{n}$ and hence changes its length. The last term $(\mathbf{n}\cdot\mathbf{D}\cdot\mathbf{n})\,\mathbf{n}$ projects back the straining of $\mathbf{n}$ so that the length of $\mathbf{n}$ is preserved. Note that $\mathbf{n}$ is a unit vector with $\|\mathbf{n}\| = 1$. It means that equation (3.12) preserves the length of $\mathbf{n}$ [88]. In order to verify this preservation property, we calculate the inner product of $\mathbf{n}$ to both sides of equation (3.12):

$$\begin{aligned}\frac{1}{2}\frac{\mathrm{D}\mathbf{n}\cdot\mathbf{n}}{\mathrm{D}t} &= \mathbf{n}\cdot\boldsymbol{\Omega}\cdot\mathbf{n} + \kappa\left[\mathbf{n}\cdot\mathbf{D}\cdot\mathbf{n} - \mathbf{n}\cdot(\mathbf{n}\cdot\mathbf{D}\cdot\mathbf{n})\,\mathbf{n}\right]\\ &= \boldsymbol{\Omega}:\mathbf{nn} + \kappa\left[\mathbf{n}\cdot\mathbf{D}\cdot\mathbf{n} - (\mathbf{n}\cdot\mathbf{D}\cdot\mathbf{n})\,\mathbf{n}\cdot\mathbf{n}\right]\\ &= \kappa\,(\mathbf{n}\cdot\mathbf{D}\cdot\mathbf{n})(1-\mathbf{n}\cdot\mathbf{n}),\end{aligned} \tag{3.14}$$

where $\mathbf{n}\cdot\boldsymbol{\Omega}\cdot\mathbf{n} = \boldsymbol{\Omega}:\mathbf{nn} = 0$, because $\boldsymbol{\Omega}$ is skew-symmetric and $\mathbf{nn}$ is symmetric. Equation (3.14) implies that if the initial condition of the Jeffery equation (3.12) satisfies $\mathbf{n}\cdot\mathbf{n} = \|\mathbf{n}\|^2 = 1$, then the condition $\mathbf{n}\cdot\mathbf{n} = \|\mathbf{n}\|^2 = 1$ is satisfied for all times.

Often in a suspension, there exists a huge number of particles that are influenced by the carrier flow field as well as the Brownian motion. Thus, the particle orientation is described via a distribution function $\Psi(\mathbf{n};\mathbf{x},t)$ which is the probability density of finding a particle with the orientation $\mathbf{n}$ at the position $\mathbf{x}$ in space and at the time instant t. The conservation of probability is expressed in the form of a Fokker-Planck equation [71]:

$$\frac{\mathrm{D}\Psi}{\mathrm{D}t} = \frac{\partial\Psi}{\partial t} + \mathbf{U}\cdot\boldsymbol{\nabla}\Psi = -\boldsymbol{\nabla}_{\mathbf{n}}\cdot\left(\Psi\frac{\mathrm{D}\mathbf{n}}{\mathrm{D}t}\right) + D_r\Delta_{\mathbf{n}}\Psi, \tag{3.15}$$

where $\boldsymbol{\nabla}_{\mathbf{n}}$ and $\Delta_{\mathbf{n}}$ are the Nabla and Laplacian operators defined on the surface of the unit

sphere. The time derivative of the orientation vector $\dot{\mathbf{n}} = \mathrm{D}\mathbf{n}/\mathrm{D}t$ that appears in equation (3.15) is given by the right-hand side of the Jeffery equation (3.12). Equation (3.15) consists of a drift term $\boldsymbol{\nabla}_{\mathbf{n}} \cdot (\Psi \dot{\mathbf{n}})$ and a diffusion term $D_r \Delta_{\mathbf{n}} \Psi$. The drift term envelopes the effect of the carrier flow field through $\boldsymbol{\Omega}$ and $\mathbf{D}$ in equation (3.12). The diffusion term contains the effect of the rotary Brownian motion. This means that the probability is convected by the flow field and is diffused by the rotary Brownian motion. This convection-diffusion process occurs on the surface of the unit sphere. The advective term $\mathbf{U} \cdot \boldsymbol{\nabla} \Psi$ shows that the probability is advected in the physical space by the carrier flow field. Thus, the Fokker-Planck equation (3.15) is defined in the physical space as well as in the conformation space, i.e. $\Psi = \Psi(\mathbf{n}; \mathbf{x}, t) = \Psi\left(\varphi, \vartheta, x, y, z, t\right)$. φ and ϑ are the azimuth and zenith angles of the spherical coordinate system, respectively. The spherical coordinate system is used because the conformation space is the surface of the unit sphere. The Fokker-Planck equation is subjected to periodic boundary conditions in both azimuthal and zenithal directions. The total stochastic mass over the sphere must be unity for all times:

$$\iint_{\mathbf{S}} \Psi \, \mathrm{d}S(\mathbf{n}) = 1. \tag{3.16}$$

Equation (3.15) fulfills this condition. This can be verified by integrating both sides of equation (3.15) over $\mathbf{S}$:

$$\begin{aligned} \frac{\mathrm{D}}{\mathrm{D}t} \iint_{\mathbf{S}} \Psi \, \mathrm{d}S(\mathbf{n}) &= -\iint_{\mathbf{S}} \boldsymbol{\nabla}_{\mathbf{n}} \cdot \left(\Psi \frac{\mathrm{D}\mathbf{n}}{\mathrm{D}t} - D_r \boldsymbol{\nabla}_{\mathbf{n}} \Psi \right) \mathrm{d}S(\mathbf{n}) \\ &= -\iint_{\mathbf{S}} \boldsymbol{\nabla}_{\mathbf{n}} \cdot \mathbf{J}_{\Psi} \, \mathrm{d}S(\mathbf{n}), \end{aligned} \tag{3.17}$$

in which $\mathbf{J}_{\Psi} = \Psi \dot{\mathbf{n}} - D_r \boldsymbol{\nabla}_{\mathbf{n}} \Psi$ is the probability flux. Equation (3.17) is conservative over a periodic domain [90]. This means that if one starts with an initial condition which satisfies equation (3.16), the Fokker-Planck equation (3.15) guarantees the satisfaction of (3.16) for all times.

In the rheological theory of dilute suspensions, as discussed later in section 3.6, the non-Newtonian stress due to the presence of particles depends on the statistical moments of the orientation distribution function Ψ, namely its second and fourth moments:

$$\langle \mathbf{nn} \rangle_{\Psi}(\mathbf{x}, t) = \iint_{\mathbf{S}} \mathbf{nn} \, \Psi(\mathbf{n}; \mathbf{x}, t) \, \mathrm{d}S(\mathbf{n}), \tag{3.18}$$

$$\langle \mathbf{nnnn} \rangle_{\Psi}(\mathbf{x}, t) = \iint_{\mathbf{S}} \mathbf{nnnn} \, \Psi(\mathbf{n}; \mathbf{x}, t) \, \mathrm{d}S(\mathbf{n}), \tag{3.19}$$

where the dyadic products $\mathbf{nn}$ (or $\langle \mathbf{nn} \rangle_{\Psi}$) and $\mathbf{nnnn}$ (or $\langle \mathbf{nnnn} \rangle_{\Psi}$) are second and fourth rank tensors, respectively. All odd-ordered moments vanish due to the symmetry of the orien-

tation distribution function. The moments are weighted averages over the sphere with the orientation distribution function Ψ as the weighting kernel. The subscript $\langle\cdots\rangle_\Psi$ is introduced to distinguish between the ensemble average of turbulent quantities and the averaging with respect to the orientation distribution function Ψ. The integrals (3.18) and (3.19) can be computed once the orientation distribution function is known. From definitions (3.18) and (3.19) we conclude that the second and fourth moments are fully symmetric. Furthermore, the following properties for the second and fourth moments can be easily derived from their definitions:

$$\begin{aligned} \mathrm{tr}\left\{\langle\mathbf{nn}\rangle_\Psi\right\} = \mathbf{1}:\langle\mathbf{nn}\rangle_\Psi &= \iint_S \mathbf{1}:\mathbf{nn}\;\Psi(\mathbf{n};\mathbf{x},t)\,\mathrm{d}S(\mathbf{n}) \\ &= \iint_S \Psi(\mathbf{n};\mathbf{x},t)\,\mathrm{d}S(\mathbf{n}) = 1, \end{aligned} \tag{3.20}$$

$$\begin{aligned} \mathbf{1}:\langle\mathbf{nnnn}\rangle_\Psi &= \iint_S \mathbf{1}:\mathbf{nnnn}\;\Psi(\mathbf{n};\mathbf{x},t)\,\mathrm{d}S(\mathbf{n}) \\ &= \iint_S \mathbf{nn}\;\Psi(\mathbf{n};\mathbf{x},t)\,\mathrm{d}S(\mathbf{n}) = \langle\mathbf{nn}\rangle_\Psi, \end{aligned} \tag{3.21}$$

in which the relation $\mathbf{1}:\mathbf{nn} = \mathbf{n}\cdot\mathbf{n} = \|\mathbf{n}\|^2 = 1$ is used.

3.4. Moment Approximation

Since the non-Newtonian stress depends on the second and fourth moments of the orientation distribution function (see section 3.6), it could be of advantage to directly compute these moments without computing the orientation distribution function. In this approach, an evolution equation for the desired moment is required. To this aim, we first differentiate the definition of the desired moment, e.g. equation (3.18), with respect to time:

$$\frac{\mathrm{D}\langle\mathbf{nn}\rangle_\Psi}{\mathrm{D}t} = \iint_S \mathbf{nn}\,\frac{\mathrm{D}\Psi}{\mathrm{D}t}\,\mathrm{d}S(\mathbf{n}). \tag{3.22}$$

Introducing the Fokker-Planck equation (3.15) into equation (3.22) yields

$$\frac{\mathrm{D}\langle\mathbf{nn}\rangle_\Psi}{\mathrm{D}t} = \iint_S \mathbf{nn}\,\left[-\boldsymbol{\nabla}_\mathbf{n}\cdot\left(\Psi\frac{\mathrm{D}\mathbf{n}}{\mathrm{D}t}\right) + D_r\Delta_\mathbf{n}\Psi\right]\,\mathrm{d}S(\mathbf{n}). \tag{3.23}$$

Integrating by parts and using the normalization condition (3.16) give

$$\begin{aligned}\frac{\mathrm{D}\langle \mathbf{nn}\rangle_\Psi}{\mathrm{D}t} &= \boldsymbol{\Omega}\cdot\langle \mathbf{nn}\rangle_\Psi + \langle \mathbf{nn}\rangle_\Psi\cdot\boldsymbol{\Omega}^{\mathrm{T}} \\ &\quad + \kappa\left[\mathbf{D}\cdot\langle \mathbf{nn}\rangle_\Psi + \langle \mathbf{nn}\rangle_\Psi\cdot\mathbf{D} - 2\mathbf{D}:\langle \mathbf{nnnn}\rangle_\Psi\right] \\ &\quad + 2D_r\left[\mathbf{1} - 3\langle \mathbf{nn}\rangle_\Psi\right].\end{aligned} \tag{3.24}$$

Equation (3.24) is obviously not closed, i.e. the fourth moment $\langle \mathbf{nnnn}\rangle_\Psi$ appears in the evolution equation for the second moment $\langle \mathbf{nn}\rangle_\Psi$. This poses a closure problem that occurs in the passage from the distribution function to the moments in nonlinear systems [101]. One can derive an evolution equation for the fourth moment. But then, it depends on the sixth moment and so fourth.

3.5. Moment Closure Models

In order to solve equation (3.24), a closure model expressing the fourth moment in terms of the second moment is required. The closure model for the fourth moment $\langle \mathbf{nnnn}\rangle_\Psi$ can be written either explicitly as

$$\langle \mathbf{nnnn}\rangle_\Psi = \mathbf{F}\left(\langle \mathbf{nn}\rangle_\Psi\right), \tag{3.25}$$

or implicitly as

$$\mathbf{D}:\langle \mathbf{nnnn}\rangle_\Psi = \mathbf{f}\left(\langle \mathbf{nn}\rangle_\Psi\right), \tag{3.26}$$

where $\mathbf{F}$ and $\mathbf{f}$ are fourth- and second-rank tensor-valued functions, respectively. There exist several closure models in the literature. Some of them are briefly presented in the following.

1. **Linear closure:**

   In this closure model which was proposed by Hand [44], the fourth moment $\langle \mathbf{nnnn}\rangle_\Psi$ is expanded in terms of the identity tensor and the second moment $\langle \mathbf{nn}\rangle_\Psi$. The dependence on $\langle \mathbf{nn}\rangle_\Psi$ is linear.

   $$\mathbf{D}:\langle \mathbf{nnnn}\rangle_\Psi = -\frac{2}{35}\mathbf{D} + \frac{1}{7}\left[2\langle \mathbf{nn}\rangle_\Psi\cdot\mathbf{D} + 2\mathbf{D}\cdot\langle \mathbf{nn}\rangle_\Psi + \left(\langle \mathbf{nn}\rangle_\Psi:\mathbf{D}\right)\mathbf{1}\right]. \tag{3.27}$$

   This model is exact for a random distribution of fiber orientations (i.e., an isotropic suspension).

2. **Quadratic closure:**

   The fourth moment $\langle \mathbf{nnnn}\rangle_\Psi$ is a quadratic function of the second moment $\langle \mathbf{nn}\rangle_\Psi$ in this model:

   $$\langle \mathbf{nnnn}\rangle_\Psi^{\mathrm{quad}} = \langle \mathbf{nn}\rangle_\Psi\langle \mathbf{nn}\rangle_\Psi, \tag{3.28}$$

i.e. the fourth moment $\langle \mathbf{nnnn} \rangle_\Psi$ equals the dyadic product of the second moment $\langle \mathbf{nn} \rangle_\Psi$ by itself. This closure deserves attention for its simplicity and stability. It is exact when the fibers are fully aligned.

3. **Hybrid closure:**

The hybrid closure approximation of Advani and Tucker [1] reads

$$\langle \mathbf{nnnn} \rangle_\Psi^{\text{hyb}} = \left[(1-f) \langle \mathbf{nnnn} \rangle_\Psi^{\text{lin}} + f \langle \mathbf{nnnn} \rangle_\Psi^{\text{quad}} \right], \tag{3.29}$$

which is a weighted average of the linear and quadratic closures and the scalar f is to be chosen. It is a measure of orientation, since $f = 0$ gives an exact closure (linear) if the suspension is isotropic while $f = 1$ gives an exact closure (quadratic) if the fibers are fully aligned. The scalar parameter f in three-dimensional flows is often defined as

$$f = 1 - 27 \det \left(\langle \mathbf{nn} \rangle_\Psi \right). \tag{3.30}$$

4. **Hinch & Leal closure:**

Hinch and Leal [48, 49] proposed a closure which is an interpolation between some known solutions of the Fokker-Planck equation in two-dimensional flows:

$$\begin{aligned} \langle \mathbf{nnnn} \rangle_\Psi^{\text{HL}} : \mathbf{D} = \frac{1}{5} \Big[& 6 \langle \mathbf{nn} \rangle_\Psi \cdot \mathbf{D} \cdot \langle \mathbf{nn} \rangle_\Psi - \langle \mathbf{nn} \rangle_\Psi \langle \mathbf{nn} \rangle_\Psi : \mathbf{D} \\ & -2\, \mathbf{1} \langle \mathbf{nn} \rangle_\Psi^2 : \mathbf{D} + 2\, \mathbf{1} \langle \mathbf{nn} \rangle_\Psi : \mathbf{D} \Big]. \end{aligned} \tag{3.31}$$

It is a quadratic polynomial in the components of $\langle \mathbf{nn} \rangle_\Psi$. It has the drawback that it gives non-physical results in some flows, e.g. in biaxial elongational flow [2]. Therefore, it cannot be trusted in complex three-dimensional turbulent flows.

5. **Invariant-Based Optimal Fitting closure (IBOF):**

The IBOF closure of Chung and Kwon [16] is one of the best closures available to date. The fourth moment $\langle \mathbf{nnnn} \rangle_\Psi$ is expressed in terms of the symmetric parts of the dyadic products of the identity tensor $\mathbf{1}$ and the second moment $\langle \mathbf{nn} \rangle_\Psi$:

$$\begin{aligned} \langle \mathbf{nnnn} \rangle_\Psi^{\text{IBOF}} = & \beta_1 \mathbf{S} \{ \mathbf{1}\, \mathbf{1} \} + \beta_2 \mathbf{S} \{ \mathbf{1} \langle \mathbf{nn} \rangle_\Psi \} + \beta_3 \mathbf{S} \{ \langle \mathbf{nn} \rangle_\Psi \langle \mathbf{nn} \rangle_\Psi \} \\ & + \beta_4 \mathbf{S} \{ \mathbf{1} (\langle \mathbf{nn} \rangle_\Psi \cdot \langle \mathbf{nn} \rangle_\Psi) \} \\ & + \beta_5 \mathbf{S} \{ \langle \mathbf{nn} \rangle_\Psi (\langle \mathbf{nn} \rangle_\Psi \cdot \langle \mathbf{nn} \rangle_\Psi) \} \\ & + \beta_6 \mathbf{S} \{ (\langle \mathbf{nn} \rangle_\Psi \cdot \langle \mathbf{nn} \rangle_\Psi) (\langle \mathbf{nn} \rangle_\Psi \cdot \langle \mathbf{nn} \rangle_\Psi) \}. \end{aligned} \tag{3.32}$$

The tensor operator $\mathbf{S}$ returns the symmetric part of its argument $\mathbf{T} = T_{ijkl} \mathbf{e}_i \mathbf{e}_j \mathbf{e}_k \mathbf{e}_l$:

$$\begin{aligned} \mathbf{S}\{\mathbf{T}\} = \tfrac{1}{24} \big[& T_{ijkl} + T_{jikl} + T_{ijlk} + T_{jilk} + T_{klij} + T_{lkij} + T_{klji} + T_{lkji} + T_{ikjl} \\ & + T_{kijl} + T_{jlik} + T_{ljik} + T_{jlki} + T_{ljki} + T_{iljk} + T_{lijk} + T_{ilkj} + T_{likj} \\ & + T_{jkil} + T_{kjil} + T_{jkli} + T_{kjli} + T_{iklj} + T_{kilj} \big] \mathbf{e}_i \mathbf{e}_j \mathbf{e}_k \mathbf{e}_l, \end{aligned} \tag{3.33}$$

where T_{ijkl}'s are the Cartesian components of the fourth rank tensor $\mathbf{T}$, and $\mathbf{e}_i$'s are the Cartesian orthonormal basis vectors. The coefficients β_1 to β_6 are functions of the second and third invariants of the second moment $\langle \mathbf{nn} \rangle_\Psi$, denoted by II and III, respectively. Analytical expressions for $\beta_{1,2,5}$ in terms of $\beta_{3,4,6}$ and the invariants of $\langle \mathbf{nn} \rangle_\Psi$ can be derived [16]:

$$\begin{aligned}\beta_1 = \tfrac{3}{5}\Big[&-\tfrac{1}{7} + \tfrac{1}{5}\beta_3\left(\tfrac{1}{7} + \tfrac{4}{7}II + \tfrac{8}{3}III\right) - \beta_4\left(\tfrac{1}{5} - \tfrac{8}{15}II - \tfrac{14}{15}III\right) \\ &-\beta_6\left(\tfrac{1}{35} - \tfrac{4}{35}II - \tfrac{24}{105}III + \tfrac{16}{15}II\,(III) + \tfrac{8}{35}II^2\right)\Big],\end{aligned} \tag{3.34}$$

$$\begin{aligned}\beta_2 = \tfrac{6}{7}\Big[&1 - \tfrac{1}{5}\beta_3\,(1 + 4II) + \tfrac{7}{5}\beta_4\left(\tfrac{1}{6} - II\right) \\ &-\beta_6\left(-\tfrac{1}{5} + \tfrac{4}{5}II + \tfrac{2}{3}III - \tfrac{8}{5}II^2\right)\Big],\end{aligned} \tag{3.35}$$

$$\beta_5 = -\tfrac{4}{5}\beta_3 - \tfrac{7}{5}\beta_4 - \tfrac{6}{5}\beta_6\left(1 - \tfrac{4}{3}II\right). \tag{3.36}$$

β_3, β_4 and β_6 are obtained by fifth-order polynomial fitting in terms of the invariants:

$$\begin{aligned}\beta_i = {} & a\,(i,1) + a\,(i,2)\,II + a\,(i,3)\,II^2 + a\,(i,4)\,III + a\,(i,5)\,III^2 \\ & + a\,(i,6)\,II\,(III) + a\,(i,7)\,II^2 III + a\,(i,8)\,(II)\,III^2 \\ & + a\,(i,9)\,II^3 + a\,(i,10)\,III^3 + a\,(i,11)\,II^3 III + a\,(i,12)\,II^2 III^2 \\ & + a\,(i,13)\,(II)\,III^3 + a\,(i,14)\,II^4 + a\,(i,15)\,III^4 + a\,(i,16)\,II^4 III \\ & + a\,(i,17)\,II^3 III^2 + a\,(i,18)\,II^2 III^3 + a\,(i,19)\,(II)\,III^4 \\ & + a\,(i,20)\,II^5 + a\,(i,21)\,III^5, \qquad (i = 3,4,6).\end{aligned} \tag{3.37}$$

The $3 \times 21 = 63$ fitting coefficients $a\,(i,j)$ with $i = 3,4,6$ and $j = 1,\ldots,21$ are obtained by using least-square fitting to the exact solutions of the Fokker-Planck equation in a number of simple flows. The numerical values of the fitting coefficients are given in appendix A.

6. Normalization scheme:[1]

The normalization scheme is a computationally efficient alternative to existing closure models. In the following, we present the principles of this model.

It is already pointed out in section 3.3 that the trace of $\langle \mathbf{nn} \rangle_\Psi$, noted I, must always be 1.0 (see equation (3.20)). Here, we check whether this condition is held by the moment evolution equation (3.24). We first recall relations used in the subsequent derivation. $\mathbf{1} : \mathbf{A} \cdot \mathbf{B} = \mathbf{A} : \mathbf{B}$ holds for two arbitrary second-order tensors $\mathbf{A}$ and $\mathbf{B}$, and the identity tensor $\mathbf{1}$. Here the symbols : and $\cdot$ stand for contraction and scalar multiplication of tensors, respectively. The contraction of a symmetric tensor with an antisymmetric tensor is zero, i.e. $\mathbf{\Omega} : \langle \mathbf{nn} \rangle_\Psi = \langle \mathbf{nn} \rangle_\Psi : \mathbf{\Omega}^{\mathrm{T}} = 0$. Due to the symmetry of $\mathbf{D}$ and $\langle \mathbf{nn} \rangle_\Psi$, the relation $\mathbf{D} : \langle \mathbf{nn} \rangle_\Psi = \langle \mathbf{nn} \rangle_\Psi : \mathbf{D}$ holds. It is proved that $\langle \mathbf{nnnn} \rangle_\Psi : \mathbf{1} = \langle \mathbf{nn} \rangle_\Psi$ in equation (3.21).

[1] Materials presented here have been published in [88].

Then, it is straightforward to show that $\mathbf{1} : \mathbf{D} : \langle \mathbf{nnnn} \rangle_\Psi = \mathbf{D} : \langle \mathbf{nn} \rangle_\Psi$.

Contracting both sides of equation (3.24) with the identity tensor $\mathbf{1}$ gives

$$\begin{aligned} \frac{\mathrm{D}I}{\mathrm{D}t} &= \boldsymbol{\Omega} : \langle \mathbf{nn} \rangle_\Psi + \langle \mathbf{nn} \rangle_\Psi : \boldsymbol{\Omega}^{\mathrm{T}} \\ &\quad + \kappa \left[\mathbf{D} : \langle \mathbf{nn} \rangle_\Psi + \langle \mathbf{nn} \rangle_\Psi : \mathbf{D} - 2\mathbf{1} : \mathbf{D} : \langle \mathbf{nnnn} \rangle_\Psi \right] + 6D_r (1 - I), \end{aligned} \tag{3.38}$$

where I is the trace of $\langle \mathbf{nn} \rangle$. Using all relations mentioned above, the terms in the square bracket of (3.38) cancel and equation (3.38) reduces to

$$\frac{\mathrm{D}I}{\mathrm{D}t} = 6D_r (1 - I), \tag{3.39}$$

whose general solution reads

$$I(t) = 1 - C \exp\left(-6D_r t\right), \tag{3.40}$$

where C is the integration constant. The initial condition $I(t = 0) = 1.0$ thus guarantees $I(t) = 1.0$ for all times. The above discussion also shows that any closure model that fulfills the property $\langle \mathbf{nnnn} \rangle_\Psi : \mathbf{1} = \langle \mathbf{nn} \rangle_\Psi$ ensures the conservation of I in time.

From the evolution equation (3.39), it turns out that a closure model has to fulfill the condition $\langle \mathbf{nnnn} \rangle_\Psi : \mathbf{1} = \langle \mathbf{nn} \rangle_\Psi$ in order to ensure the conservation of I in time. Here we present a computationally efficient scheme that guarantees this condition.

If we omit the term containing the fourth moment in equation (3.24), a closure model is no longer required. However, the trace of $\langle \mathbf{nn} \rangle_\Psi^*$ is not conserved anymore and the evolution equation (3.39) for I^* reads

$$\frac{\mathrm{D}I^*}{\mathrm{D}t} = 2\kappa\, \mathbf{D} : \langle \mathbf{nn} \rangle_\Psi^* + 6D_r (1 - I^*). \tag{3.41}$$

$()^*$ denotes the quantities that are obtained by removing the closure term in equation (3.24). Equation (3.41) means that the norm of the orientation vector $\mathbf{n}$ differs from 1.0. Therefore, a normalization procedure is required at each time step: the second moment $\langle \mathbf{nn} \rangle_\Psi$ is rescaled so that its trace is 1.0. In the most trivial way, this can be done by dividing all components of $\langle \mathbf{nn} \rangle_\Psi$ by its trace I. The algorithm thus reads

a) The second moment is advanced one step in time by using the modified evolution equation

$$\begin{aligned} \frac{\mathrm{D} \langle \mathbf{nn} \rangle_\Psi^*}{\mathrm{D}t} &= \boldsymbol{\Omega} \cdot \langle \mathbf{nn} \rangle_\Psi^* + \langle \mathbf{nn} \rangle_\Psi^* \cdot \boldsymbol{\Omega}^{\mathrm{T}} + \\ &\quad \kappa \left[\mathbf{D} \cdot \langle \mathbf{nn} \rangle_\Psi^* + \langle \mathbf{nn} \rangle_\Psi^* \cdot \mathbf{D} \right] + 2D_r \left[\mathbf{1} - 3 \langle \mathbf{nn} \rangle_\Psi^* \right]. \end{aligned} \tag{3.42}$$

This yields the intermediate second moment $\langle \mathbf{nn} \rangle_\Psi^*$ which does not satisfy the condition $\mathrm{tr}\left\{ \langle \mathbf{nn} \rangle_\Psi^* \right\} = 1.0$.

b) The trace of $\langle \mathbf{nn} \rangle^*_\Psi$, i.e. $I^* = \mathrm{tr}\left\{ \langle \mathbf{nn} \rangle^*_\Psi \right\}$, is computed.

c) The second moment $\langle \mathbf{nn} \rangle_\Psi$ at the new time level is computed by

$$\langle \mathbf{nn} \rangle_\Psi = \frac{\langle \mathbf{nn} \rangle^*_\Psi}{I^*}. \tag{3.43}$$

Here, we analytically prove that the above algorithm is equivalent to the solution of equation (3.24) using the quadratic closure model

$$\langle \mathbf{nnnn} \rangle^{\mathrm{quad}}_\Psi = \langle \mathbf{nn} \rangle_\Psi \langle \mathbf{nn} \rangle_\Psi . \tag{3.44}$$

Differentiating equation (3.43) with respect to time yields

$$\frac{\mathrm{D} \langle \mathbf{nn} \rangle_\Psi}{\mathrm{D}t} = \frac{I^* \, \mathrm{D} \langle \mathbf{nn} \rangle^*_\Psi / \mathrm{D}t - \langle \mathbf{nn} \rangle^*_\Psi \, \mathrm{D}I^*/\mathrm{D}t}{I^{*2}}. \tag{3.45}$$

The right-hand side is evaluated at $\langle \mathbf{nn} \rangle^*_\Psi = \langle \mathbf{nn} \rangle_\Psi$ and $I^* = 1.0$. This is the point at which the result of the new scheme is physical. Substituting $\mathrm{D} \langle \mathbf{nn} \rangle^*_\Psi / \mathrm{D}t$ with equation (3.42) and $\mathrm{D}I^*/\mathrm{D}t$ with equation (3.41), and evaluating the resulting expression at $\langle \mathbf{nn} \rangle^*_\Psi = \langle \mathbf{nn} \rangle_\Psi$ and $I^* = 1.0$ gives

$$\begin{aligned} \frac{\mathrm{D} \langle \mathbf{nn} \rangle_\Psi}{\mathrm{D}t} = {} & \boldsymbol{\Omega} \cdot \langle \mathbf{nn} \rangle_\Psi + \langle \mathbf{nn} \rangle_\Psi \cdot \boldsymbol{\Omega}^{\mathrm{T}} \\ & + \kappa \left[\mathbf{D} \cdot \langle \mathbf{nn} \rangle_\Psi + \langle \mathbf{nn} \rangle_\Psi \cdot \mathbf{D} - 2\mathbf{D} : \left(\langle \mathbf{nn} \rangle_\Psi \langle \mathbf{nn} \rangle_\Psi \right) \right] \\ & + 2D_r \left[\mathbf{1} - 3 \langle \mathbf{nn} \rangle_\Psi \right], \end{aligned} \tag{3.46}$$

in which the identity $\langle \mathbf{nn} \rangle_\Psi \left(\mathbf{D} : \langle \mathbf{nn} \rangle_\Psi \right) = \mathbf{D} : \left(\langle \mathbf{nn} \rangle_\Psi \langle \mathbf{nn} \rangle_\Psi \right)$ is used. Equation (3.46) is exactly the same as equation (3.24) with $\langle \mathbf{nnnn} \rangle_\Psi$ replaced by the quadratic closure model (3.44). This equivalence between the quadratic model and the normalization scheme is numerically checked in [88].

The normalization scheme needs less computational effort than any closure model as (a) it advances a simpler differential equation in time, and (b) the closure approximation is replaced by two simple computations, i.e. steps 2 and 3 in the above algorithm.

3.6. Brenner's Rheological Theory

As pointed out in the previous chapter (in section 2.2), the momentum equation for the flow of a non-Newtonian fluid reads

$$\rho \frac{\mathrm{D}\mathbf{U}}{\mathrm{D}t} = -\boldsymbol{\nabla} p + \boldsymbol{\nabla} \cdot \left(\boldsymbol{\tau}^{\mathrm{N}} + \boldsymbol{\tau}^{\mathrm{NN}} \right). \tag{3.47}$$

The Newtonian stress $\boldsymbol{\tau}^{\mathrm{N}}$ is given by the generalized Newton's law of viscosity given by equation (2.11) for an incompressible flow. A constitutive equation for the non-Newtonian stress

$\boldsymbol{\tau}^{\mathrm{NN}}$ is still required in order to fully describe the flow of a non-Newtonian fluid. This is the central role of the rheology to provide such constitutive models. The non-Newtonian stress due to the spheroidal particles depends on the strain-rate tensor and the particles conformation [7]. The particles conformation is described by the orientation distribution function Ψ. Brenner [11] has developed a rheological theory for dilute suspensions of Brownian axisymmetric particles, e.g. spheroids, symmetric double cones, circular cylinders and spherical dumbbells. The main message of his work can be summarized as the following. The rheological properties of a dilute suspension of the aforementioned bodies subjected to rotary Brownian motion can be expressed in terms of the second and fourth moments of the orientation distribution function, the viscosity of the carrier fluid, the volume fraction of suspended particles and five dimensionless scalar material constants. These material constants depend only on the shape of the suspended particles and are hydrodynamic in origin. The latter means that they can be derived from the solution of the creeping flow around the suspended particles.

In what follows, we briefly present the Brenner's theory [11], in which the non-Newtonian stress tensor reads

$$\begin{aligned}\boldsymbol{\tau}^{\mathrm{NN}} = {} & 2\mu_0\mathbf{D} + \mu_1\mathbf{1}\left(\mathbf{D} : \langle\mathbf{nn}\rangle_\Psi\right) + \mu_2\mathbf{D} : \langle\mathbf{nnnn}\rangle_\Psi \\ & + 2\mu_3\left(\langle\mathbf{nn}\rangle_\Psi \cdot \mathbf{D} + \mathbf{D} \cdot \langle\mathbf{nn}\rangle_\Psi\right) + 2\mu_4 D_r\left(3\langle\mathbf{nn}\rangle_\Psi - \mathbf{1}\right),\end{aligned} \tag{3.48}$$

with $\mathbf{1}$ and D_r being the identity tensor and the rotary Brownian diffusivity, respectively. $\boldsymbol{\tau}^{\mathrm{NN}}$ depends on the second and fourth moments of the orientation distribution function given by equations (3.18) and (3.19). $\mu_i, i = 0, \cdots, 4$ are the five material constants which depend on the aspect ratio of the spheroidal particles r, their volume fraction ϕ and the viscosity of the carrier fluid μ [11]:

$$\mu_0 = 5\mu\phi Q_0, \tag{3.49a}$$

$$\mu_1 = 5\mu\phi Q_1, \tag{3.49b}$$

$$\mu_2 = 5\mu\phi Q_2, \tag{3.49c}$$

$$\mu_3 = 5\mu\phi Q_3, \tag{3.49d}$$

$$\mu_4 = 5\mu\phi Q_4, \tag{3.49e}$$

with

$$Q_0 = \frac{1}{5\alpha'_{\shortparallel}}, \tag{3.50a}$$

$$Q_1 = \frac{2}{15\alpha'_{\shortparallel}}\left(1 - \frac{\alpha''_{\shortparallel}}{\alpha''_{\perp}}\right), \tag{3.50b}$$

$$Q_2 = \left(-3Q_1 - 4Q_3\right), \tag{3.50c}$$

$$Q_3 = \frac{1}{5\alpha'_{\shortparallel}}\left[\frac{2r\alpha'_{\shortparallel}}{\left(r^2+1\right)\alpha'_{\perp}} - 1\right], \tag{3.50d}$$

$$Q_4 = \frac{2\left(r^2-1\right)}{5\left(r^2\alpha_{\shortparallel} + \alpha_{\perp}\right)}, \tag{3.50e}$$

in which

$$\alpha_{\shortparallel} = \frac{2}{r^2-1}\left(r^2\beta - 1\right), \tag{3.51a}$$

$$\alpha_{\perp} = \frac{r^2}{r^2-1}\left(1-\beta\right), \tag{3.51b}$$

$$\alpha'_{\shortparallel} = \frac{r^2}{4\left(r^2-1\right)^2}\left(3\beta + 2r^2 - 5\right), \tag{3.51c}$$

$$\alpha'_{\perp} = \frac{r}{\left(r^2-1\right)^2}\left(r^2 + 2 - 3r^2\beta\right), \tag{3.51d}$$

$$\alpha''_{\shortparallel} = \frac{r^2}{4\left(r^2-1\right)^2}\left[2r^2 + 1 - \left(4r^2-1\right)\beta\right], \tag{3.51e}$$

$$\alpha''_{\perp} = \frac{r^2}{\left(r^2-1\right)^2}\left[\left(2r^2+1\right)\beta - 3\right], \tag{3.51f}$$

and

$$\beta = \frac{\cosh^{-1} r}{r\left(r^2-1\right)^{1/2}}, \quad \text{for } r > 1 \text{ (prolate spheroid)}, \tag{3.52a}$$

$$\beta = \frac{\cos^{-1} r}{r\left(1-r^2\right)^{1/2}}, \quad \text{for } r < 1 \text{ (oblate spheroid)}. \tag{3.52b}$$

Brenner [11] has shown that for the case of spherical particles ($r = 1$) we have

$$\mu_0 = \frac{5}{2}\mu\phi, \quad \mu_1 = \mu_2 = \mu_3 = \mu_4 = 0. \tag{3.53}$$

Inserting these values into the constitutive equation (3.48) yields the following expression for

the total stress

$$\boldsymbol{\tau} = \boldsymbol{\tau}^{\mathrm{N}} + \boldsymbol{\tau}^{\mathrm{NN}} = 2\left(\mu + \mu_0\right)\mathbf{D}. \tag{3.54}$$

This relation defines a Newtonian fluid with an increased effective viscosity:

$$\mu_{\mathrm{eff}} = \mu + \mu_0 = \mu\left(1 + \frac{5}{2}\phi\right). \tag{3.55}$$

Equation (3.55) is the well-known Einstein's formula (equation (3.1)) [27, 28] for the viscosity of a dilute suspension of spherical particles in a Newtonian carrier fluid. Equation (3.54) implies that when $r \to 1$, the fiber suspension shows no anisotropy and behaves like a Newtonian fluid with a higher viscosity (flow at a lower Reynolds number). Moreover, equation (3.54) shows that the effect of rotary Brownian motion vanishes at $r \to 1$, which is intuitively expected for spherical particles.

3.6.1. Limit of Zero Rotary Péclet Number

It is always useful to have a testcase for which an analytical solution exists. Then, it can be used for the validation of numerical methods and computer codes. For this purpose, in this section, we investigate the limiting case of the zero rotary Péclet number (i.e., very strong Brownian motion) which gives us a testcase with an analytical solution in the channel flow.

Due to the strong Brownian motion, the orientation of fibers tends to the isotropic state and thus, the orientation distribution function is given by

$$\Psi(\mathbf{n};\mathbf{x},t) = \frac{1}{4\pi}\left(1 + \frac{\mathbf{nn} : \mathbf{D}(\mathbf{x},t)}{2D_r} + \cdots\right). \tag{3.56}$$

Equation (3.56) states that Ψ takes the isotropic value $1/4\pi$ plus correction terms. However, the correction terms have D_r in their denominator and thus, at the limit $\mathrm{Pe}_r \to 0$ ($D_r \to \infty$), they become negligible. The orientation distribution function given in equation (3.56) yields the following second moment:

$$\langle \mathbf{nn} \rangle_{\Psi} = \frac{\mathbf{1}}{3} + \frac{\mathbf{D}}{15D_r} + \cdots. \tag{3.57}$$

Again, D_r appears in the denominator of the correction term and at the limit $D_r \to \infty$, we get the isotropic form of the second moment:

$$\langle \mathbf{nn} \rangle_{\Psi} = \frac{\mathbf{1}}{3}. \tag{3.58}$$

The linear closure of Hand [44] is exact in an isotropic situation. Thus, the fourth moment contracted with the strain-rate tensor $\mathbf{D}$ is given by equation (3.27). Substitution of equation (3.57) in the Brownian contribution to the stress, i.e. the last term of equation (3.48), gives

the following expression:

$$2\mu_4 D_r \left(3\left\langle \mathbf{nn}\right\rangle_\Psi - \mathbf{1}\right) = 2\mu_4 D_r \left(\mathbf{1} + \frac{\mathbf{D}}{5D_r} - \mathbf{1}\right) = \frac{2}{5}\mu_4 \mathbf{D}. \tag{3.59}$$

Inserting equations (3.58), (3.27) and (3.59) into the Brenner's stress formula (3.48) yields the following relation for the non-Newtonian stress:

$$\boldsymbol{\tau}^{\mathrm{NN}}_{\mathrm{isotropic}} = \left(2\mu_0 + \frac{2}{15}\mu_2 + \frac{4}{3}\mu_3 + \frac{2}{5}\mu_4\right)\mathbf{D}. \tag{3.60}$$

The total stress then reads

$$\boldsymbol{\tau} = \boldsymbol{\tau}^{\mathrm{N}} + \boldsymbol{\tau}^{\mathrm{NN}}_{\mathrm{isotropic}} = 2\left(\mu + \mu_0 + \frac{1}{15}\mu_2 + \frac{2}{3}\mu_3 + \frac{1}{5}\mu_4\right)\mathbf{D} = 2\mu_{\mathrm{eff}}\mathbf{D}. \tag{3.61}$$

Equation (3.61) shows that the suspension flows like an isotropic Newtonian fluid with a higher viscosity

$$\begin{aligned}\mu_{\mathrm{eff}} &= \mu + \mu_0 + \frac{1}{15}\mu_2 + \frac{2}{3}\mu_3 + \frac{1}{5}\mu_4 \\ &= \mu\left[1 + \frac{5}{2}\phi\left(2Q_0 + \frac{2}{15}Q_2 + \frac{4}{3}Q_3 + \frac{2}{5}Q_4\right)\right],\end{aligned} \tag{3.62}$$

and, thus, at a lower Reynolds number. Recalling the Einstein's relation (3.55), equation (3.62) is analogous to the case of a dilute suspension of spherical particles in a Newtonian carrier fluid with the effective volume fraction

$$\phi_{\mathrm{eff}} = \phi\left(2Q_0 + \frac{2}{15}Q_2 + \frac{4}{3}Q_3 + \frac{2}{5}Q_4\right), \tag{3.63}$$

This means, for example, that a suspension of fibers with the aspect ratio $r = 100$ at $\mathrm{Pe}_r \to 0$ is 237.5 times more effective (in increasing the viscosity) than a suspension of spheres with the same volume fraction. The ratio of the effective volume fraction to the actual volume fraction ϕ_{eff}/ϕ is a function of the particle aspect ratio r. This function is plotted in figure 3.5 for fibers with $r \leq 100$. As it has been already shown that the Brenner's stress reduces to the Einstein's formula for $r = 1$, equation (3.62) also reduces to the Einstein's viscosity formula (3.55).

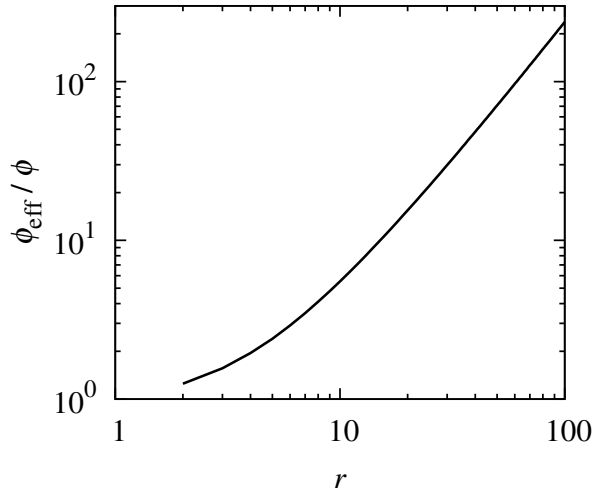

Figure 3.5: Effective volume fraction ϕ_{eff} of fiber suspension versus fiber aspect ratio r at $\text{Pe}_r \to 0$.

3.7. Hinch and Leal's Rheological Theory

Hinch and Leal have derived the following relation for the non-Newtonian stress in a series of publications [47, 48, 49]:

$$\begin{aligned}\boldsymbol{\tau}^{\text{NN}} = 2\mu\phi \big[& 2A\,\mathbf{D} : \langle \mathbf{nnnn} \rangle_\Psi + 2B \left(\langle \mathbf{nn} \rangle_\Psi \cdot \mathbf{D} + \mathbf{D} \cdot \langle \mathbf{nn} \rangle_\Psi \right) \\ & + C\,\mathbf{D} + F D_r \langle \mathbf{nn} \rangle_\Psi \big],\end{aligned} \tag{3.64}$$

where the material coefficients A, B, C and F are functions of the fiber aspect ratio r. They are given for the limiting case of $r \to \infty$ by [46]:

$$A = \frac{r^2}{4(\ln(2r) - 1.5)}, \tag{3.65a}$$

$$B = \frac{3\ln(2r) - 5.5}{r^2}, \tag{3.65b}$$

$$C = 2, \tag{3.65c}$$

$$F = \frac{3r^2}{\ln(2r) - 0.5}. \tag{3.65d}$$

These asymptotic forms correspond to the Brenner's material coefficients Q_i (see equation (3.50)) by the following relations:

$$A \equiv 1.25 Q_2, \quad B \equiv 2.5 Q_3, \quad C \equiv 5 Q_0, \quad F \equiv 15 Q_4. \tag{3.66}$$

This correspondence is shown in figures 3.6a to 3.6d. The asymptotic coefficients of the Hinch and Leal's theory are accurate for aspect ratios greater than 10. This has been also reported

by Kim and Karrila [59]. The comparison of the material coefficients implies that the full formulation of Brenner has to be considered if one studies the effect of finite aspect ratios. The Brenner's theory is also required to study the rheology of oblate spheroidal particles with $r \in (0,1)$. Paschkewitz *et al.* [104] have used the Hinch and Leal's stress formula (3.64) to study the turbulent drag reduction induced by slender fibers.

Figures 3.6a to 3.6d imply that for slender fibers (i.e., fibers with $r \gg 1$), Q_3 (B) vanishes and Q_0 (C) tends to 0.4 (2). The coefficient Q_2 (A) is dominant for non-Brownian slender fibers. The coefficient Q_4 (F) is significant and has to be taken into account for Brownian fibers. Therefore, the non-Newtonian stress can be approximated by

$$\boldsymbol{\tau}^{\mathrm{NN}} = 2\mu\phi\left(2A\mathbf{D} : \langle \mathbf{nnnn} \rangle_{\Psi} + FD_r \langle \mathbf{nn} \rangle_{\Psi}\right). \tag{3.67}$$

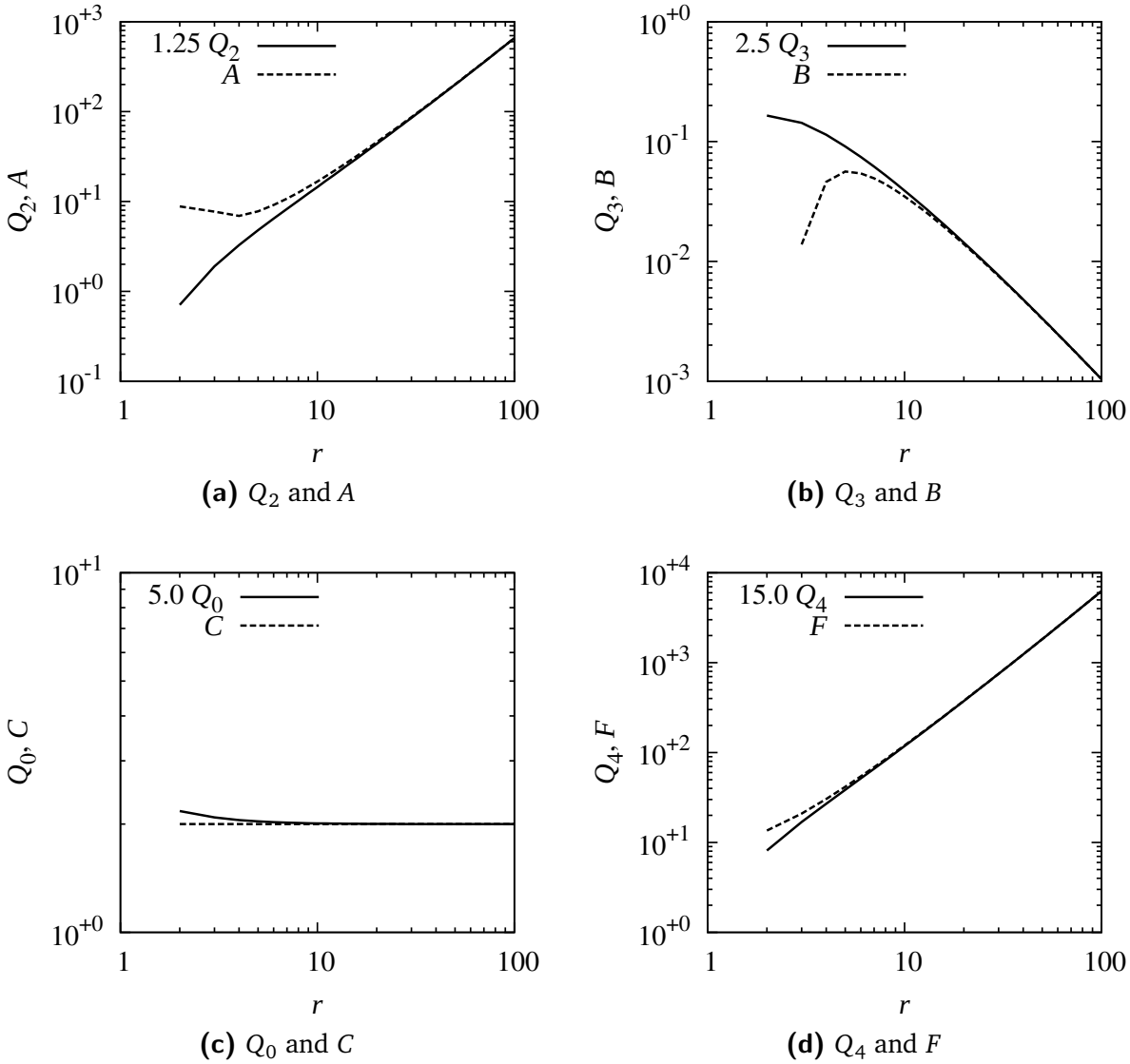

(a) Q_2 and A **(b)** Q_3 and B

(c) Q_0 and C **(d)** Q_4 and F

Figure 3.6: Material coefficients of Brenner's theory and Hinch & Leal's theory versus fiber aspect ratio r.

Gillissen *et al.* [39] have employed a stress model based on this assumption.

Another difference between the two models lies in the Brownian contribution to the non-Newtonian stress, i.e. Brenner's formulation has $2\mu_4 D_r \left(3\langle \mathbf{nn}\rangle_\Psi - \mathbf{1}\right)$ whereas Hinch and Leal's model gives $2\mu\phi F D_r \langle \mathbf{nn}\rangle_\Psi$. However, these two seemingly different models, when inserted in the momentum equation (3.47), lead to the same flow field. This can be proved by considering that the divergence of the non-Newtonian stress tensor appears in the momentum equation (3.47), that is $\boldsymbol{\nabla}\cdot\boldsymbol{\tau}^{\mathrm{NN}}$, which for the Brownian contribution of the Brenner's formulation yields $2\mu_4 D_r \boldsymbol{\nabla}\cdot\left(3\langle \mathbf{nn}\rangle_\Psi - \mathbf{1}\right) = 2\mu_4 D_r \left(3\boldsymbol{\nabla}\cdot\langle \mathbf{nn}\rangle_\Psi - \boldsymbol{\nabla}\cdot\mathbf{1}\right)$. The identity tensor $\mathbf{1}$ is a constant whose divergence vanishes and thus, the two models are indeed the same when substituted in the momentum equation (3.47). It can also be proved in another way. From tensor calculus we know that $\boldsymbol{\nabla}\cdot\mathbf{1} = \boldsymbol{\nabla}(1)$, i.e. the divergence of the identity tensor equals the gradient of the scalar 1 (which is also zero). Applying this to the momentum equation (3.47), we observe that $\boldsymbol{\nabla}(1)$ is absorbed in the pressure-gradient term, that is $\boldsymbol{\nabla}p - 2\mu_4 D_r \boldsymbol{\nabla}(1) = \boldsymbol{\nabla}\left(p - 2\mu_4 D_r\right) = \boldsymbol{\nabla}p_1$ with p_1 being a new pressure. We know that in an incompressible flow, the absolute value of pressure is immaterial and the pressure gradient is important. Therefore, the addition of a constant to the pressure field is immaterial as well and does not affect the flow field.

4. Numerical Methods

The governing equations of turbulent flows, as reviewed in chapter 2, are complicated enough to prevent analytical solutions. Thus, their numerical solution is used in turbulence research. Still, a direct numerical simulation can be prohibitively expensive. In the present work additionally, we have to compute the fiber orientation and then, to couple the flow solver with the fiber orientation solver. Therefore, one needs well-suited numerical methods which are efficiently implemented in the form of a computer code. Due to the tremendous amount of computations, such simulations are often performed on massively parallelized supercomputers.

In this chapter, we describe the existing numerical methods used for the DNS of the non-Newtonian flow in section 4.1. In section 4.2, we discuss the numerical methods developed for the computation of the fiber orientation. Section 4.3 describes the parallelization strategy. Finally, we present the validation of the numerical methods and the computer codes in section 4.4.

4.1. DNS Solver

A three-dimensional unsteady incompressible flow solver (called `MGLET`) which has been developed for DNS and LES of turbulent flows is used in this work. The code is written in `FORTRAN` and belongs to the Fachgebiet Hydromechanik at the Technische Universität München. In the following, we briefly present the numerical methods implemented in this code.

4.1.1. Projection Method

The projection method of Chorin [15] and Temam [124] is used for the solution of the unsteady incompressible Navier-Stokes equations:

$$\frac{\partial \mathbf{U}}{\partial t} = \mathbf{C} + \mathbf{D} + \mathbf{P}, \tag{4.1}$$

where $\mathbf{C}$, $\mathbf{D}$ and $\mathbf{P}$ are symbolic notations for the convective, diffusive and pressure terms, respectively. Here, an explicit Euler integration of equation (4.1) is presented. Any other explicit time integration scheme can be applied similarly. Application of the explicit Euler scheme on equation (4.1) yields

$$\tilde{\mathbf{U}}^{n+1} = \mathbf{U}^n + \Delta t \left[\mathbf{C}^n + \mathbf{D}^n + \mathbf{P}^n\right], \tag{4.2}$$

in which the superscript n means the current (known) time step and $n+1$ stands for the next (unknown) time step. The provisional velocity field $\tilde{\mathbf{U}}^{n+1}$ is not divergence-free, i.e. it does not fulfill the continuity equation (2.9). The pressure has to be implicitly evaluated at the next time level in order to get a solenoidal velocity field $\mathbf{U}^{n+1}$:

$$\mathbf{U}^{n+1} = \mathbf{U}^n + \Delta t \left[\mathbf{C}^n + \mathbf{D}^n + \mathbf{P}^{n+1} \right], \tag{4.3}$$

Subtracting equation (4.2) from equation (4.3) gives

$$\begin{aligned} \mathbf{U}^{n+1} - \tilde{\mathbf{U}}^{n+1} &= \Delta t \left[\mathbf{P}^{n+1} - \mathbf{P}^n \right] \\ &= \Delta t \cdot \mathrm{d}\mathbf{P}^{n+1}. \end{aligned} \tag{4.4}$$

Taking the divergence of equation (4.4) and considering $\boldsymbol{\nabla} \cdot \mathbf{U}^{n+1} = 0$, we have

$$-\boldsymbol{\nabla} \cdot \tilde{\mathbf{U}}^{n+1} = \Delta t \, \boldsymbol{\nabla} \cdot \mathrm{d}\mathbf{P}^{n+1}. \tag{4.5}$$

$\mathrm{d}\mathbf{P}^{n+1}$ is related to the gradient of the pressure correction $\mathrm{d}p^{n+1}$ via

$$\mathrm{d}\mathbf{P}^{n+1} = -\frac{1}{\rho} \boldsymbol{\nabla} \mathrm{d}p^{n+1} \tag{4.6}$$

Substituting equation (4.6) into equation (4.5) yields the following Poisson equation for the pressure correction $\mathrm{d}p^{n+1}$:

$$\boldsymbol{\nabla}^2 \mathrm{d}p^{n+1} = \frac{\rho}{\Delta t} \boldsymbol{\nabla} \cdot \tilde{\mathbf{U}}^{n+1}. \tag{4.7}$$

Once the Poisson equation (4.7) is solved and the pressure correction $\mathrm{d}p^{n+1}$ is known, the pressure and the solenoidal velocity fields are obtained by the following correction steps:

$$p^{n+1} = p^n + \mathrm{d}p^{n+1}, \tag{4.8}$$

$$\mathbf{U}^{n+1} = \tilde{\mathbf{U}}^{n+1} - \frac{\Delta t}{\rho} \boldsymbol{\nabla} \mathrm{d}p^{n+1}. \tag{4.9}$$

The solution algorithm can thus be summarized as follows:

1. Compute the provisional velocity field using equation (4.2).
2. Solve the Poisson equation (4.7).
3. Update the pressure and velocity fields using equations (4.8) and (4.9), respectively.

All these three steps involve spatial discretization, i.e. for convective, diffusive and pressure terms in step 1, for the Laplacian and divergence operators in step 2, and for the gradient operator in step 3. The spatial discretization is discussed in subsection 4.1.2. Step 1 involves the time integration for which a third-order low-storage Runge-Kutta scheme [132] is used in the present work. The steps 2 and 3 are performed for every Runge-Kutta substep. The time integration is addressed in subsection 4.1.3. The solution of the Poisson equation in step 2 is

often the most expensive part in an incompressible flow solver. This is shortly presented in subsection 4.1.4.

4.1.2. Spatial Discretization

MGLET uses a cell-centered finite volume method for the spatial discretization. The finite volume method is based on the integral form of the conservation laws. Therefore, the method is locally and globally conservative. The conservation property is very advantageous in computational fluid dynamics applications. The integral form of the incompressible Navier-Stokes equations reads

$$\iint_{\partial\Omega} \mathbf{U}\cdot\mathrm{d}\mathbf{S} = 0, \tag{4.10}$$

$$\frac{\partial}{\partial t}\iiint_{\Omega} \rho\,\mathbf{U}\,\mathrm{d}V + \iint_{\partial\Omega} \rho\,\mathbf{U}\mathbf{U}\cdot\mathrm{d}\mathbf{S} = -\iint_{\partial\Omega} p\,\mathbf{1}\cdot\mathrm{d}\mathbf{S} + \iint_{\partial\Omega}\left(\boldsymbol{\tau}^{\mathrm{N}}+\boldsymbol{\tau}^{\mathrm{NN}}\right)\cdot\mathrm{d}\mathbf{S}, \tag{4.11}$$

where Ω is the solution domain and $\partial\Omega$ is the surface surrounding Ω. Equations (4.10) and (4.11) are valid globally and locally. This means that Ω can be the whole computational domain or a finite volume cell. Considering the Newton's law of viscosity for incompressible flow (2.11), equation (4.11) reduces to

$$\begin{aligned}\frac{\partial}{\partial t}\iiint_{\Omega} \rho\,\mathbf{U}\,\mathrm{d}V + \iint_{\partial\Omega} \rho\,\mathbf{U}\mathbf{U}\cdot\mathrm{d}\mathbf{S} = &-\iint_{\partial\Omega} p\,\mathbf{1}\cdot\mathrm{d}\mathbf{S} \\ &+\iint_{\partial\Omega} 2\mu\,\mathbf{D}\cdot\mathrm{d}\mathbf{S} + \iint_{\partial\Omega}\boldsymbol{\tau}^{\mathrm{NN}}\cdot\mathrm{d}\mathbf{S}.\end{aligned} \tag{4.12}$$

In the finite volume method, the change in the volume-averaged quantity is related to the surface fluxes and possibly source term(s).

As can be deduced from equation (4.12), the finite volume discretization involves a numerical approximation of volume and surface integrals, as well as the first derivative. These operations can be done in different ways, resulting in different orders of accuracy. The details can be found in [30]. Currently, two versions of MGLET are available. A second-order version has been under development for more than two decades [76, 73]. Recently, Hokpunna has developed a fourth-order finite volume method in MGLET [50, 51]. The second-order version is used for the Monte-Carlo simulations in the present work (see chapter 5).

4.1.3. Time Integration

An explicit Euler time stepping of the Navier-Stokes equations has been explained in section 4.1.1. The explicit Euler is only first-order accurate and has a small stability region for the

convection-diffusion equation while it is unstable for a pure convection problem. Therefore, it is desirable to employ a high-order method which has better stability properties. To this aim, a low-storage third-order Runge-Kutta scheme (RK3) [132] is used for the time advancement of the momentum equation. Such a low-storage Runge-Kutta scheme for the generic differential equation

$$\frac{\mathrm{d}u}{\mathrm{d}t} = f(u), \quad u(t=0) = u_0, \tag{4.13}$$

reads

$$1^{\text{st}} \text{ substep}: \quad S_1 = f(u_0), \quad u_{11} = u_0 + \frac{1}{3}\Delta t S_1, \tag{4.14a}$$

$$2^{\text{nd}} \text{ substep}: \quad S_2 = f(u_{11}) - \frac{5}{9}S_1, \quad u_{12} = u_{11} + \frac{15}{16}\Delta t S_2, \tag{4.14b}$$

$$3^{\text{rd}} \text{ substep}: \quad S_3 = f(u_{12}) - \frac{153}{128}S_2, \quad u_1 = u_{12} + \frac{8}{15}\Delta t S_3. \tag{4.14c}$$

The stability diagrams of the third-order Runge-Kutta and the explicit Euler schemes for the model ordinary differential equation

$$\frac{\mathrm{d}y}{\mathrm{d}t} = \lambda y, \quad \lambda = \lambda_R + i\lambda_I, \tag{4.15}$$

with $i^2 = -1$, are plotted in figure 4.1. The stability region of the Runge-Kutta method is extended over the imaginary axis, i.e. the Runge-Kutta scheme is conditionally stable for convection-dominated problems. This is an important feature which makes the Runge-Kutta method a good candidate for simulation of high Reynolds number flows. The incompressibility is enforced at each Runge-Kutta substep by solving the Poisson equation (4.7), the pressure correction (4.8) and the velocity correction (4.9). In all simulations reported in this work, the time step Δt is chosen such that the Courant-Friedrichs-Lewy number

$$\text{CFL} = \max_j \left\{ \left| \frac{U_j \Delta t}{\Delta x_j} \right| \right\}, \quad j = 1, 2, 3, \tag{4.16}$$

is below 0.5.

4.1.4. Solution of the Poisson Equation

The Poisson equation (4.7) can be solved either directly or iteratively. Although iterative solvers are generally preferred in computational fluid dynamics applications, an efficient direct solver based on the fast Fourier transform (FFT) can be tailored for the channel flow. In this thesis, we tested both iterative and direct solvers whose principles are explained in the

sequel.

The iterative solver used in this work is the strongly implicit procedure (SIP) of Stone [121]. It is based on an incomplete LU decomposition. The SIP usually converges in a few iterations and hence, it is vastly used in computational fluid dynamics. The details of the SIP can be found in [121, 30]. `FORTRAN` implementations of SIP for two- and three-dimensional problems are provided as supplementary materials to [30].

The direct solution of the Poisson's equation (4.7) in three-dimensional simulations with a large number of grid cells, which is typical for DNS, is prohibitively expensive. For the case of a channel flow however, one can take the advantage of the two periodic directions, i.e. the streamwise and the spanwise directions. These directions have to be equidistantly discretized, which is often the case in the simulation of a turbulent channel flow. Fast Fourier transforming its both sides, the three-dimensional Poisson equation (4.7) reduces to a tridiagonal system in the wall-normal direction for each wavenumber. A tridiagonal system can be efficiently solved by the TDMA algorithm. The details of such an FFT-based solver can be found in [24, 81].

Our numerical experiments show that the SIP solver is faster than the direct solver, though the latter leads to a smaller divergence of the velocity field. Therefore, we chose to use the SIP solver due to its computational efficiency.

4.1.5. Numerical Grid

`MGLET` uses a staggered arrangement of variables within an orthogonal non-equidistant Carte-

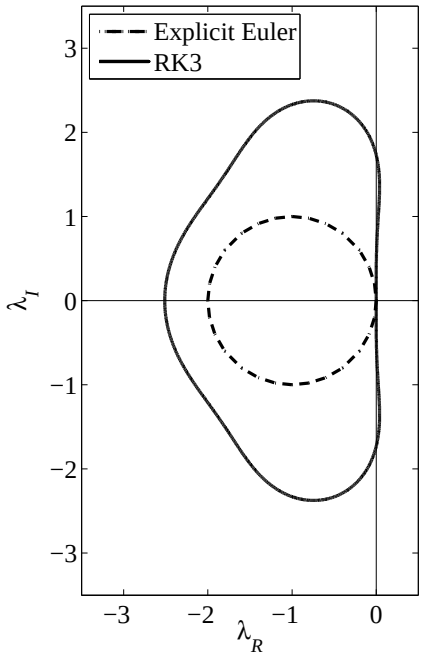

Figure 4.1: Stability diagrams for explicit Euler and third-order Runge-Kutta (RK3) methods.

sian grid. A staggered arrangement of flow variables means that the pressure and the passive scalars (if any) are stored at the cell centers, while the velocity components are stored at the cell faces. This situation is shown in figure 4.2. In our implementation, the non-Newtonian stress $\boldsymbol{\tau}^{\mathrm{NN}}$ is also stored at pressure nodes, i.e. at the cell centers. Let $\left(x_i, y_j, z_k\right)$ and $\left(x_{i+1}, y_{j+1}, z_{k+1}\right)$ denote the position of the pressure nodes (i, j, k) and $(i+1, j+1, k+1)$, respectively. The Cartesian components of the velocity vector U_{ijk}, V_{ijk} and W_{ijk} are respectively stored at $\left(x_{i+1/2}, y_j, z_k\right)$, $\left(x_i, y_{j+1/2}, z_k\right)$ and $\left(x_i, y_j, z_{k+1/2}\right)$ with

$$x_{i+1/2} = \frac{x_i + x_{i+1}}{2}, \tag{4.17}$$

$$y_{j+1/2} = \frac{y_j + y_{j+1}}{2}, \tag{4.18}$$

$$z_{k+1/2} = \frac{z_k + z_{k+1}}{2}. \tag{4.19}$$

The use of staggered grids in computational fluid dynamics has been introduced by Harlow and Welch in 1965 [45]. Since then, it has been extensively used in numerical simulations of the Navier-Stokes equations, especially for incompressible flows. It has two main advantages as compared to a collocated arrangement of the flow variables. First, it does not lead to the even-odd decoupling and spurious oscillations in pressure. These oscillations can occur in a collocated grid if the central difference scheme is used, though they can be avoided by the Rhie-Chow interpolation scheme [110]. Second, the use of a staggered grid allows us not to specify explicit boundary conditions for the solution of the Poisson equation in the projection method [57]. There are also flow solvers based on spectral methods that do not require *ad hoc* boundary conditions for pressure on non-staggered grids [82]. But this is not often the case for non-spectral flow solvers.

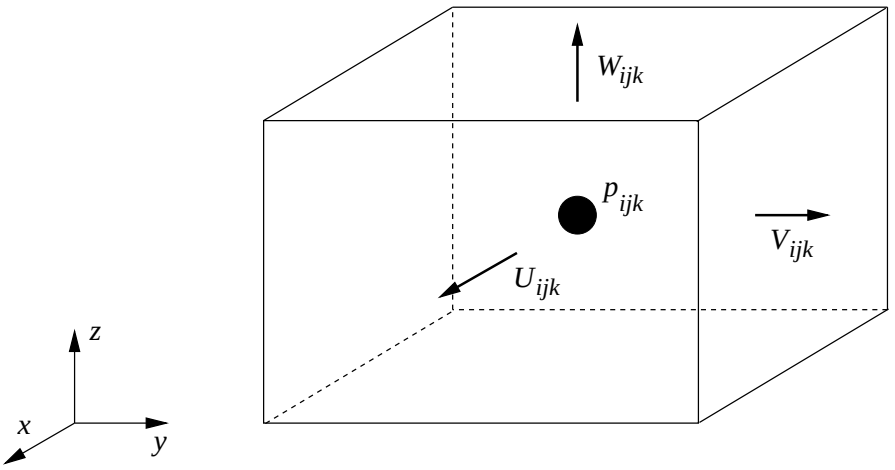

Figure 4.2: Cartesian grid with staggered arrangement of flow variables. Shown is the cell i, j, k.

4.2. Fiber Dynamics Solver

A framework for the simulation of fiber dynamics has been implemented and merged with MGLET, and has been coupled to the existing DNS solver explained above. It consists of several parts that are described in this section.

4.2.1. General Framework

The general framework of the fiber suspension simulator is explained in this subsection, and its constituents are presented in more detail in the subsequent subsections.

The fibers are treated in a Lagrangian manner. The Lagrangian particles are initialized within the flow domain. At each time step, the velocity vector and the velocity gradient tensor at the position of every particle are computed by interpolating and differentiating from the Eulerian velocity field. Using the velocity gradient tensor, the conformation of fibers is computed by a Monte-Carlo method. We have also developed a moment approximation solver which requires a moment closure model. Since the performance of the closure model is questionable (see subsection 4.4.2), we chose to use the direct Monte-Carlo solver in this thesis. The fiber conformation is used to calculate the Lagrangian field of the non-Newtonian stress at particle positions. The Lagrangian field of the non-Newtonian stress is then transferred to the pressure nodes to obtain the Eulerian field of the non-Newtonian stress, which is supplied to the DNS solver. At this point, the position of the Lagrangian particles is advanced by using the Lagrangian velocity field. Afterwards, the boundary conditions are enforced to the particles. Finally, one time step of the DNS solver is performed. The same time step size Δt is used for the time advancement of the flow field, fiber conformation and particle position. These steps are explained in details in the subsequent subsections.

4.2.2. Particle Tracking Method

Our Lagrangian simulation of fibers is based on a particle tracking method. The translational inertia and the spatial Brownian motion of particles are neglected in the present work, as discussed in section 3.1. Therefore, the change in the position of a particle is governed by the following kinematic relation:

$$\frac{\mathrm{d}\mathbf{x}_p}{\mathrm{d}t} = \mathbf{U}\left(\mathbf{x}_p, t\right), \tag{4.20}$$

with the initial condition

$$\mathbf{x}_p\left(t=0\right) = \mathbf{x}_{p,0}. \tag{4.21}$$

$\mathbf{U}\left(\mathbf{x}_p, t\right)$ is the fluid velocity at the particle position $\mathbf{x}_p$ and at the time instant t. Equation (4.20) is integrated in time using an explicit Euler scheme:

$$\mathbf{x}_p^{n+1} = \mathbf{x}_p^n + \Delta t \cdot \mathbf{U}\left(\mathbf{x}_p^n, t^n\right), \tag{4.22}$$

where n is the known time level and $n+1$ is the unknown time level.

The carrier fluid velocity field is given by the DNS solver on an Eulerian grid. However, at each time step, the Lagrangian velocity field at the position of all particles is required for the solution of equation (4.20). The Lagrangian velocity field is obtained by interpolating from the Eulerian DNS field. Various interpolation schemes can be used for this purpose. The effect of such interpolation has been studied in the literature. Yeung and Pope [134] have studied interpolation schemes based on Taylor series expansion and cubic splines in a spectral simulation of isotropic turbulence, and concluded that accurate estimates of Lagrangian statistics can be obtained by either third-order Taylor series interpolation or cubic splines. Balachandar and Maxey [5] have investigated the Lagrangian velocity interpolation in a spectral simulation of isotropic turbulence with different schemes. They found out that for poorly resolved simulations, one needs a highly accurate interpolation scheme. But if the simulation is well resolved, a lower order scheme performs well. Kontomaris *et al.* [62] have studied the velocity interpolation scheme in a spectral simulation of turbulent channel flow. They used Lagrange polynomials up to order six in the periodic directions and Chebyshev polynomials in the wall-normal direction, and found out that the particle statistics is well represented in the channel. Terrapon [125] has studied the effect of different interpolation schemes on the Lagrangian simulation of polymer-induced turbulent drag reduction in a channel flow. His observation was that the difference between various schemes is modest in contrary to the above-mentioned reports. His argument was that his flow solver uses a second-order finite difference method while the studies before were all using spectral methods. In the present work, we use a second-order mass-conservative interpolation scheme developed by Meyer and Jenny [79], and implemented in `MGLET` by Gobert [41].

The velocity gradient tensor at each particle position is needed in order to compute the fiber conformation. It is computed at the cell corners by using a fourth-order scheme. Then, third-order Lagrange polynomials are used to interpolate the velocity gradient tensor at the particle positions. This scheme ensures the continuity of the velocity gradient tensor in time. It has been developed and implemented in `MGLET` by Manhart [71].

The boundary conditions for particles are the following. Periodicity is assumed in streamwise and spanwise directions. This means that if a particle leaves the computational domain from one side, it enters the domain from the opposite side. In the wall-normal direction, a bouncing condition is enforced at the walls. This means that if a particle hits the wall, it comes back to the domain with opposite velocity in the wall-normal direction, i.e. a fully elastic impact to the wall is assumed. This is justified because fluid particles are being transported in our simulations.

4.2.3. Monte-Carlo Simulation

Our approach to compute the fiber conformation in the present work is the Monte-Carlo method. It is basically a stochastic simulator of the Fokker-Planck equation (3.15). The method has been developed by Manhart [71, 72]. It has been validated in simple flows [70, 71], and used in one-way coupled simulations to study the rheology [71] and viscoelastic

behavior [72] of dilute Brownian fiber suspensions in a turbulent channel flow. The validation has been done by comparing the results with the analytical solution of Okagawa *et al.* [98], and the experiments of Frattini and Fuller [33]. In the following, we present the principles of the Monte-Carlo solver.

The Monte-Carlo simulator is based on the Jeffery equation

$$\frac{\mathrm{D}\mathbf{n}}{\mathrm{D}t} = \boldsymbol{\Omega}\cdot\mathbf{n} + \kappa\left[\mathbf{D}\cdot\mathbf{n} - (\mathbf{n}\cdot\mathbf{D}\cdot\mathbf{n})\,\mathbf{n}\right] + \boldsymbol{\Gamma}(t), \tag{4.23}$$

to which a stochastic term $\boldsymbol{\Gamma}(t)$ is added. The stochastic term represents the rotary Brownian motion. Strictly speaking, the stochastic process that is used to simulate a Brownian motion is not differentiable. Therefore, equation (4.23) should be written in the form of a Langevin equation:

$$\mathrm{d}\mathbf{n} = \boldsymbol{\mu}(\mathbf{n},t)\,\mathrm{d}t + \sigma(\mathbf{n},t)\,\mathrm{d}\mathbf{W}_t, \tag{4.24}$$

where the first and the second terms in the right-hand side represent the drift and the diffusion terms in the Fokker-Planck equation (3.15), respectively. They are given by

$$\boldsymbol{\mu}(\mathbf{n},t) = \boldsymbol{\Omega}\cdot\mathbf{n} + \kappa\left[\mathbf{D}\cdot\mathbf{n} - (\mathbf{n}\cdot\mathbf{D}\cdot\mathbf{n})\,\mathbf{n}\right] \tag{4.25}$$

$$\sigma(\mathbf{n},t) = \sqrt{2D_r}. \tag{4.26}$$

In equation (4.24), $\mathrm{d}\mathbf{W}_t$ is the increment of a three-dimensional Wiener process $\mathbf{W}_t$ that is used to numerically simulate the diffusion term in the Fokker-Planck equation (3.15) [100]. A Wiener process $\mathbf{W}_t$ has the following properties:

$$\left\langle \mathbf{W}_t \right\rangle = \mathbf{0}, \quad \left\langle \mathbf{W}_{t_1}\mathbf{W}_{t_2} \right\rangle = \min\left\{t_1,t_2\right\}\mathbf{1}, \quad t_1 \neq t_2. \tag{4.27}$$

The increment of a Wiener process $\mathrm{d}\mathbf{W}_t$ possesses the following properties:

$$\left\langle \mathrm{d}\mathbf{W}_t \right\rangle = \mathbf{0}, \quad \left\langle \mathrm{d}\mathbf{W}_t\,\mathrm{d}\mathbf{W}_t \right\rangle = |\mathrm{d}t|\,\mathbf{1}, \quad \mathrm{d}\mathbf{W}_t = \mathbf{W}_{t+\mathrm{d}t} - \mathbf{W}_t. \tag{4.28}$$

The second moment (the mean-square) of the increment of a Wiener process grows linearly with the time interval $\mathrm{d}t$. This means that it describes a diffusion process [100]. A single realization of a one-dimensional Wiener process is shown in figure 4.3. It can be seen that the Wiener process $\mathbf{W}_t$ belongs to the class of $\mathscr{C}^0$ functions, i.e. it is continuous in time while it is not differentiable with respect to time.

A Wiener process is a Markov process [63] and hence, the orientation vector $\mathbf{n}(t)$ obtained by solving equation (4.24) is also a Markov process. A Markov process is a stochastic process whose state at a next time level $t+\mathrm{d}t$ does not depend on the history of the process on $[0,t]$, but only on the current time level t. This means that in order to integrate equation (4.24), we do not need to store the whole history of the orientation vector $\mathbf{n}$, but rather use a standard single step time integrator, e.g. the explicit Euler scheme, to numerically integrate from $\mathbf{n}(t)$ to $\mathbf{n}(t+\mathrm{d}t)$. The solution of the Langevin equation (4.24) at time instant t is given

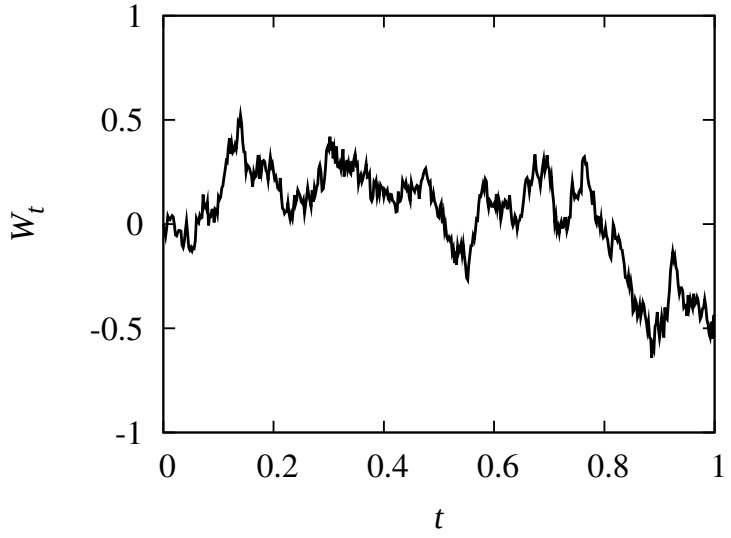

Figure 4.3: One realization of a one-dimensional Wiener process.

by

$$\mathbf{n}(t) = \mathbf{n}_0 + \int_0^t \boldsymbol{\mu}\left(\mathbf{n}, t'\right) \mathrm{d}t' + \int_0^t \sigma\left(\mathbf{n}, t'\right) \mathrm{d}\mathbf{W}_{t'}, \tag{4.29}$$

where $\mathbf{n}_0$ is the initial condition. Equation (4.29) defines an Itô process with the drift term expressed as an integral in time:

$$\int_0^t \boldsymbol{\mu}\left(\mathbf{n}, t'\right) \mathrm{d}t',$$

and the diffusion term expressed as an Itô integral, i.e. an integral with respect to the Wiener process:

$$\int_0^t \sigma\left(\mathbf{n}, t'\right) \mathrm{d}\mathbf{W}_{t'}.$$

A single explicit Euler time step of the Langevin equation (4.24) is obtained by integrating from t to $t + \Delta t$:

$$\mathbf{n}(t + \Delta t) = \mathbf{n}(t) + \boldsymbol{\mu}(\mathbf{n}(t), t)\,\Delta t + \sigma\left(\mathbf{n}(t), t\right) \mathrm{d}\mathbf{W}_t. \tag{4.30}$$

The increment of the Wiener process $\mathrm{d}\mathbf{W}_t$ can be simulated by a random number generator with a uniform distribution [100, 71]. Such a random number generator is usually available in computer programming languages, e.g. the `random_number` subroutine in `FORTRAN`. Otherwise, one can implement his own random number generator subroutine, as is done in `MGLET`. The intensity of the uniform random numbers used to simulate the Wiener process in equation

(4.30) is given by [100, 71]

$$B_{\text{uni}} = \sqrt{12\Delta t}\,. \tag{4.31}$$

This means that the diffusion term $\sigma\,\mathrm{d}\mathbf{W}_t$ in equation (4.30) can be simulated by a set of uniform random numbers with the intensity

$$B_{\text{uni,d}} = \sigma B_{\text{uni}} = \sqrt{24\Delta t D_r}\,, \tag{4.32}$$

which solely depends on the Brownian diffusivity D_r and the time step size Δt.

We have proved in section 3.3 that the Jeffery equation preserves the length of the orientation vector $\mathbf{n}$. It shall be noted here that this does not hold in general when the stochastic term $\boldsymbol{\Gamma}$ is added to the Jeffery equation, i.e.

$$\frac{1}{2}\frac{\mathrm{D}\mathbf{n}\cdot\mathbf{n}}{\mathrm{D}t} = \boldsymbol{\Gamma}\cdot\mathbf{n}. \tag{4.33}$$

This means that the length of $\mathbf{n}$ is preserved if the stochastic term and the orientation vector are orthogonal, i.e. $\boldsymbol{\Gamma}\perp\mathbf{n}$ or $\boldsymbol{\Gamma}\cdot\mathbf{n}=0$. Alternatively, one can normalize the orientation vector $\mathbf{n}$ at each time step so that its length remains unity. This approach is taken in the present work and it is proved in [71] that it yields the exact solution of the Fokker-Planck equation in simple flows. There is also a possibility to write the Langevin equation (4.24) in such a way that it preserves the length of $\mathbf{n}$. We do not use such an approach in this work and thus, it is not discussed any further.

From the rheological theory of Brenner [11], as discussed in section 3.6, the non-Newtonian stress tensor that is needed for the momentum equation (4.12) depends on the second and fourth moments of the fiber orientation distribution function. Thus, one has to compute the second and fourth moments which depend on the orientation distribution function. Our Monte-Carlo simulator solves the Langevin equation (4.24) for an ensemble of N_f sampling fibers. The orientation distribution function Ψ can be computed from the ensemble of the sampling fibers via

$$\Psi(\tilde{\mathbf{n}}) = \frac{1}{N_f}\sum_{i=1}^{N_f}\delta\left(\tilde{\mathbf{n}}-\mathbf{n}_i\right), \tag{4.34}$$

where δ is the Dirac delta function, $\tilde{\mathbf{n}}$ is a specific orientation at which the orientation distribution function is evaluated, and $\mathbf{n}_i$ is the orientation of an individual sampling fiber. Definition

(4.34) satisfies the normalization condition (3.16), namely

$$\begin{aligned}\iint_S \Psi(\tilde{\mathbf{n}})\,\mathrm{d}S(\tilde{\mathbf{n}}) &= \iint_S \frac{1}{N_f}\sum_{i=1}^{N_f}\delta\left(\tilde{\mathbf{n}}-\mathbf{n}_i\right)\mathrm{d}S(\tilde{\mathbf{n}}) \\ &= \frac{1}{N_f}\sum_{i=1}^{N_f}\iint_S \delta\left(\tilde{\mathbf{n}}-\mathbf{n}_i\right)\mathrm{d}S(\tilde{\mathbf{n}}) \\ &= \frac{1}{N_f}\sum_{i=1}^{N_f} 1 = \frac{1}{N_f}\cdot N_f = 1.\end{aligned} \tag{4.35}$$

Introducing the orientation distribution function (4.34) to the definition of the second moment (3.18) yields

$$\begin{aligned}\langle \mathbf{nn}\rangle_\Psi &= \iint_S \tilde{\mathbf{n}}\tilde{\mathbf{n}}\,\Psi(\tilde{\mathbf{n}})\,\mathrm{d}S(\tilde{\mathbf{n}}) = \iint_S \tilde{\mathbf{n}}\tilde{\mathbf{n}}\,\frac{1}{N_f}\sum_{i=1}^{N_f}\delta\left(\tilde{\mathbf{n}}-\mathbf{n}_i\right)\mathrm{d}S(\tilde{\mathbf{n}}) \\ &= \frac{1}{N_f}\sum_{i=1}^{N_f}\iint_S \tilde{\mathbf{n}}\tilde{\mathbf{n}}\,\delta\left(\tilde{\mathbf{n}}-\mathbf{n}_i\right)\mathrm{d}S(\tilde{\mathbf{n}}) = \frac{1}{N_f}\sum_{i=1}^{N_f}\mathbf{n}_i\,\mathbf{n}_i\end{aligned} \tag{4.36}$$

The derivation is similar for the fourth moment. Thus, the second and fourth moments of the orientation distribution function which are required to compute the non-Newtonian stress tensor are given by

$$\langle \mathbf{nn}\rangle_\Psi = \frac{1}{N_f}\sum_{i=1}^{N_f}\mathbf{n}_i\,\mathbf{n}_i, \tag{4.37}$$

$$\langle \mathbf{nnnn}\rangle_\Psi = \frac{1}{N_f}\sum_{i=1}^{N_f}\mathbf{n}_i\,\mathbf{n}_i\,\mathbf{n}_i\,\mathbf{n}_i. \tag{4.38}$$

In our implementation, we directly compute $\mathbf{D} : \langle \mathbf{nnnn}\rangle_\Psi$ instead of $\langle \mathbf{nnnn}\rangle_\Psi$. This is done for the sake of CPU-time efficiency and reduction in memory requirements.

Equations (4.37) and (4.38) mean that the moments are computed by ensemble averaging over the set of the sampling fibers. The number of sampling fibers N_f has to be sufficiently large in order to obtain accurate moments. The accuracy of the method depends on the number of samples, like any other Monte-Carlo method. Manhart [71] has studied the convergence with respect to the number of samples N_f.

The initial condition of the fiber orientation in all simulations presented in this work is a uniform (isotropic) state which corresponds to the following constant orientation distribution function

$$\Psi = \frac{1}{4\pi}. \tag{4.39}$$

This is achieved by uniformly distributing the sampling fibers over the surface of the unit sphere **S**.

At each Lagrangian particle, the non-Newtonian stress tensor and hence the second and fourth moments are to be computed. This task requires an ensemble of N_f fibers to be transported with the Lagrangian particles. It means that the Lagrangian Monte-Carlo simulation consists of N_p Lagrangian particles (pathlines), each of which carrying an ensemble of N_f sampling fibers. This strategy is schematically depicted in figure 4.4.

4.2.4. Moment Approximation Simulation

The second and fourth moments of the orientation distribution function are needed for the computation of the non-Newtonian stress tensor. Therefore, one can use the moment evolution equation (3.24) to directly compute the required moments at a cheaper computational cost. The problem is that the moment evolution equation (3.24) is not mathematically closed, and one has to seek an appropriate closure model. There exist several such models, as already discussed in subsection 3.5. The accuracy of these closures in a complicated, three-dimensional, unsteady, vortical, turbulent flow is indeed questionable. The numerical solution of the moment approximation equation (3.24) is performed in a Lagrangian frame of reference. This means that each Lagrangian particle (on a pathline) carries the second moment $\langle \mathbf{nn} \rangle_\Psi$ of the orientation distribution function. This concept is schematically shown in figure 4.5.

Here, we present the time integration of the moment approximation equation (3.24) using the explicit Euler scheme. We have implemented the second- and third-order Runge-Kutta schemes as well. Our numerical tests show that the explicit Euler scheme is stable and produces accurate results. Therefore, we chose to use the explicit Euler method due to its lower computational cost. A single explicit Euler time step of the moment approximation equation (3.24) reads

$$\begin{aligned} \langle \mathbf{nn} \rangle_\Psi^{n+1} = \langle \mathbf{nn} \rangle_\Psi^{n} + \Delta t \Big[& \boldsymbol{\Omega}^n \cdot \langle \mathbf{nn} \rangle_\Psi^{n} + \langle \mathbf{nn} \rangle_\Psi^{n} \cdot \boldsymbol{\Omega}^{\mathrm{T},n} \\ & + \kappa \big(\mathbf{D}^n \cdot \langle \mathbf{nn} \rangle_\Psi^{n} + \langle \mathbf{nn} \rangle_\Psi^{n} \cdot \mathbf{D}^n - 2\mathbf{D}^n : \langle \mathbf{nnnn} \rangle_\Psi^{n} \big) \\ & + 2D_r \big(\mathbf{1} - 3 \langle \mathbf{nn} \rangle_\Psi^{n} \big) \Big], \end{aligned} \tag{4.40}$$

where the superscripts n and $n+1$ indicate the known quantities at the current time level and the unknown quantities at the next time level, respectively. The rotation-rate tensor $\boldsymbol{\Omega}^n$ and the strain-rate tensor $\mathbf{D}^n$ are provided by the DNS, and then interpolated to the particle positions, similar to the Monte-Carlo solver. The fourth moment $\langle \mathbf{nnnn} \rangle_\Psi^n$ is computed from the second moment $\langle \mathbf{nn} \rangle_\Psi^n$ using a moment closure model, as discussed in subsection 3.5. The uniform orientation state described by the constant orientation distribution function (4.39)

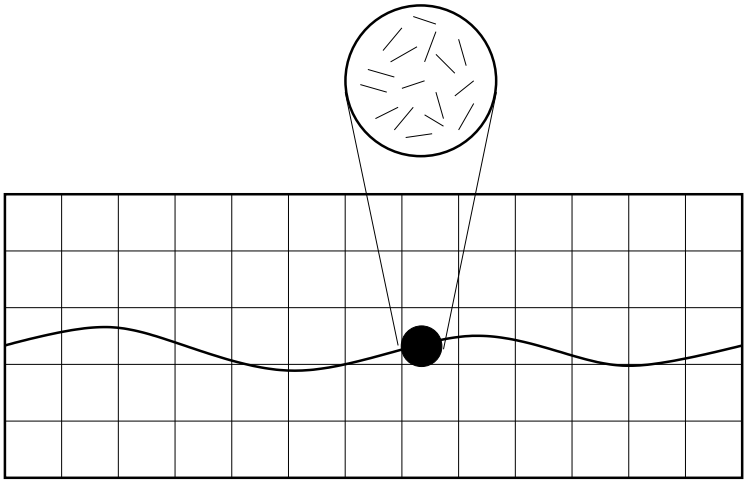

Figure 4.4: Schematic sketch of the Lagrangian Monte-Carlo simulation within the background Eulerian DNS grid. Shown is the Lagrangian path of a particle which carries an ensemble of sampling fibers.

corresponds to the following isotropic second moment

$$\langle \mathbf{nn} \rangle_{\Psi} = \frac{1}{3}\,\mathbf{1} = \begin{pmatrix} \frac{1}{3} & 0 & 0 \\ 0 & \frac{1}{3} & 0 \\ 0 & 0 & \frac{1}{3} \end{pmatrix}, \tag{4.41}$$

which is used as the initial condition to solve the second moment evolution equation (3.24).

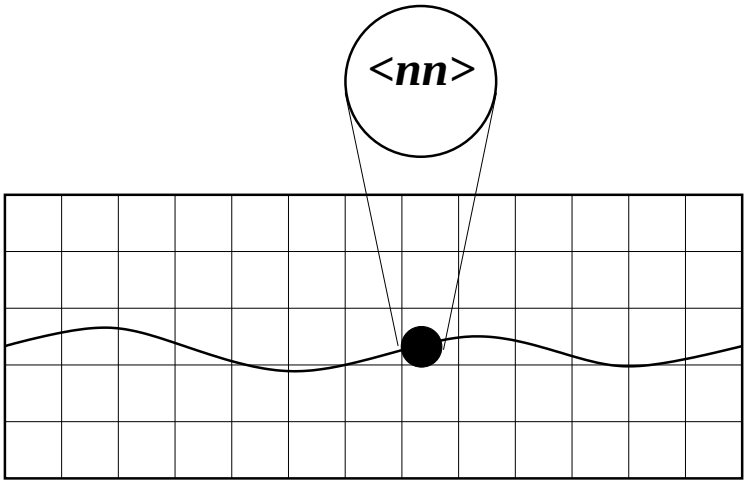

Figure 4.5: Schematic sketch of the Lagrangian moment approximation simulation within the background Eulerian DNS grid. Shown is the Lagrangian path of a particle which carries the second moment $\langle \mathbf{nn} \rangle_{\Psi}$.

4.2.5. Computation of Non-Newtonian Stress

Once the second and fourth moments of the orientation distribution function are computed, either by the Monte-Carlo solver or by the moment approximation method, the non-Newtonian stress tensor at each particle position is computed using the constitutive equation (3.48) of Brenner [11], as discussed in section 3.6. Equation (3.48) is a tensorial algebraic equation and hence, the non-Newtonian stress is computed in a straightforward manner without any difficulty. This leads to the Lagrangian field of the non-Newtonian stress. However, our DNS solver works in an Eulerian frame and requires the Eulerian field of the non-Newtonian stress.

Transition from the Lagrangian to the Eulerian field of $\boldsymbol{\tau}^{\mathrm{NN}}$ can be done in a multitude of ways, e.g. interpolation and averaging procedures. Manhart [74] has employed an interpolation scheme for this purpose. In the present work, we use an averaging procedure. A similar approach has been used by Terrapon [125] for the Lagrangian simulation of turbulent drag reduction by flexible polymers. In the following, the averaging procedure for a generic finite volume cell is explained.

Consider a two-dimensional finite volume cell, as depicted in figure 4.6. We use a two-dimensional cell for the sake of simplicity. The three-dimensional situation will be similar. Assume that N_{pc} Lagrangian particles exist in this specific cell at a specific time step. The non-Newtonian stress tensor $\boldsymbol{\tau}_p^{\mathrm{NN}}$ is known at each particle position. The non-Newtonian stress tensor assigned to the pressure node (cell center) is obtained by averaging over all particles within the cell:

$$\boldsymbol{\tau}^{\mathrm{NN}} = \frac{1}{N_{pc}} \sum_{p=1}^{N_{pc}} \boldsymbol{\tau}_p^{\mathrm{NN}}. \tag{4.42}$$

The averaging procedure is justified because the nodal value represents the cell-averaged

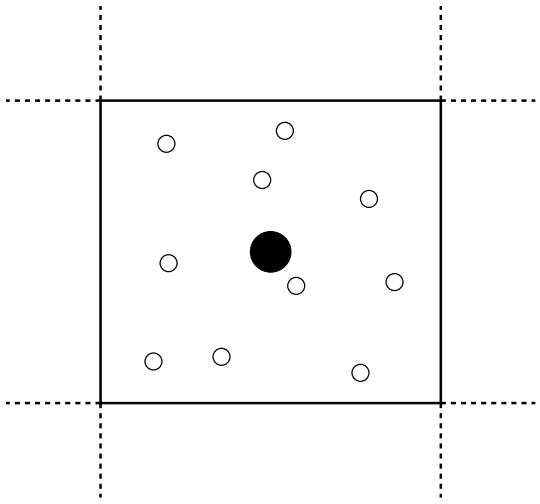

Figure 4.6: Two-dimensional finite volume cell. Filled circle represents the pressure node and the hollow circles represent the Lagrangian particles.

quantity in a finite volume context.

This procedure needs at least one Lagrangian particle per finite volume cell. There are different ways to guarantee this requirement. Terrapon [125] used a particle construction-destruction algorithm. In this manner, if a computational cell contains a lot of particles, the redundant particles are removed in order to reduce the computational overhead. On the other hand, if a computational cell contains too few particles, the additional particles are constructed from the neighboring particles. Another approach, which is used in this work, is to start with a sufficiently large number of particles to ensure the existence of the minimum required particles in each and every finite volume cell. The former procedure is computationally more efficient, but it introduces numerical diffusion [125].

4.3. Parallelization

The direct numerical simulation reported in this work is performed using 2 097 152 grid cells with the second-order version of `MGLET`. The Monte-Carlo simulations contain 65 536 000 particle clusters with each cluster having 100 sampling fibers. This results in a total number of 6 553 600 000 fibers. Each fiber has three degrees of freedom, i.e. three components of $\mathbf{n}$. These numbers show that the reported simulation demands a great amount of computational resources. It cannot be done on a serial machine in a timely manner. For example, Gillissen *et al.* [39] have pointed out that 100 years of CPU time are required to accomplish a Lagrangian simulation of fiber-induced drag reduction in a channel flow on a single AMD Opteron 2 GHz processor using their code. Thus, we have performed the simulations on a massively parallelized machine, SGI-Altix HLRB2, available at the Leibniz supercomputing center (LRZ) in Munich. We have used 128 processing elements for the Monte-Carlo simulation. The parallelization strategy is explained in the sequel.

We parallelize the code based on the Lagrangian paths. This means that each processing element computes a DNS of the whole Eulerian field plus a portion of the Lagrangian particles. This is justified because most of the CPU-time is spent in the Lagrangian part of the computation. A complete time step of our parallel solver is done in the following way. All processing elements perform a time step of the Lagrangian calculation and compute the Eulerian field of the non-Newtonian stress by averaging. Then, they communicate the Eulerian field of the non-Newtonian stress so that all processors receive the complete field. At this stage, each processor is able to perform a time step of the Eulerian DNS. Since the communication is over the Eulerian non-Newtonian stress, it does not depend on the number of particles, but rather on the number of finite volume cells. This means that we have a constant communication time regardless of the number of particles, if the number of finite volume cells does not vary. The parallelization is done in this manner because the number of particles can be orders of magnitude more than the number of finite volume cells. The message passing interface (MPI) library is used in this work for the parallelization.

Table 4.1 shows the CPU-time of the different parts of the computation in a single time step of the Monte-Carlo simulation. In this table, search index is the procedure to find the

cell in which a specific particle is located. This is done for all particles at each time step. It can be seen that most of the CPU-time in the Monte-Carlo simulation is dedicated to the communications (32.6%) and the computation of the second and fourth moments (16.4% each) by ensemble averaging.

Table 4.1: CPU-time profile of the Monte-Carlo solver with 128^3 grid points on 128 processing elements each of which computing 512 000 particle clusters, each cluster having 100 sampling fibers.

Procedure	CPU-time $[s]$
Search index	0.10
Lagrangian velocity	0.54
Lagrangian velocity gradient	1.39
Jeffery's equation	1.80
Second moment $\langle \mathbf{nn} \rangle_\Psi$	4.53
Fourth moment $\langle \mathbf{nnnn} \rangle_\Psi$	4.53
Lagrangian non-Newtonian stress	0.10
Eulerian non-Newtonian stress	1.51
Communication	9.02
Non-Newtonian stress statistics	1.0
Particle position advancement	0.004
Particle boundary condition	0.004
DNS	3.10
Total	27.63

4.4. Validation

Validation of the numerical methods and the computer code implementation of the above-mentioned algorithms is done in three stages. In subsection 4.4.1, we present the DNS of a Newtonian channel flow at a nominal shear Reynolds number $\mathrm{Re}_\tau = 180$, and compare its results with reference data from the literature. The validation of the Monte-Carlo solver in a simple shear flow is presented in subsection 4.4.2. The results of the moment approximation solver are also shown in subsection 4.4.2 for comparison. Finally, in subsection 4.4.3, we validate our proposed two-way coupled solver for fiber suspensions in a channel flow at the limit of zero rotary Péclet number.

4.4.1. DNS of Newtonian Turbulent Channel Flow

A fully-developed turbulent channel flow at a nominal shear Reynolds number $\mathrm{Re}_\tau = 180$ is directly simulated. This specific Reynolds number is chosen to match the reference DNS data

of Kim *et al.* [58] (referred to as "KMM 1987" hereafter) and Moser *et al.* [94] (referred to as "MKM 1999" hereafter) for which an online statistical database is available [95]. The simulation is performed using the second-order version of `MGLET`. The size of the computational box and the grid resolution of the simulation are reported in table 4.2, and compared with those of the reference DNS's. Δz^+_{min} is very small in the reference spectral simulations due to the Chebyshev-tau formulation they have used.

The mean velocity profile in inner layer scaling is plotted in figure 4.7, and compared with the reference DNS data. A good agreement among the profiles is observed. The guidelines in figure 4.7 are the linear law $\langle U\rangle^+ = z^+$ and the von Kármán logarithmic law $\langle U\rangle^+ = 2.5\ln z^+ + 5.5$.

In order to validate the second-order statistics, turbulence intensities u^+_{rms}, v^+_{rms} and w^+_{rms} are plotted in figures 4.8, 4.9 and 4.10, respectively. The agreement between our results and the reference solution is good but not excellent. It should be noted that the reference solution

Table 4.2: Computational domain size and grid resolution for DNS of turbulent channel flow at $\text{Re}_\tau = 180$.

Simulation	L_x	L_y	L_z	N_x	N_y	N_z	Δx^+	Δy^+	Δz^+_{min}
Present	$3\pi h$	$2\pi h$	$2h$	128	128	128	13.25	8.84	0.675
KMM 1987	$4\pi h$	$2\pi h$	$2h$	192	160	129	11.78	7.07	0.054
MKM 1999	$4\pi h$	$\frac{4}{3}\pi h$	$2h$	128	128	129	17.67	5.89	0.054

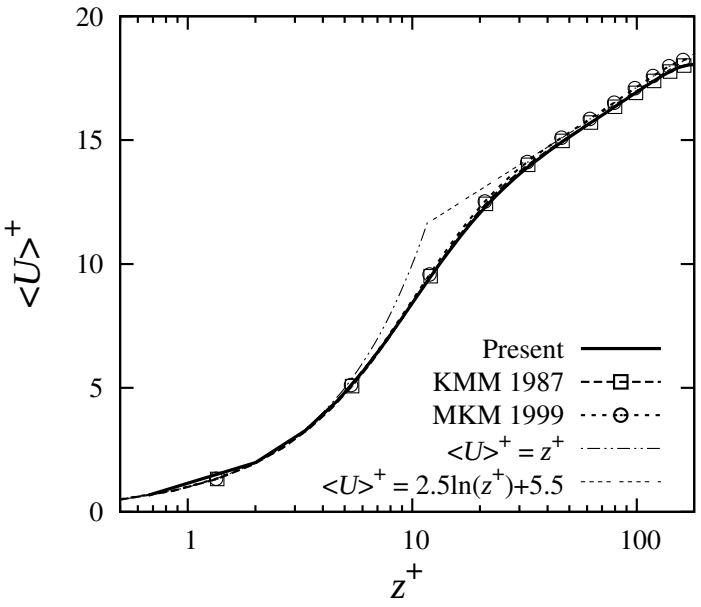

Figure 4.7: Mean velocity profiles in inner layer scaling compared with reference DNS data of KMM 1987 [58] and MKM 1999 [94] at $\text{Re}_\tau = 180$.

is obtained by a highly resolved spectral simulation.

Figure 4.11 shows the one-dimensional energy spectrum in the streamwise direction at wall distance $z^+ = 10$, compared with the reference DNS of MKM 1999 [94]. The spectra are normalized by the energy of the first wavenumber, and averaged in the spanwise direction. The agreement is good. At the end of the spectrum, at high wavenumbers, the spectrum of our second-order code drops much faster than that of the spectral code. This behavior is typical for low-order methods [51].

Finally, in table 4.3, we present the bulk flow variables obtained from our DNS and compare them with the DNS data of Kim *et al.* [58]. The reference DNS data have been validated by comparison with the experimental data compiled by Dean [19]. The agreement between our results and the reference DNS data is good within less than 2% relative error. The only exception is the Reynolds number Re_c based on the centerline velocity U_c with 2.62% relative error. The source of errors is mainly conjectured to be the difference between the codes and grid resolutions. Kim *et al.* used a fully spectral code with about 4×10^6 grid points (spectral modes) while we use a second-order finite volume code with 2.1×10^6 computational cells. The other difference is that their code adjusts the mean pressure gradient such that a nominally constant bulk velocity is achieved. Our code however, works with a constant pressure gradient.

Some terms in table 4.3 have to be clarified. U_c is the mean centerline velocity. C_f and C_{f_0} are the friction coefficients based on the bulk and centerline velocities, respectively. δ^* and θ are the displacement and momentum thicknesses of the boundary layer, respectively, and are

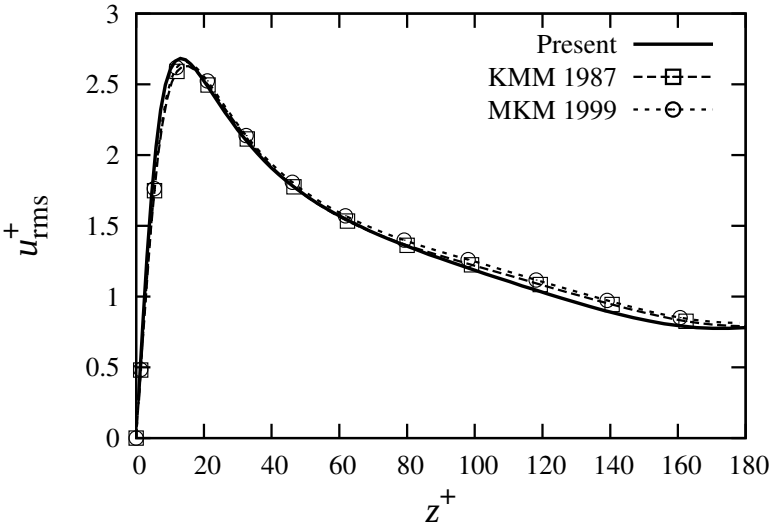

Figure 4.8: Streamwise turbulence intensity in inner layer scaling compared with reference DNS data of KMM 1987 [58] and MKM 1999 [94] at $\mathrm{Re}_\tau = 180$.

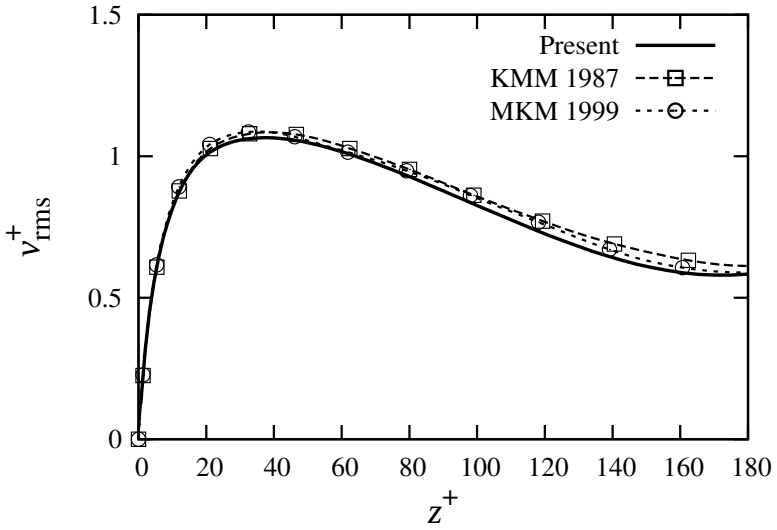

Figure 4.9: Spanwise turbulence intensity in inner layer scaling compared with reference DNS data of KMM 1987 [58] and MKM 1999 [94] at $\mathrm{Re}_\tau = 180$.

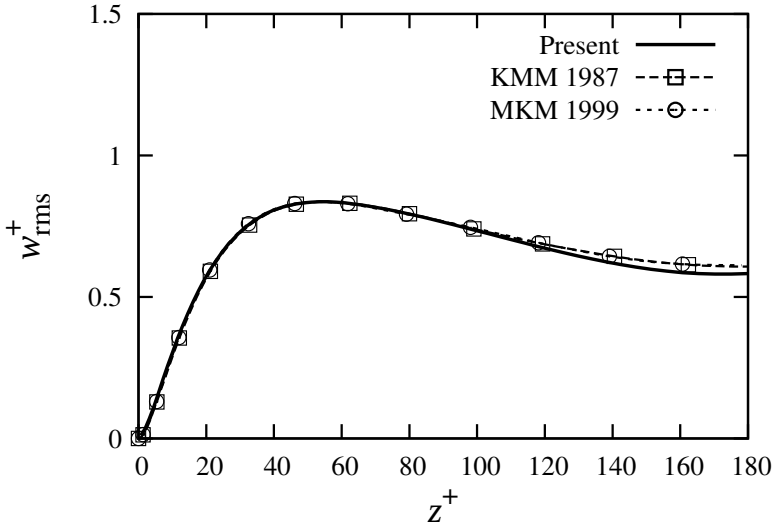

Figure 4.10: Wall-normal turbulence intensity in inner layer scaling compared with reference DNS data of KMM 1987 [58] and MKM 1999 [94] at $\mathrm{Re}_\tau = 180$.

defined by

$$\delta^* = \int_0^h \left(1 - \frac{\langle U \rangle}{U_c}\right) \mathrm{d}z, \quad \theta = \int_0^h \frac{\langle U \rangle}{U_c} \left(1 - \frac{\langle U \rangle}{U_c}\right) \mathrm{d}z. \tag{4.43}$$

$H = \delta^*/\theta$ is the boundary-layer shape factor.

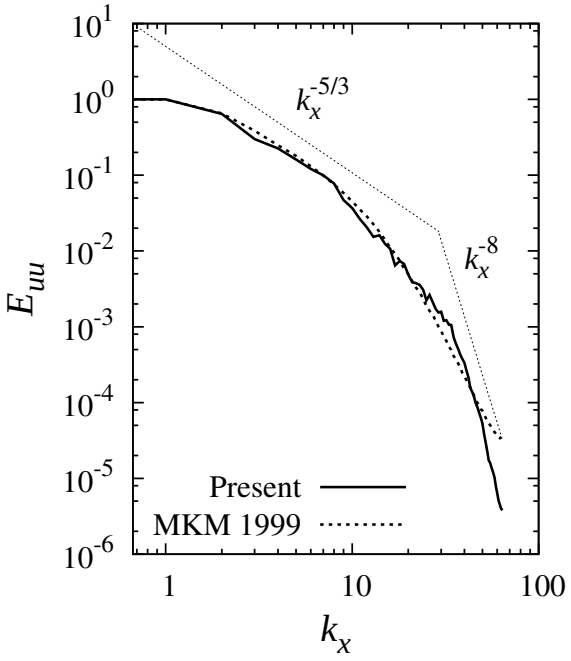

Figure 4.11: One-dimensional energy spectrum in streamwise direction at $z^+ = 10$, compared with reference DNS data of MKM 1999 [94] at $\mathrm{Re}_\tau = 180$. Spectra are normalized by the energy of the first wavenumber and averaged over the spanwise direction.

Figure 4.12: Schematic geometry of simple shear flow.

Table 4.3: Bulk flow variables compared with DNS data of Kim *et al.* [58].

Variable	Present DNS	Kim *et al.* DNS	Relative error
$\mathrm{Re}_\tau = \dfrac{u_\tau h}{\nu}$	178.17	180	1.01%
$\mathrm{Re}_c = \dfrac{U_c h}{\nu}$	3214	3300	2.62%
$\mathrm{Re}_b = \dfrac{U_b 2h}{\nu}$	5543	5600	1.01%
$\dfrac{U_b}{u_\tau}$	15.556	15.63	0.48%
$\dfrac{U_c}{u_\tau}$	18.037	18.20	0.90%
$\dfrac{U_c}{U_b}$	1.1595	1.16	0.04%
$C_f = \dfrac{\tau_w}{\frac{1}{2}\rho U_b^2}$	8.265×10^{-3}	8.18×10^{-3}	1.04%
$C_{f_0} = \dfrac{\tau_w}{\frac{1}{2}\rho U_c^2}$	6.148×10^{-3}	6.04×10^{-3}	1.79%
$\dfrac{\delta^*}{h}$	0.139	0.141	1.62%
$\dfrac{\theta}{h}$	0.0873	0.087	0.38%
$H = \dfrac{\delta^*}{\theta}$	1.59	1.62	1.95%

4.4.2. Validation of the Fiber Orientation Solvers

In this subsection, we validate the developed fiber orientation solvers in a simple shear flow, i.e. the flow between two parallel walls in the absence of a pressure gradient. The bottom wall is kept at rest while the top wall is moving with a constant velocity U in x direction. The flow depth in y direction is infinity. The distance between two walls is h. In a simple shear flow, the only non-zero velocity component is the streamwise one, and it is a linear function of the wall distance z, i.e. $u = \dot{\gamma} z$, in which $\dot{\gamma} = U/h$ is the constant shear rate. This flow configuration is schematically sketched in figure 4.12.

For the case of non-Brownian fibers, Jeffery [54] has analytically shown that a suspended fiber rotates periodically with the time period

$$T = \frac{2\pi \left(r + r^{-1}\right)}{\dot{\gamma}}. \tag{4.44}$$

Okagawa *et al.* [98] have analytically solved the Fokker-Planck equation for a dilute suspension of non-Brownian fibers in a simple shear flow. They have obtained the following orientation distribution as a function of time and the azimuthal and zenithal angles of spherical coordinate:

$$\Psi = \frac{1}{4\pi \left[\cos^2\vartheta + \Lambda^2 \sin^2\vartheta\right]}, \tag{4.45}$$

$$\Lambda^2 = \Lambda_1 \sin^2\varphi + \frac{1}{2}\Lambda_2 \sin 2\varphi + \Lambda_3 \cos^2\varphi, \tag{4.46}$$

$$\Lambda_1 = \frac{1}{2}\left[1 + \frac{1}{r^2} + \left(1 - \frac{1}{r^2}\right)\cos\frac{4\pi t}{T}\right], \tag{4.47}$$

$$\Lambda_2 = \left(\frac{1}{r} - r\right)\sin\frac{4\pi t}{T}, \tag{4.48}$$

$$\Lambda_3 = \frac{1}{2}\left[1 + r^2 + \left(1 - r^2\right)\cos\frac{4\pi t}{T}\right], \tag{4.49}$$

where T is the Jeffery period given by equation (4.44). The analytical solution (4.45) corresponds to a uniform initial condition $\Psi(t = 0) = 1/4\pi$. This can be verified by setting $t = 0$ in equations (4.45) to (4.49).

Figure 4.13 shows the distribution of the sampling fibers over the unit sphere for non-Brownian fibers in a Jeffery half-period, obtained by the Monte-Carlo solver. Starting from a uniformly distributed state, as shown in figure 4.13a, we observe that the fibers are getting more and more oriented with the shear direction in time. This behavior continues until $t = T/4$ (see figure 4.13d) and then, the fiber orientation changes towards a uniform state again. The orientation state exactly reaches the initial condition at time $t = T/2$. This periodicity is observed only for non-Brownian fibers corresponding to $\mathrm{Pe}_r \to \infty$, with the rotary Péclet

number defined as

$$\mathrm{Pe}_r = \frac{\dot{\gamma}}{D_r}. \tag{4.50}$$

At this stage, we present the second moment $\langle \mathbf{nn} \rangle_\Psi$ computed by the Monte-Carlo and the moment approximation solvers, and compare it with the analytical solution (4.45). The fiber aspect ratio is $r = 5$. The Monte-Carlo solver runs with 1000 sampling fibers. The moment approximation solver runs with the quadratic, hybrid and IBOF closure models. Figures 4.14 and 4.15 show the $\langle n_1 n_1 \rangle_\Psi$ and $\langle n_1 n_3 \rangle_\Psi$ components of $\langle \mathbf{nn} \rangle_\Psi$. The Monte-Carlo result perfectly matches the analytical solution. The IBOF result can be hardly seen as it almost coincides with the Monte-Carlo solution. Hybrid closure overpredicts $\langle n_1 n_1 \rangle_\Psi$ and under predicts the Jeffery period. The quadratic closure also overpredicts $\langle n_1 n_1 \rangle_\Psi$, even more than the hybrid closure, but it correctly predicts the Jeffery period. The same behavior is seen in other components of $\langle \mathbf{nn} \rangle_\Psi$ and hence, are not presented here.

The performance of fiber orientation solvers in the presence of Brownian motion is investigated by looking at the fiber orientation in a simple shear flow at $\mathrm{Pe}_r = 100$. In this case, the fiber orientation is not periodic in time. Figures 4.16 and 4.17 show the $\langle n_1 n_1 \rangle_\Psi$ and $\langle n_1 n_3 \rangle_\Psi$ components of $\langle \mathbf{nn} \rangle_\Psi$ for $\mathrm{Pe}_r = 100$. None of the closure models can reproduce the Monte-Carlo results. Still, the IBOF closure yields the most accurate results among all investigated closure models at the highest computational cost. The noise in the Monte-Carlo result is due to the stochastic term (Wiener process) which is simulated by random numbers. A smoother curve can be obtained by using more sampling fibers, at a higher computational cost.

More detailed results on the validation of the Monte-Carlo solver including the effect of time step size and the number of samples can be found in [70, 71]. Further information on the performance of the closure models in simple and turbulent flows can be found in [102, 104, 38, 89, 87]

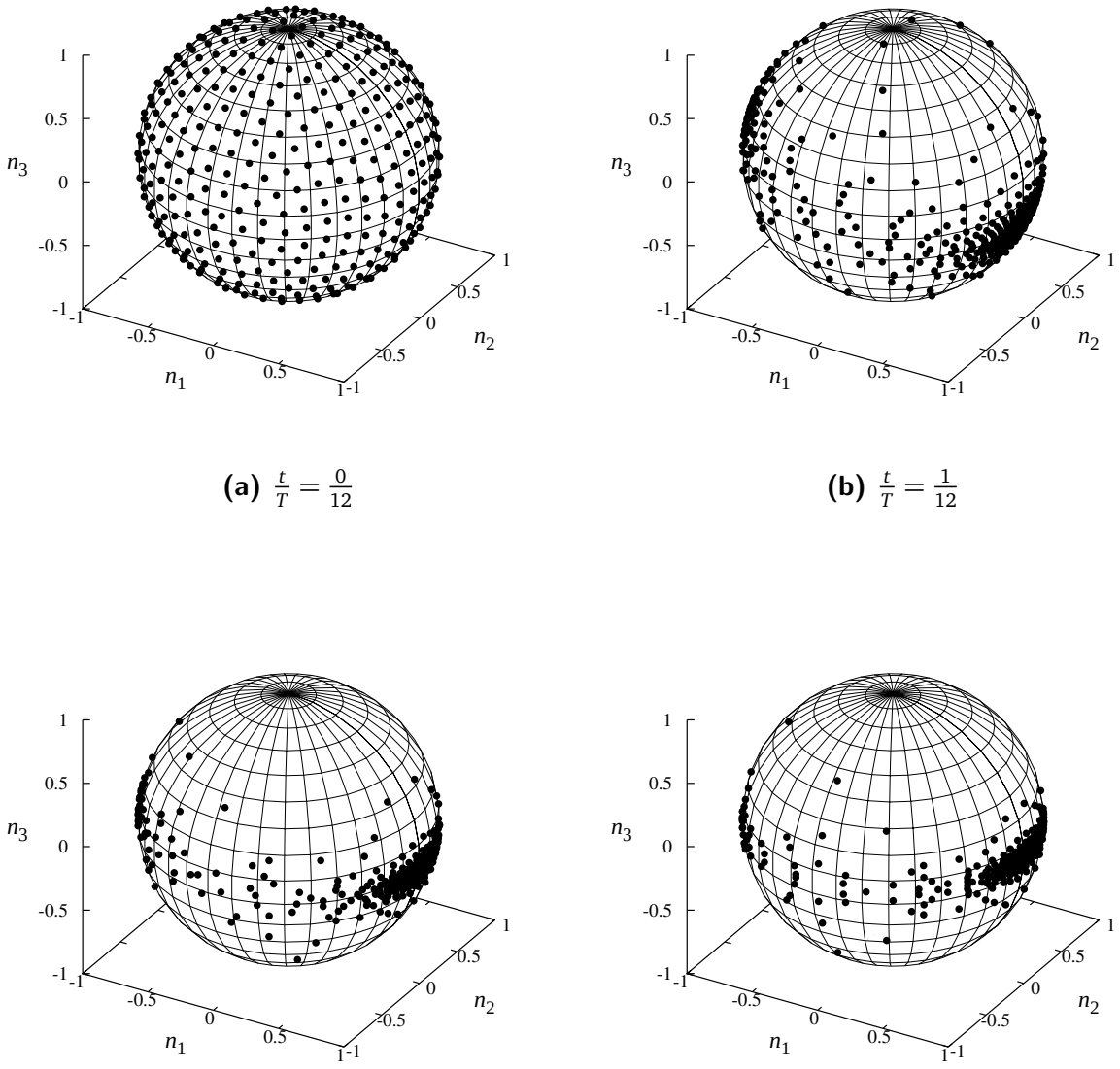

(a) $\frac{t}{T} = \frac{0}{12}$ **(b)** $\frac{t}{T} = \frac{1}{12}$

(c) $\frac{t}{T} = \frac{2}{12}$ **(d)** $\frac{t}{T} = \frac{3}{12}$

Figure 4.13: Instantaneous orientation distribution of non-Brownian particles on the unit sphere obtained by the direct Monte-Carlo simulation with 500 particles in a Jeffery half period $T/2$.

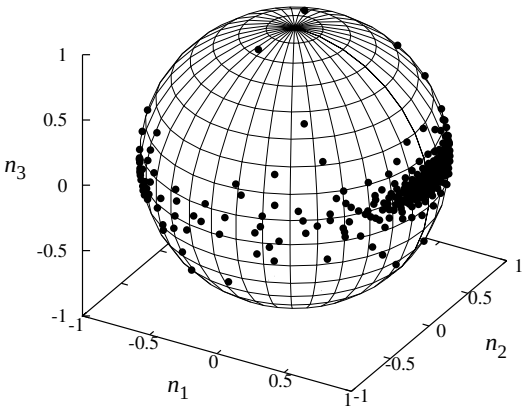

(e) $\frac{t}{T} = \frac{4}{12}$

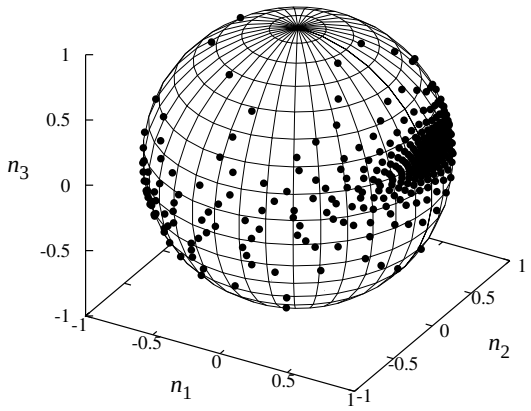

(f) $\frac{t}{T} = \frac{5}{12}$

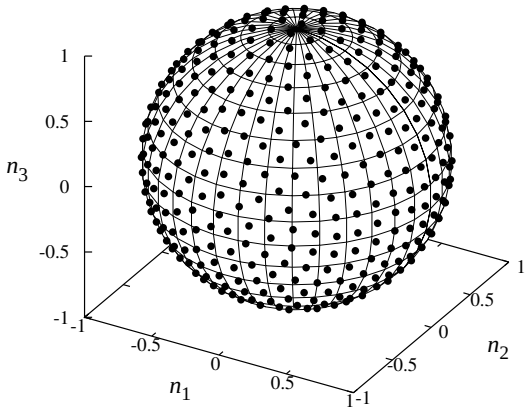

(g) $\frac{t}{T} = \frac{6}{12}$

Figure 4.13: Instantaneous orientation distribution of non-Brownian particles on the unit sphere obtained by the direct Monte-Carlo simulation with 500 particles in a Jeffery half period $T/2$ (continued).

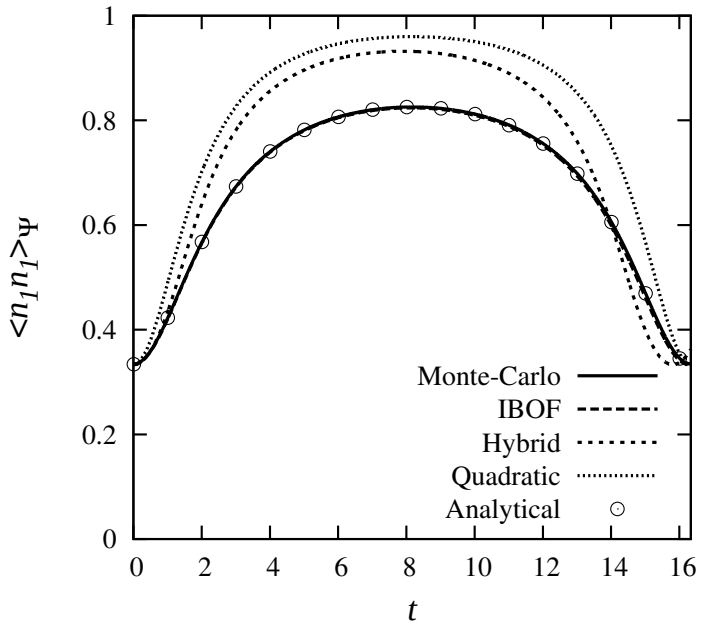

Figure 4.14: $\langle n_1 n_1 \rangle_\Psi$ component of the second moment for non-Brownian fibers with $r = 5$ in a Jeffery half period.

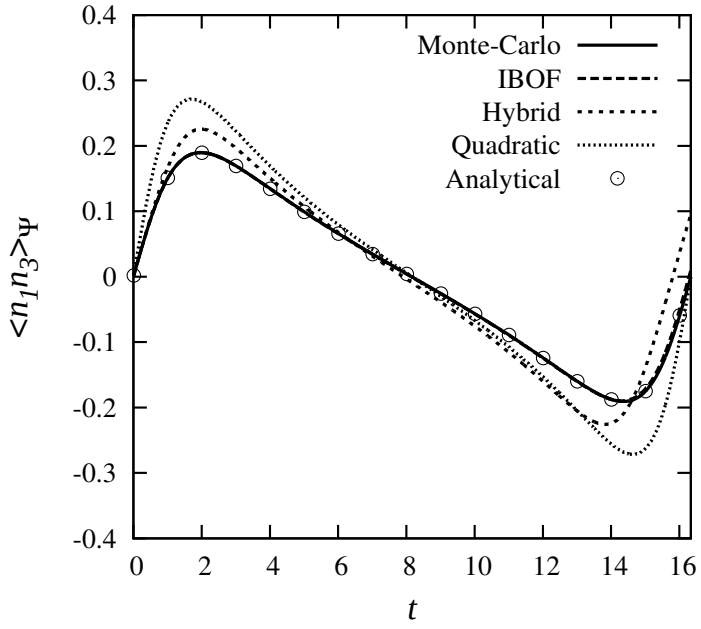

Figure 4.15: $\langle n_1 n_3 \rangle_\Psi$ component of the second moment for non-Brownian fibers with $r = 5$ in a Jeffery half period.

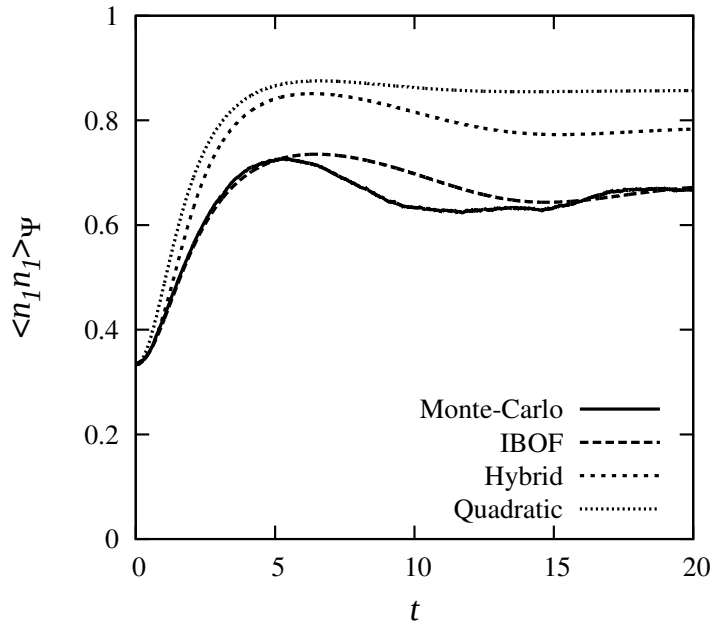

Figure 4.16: $\langle n_1 n_1 \rangle_\Psi$ component of the second moment for non-Brownian fibers with $r = 5$ in a Jeffery half period.

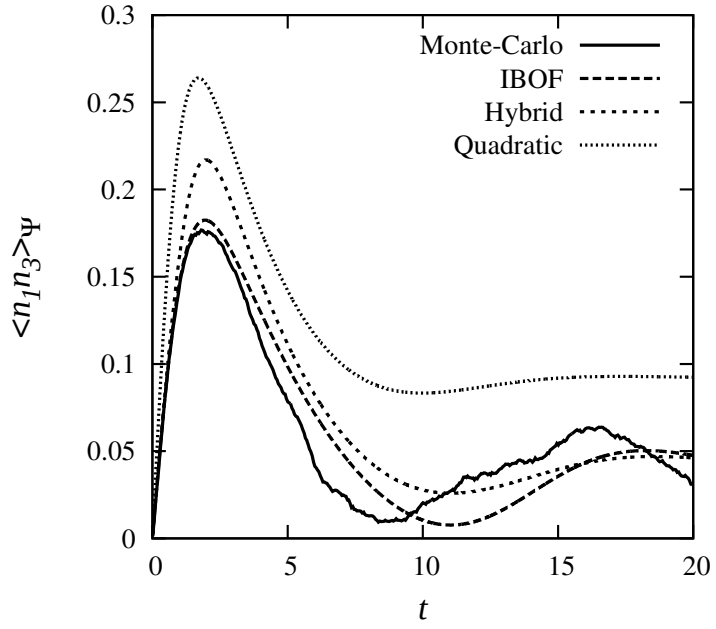

Figure 4.17: $\langle n_1 n_3 \rangle_\Psi$ component of the second moment for non-Brownian fibers with $r = 5$ in a Jeffery half period.

4.4.3. Validation of the Two-Way Coupled Solver

It has been shown in subsection 3.6.1 that the fiber suspension behaves similar to a Newtonian fluid with a higher viscosity at the limit of $\mathrm{Pe}_r \to 0$. The increase in viscosity is given by equation (3.62). The fiber aspect ratio and volume fraction can be chosen such that the increased viscosity in the limit of $\mathrm{Pe}_r \to 0$ results in a laminar flow. The analytical solution of the Navier-Stokes equations for laminar channel flow reads

$$\langle U \rangle (z) = -\frac{1}{\mu_{\mathrm{eff}}} \frac{\mathrm{d} \langle p \rangle}{\mathrm{d}x} hz \left(1 - \frac{z}{2h}\right). \tag{4.51}$$

Equation (4.51) shows that a negative pressure gradient $\mathrm{d} \langle p \rangle / \mathrm{d}x$ results in a positive velocity $\langle U \rangle$ in the streamwise direction x.

This provides a benchmark with an analytical solution that can be used to validate our two-way coupled fiber suspension solver. To this aim, a simulation is conducted by setting $r = 150$ and $\phi = 0.01$ at the limit of $\mathrm{Pe}_r \to 0$. In the following simulation, the Brownian contribution to the stress, i.e. the term proportional to Q_4 in equation (3.62), has been switched off and thus, the relative effective viscosity reads

$$\frac{\mu_{\mathrm{eff}}}{\mu} = \left[1 + \frac{5}{2}\phi \left(2Q_0 + \frac{2}{15}Q_2 + \frac{4}{3}Q_3\right)\right]. \tag{4.52}$$

This is justified because we do not extract physical arguments on this flow here, and it is only used for the validation of the coupling algorithm and parallelization. Equation (4.52) yields a numerical value of $\mu_{\mathrm{eff}}/\mu = 4.584$ for the above-mentioned parameters.

The computed bulk velocity is $U_b = 0.835\ m/s$ which is in line with the analytical value of $U_b = 0.829\ m/s$ within 0.72% relative error. The analytical value is obtained by

$$U_b = \frac{1}{2h} \int_0^{2h} \langle U \rangle (z)\, \mathrm{d}z = -\frac{1}{3\mu_{\mathrm{eff}}} \frac{\mathrm{d} \langle p \rangle}{\mathrm{d}x} h^2. \tag{4.53}$$

The computed maximum velocity at the centerline is $U_c = 1.245\ m/s$ which is within 0.12% relative error to the analytical value $U_c = 1.2435\ m/s$. The analytical value is evaluated from the analytical solution (4.51):

$$U_c = \langle U \rangle (z = h) = -\frac{1}{2\mu_{\mathrm{eff}}} \frac{\mathrm{d} \langle p \rangle}{\mathrm{d}x} h^2. \tag{4.54}$$

The laminar parabolic velocity profile obtained from the developed DNS solver is plotted in figure 4.18, and compared with the analytical solution (4.51). A very good agreement is observed.

In addition to the velocity profile, one can inspect the shear stress profiles across the

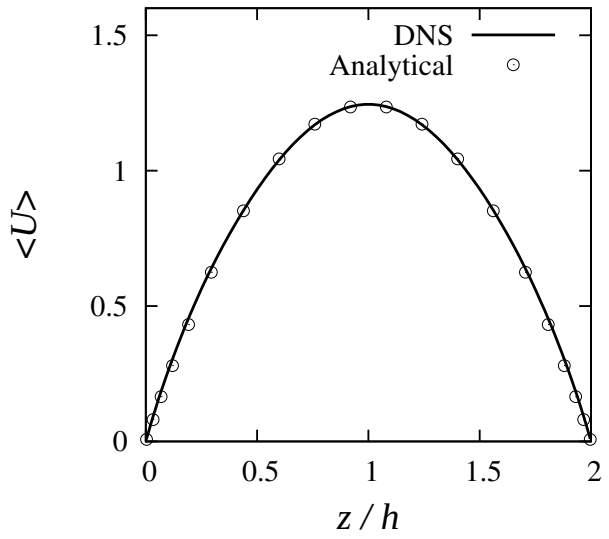

Figure 4.18: Velocity profile of fiber suspension in channel flow with volume fraction $\phi = 0.01$ and fiber aspect ratio $r = 150$ at $\mathrm{Pe}_r \to 0$, compared with the analytical solution.

channel width. The total shear stress

$$\left\langle \tau_{13}^{\text{total}} \right\rangle = \left\langle \tau_{13}^{\text{N}} \right\rangle + \left\langle \tau_{13}^{\text{NN}} \right\rangle = \mu_{\text{eff}} \frac{\mathrm{d}\langle U \rangle}{\mathrm{d}z}, \tag{4.55}$$

is composed of the Newtonian contribution

$$\left\langle \tau_{13}^{\text{N}} \right\rangle = \mu \frac{\mathrm{d}\langle U \rangle}{\mathrm{d}z}, \tag{4.56}$$

and the non-Newtonian contribution $\left\langle \tau_{13}^{\text{NN}} \right\rangle$. At the limit of $\mathrm{Pe}_r \to 0$, which is investigated here, we have

$$\left\langle \tau_{13}^{\text{NN}} \right\rangle = \mu^{\text{NN}} \frac{\mathrm{d}\langle U \rangle}{\mathrm{d}z}, \tag{4.57}$$

in which $\mu^{\text{NN}} = \mu_{\text{eff}} - \mu$. The computed shear stress profiles are shown in figure 4.19, and are compared with the corresponding analytical profiles. The shear stress balance can be used as an indicator of the statistical steady state [58]. Thus, the match between the computed and the analytical profiles also indicates that the statistical steady state has been reached in our simulation.

4.5. Summary

A numerical algorithm is presented for the simulation of dilute fiber suspensions in turbulent flows. It is based on an Eulerian DNS solver for the non-Newtonian incompressible Navier-Stokes equations and a Lagrangian particle tracking solver for the suspended fibers. Two

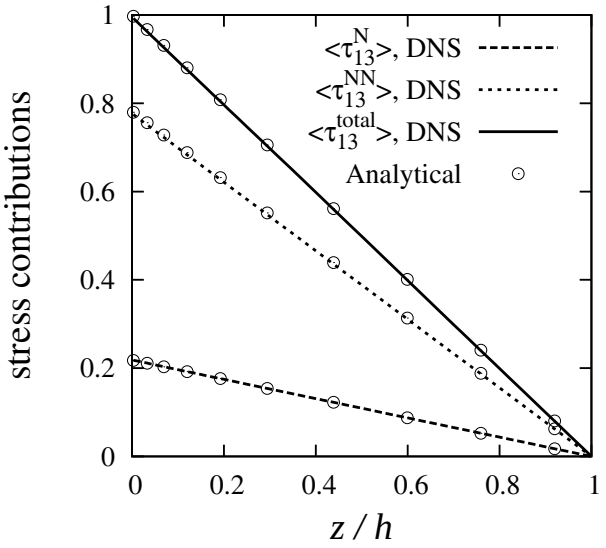

Figure 4.19: Shear stress profiles of fiber suspension in channel flow with volume fraction $\phi = 0.01$ and fiber aspect ratio $r = 150$ at $\mathrm{Pe}_r \to 0$, compared with the analytical solution.

particle solvers have been developed to compute the fiber conformation, i.e. a direct Monte-Carlo solver and a moment approximation one. The Eulerian DNS and the particle solvers are two-way coupled. The principles of the solvers and the coupling procedure are explained. Due to the tremendous amount of computational burden, the code is parallelized. The parallelization algorithm and the time profiling of the simulation are presented. Finally, the method and the code are validated. The validation is shown in three parts for the flow solver, fiber conformation solvers and the two-way coupled solver.

5. Monte-Carlo Simulation of Turbulent Drag Reduction in Channel Flow

In this chapter, we present the results of the Monte-Carlo simulation of turbulent drag reduction by rigid fibers in a channel flow at $\mathrm{Re}_\tau = 180$. The numerical algorithm has been explained in the previous chapter. For the Monte-Carlo simulation, we use the second-order version of `MGLET` with the SIP iterative solver for the Poisson equation.

This chapter is organized as follows. The simulation parameters including the fiber parameters, computational domain and grid resolution are presented in the next section. Section 5.2 contains the results of the direct Monte-Carlo simulation of turbulent drag reduction in a channel flow using rigid fibers. The results are presented in the following subsections; The mean velocity profile in subsection 5.2.1, turbulence intensities and the Reynolds shear stress in subsection 5.2.2, the total shear balance in subsection 5.2.3, the quadrant analysis in subsection 5.2.5, the probability density function of fluctuating velocities in subsection 5.2.6, the Lumley anisotropy map in subsection 5.2.7, the pressure-strain correlation in subsection 5.2.8, the analysis of the pressure-strain correlation using a Green's function solution of the Poisson equation in subsection 5.2.9, the analysis of the strain fluctuations in subsection 5.2.10, the vorticity field in subsection 5.2.11 and the near-wall partial enstrophy in subsection 5.2.12.

5.1. Simulation Parameters

This section contains detailed information on numerical and physical parameters of the presented simulation.

The reported simulation is performed on 128 processing elements of the SGI-Altix HLRB2 machine at the Leibniz Supercomputing Center (LRZ) in Munich. A fully-developed Newtonian channel flow at a nominal shear Reynolds number $\mathrm{Re}_\tau = 180$ is used as the initial condition for the fibrous flow. After the introduction of fibers, the flow has developed over a period of 30 flow-through time units $t_{\mathrm{FT}} = L_x/U_b$. Following this development time, turbulence statistics have been collected for a period of about 65 flow-through time units. The sampling is performed at every 40th time step. The non-dimensional time step size is $\Delta t \cdot U_b/h = 0.01$ that ensures CFL < 0.5 during the simulation.

5.1.1. Fiber Parameters

Geometrical and rheological properties of the suspended fibers are defined in chapter 3. In this subsection, we tabulate the numerical values of these properties for the presented simulation in table 5.1.

The chosen concentration parameter (volume fraction) does not fit into the range of dilute suspensions. However, we use the model of a dilute suspension in our simulation. Although it is not rigorously correct, it is often used by researchers in the field. For example, the concentration parameter in simulations of Paschkewitz *et al.* [104] and Gillissen *et al.* [38] was $nL^3 = 18$ and $nL^3 = 50$, respectively. But, they still used the dilute suspension model. Paschkewitz [104] also used the semi-dilute model of Shaqfeh and Fredrickson [117] for non-Brownian fibers and concluded that, for high aspect ratio fibers, the semi-dilute model qualitatively behaves similar to the dilute model.

The choice of 100 fibers per cluster is a good compromise between accuracy and numerical effort. It leads to relatively smooth solutions along a Lagrangian path [74]. With a number of 6.55×10^7 Lagrangian paths (clusters), we can estimate the density of clusters in the closest grid cells to the wall, i.e. the smallest cells. This cell has a height of $0.0075h$ and thus, on average, we have

$$\frac{6.55 \times 10^7}{128 \times 128 \times 2h/0.0075h} = 15,$$

particle clusters in each of these cells, which adds up to about 1500 fibers in a cell. This guarantees a smooth stress field. If the Lagrangian paths are initialized randomly, the average density is maintained because the flow is incompressible and the particles follow the flow instantaneously.

Table 5.1: Fiber properties of the reported simulation

Parameter	Symbol/Relation	Value
Aspect ratio	r	100
Shape factor	$\kappa = \frac{r^2-1}{r^2+1}$	0.9998
Concentration parameter	nL^3	18
Volume fraction	$\phi = \frac{4\pi nL^3}{3r^2}$	7.54×10^{-3}
Brownian diffusivity	D_r	0.001
Rotary Pećlet number	$\mathrm{Pe}_r = \frac{U_b}{hD_r}$	1000
Number of fiber clusters	N_p	6.55×10^7
Number of fibers per cluster	N_f	100
Total number of fibers	$N_t = N_f \cdot N_p$	6.55×10^9

5.1.2. Computational Domain and Grid Resolution

The computational domain is a box with dimensions given in table 4.2. This choice of domain is made based on the previous simulations in the literature. Table 5.2 shows the computational box size, grid resolution and Reynolds number of the previous simulations. The letters E and L in table 5.2 stand for Eulerian and Lagrangian simulations, respectively. Paschkewitz *et al.* [104] have used the minimal channel of Jiménez and Moin [55] for a simulation at $\mathrm{Re}_\tau = 300$. Gillissen *et al.* [38] have used a domain for Eulerian simulations which is comparable to our domain. In the same reference, they have used a smaller domain for Lagrangian one-way coupled simulations. In another reference, Gillissen *et al.* [39] had the minimal channel. However, their domain was larger than the minimal channel in spanwise direction by a factor of 1.5.

The comparison made in table 5.2 justifies our choice of domain size. Moreover, we look at the two-point velocity correlations in streamwise and spanwise directions. The two-point correlation function R_{ij} in streamwise and spanwise directions is defined as

$$R_{ij}\left(r_x^+, z^+\right) = \left\langle u_i\left(x^+ + r_x^+, y^+, z^+\right) u_j\left(x^+, y^+, z^+\right)\right\rangle, \tag{5.1}$$

$$R_{ij}\left(r_y^+, z^+\right) = \left\langle u_i\left(x^+, y^+ + r_y^+, z^+\right) u_j\left(x^+, y^+, z^+\right)\right\rangle. \tag{5.2}$$

R_{ij} is independent of x^+ and y^+ due to the statistical homogeneity of the flow in streamwise and spanwise directions. Figures 5.1a to 5.1d show the two-point velocity correlation functions in the streamwise and spanwise directions at $z^+ = 10.5$ and at the channel centerline. All the two-point correlations fall to nearly zero within the first half of the computational domain in x and y directions. This affirms the adequacy of the domain size. The two-point correlation R_{11} in the wall region shown in figure 5.1c is specifically interesting as it shows the

Table 5.2: Comparison of the computational domain size and grid resolution of the present work with previous simulations for DNS of turbulent drag-reduced channel flow.

Simulation	Coupling	Re_τ	L_x	L_y	L_z	N_x	N_y	N_z
Present work, L	2-way	180	$3\pi h$	$2\pi h$	$2h$	128	128	128
Paschkewitz *et al.* [104], E	2-way	300	πh	h	$2h$	80	80	141
Paschkewitz *et al.* [105], L	1-way	300	πh	h	$2h$	80	80	141
Gillissen *et al.* [38], E	2-way	180	$10h$	$5h$	$2h$	96	96	96
Gillissen *et al.* [38], L	1-way	180	$6h$	$3h$	$2h$	96	96	96
Gillissen *et al.* [39], E	2-way	180	$3h$	$1.5h$	$2h$	48	48	192
Gillissen *et al.* [39], L	1-way	180	$3h$	$1.5h$	$2h$	48	48	192

mean streak spacing. The first negative minimum of R_{11} for Newtonian flow occurs at $r_y^+ \approx 52$ which is consistent with the findings of Kim *et al.* [58]. This corresponds to a mean streak spacing of 104 in wall units. The first negative minimum of R_{11} for the drag-reduced flow takes place at $r_y^+ \approx 76$ which implies a mean streak spacing of 152 in wall units. This means that the streaks are coarsened by a factor of nearly 1.5 in the drag-reduced flow as compared to the Newtonian flow. This is in line with the findings of Paschkewitz *et al.* [102, 104]. Figure 5.2 shows the mean streak spacing in the spanwise direction as a function of the wall distance z^+ for Newtonian and fibrous flows. The DNS data of MKM 1999 are also plotted for comparison. Our results for Newtonian flow matches well with the reference DNS data. The

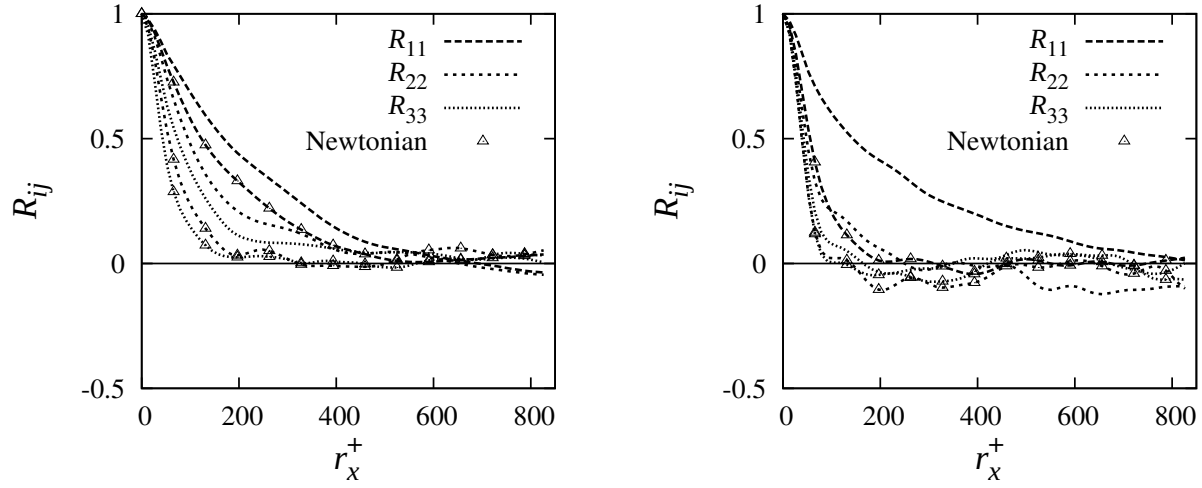

(a) Streamwise at $z^+ = 10.5$

(b) Streamwise at channel centerline

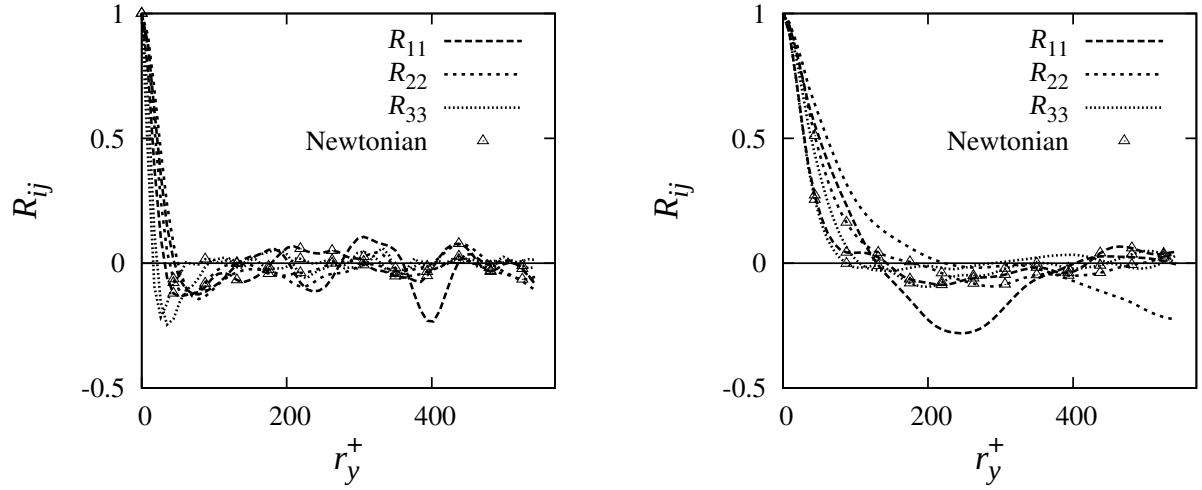

(c) Spanwise at $z^+ = 10.5$

(d) Spanwise at channel centerline

Figure 5.1: Two-point velocity correlations in streamwise and spanwise directions at $z^+ = 10.5$ and at channel centerline for the Newtonian and fibrous flows.

coarsening of the streaks is obvious from figure 5.2.

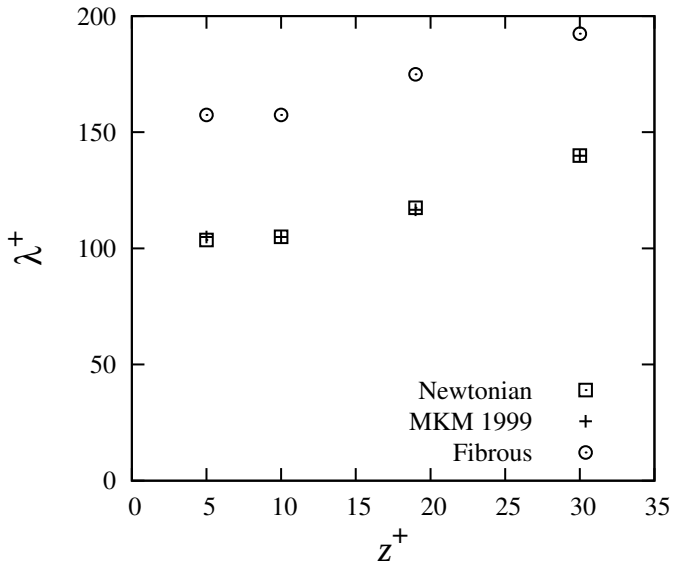

Figure 5.2: Variation of mean spanwise streak spacing in wall units estimated from the two-point correlation $R_{uu}(y)$.

The increase in streak spacing is a well-known feature of polymeric drag-reduced flows that is shown in figures 5.3a and 5.3b for Newtonian and drag-reduced flows, respectively. The black rectangles plotted in figure 5.3b show the domain size in the x-y plane of the previously published simulations of fiber suspension flows (compare with table 5.2). The minimal channel can hardly accommodate a repetitive pattern which is a representative of the near-wall streaks. Thus, one can argue that the minimal channel is not the optimal choice to study the drag reduction at this low Reynolds number, though it offers a great reduction in the computational burden. Paschkewitz *et al.* [104] have used a minimal channel for the simulation of drag reduction at $\mathrm{Re}_\tau = 300$. In that case, the extent of the domain in the spanwise direction is 300 wall units, instead of 180 wall units at $\mathrm{Re}_\tau = 180$. It means that their domain extent is nearly twice the mean streak spacing.

The one-dimensional power spectra E_{uu}, E_{vv}, E_{ww}, $E_{\tau_{11}^{\mathrm{NN}}}$, $E_{\tau_{13}^{\mathrm{NN}}}$ and $E_{\tau_{33}^{\mathrm{NN}}}$ are plotted in figures 5.4a to 5.4l. The spectra in streamwise direction are averaged in the spanwise direction and vice versa. The power spectra of E_{uu} in the streamwise direction, especially in the channel centerline, decay faster and have a slope greater than -8. This is a result of the second-order spatial discretization scheme which is used in our finite volume DNS solver. The power spectrum of the wall-normal velocity E_{ww} in the spanwise direction in the near-wall region shows about one decade of decay. Also in the reference DNS of Kim *et al.* , this spectrum has the least decay. Generally, the velocity spectra of the fibrous flow decay faster than those of the Newtonian flow. This indicates that we are on the safe side regarding the grid resolution for velocities. The velocity power spectra tend to become horizontal at their very end. Also, the velocity power spectra of the drag-reduced flow have a steeper slope than $-5/3$ in the

inertial subrange. These two effects are observed in the experimental findings of McComb and Chan [78] using an aqueous asbestos fiber suspension in a pipe flow at $\mathrm{Re} = 1.4 \times 10^4$.

The power spectra of $E_{\tau_{13}^{\mathrm{NN}}}$ decay by about two decades, similar to the observations of Paschkewitz [102]. The exception is again the spectrum in spanwise direction in the wall region $z^+ = 10.5$ which only shows about one decade of decay. This is comparable with the spectrum obtained by Paschkewitz *et al.* [104] using the local artificial dissipation (LAD) scheme. The power spectra of other components of the non-Newtonian stress tensor are also presented for the sake of completeness. Generally, the decay of the stress power spectra is not as good as those of velocities. The reason, as pointed out by Paschkewitz *et al.* [104], is that the fiber conformation is governed by a pure convective equation without any diffusion. As a consequence, the non-Newtonian stress field develops scales smaller than the Kolmogorov's scale. This situation is similar to the transport of passive scalars at high Schmidt numbers (the Batchelor's microscale).

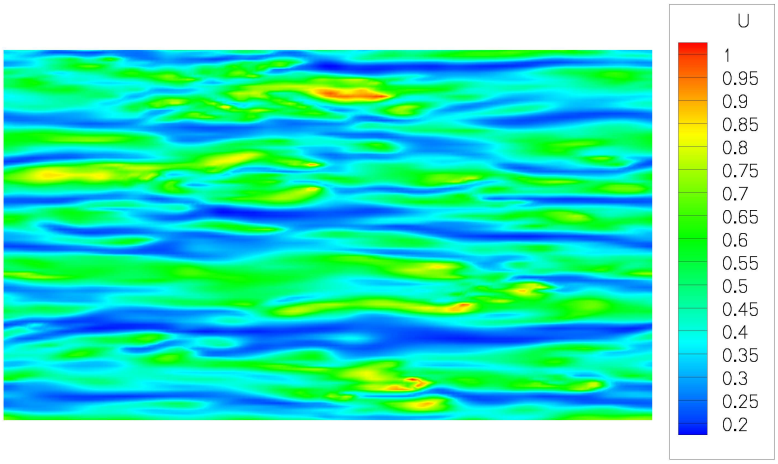

(a) Newtonian flow

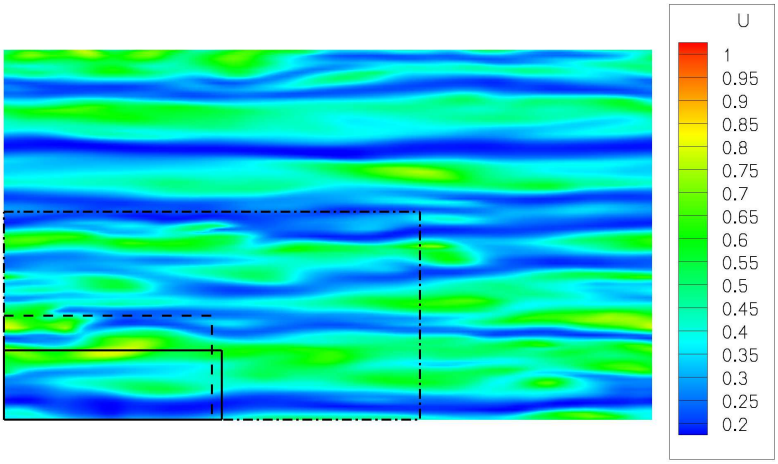

(b) Drag-reduced flow

Figure 5.3: Streak patterns in x-y plane at $z^+ = 10.5$ for (a) Newtonian and (b) drag-reduced flows. Rectangles show the domain size of previous simulations: —, minimal channel $(\pi h, h, 2h)$; – – –, $(3h, 1.5h, 2h)$; –·–, $(6h, 3h, 2h)$.

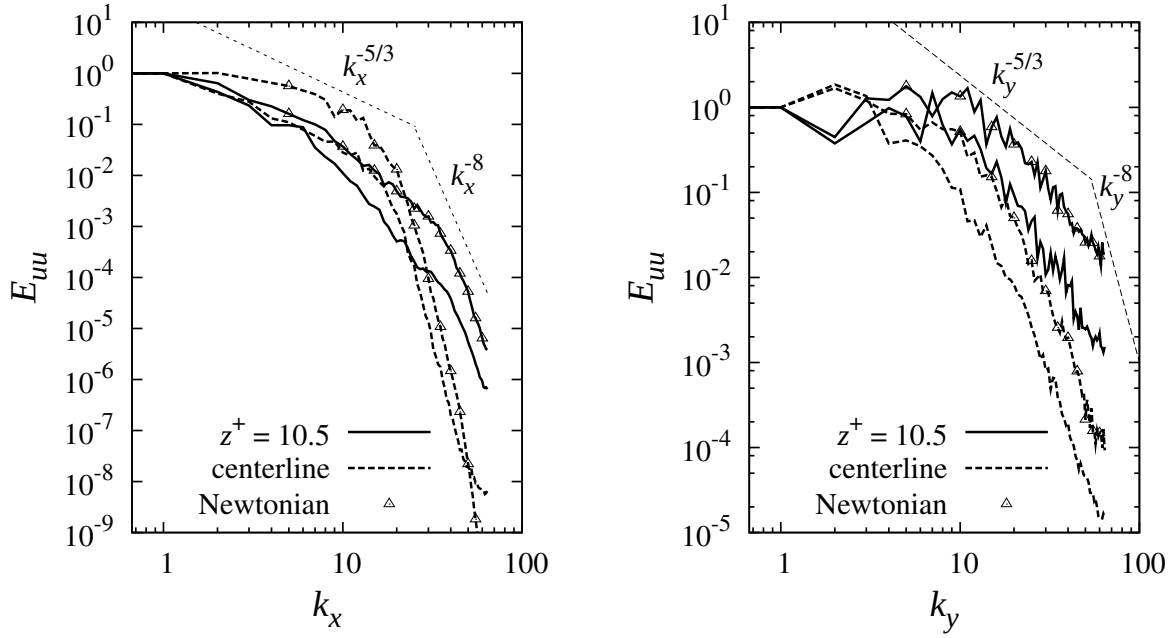

(a) E_{uu} in streamwise direction

(b) E_{uu} in spanwise direction

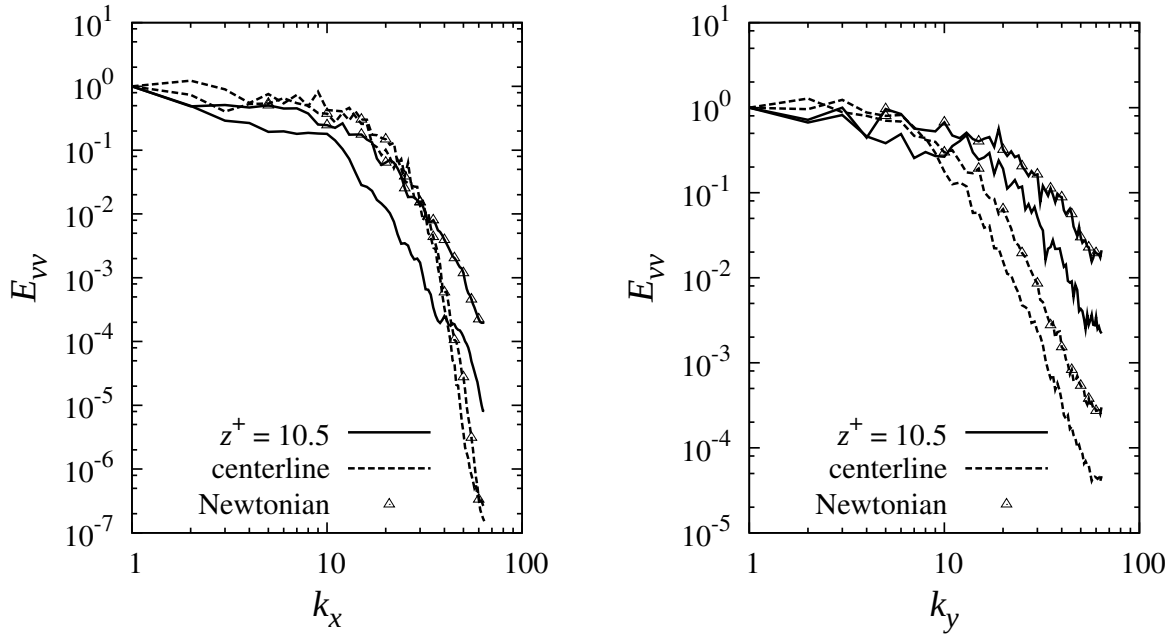

(c) E_{vv} in streamwise direction

(d) E_{vv} in spanwise direction

Figure 5.4: Power spectra of velocity components and non-Newtonian stress. The spectra are normalized by the energy of the first mode.

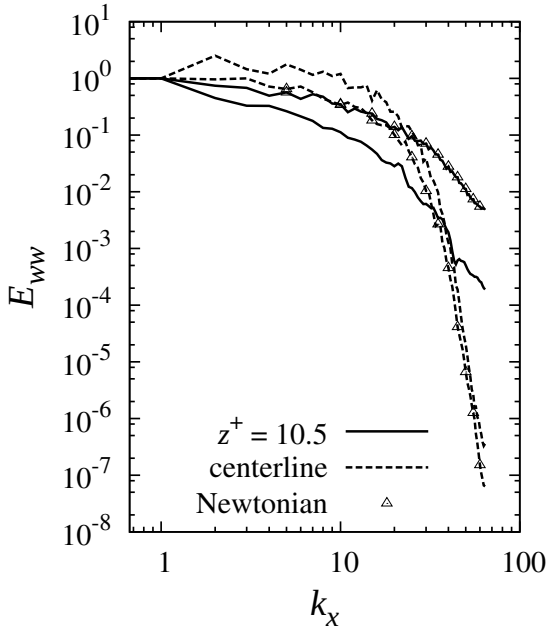

(e) E_{ww} in streamwise direction

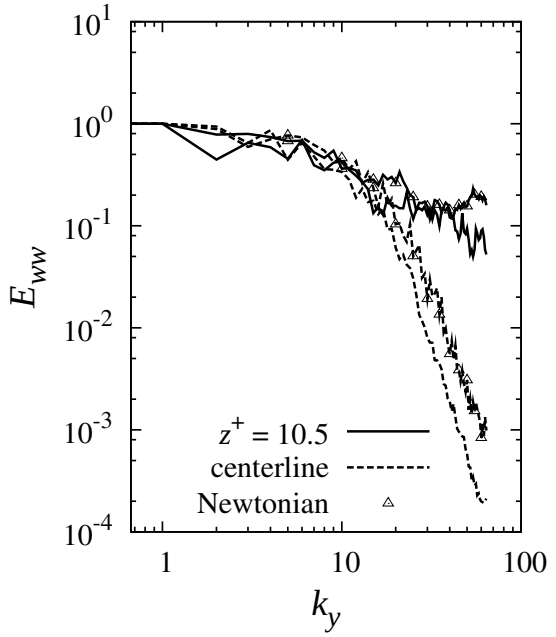

(f) E_{ww} in spanwise direction

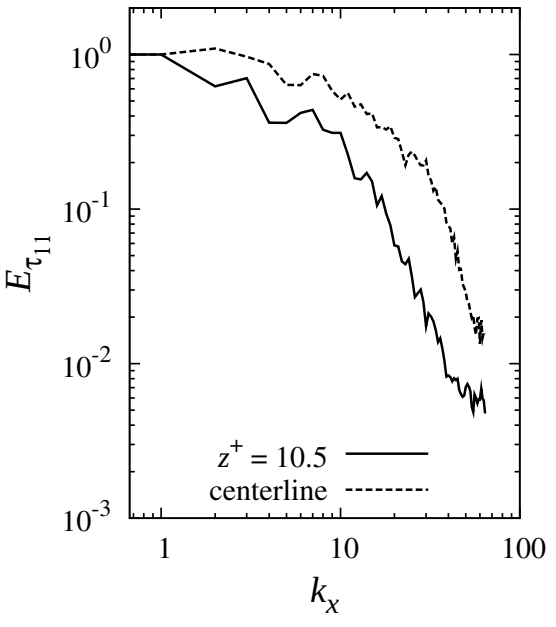

(g) $E_{\tau_{11}^{NN}}$ in streamwise direction

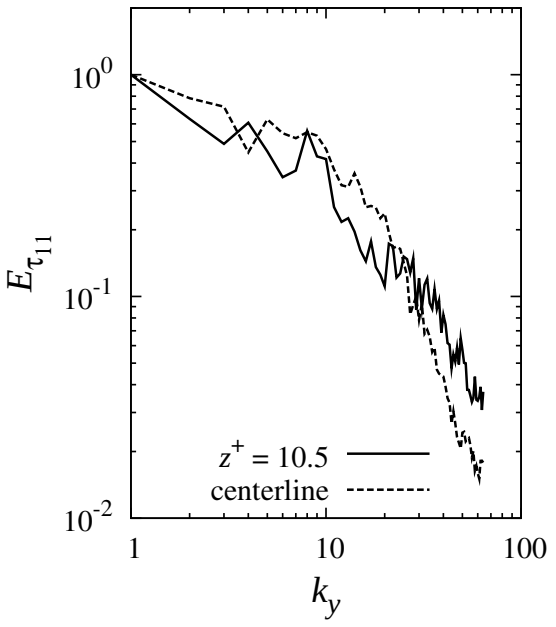

(h) $E_{\tau_{11}^{NN}}$ in spanwise direction

Figure 5.4: Power spectra of velocity components and non-Newtonian stress. The spectra are normalized by the energy of the first mode (continued).

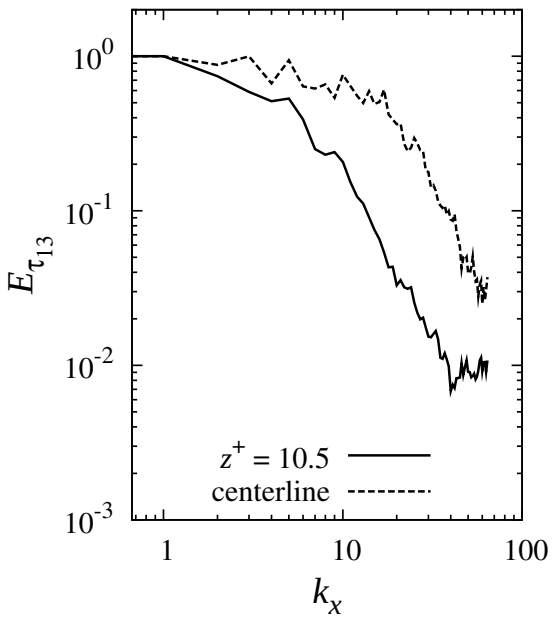

(i) $E_{\tau_{13}^{NN}}$ in streamwise direction

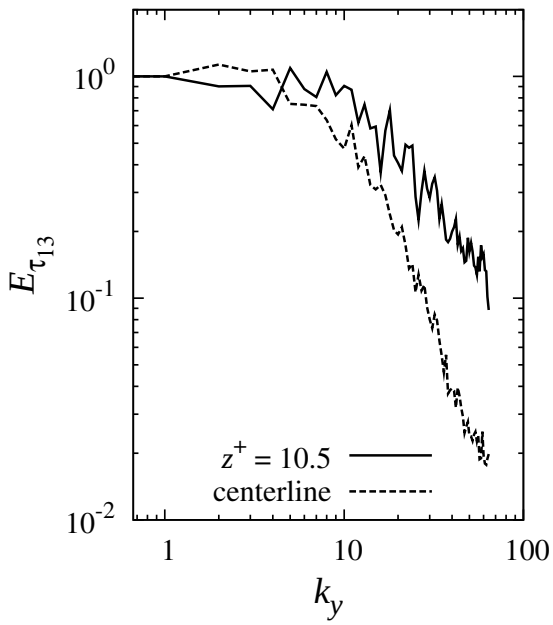

(j) $E_{\tau_{13}^{NN}}$ in spanwise direction

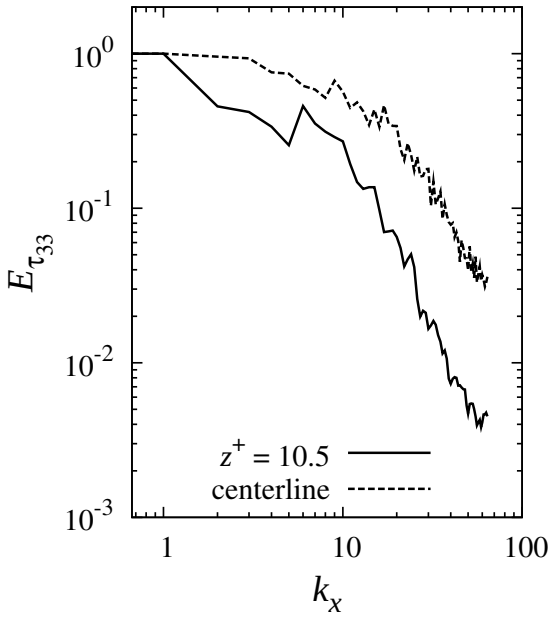

(k) $E_{\tau_{33}^{NN}}$ in streamwise direction

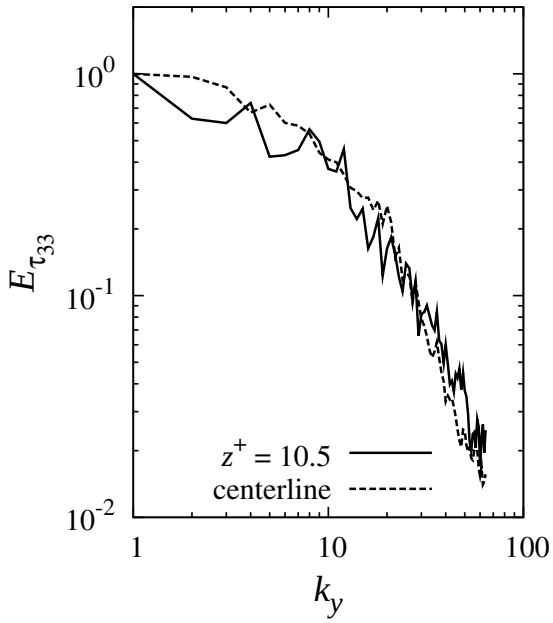

(l) $E_{\tau_{33}^{NN}}$ in spanwise direction

Figure 5.4: Power spectra of velocity components and non-Newtonian stress. The spectra are normalized by the energy of the first mode (continued).

5.2. Results

In this section, we present the results of the direct Monte-Carlo simulation of turbulent drag reduction by rigid fibers in a channel flow at a nominal shear Reynolds number $\mathrm{Re}_\tau = 180$. The known features of the polymeric drag-reduced turbulent channel flow can be summarized as:

1. Increased spacing and coarsening of streamwise streaks
2. Enhanced streamwise turbulence intensity
3. Reduced spanwise and wall-normal turbulence intensities
4. Reduced Reynolds shear stress
5. Parallel shift of the logarithmic law in low drag reduction
6. Increase in the slope of the logarithmic law in high drag reduction
7. Damping of small spatial scales
8. Reduced streamwise vorticity fluctuations

The first item is reflected in figures 5.2, 5.3a and 5.3b. Other items are investigated in the sequel.

Our simulation tool works with a constant mean pressure gradient which acts as the driving force for the flow. A constant mean pressure gradient implies a constant total wall shear stress:

$$\tau_w = \mu \left.\frac{\mathrm{d}\langle U\rangle}{\mathrm{d}z}\right|_w + \left.\left\langle \tau_{13}^{\mathrm{NN}} \right\rangle\right|_w = -h\frac{\mathrm{d}\langle p\rangle}{\mathrm{d}x}, \tag{5.3}$$

where $\left.\left\langle \tau_{13}^{\mathrm{NN}} \right\rangle\right|_w$ is the mean non-Newtonian shear stress at the wall.

Additionally, a constant mean pressure gradient means that the drag reduction is seen as an increase in the bulk streamwise velocity. This is in contrast to the approach where the bulk streamwise velocity is set constant and the drag reduction is observed as a decrease in the required driving mean pressure gradient. The former approach has been used, for example, by den Toonder *et al.* [20] while the latter has been employed by Paschkewitz *et al.* [104]. The development of the bulk velocity U_b over the sampling time is shown in figure 5.5. It can be assumed that a statistical steady state is reached in both cases. An increase of about 9.1% in the bulk velocity is observed which is attributed to the drag-reducing effect of the suspended fibers. The percentage drag reduction ($DR\%$) is 15.99%. Paschkewitz *et al.* [104], for a channel flow at $\mathrm{Re}_\tau = 300$, have obtained percentage drag reductions of 18.5% and 13.4% using hybrid and IBOF closure models, respectively. The aspect ration and volume fraction of the fibers, and the Péclet number was similar to ours in their simulations. Our result lies in between the results of the hybrid and IBOF closures.

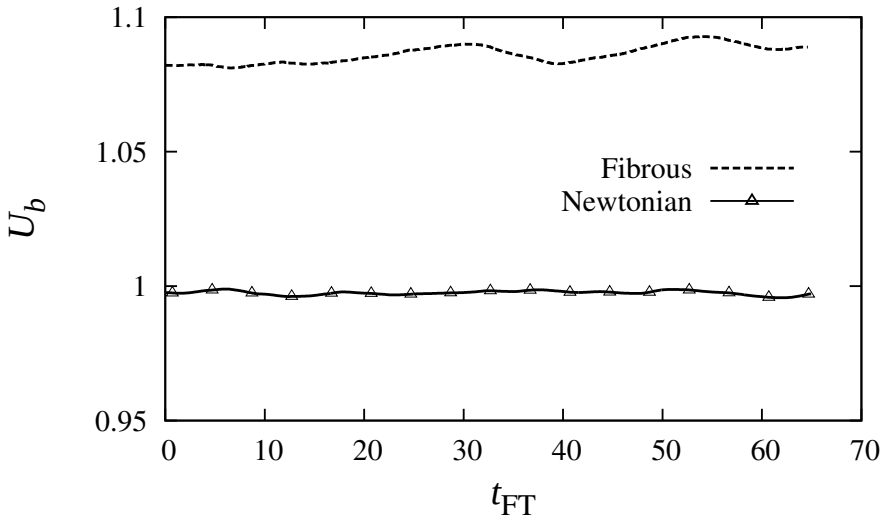

Figure 5.5: Bulk streamwise velocity of the Newtonian and fibrous flows versus the flow-through time unit t_{FT}. Shown is the time span used for turbulence statistics.

5.2.1. Mean Velocity Profile

The mean streamwise velocity profile is plotted in figure 5.6 as a function of wall distance z/h. The increase in mean velocity is indicative of drag reduction, as reflected by the bulk velocity diagram presented in figure 5.5.

More instructive than the mean velocity profile in the physical coordinates is the mean

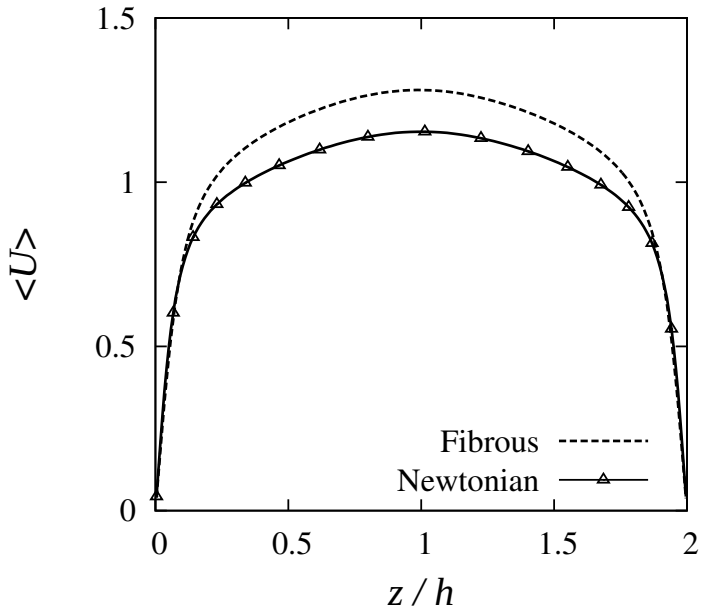

Figure 5.6: Mean streamwise velocity profile of the Newtonian and fibrous flows versus the wall distance z/h.

velocity profile in inner scaling which is plotted in figure 5.7. We observe that the velocity profile of the drag-reduced flow starts to deviate from that of the Newtonian flow in the buffer layer. The logarithmic region is shifted which is an indication of the thickened viscous sublayer. Furthermore, the slope of the logarithmic region changes from 2.5 to about 3.0 (see the guideline $\langle U\rangle^+ = 3.0\ln\left(z^+\right) + 6.5$ in figure 5.7).

Often in wall bounded flows, the overlap region between the inner and outer scalings is approximated by a logarithmic law due to Millikan [80]. George and Castillo [36] and Barenblatt *et al.* [6] have proposed a power law fit for the overlap region. Moser *et al.* [94] have analyzed the power law fit in DNS of turbulent channel flows at $\mathrm{Re}_\tau = 180, 395$ and 590, by looking at the diagnostic quantities γ and β defined via

$$\gamma = z^+ \frac{\mathrm{d}\langle U\rangle^+}{\mathrm{d}z^+}, \tag{5.4}$$

$$\beta = \frac{z^+}{\langle U\rangle^+} \frac{\mathrm{d}\langle U\rangle^+}{\mathrm{d}z^+}. \tag{5.5}$$

If γ equals a constant $\bar{\gamma}$ in a region, then a logarithmic profile with the von Kármán constant $\kappa = 1/\bar{\gamma}$ can be fitted. If β is constant ($= \bar{\beta}$) in a region, then a power law profile $\langle U\rangle^+ = A\left(z^+\right)^n$ with $n = \bar{\beta}$ can be fitted.

At the low Reynolds number we are considering, the logarithmic law region hardly exists [94]. For the Newtonian flow, figure 5.8 shows that the region with modest variation in γ grows linearly with a small positive slope. This is consistent with findings of Moser *et al.* [94]. For the drag-reduced flow, we observe two effects. First, the region with modest variation in

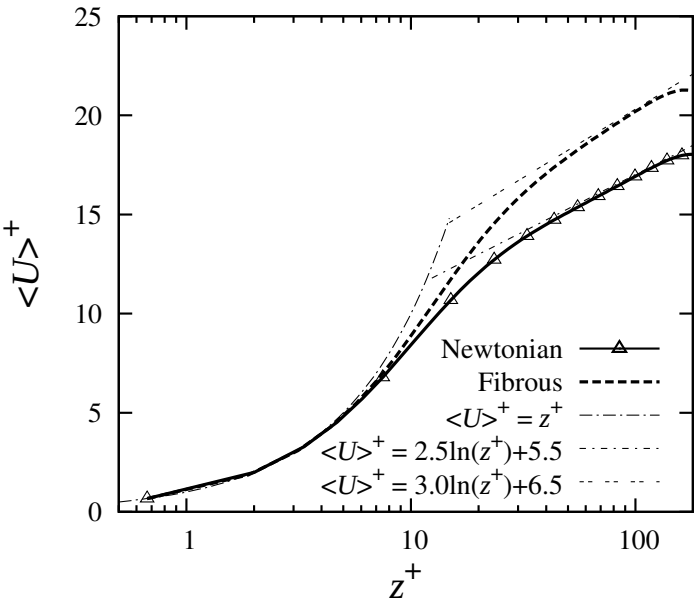

Figure 5.7: Mean streamwise velocity profile of the Newtonian and fibrous flows in inner scaling versus the wall distance z^+.

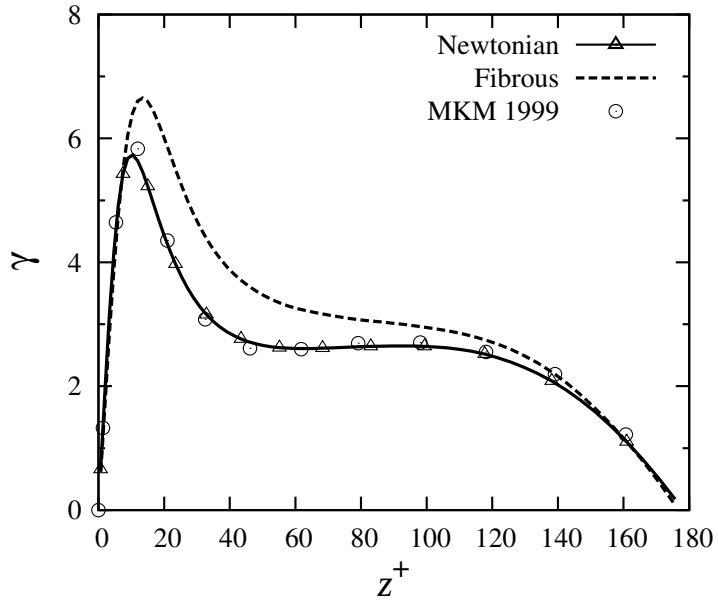

Figure 5.8: Diagnostic quantity γ versus the wall distance z^+. Region with constant γ follows a logarithmic law.

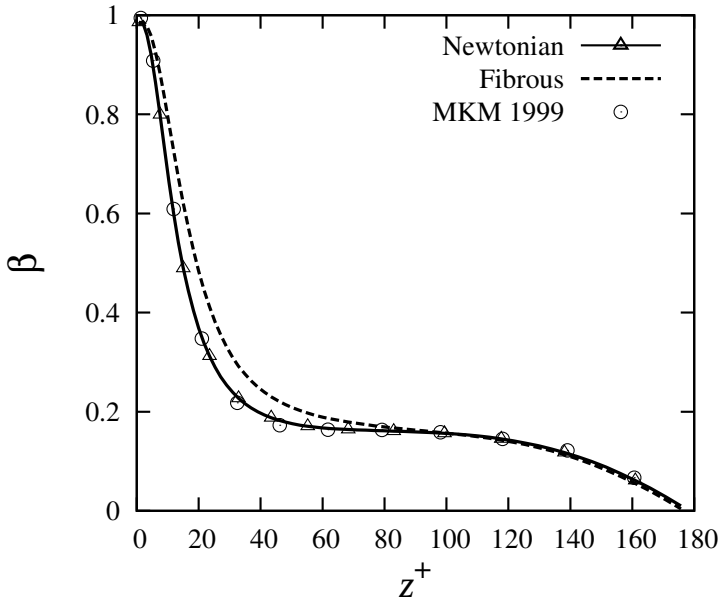

Figure 5.9: Diagnostic quantity β versus the wall distance z^+. Region with constant β follows a power law.

γ exists at a higher value of γ, approximately 3, which corresponds to a higher slope of the logarithmic profile (lower value of the von Kármán constant κ). The logarithmic profile with slope 3 is shown in figure 5.7. This means that the slope of the logarithmic region in the fibrous drag-reduced flow is slightly increased, though it is not as pronounced as that of the flexible

polymers. The second observation is that, unlike the Newtonian counterpart, γ has a small negative slope in the nominally constant region. The negative slope implies that if we assume various logarithmic profiles tangent to the velocity profile at each z^+, their slope decreases with increasing z^+. This fact can be seen in figure 5.7.

The diagnostic parameter β is plotted in figure 5.9 for the Newtonian and fibrous flows. Similar to the γ curve, β shows a negative slope in the region with modest variation. From the behavior of both γ and β one can conclude that the fit to both logarithmic and power law profiles is deteriorated in the drag-reduced flow. This is not surprising as the number of scales is reduced.

5.2.2. Turbulence Intensities and Reynolds Shear Stress

From experimental and numerical data compiled on polymer-induced turbulent drag reduction, it is well known that the turbulence intensities (root-mean-square of velocity fluctuations) and the Reynolds shear stress $\langle uw \rangle$ are modified in the following manner. The streamwise turbulence intensity increases while the spanwise and wall-normal intensities decrease. The Reynolds shear stress $\langle uw \rangle$ decreases as well. Figure 5.10 shows the turbulence intensities normalized by the shear velocity u_τ, and denoted by u^+_{rms}, v^+_{rms} and w^+_{rms} in streamwise, spanwise and wall-normal directions, respectively. The behavior explained above is observed. Also, an outward shift in the peak of u^+_{rms} is seen which is indicative of the viscous sublayer thickening. This shift has been observed in the previous polymer-induced drag reduction simulations.

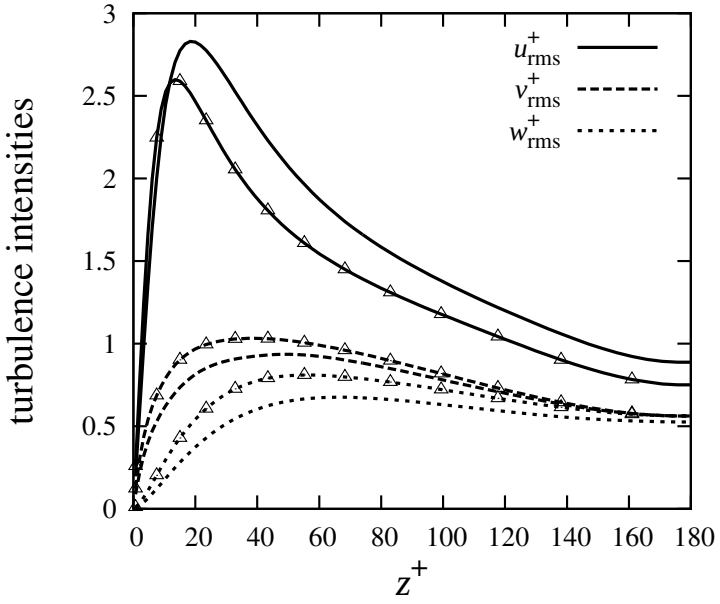

Figure 5.10: Turbulence intensity profiles of the Newtonian and fibrous flows in inner scaling versus the wall distance z^+, Newtonian with $\triangle$ and fibrous without symbol.

The Reynolds shear stress $\langle uw \rangle$ profiles of the Newtonian and the drag-reduced flows are plotted in figure 5.11 in inner scaling. The shear stress level of the drag-reduced flow is decreased compared to that of the Newtonian flow. This trend is in agreement with previous findings on polymer-induced turbulent drag reduction. The Reynolds shear stress $\langle uw \rangle$ is responsible for the production of the turbulent kinetic energy in the wall region of the turbulent channel flow. The reduction in the level of $\langle uw \rangle$ in fibrous flow indicates a weakening of the turbulence production mechanism. This is also in agreement with the previous findings. The flow relaminarization in the near-wall region resulting in the thickening of the viscous sublayer can be attributed to the reduction in the level of $\langle uw \rangle$. We shall revisit the $\langle uw \rangle$ profile in subsection 5.2.3 when considering the total shear stress balance across the channel width.

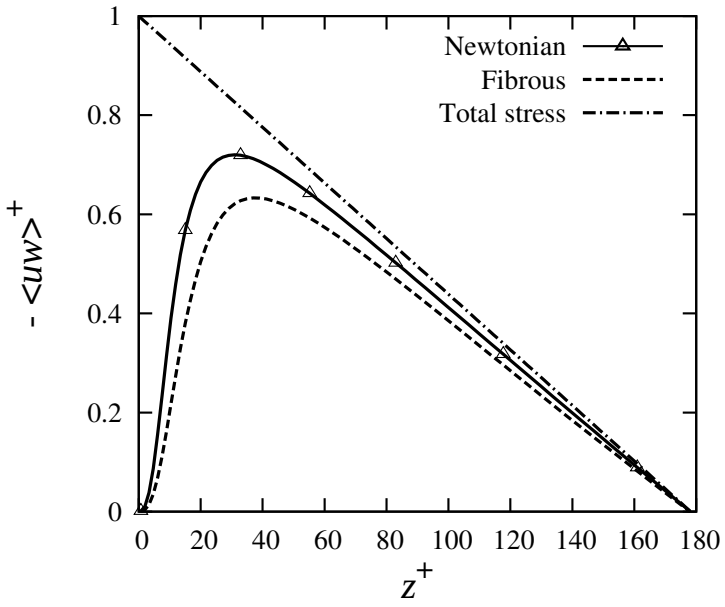

Figure 5.11: Reynolds shear stress profile of the Newtonian and fibrous flows in inner scaling versus the wall distance z^+.

Now, we turn to the reduction in the peak of $\langle uw \rangle$. Such a reduction can be a result of one or a combination of the following reasons:

1. Reduction in u_{rms}.
2. Reduction in w_{rms}.
3. Reduction in the correlation coefficient between u' and w', defined as

$$R\{u', w'\} = \frac{-\langle uw \rangle}{u_{\text{rms}} w_{\text{rms}}}. \tag{5.6}$$

We study these three possibilities to find out which one(s) is (are) responsible for the change in the Reynolds shear stress $\langle uw \rangle$. Profiles of u_{rms} and w_{rms} are plotted in figure 5.10. One

observes that u_{rms} is increased while w_{rms} is decreased. The correlation coefficient is shown in figure 5.12 for the Newtonian and drag-reduced flows. The reference DNS data of MKM 1999 are also plotted for comparison. Kim *et al.* [58] have discussed that the correlation coefficient is relatively insensitive to the Reynolds number. Here, we observe that the correlation coefficient is relatively insensitive to drag reduction. Thus, one can argue that the effect of the correlation coefficient on the reduction in Reynolds shear stress is modest. The effect of the increase in u_{rms} is overwhelmed by the influence from the reduction in w_{rms}. To verify this argument, we rearrange equation (5.6) in the following form:

$$|\langle uw\rangle| = u_{\text{rms}} w_{\text{rms}} \left| R\left\{u', w'\right\}\right|, \tag{5.7}$$

and hence

$$\left|\frac{\langle uw\rangle^{\text{NN}}}{\langle uw\rangle^{\text{N}}}\right| = \frac{u_{\text{rms}}^{\text{NN}} w_{\text{rms}}^{\text{NN}}}{u_{\text{rms}}^{\text{N}} w_{\text{rms}}^{\text{N}}} \left|\frac{R^{\text{NN}}\left\{u', w'\right\}}{R^{\text{N}}\ \left\{u', w'\right\}}\right|. \tag{5.8}$$

The influence of the correlation coefficient is neglected by assuming $\left|R^{\text{NN}}/R^{\text{N}}\right| = 1$. Thus, the reduction in the peak of $\langle uw\rangle$ at $z^+ = 30$ is predicted by formula (5.8) to be $\langle uw\rangle^{\text{NN}} / \langle uw\rangle^{\text{N}} = 0.90$ which is within 4.4% of the actual value 0.862 (see figure 5.11). w_{rms} is relatively stronger reduced than u_{rms} increased.

5.2.3. Total Shear Stress Balance

The balance of the total shear stress across the channel width is a good indication of the accuracy of the simulation and the quality of the turbulence statistics. It also affirms that the

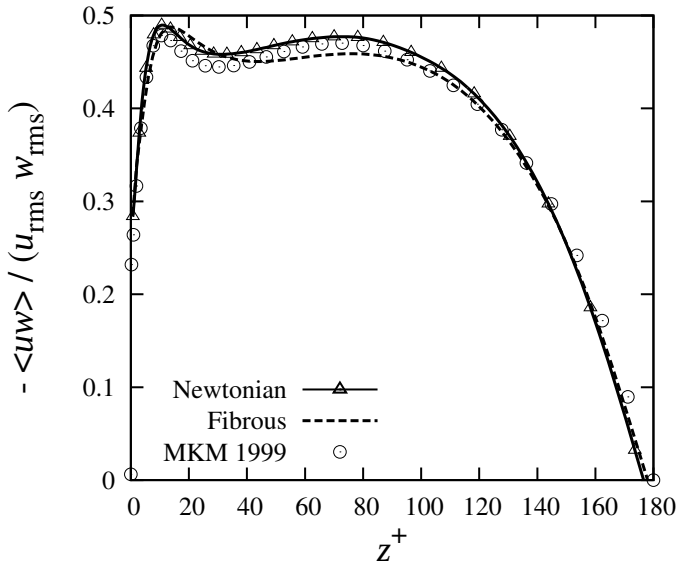

Figure 5.12: Correlation coefficient between u' and w' of the Newtonian and fibrous flows versus the wall distance z^+.

statistical steady state is achieved [58] and the mean flow field fulfills the integral momentum balance. Integration of the mean momentum (Reynolds) equation in wall-normal direction yields

$$\tau_{13}^{\text{total}} = \mu \frac{\mathrm{d}\langle U\rangle}{\mathrm{d}z} - \rho\langle uw\rangle + \left\langle \tau_{13}^{\text{NN}} \right\rangle = \tau_w + \frac{\mathrm{d}\langle p\rangle}{\mathrm{d}x} z = -h \frac{\mathrm{d}\langle p\rangle}{\mathrm{d}x}\left(1 - \frac{z}{h}\right). \tag{5.9}$$

Thus, the total shear stress τ_{13}^{total} is composed of the following contributions: the viscous shear stress $\mu\,\mathrm{d}\langle U\rangle/\mathrm{d}z$, the Reynolds (turbulent) shear stress $-\rho\langle uw\rangle$ and the non-Newtonian stress $\left\langle \tau_{13}^{\text{NN}} \right\rangle$. We observe in figure 5.13 that the sum of these three nonlinear contributions balances on the theoretical straight line. This confirms that the flow is statistically in equilibrium.

Using the shear stress balance (5.9), we can construct a simple model to investigate the effect of the non-Newtonian shear stress $\left\langle \tau_{13}^{\text{NN}} \right\rangle$. Here, we study a vanishing non-Newtonian contribution, i.e. $\left\langle \tau_{13}^{\text{NN}} \right\rangle = 0$. Furthermore, we assume that the Reynolds shear stress is the same as the one of the drag-reduced flow, shown in figure 5.13. Integrating the shear stress balance equation (5.9) along the channel width yields the modified velocity profile plotted in figure 5.14. Obviously, we reach higher drag reduction by assuming $\left\langle \tau_{13}^{\text{NN}} \right\rangle = 0$. The modified velocity profile has a greater slope of the logarithmic law, 5.5 as compared to 2.5 for the Newtonian flow, and it is moved towards the Virk's maximum drag reduction profile $\langle U\rangle^+ = 11.7\ln z^+ - 17$ [130]. The change in the profile due to neglecting $\left\langle \tau_{13}^{\text{NN}} \right\rangle$ can be explained as follows. Due to the vanishing $\left\langle \tau_{13}^{\text{NN}} \right\rangle$, the velocity profile has to change in order to establish the total stress balance (5.9). Because of the reduced Reynolds shear stress, the

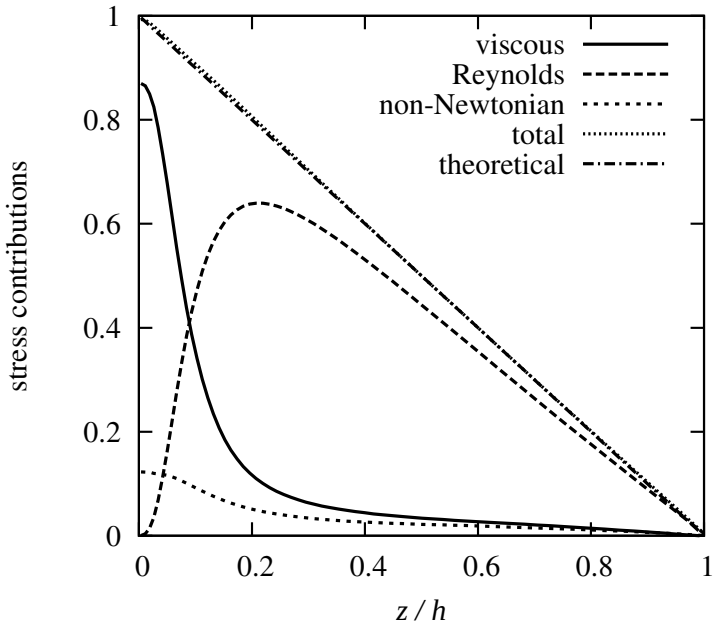

Figure 5.13: Shear stress balance of drag-reduced flow versus the global coordinate z/h. Stresses are normalized by the wall shear stress.

profile also differs from the Newtonian one. The modification in the velocity profile modifies the viscous shear stress and compensates the vanishing $\left\langle \tau_{13}^{\mathrm{NN}} \right\rangle$. The modified and unmodified viscous shear stresses are plotted in figure 5.15 along with the Reynolds shear stress and the total shear stress.

Another observation is that the mean velocity profiles of both drag-reduced flows do not lie, even partly, on the maximum drag reduction (MDR) line. This is somewhat different from the observation in the drag reduction induced by flexible polymers, where the mean velocity profile follows the MDR line up to a cross-over point which depends on the polymer concentration and the Reynolds number, and then crosses back to a Newtonian-like profile [9, 107].

This simplified model can explain the drag-reducing effectiveness of high-aspect-ratio fibers. Manhart [71] has shown, in one-way coupled simulations, that low-aspect-ratio fibers lead to high levels of $\langle \tau_{13} \rangle$, and argued that they are not suitable for drag reduction. Later, Paschkewitz *et al.* [104] have demonstrated, using two-way coupled simulations, that this argument holds, which is also in line with experimental findings of Radin *et al.* [108] who observed that particles with aspect ratios less that 25 to 35 do not lead to drag reduction.

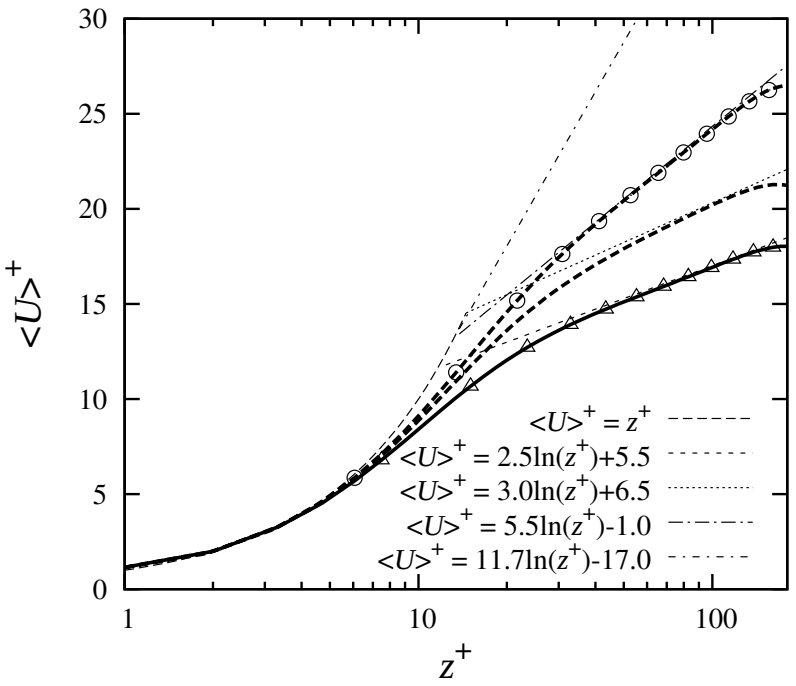

Figure 5.14: Mean streamwise velocity profile of the Newtonian and fibrous flows in inner scaling versus the wall distance z^+, Newtonian flow with $\triangle$, fibrous flow without symbol and modified fibrous flow ($\left\langle \tau_{13}^{\mathrm{NN}} \right\rangle = 0$) with $\circ$.

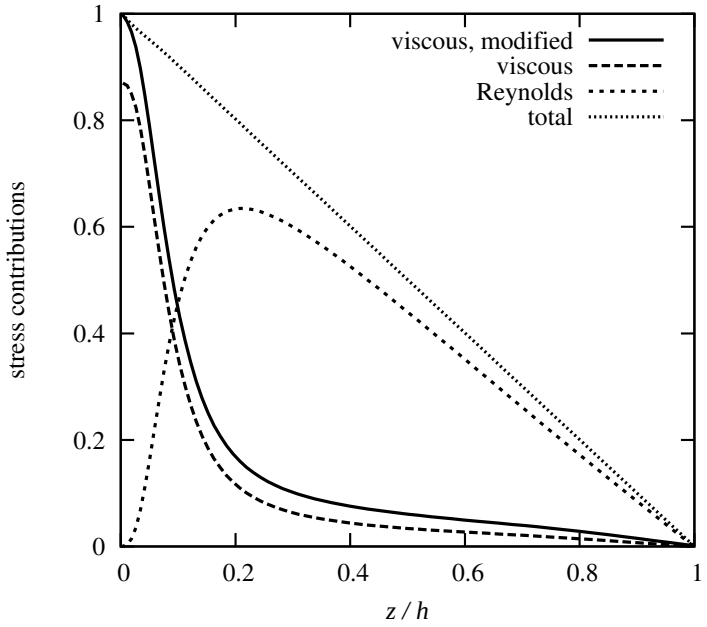

Figure 5.15: Shear stress balance of the modified drag-reduced flow versus the global coordinate z/h. The viscous shear stress of the unmodified drag-reduced flow is also plotted. Stresses are normalized by the wall shear stress.

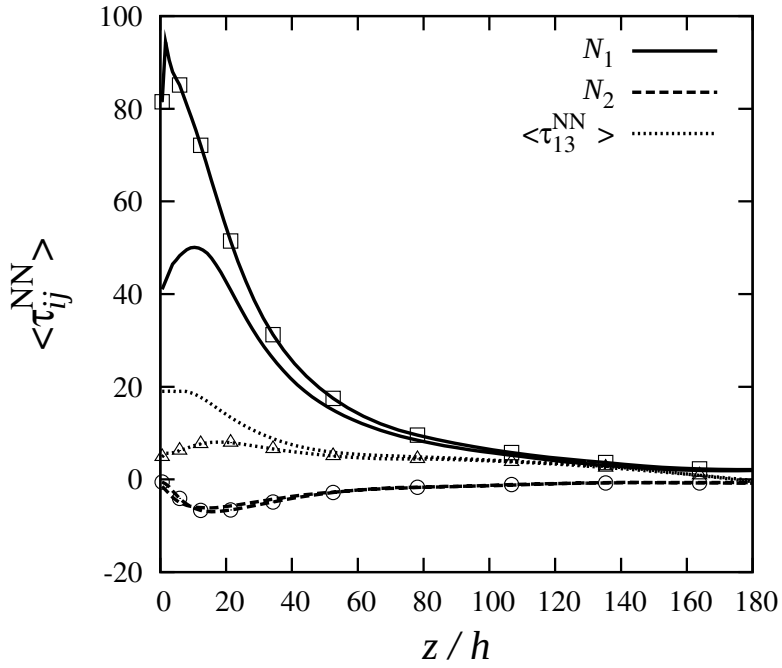

Figure 5.16: Mean non-Newtonian stresses obtained by the Monte-Carlo simulation (without symbol) and by the hybrid moment closure model (with symbols). Shown are the normal stress differences $N_1 = \left\langle \tau_{11}^{\mathrm{NN}} \right\rangle - \left\langle \tau_{33}^{\mathrm{NN}} \right\rangle$ and $N_2 = \left\langle \tau_{33}^{\mathrm{NN}} \right\rangle - \left\langle \tau_{22}^{\mathrm{NN}} \right\rangle$, and the shear stress $\left\langle \tau_{13}^{\mathrm{NN}} \right\rangle$.

5.2.4. Non-Newtonian Stresses

The mean non-Newtonian stresses are presented in figure 5.16, and are compared with the results obtained by the moment approximation approach using the hybrid closure model. The moment approximation simulation is also done by the developed code, as explained in chapter 4. The normal stress differences $N_1 = \left\langle \tau_{11}^{\mathrm{NN}} \right\rangle - \left\langle \tau_{33}^{\mathrm{NN}} \right\rangle$ and $N_2 = \left\langle \tau_{33}^{\mathrm{NN}} \right\rangle - \left\langle \tau_{22}^{\mathrm{NN}} \right\rangle$ are shown instead of the normal stresses themselves. The non-Newtonian shear stress τ_{13}^{NN} is also shown. All values are normalized by the viscosity of the carrier fluid and the volume fraction of the suspended fibers. The results of the hybrid closure differ from those of the direct simulation, quantitatively as well as qualitatively. The only exception is the second normal stress difference N_2, for which a good agreement is established. These observations are in line with the findings of Paschkewitz *et al.* [102, 105]. The direct simulation predicts a higher level of shear stress at the wall, which results in a lower amount of drag reduction, as compared to the prediction of the hybrid closure. These observations confirm the need for a direct method to simulate the drag reduction, whose results are independent of any closure model.

5.2.5. Quadrant Analysis

We have observed that the Reynolds shear stress $\langle uw \rangle$ decreases in the drag-reduced flow (see figure 5.11). This decrease modifies the total shear stress balance, as shown in subsection 5.2.3. It also reduces the turbulent kinetic energy production $-\langle uw \rangle \, \mathrm{d}\langle U \rangle / \mathrm{d}z$ [106]. We have already examined the reduction in $\langle uw \rangle$ by analyzing its correlation coefficient, see equation (5.8). In this subsection, we perform a quadrant analysis of the Reynolds shear stress. This helps us to find out how the quadrant events contribute to the reduction in $\langle uw \rangle$. The u-w plane consists of four quadrants, as shown in figure 5.17. The first ($Q1$) and third ($Q3$) quadrants contribute positively to $\langle uw \rangle$ and hence negatively to the turbulent production. Conversely, the second ($Q2$) and fourth ($Q4$) quadrants produce negative Reynolds shear stress and hence lead to positive turbulent production. A $Q1$ event ($u > 0$ and $w > 0$) corresponds to an outward motion of high-speed fluid away from the wall. An event with $u < 0$

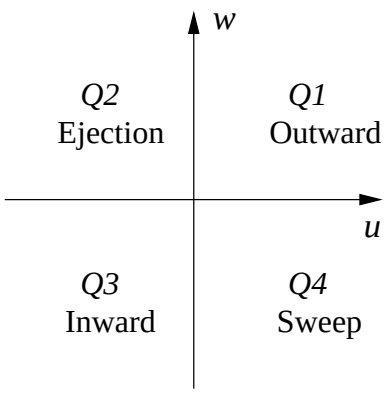

Figure 5.17: Four quadrants of the u-w plane.

and $w > 0$ ($Q2$) describes an ejection of low-speed fluid into the high-speed stream. The third quadrant $Q3$ represents events with $u < 0$ and $w < 0$, i.e. inward motion of low-speed fluid to the wall. Finally, an event with $u > 0$ and $w < 0$ falls into the fourth quadrant $Q4$ and describes the sweep of low-speed region by high-speed fluid.

For the Newtonian turbulent channel flow, it is well known that the $Q2$ and $Q4$ events are more frequent than the $Q1$ and $Q3$ events. In the near-wall region, the sweep ($Q4$) events are dominant. At a specific wall distance, both sweep and ejection events contribute equally to the Reynolds shear stress. Above this wall distance, the ejections are more frequent than the sweeps. Figure 5.18 shows the contributions from each quadrant to the Reynolds shear stress $\langle uw \rangle$. Our results generally match well with the DNS of KMM 1987, as shown in figure 5.18.

The differences between the Newtonian and drag-reduced flows are as follows. In the drag-reduced flow, both $Q1$ and $Q3$ events contribute less to the Reynolds shear stress in the near-wall region. Away from the wall their contributions become comparable to those of the Newtonian flow. Ejections ($Q2$ events) generally contribute more to the Reynolds shear stress across the channel, especially in the near-wall region. Conversely, contribution of sweeps ($Q4$ events) is less. Their contribution especially decreases near the wall. The reduction in the

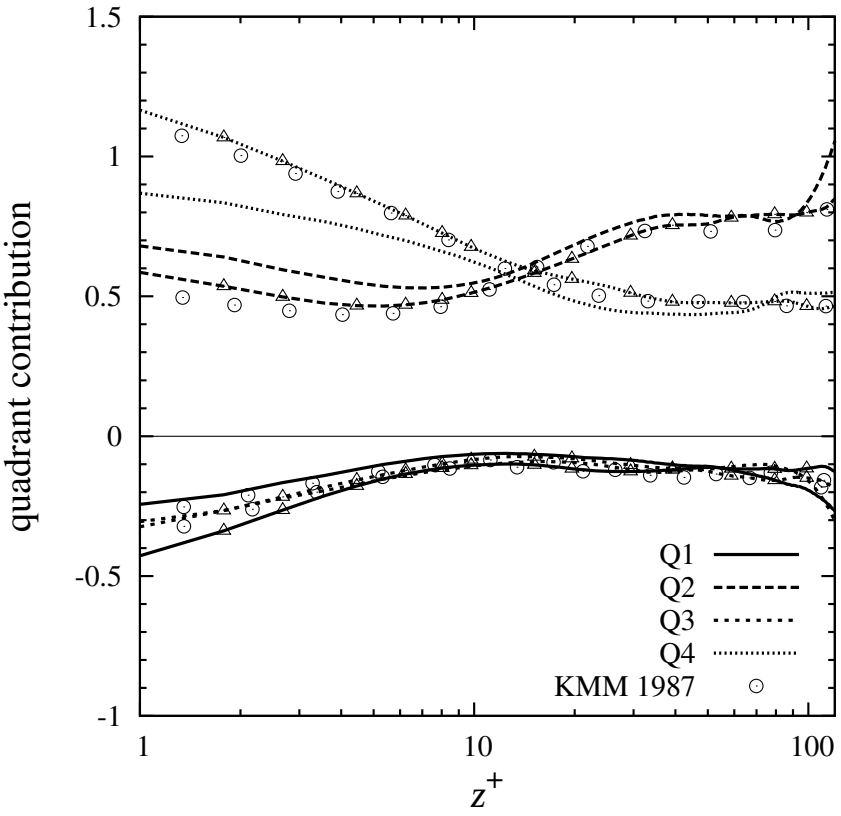

Figure 5.18: Quadrant contributions to Reynolds shear stress $\langle uw \rangle$ versus the wall distance z^+, Newtonian with $\triangle$ and fibrous without symbol.

peak of the Reynolds shear stress $\langle uw \rangle$ at $z^+ \approx 30$ (see figure 5.11) is mainly due to the reduction in the sweep events contribution. Also, the crossing point of the sweep and ejection events is moved towards the wall, which is due to the reduction in sweep and the increase in ejection contributions.

The turbulent frictional drag can be attributed to the near-wall domination of the sweep events. Because, a sweep event is an inrush of high-speed fluid towards the wall, which locally increases the wall shear rate and hence the wall shear stress. Therefore, the drag reducing effect of the suspended fibers can be related to the decrease in the near-wall sweep events. To study this conjecture in more detail, we look at the fractional contributions of the quadrants to the Reynolds shear stress at different wall distances.

Figure 5.19 shows the fractional contribution of the four quadrants to the Reynolds shear stress at $z^+ = 8$. The results of the Newtonian flow are validated by comparing to the results of KMM 1987 at $z^+ = 7.8$. The modification in the $Q1$ and $Q3$ contributions is small. The contribution of ejections ($Q2$ events) is increased. However, the contributions from intense uw events, say $-uw > 3u_{\mathrm{rms}}w_{\mathrm{rms}}$, in both Newtonian and drag-reduced flows coincide. The total contribution of the sweeps ($Q4$ events) are decreased, as already shown in figure 5.18 and discussed above. Interestingly, the contribution from intense uw events is increased, in contrast to that of the ejections.

Figure 5.20 presents the fractional contributions of the quadrants to $-\langle uw \rangle$ at a wall distance $z^+ = 12.5$. The difference between the Newtonian and fibrous flows for $Q1$ and $Q3$ events is marginal. At this wall distance, the total contributions of $Q2$ and $Q4$ events are

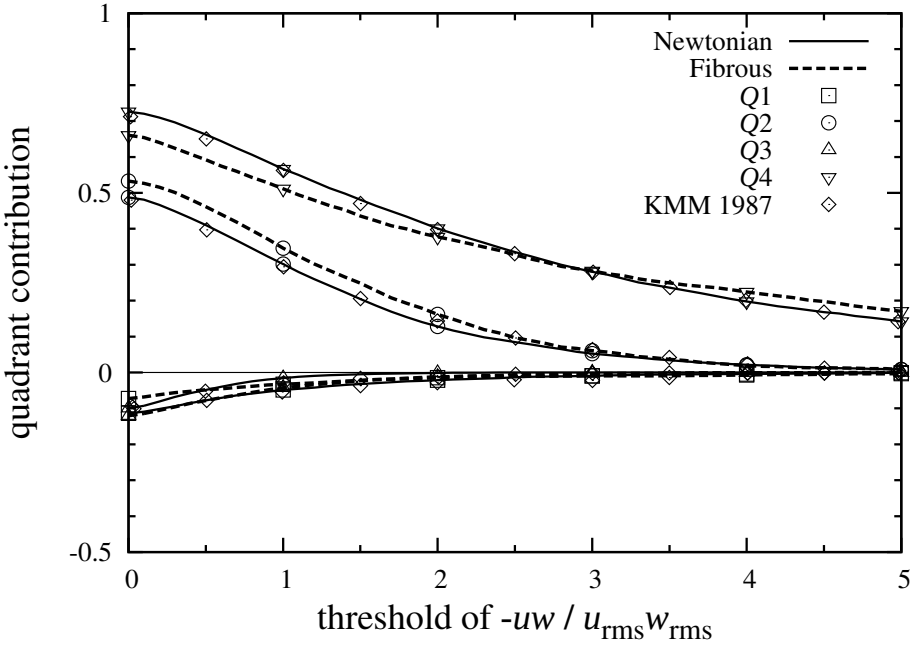

Figure 5.19: Fractional contribution to $-\langle uw \rangle$ versus the threshold of u and w fluctuations at $z^+ = 8$ for Newtonian and fibrous flows (KMM 1987 results at $z^+ = 7.8$).

almost equal. Kim *et al.* [58] have shown that for the Newtonian channel flow, when the total contributions of sweeps and ejections are equal, their fractional contributions are also the same. In contrary to the Newtonian flow, we see in figure 5.20 for the drag-reduced flow that the fractional contributions are not similar, and deviate from each other for events with $-uw > 1.5 u_{\mathrm{rms}} w_{\mathrm{rms}}$.

The quadrant fractional contributions to $-\langle uw \rangle$ at $z^+ = 50$ are shown in figure 5.21. The contributions from inward and outward interactions are similar to those of the Newtonian flow. At this wall distance, the ejections are dominant with about 80% contribution to the total Reynolds shear stress. The $Q2$ and $Q4$ contributions from intense uw events are not changed as compared to the Newtonian flow.

From figures 5.19, 5.20 and 5.21 we conclude that the suspended fibers mainly affect sweep and ejection events in the near-wall region, i.e. they increase the contribution of ejections and decrease that of sweeps.

5.2.6. Probability Density Function of the Fluctuating Velocity

We have observed that the suspended fibers decrease the contribution of sweeps and increase that of ejections by using quadrant analysis. Here, we continue the analysis by using the probability distribution function (PDF) of the fluctuating velocities. Figures 5.22, 5.23 and 5.24 show the PDF of the fluctuating streamwise, spanwise and wall-normal velocities, respectively. We observe that, for the streamwise velocity, stronger fluctuations are more probable, espe-

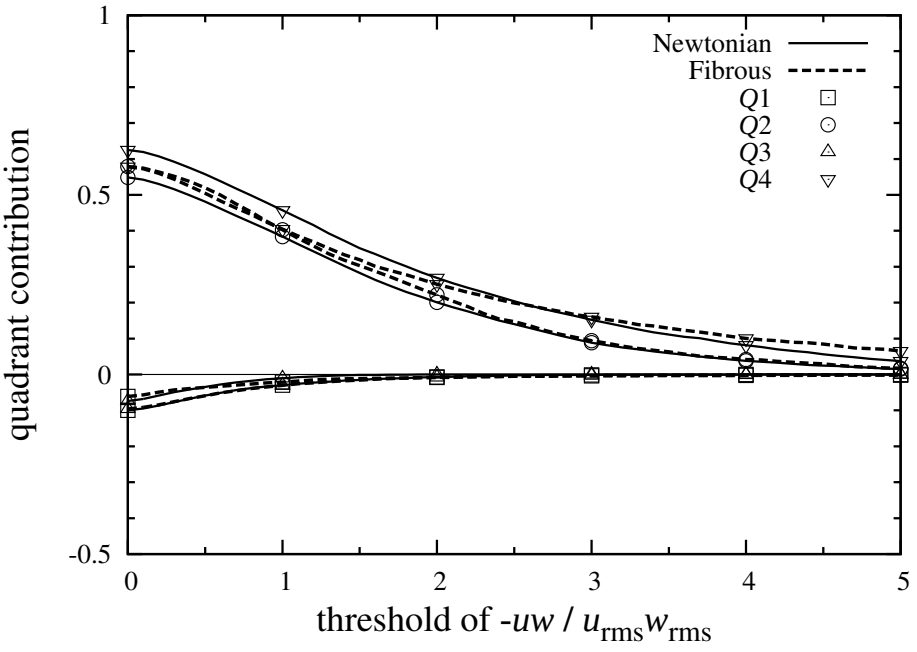

Figure 5.20: Fractional contribution to $-\langle uw \rangle$ versus the threshold of u and w fluctuations at $z^+ = 12.5$ for Newtonian and fibrous flows.

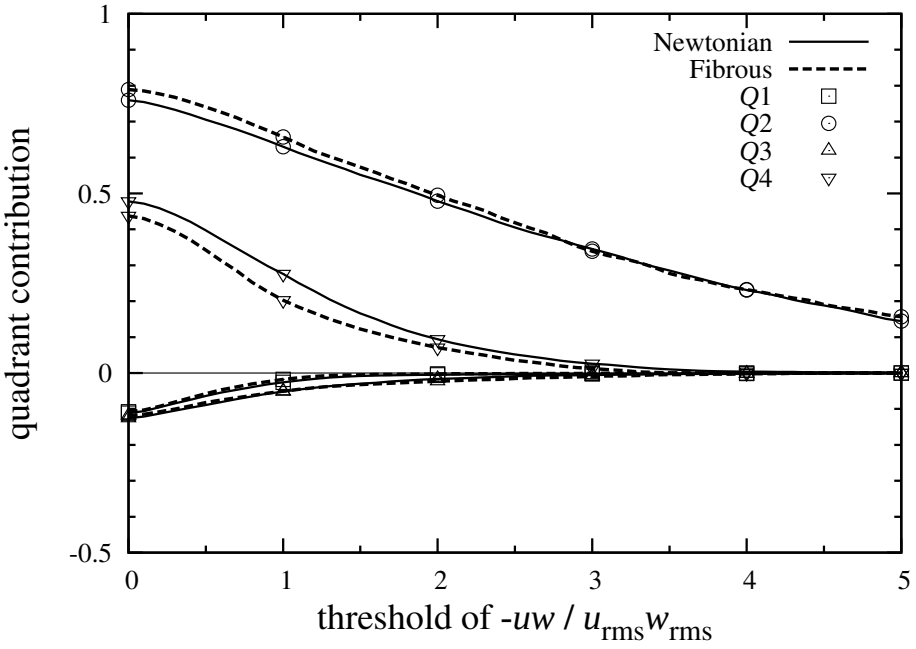

Figure 5.21: Fractional contribution to $-\langle uw \rangle$ versus the threshold of u and w fluctuations at $z^+ = 50$ for Newtonian and fibrous flows.

cially events with negative u. This is consistent with the increase in ejection contribution, as shown by the quadrant analysis in the previous subsection. It also confirms the increase in u_{rms} as the events with greater u have a larger weight. The situation is the other way around for the spanwise and wall-normal velocity fluctuations. Their PDF is narrower affirming the reduction in v_{rms} and w_{rms}. This picture is also consistent with the reduction in the Reynolds shear stress $\langle uw \rangle$. In the drag-reduced flow, we have stronger streamwise velocity fluctuations whose corresponding wall-normal velocity fluctuations are decreased, and this leads to a reduction in $\langle uw \rangle$. This is better shown in figure 5.25 which presents the distribution of u^+ and w^+ at $z^+ = 20$. We have already demonstrated that the reduction in w_{rms} is more effective than the increase in u_{rms} for decreasing $\langle uw \rangle$.

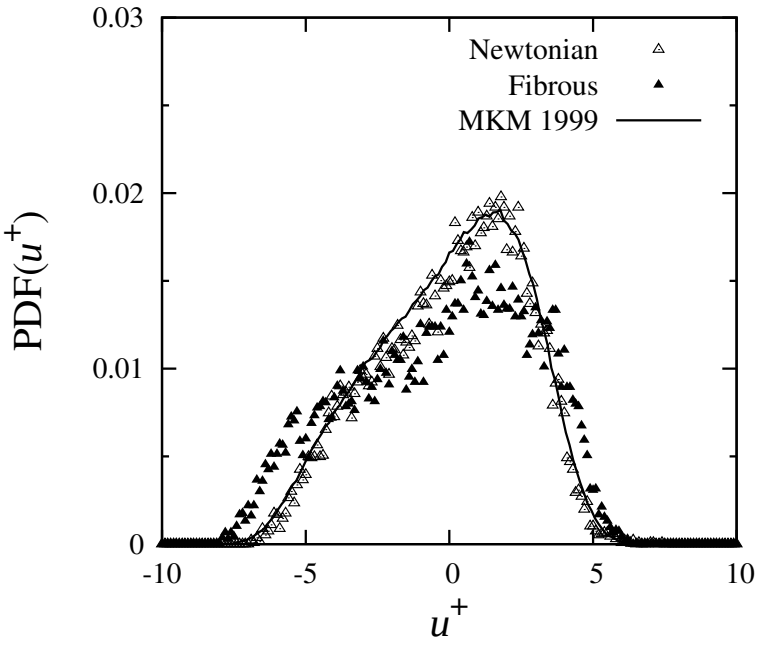

Figure 5.22: Probability distribution function (PDF) of the fluctuating streamwise velocity at $z^+ = 20$ (MKM 1999 data at $z^+ = 19$).

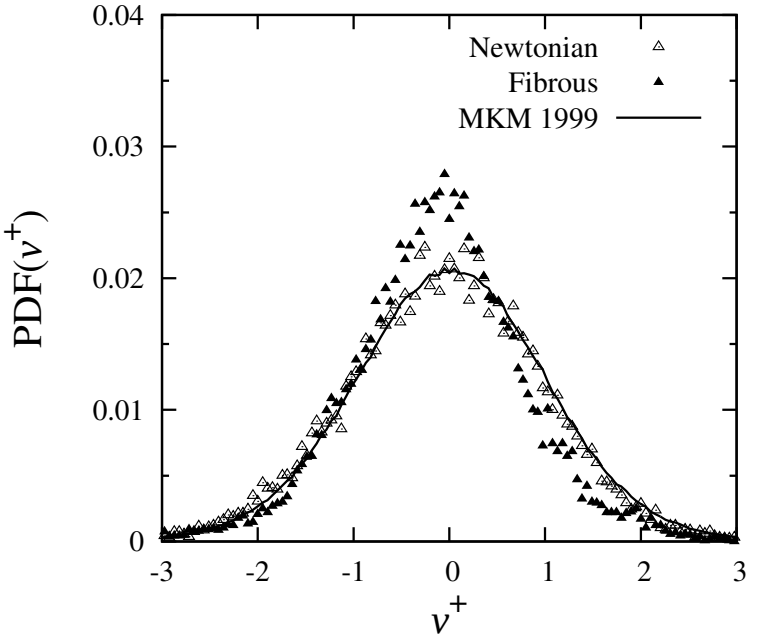

Figure 5.23: Probability distribution function (PDF) of the fluctuating spanwise velocity at $z^+ = 20$ (MKM 1999 data at $z^+ = 19$).

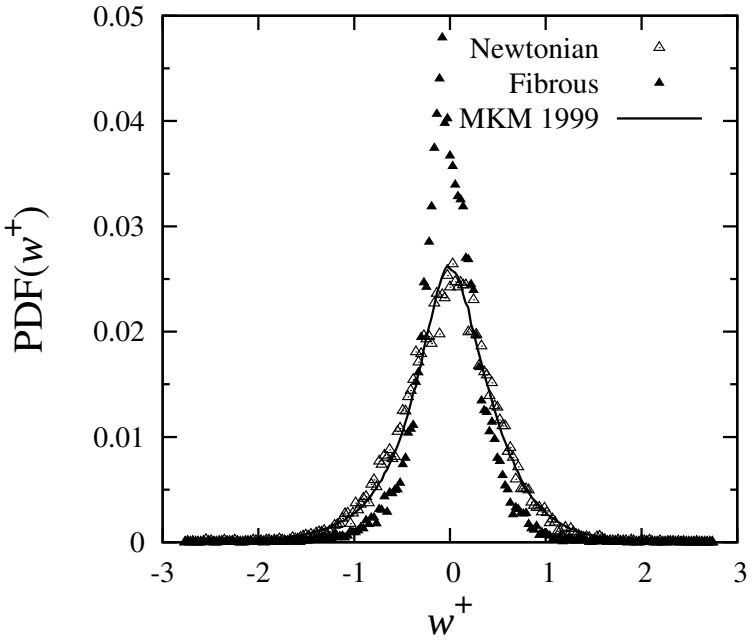

Figure 5.24: Probability distribution function (PDF) of the fluctuating wall-normal velocity at $z^+ = 20$ (MKM 1999 data at $z^+ = 19$).

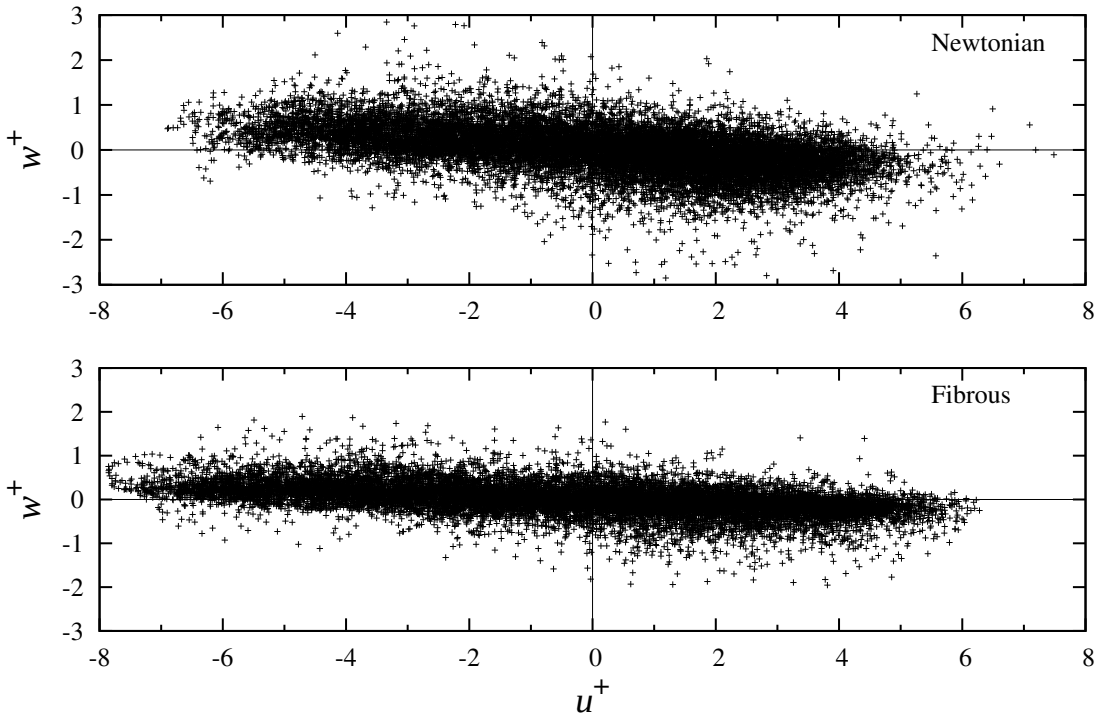

Figure 5.25: Scatter plot of the fluctuating streamwise and wall-normal velocity components (u^+, w^+) at $z^+ = 20$.

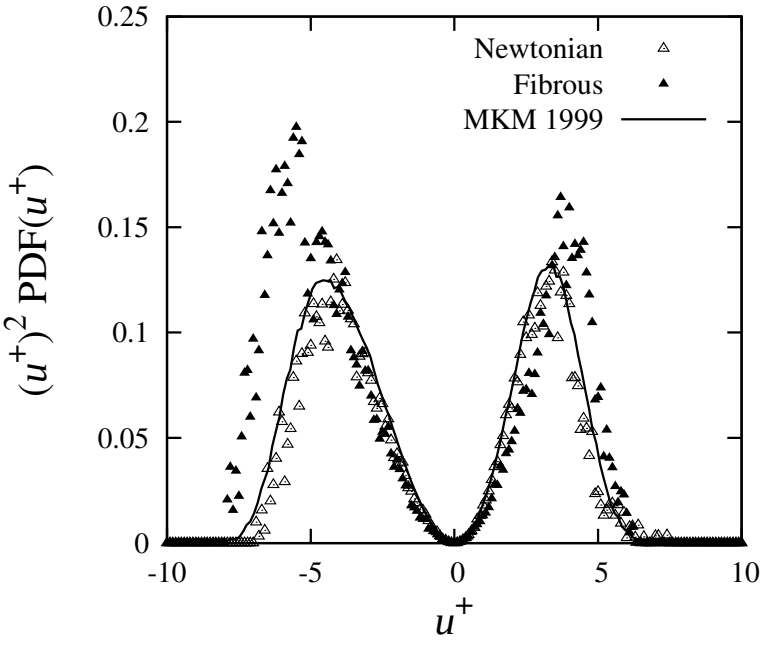

Figure 5.26: Fractional contributions to r.m.s. streamwise velocity fluctuations at $z^+ = 20$ (MKM 1999 data at $z^+ = 19$).

In order to demonstrate how the increase in u_{rms} can be explained by the change in the PDF, we turn to the definition

$$\left(u^+_{\text{rms}}\right)^2 = \langle uu \rangle^+ = \int_{-\infty}^{+\infty} u^+ u^+ \,\text{PDF}\left(u^+\right) \mathrm{d}u^+. \tag{5.10}$$

The integrand $u^+u^+\,\text{PDF}\left(u^+\right)$ is plotted in figure 5.26. Obviously, the area under the curve is increased in the fibrous flow, as compared to the Newtonian flow. Furthermore, the contribution of the events with negative u is considerably increased which is consistent with the prior discussions.

5.2.7. Lumley Anisotropy Map

We have already observed in subsection 5.2.2 that the Reynolds stress tensor is modified in the drag-reduced flow. This modification can be clearly shown by means of the Lumley anisotropy map [68]. Paschkewitz [102] has presented the Lumley anisotropy map of the drag-reduced flow and compared it with that of the carrier fluid alone. Frohnapfel *et al.* [35] have shown that this modification is a general feature of drag-reduced flows, caused by flexible polymers, fibers, surfactants, riblets, highly accelerated compressible supersonic effects and forced boundary conditions. They have found that there are mainly four modifications in the anisotropy map as compared to the Newtonian flow. First, the wall value moves along the two-component turbulence line towards the one-component turbulence state. Second, the right tip (at about $z^+ = 7.5$) moves towards the one-component turbulence state. Third,

away from the wall, the drag-reduced flow reveals more prolate axisymmetry compared to the Newtonian flow. Fourth, the drag-reduced flow is less isotropic in the channel centerline, as compared to the solvent alone.

Figure 5.27 shows the Lumley anisotropy map of the fibrous flow compared to that of the Newtonian flow. All the above-mentioned modifications are observed. Different guidelines plotted in figure 5.27 are explained in section 2.7. In order to explain the change in the anisotropy, we analyze the pressure-strain correlation in the following subsection.

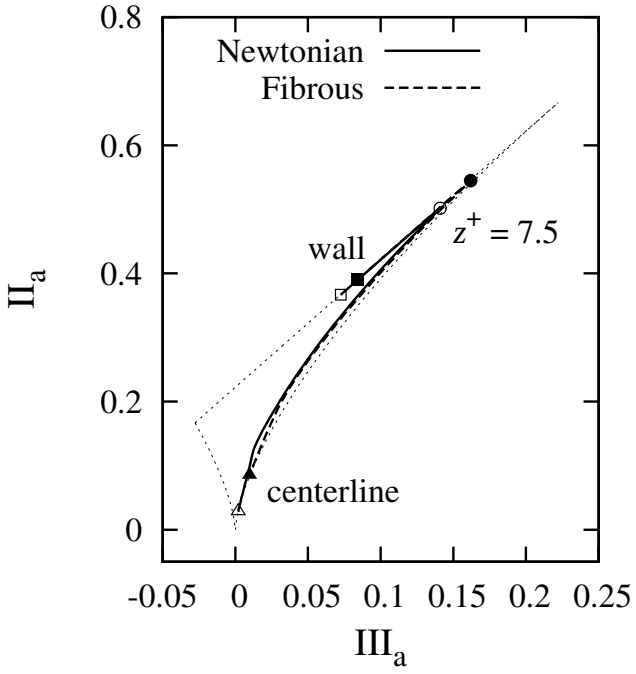

Figure 5.27: Lumley anisotropy map of the Newtonian and fibrous flows, open symbols for Newtonian flow and filled symbols for fibrous flow.

5.2.8. Pressure-Strain Correlation

It is shown in appendix B that the pressure-strain correlation redistributes the turbulent kinetic energy among components of the Reynolds stress tensor. Thus, it can explain the change in turbulence intensities, as shown in figure 5.10. Foysi *et al.* [32] studied the compressible turbulent channel flow using DNS. They also observed a change in the Reynolds normal stresses at high Mach numbers, similar to that of the drag-reduced flow. This modification was explained by analyzing the pressure-strain correlation. In this subsection, we study the pressure-strain correlation in order to analyze the modification in turbulence intensities, as reflected by figure 5.10.

In what follows, the pressure-strain correlation

$$R_{ij} = \frac{1}{\rho}\left\langle p'\left(\frac{\partial u_i}{\partial x_j} + \frac{\partial u_j}{\partial x_i}\right)\right\rangle = \frac{1}{\rho}\left\langle p' s'_{ij}\right\rangle, \tag{5.11}$$

is normalized by the wall shear stress τ_w, the bulk velocity U_b and the channel half-width h [32]:

$$R^+_{ij} = \frac{\rho h}{\tau_w U_b} R_{ij} = \frac{h}{u_\tau^2 U_b} R_{ij}. \tag{5.12}$$

The diagonal terms of the pressure-strain correlation tensor, obtained by the DNS, are plotted in figure 5.28. We theoretically know that the pressure-strain correlation tensor is traceless due to the continuity of the fluctuating velocity field, i.e. $R_{ii} = 0$ (see appendix B). This is checked in our numerical results where the maximum absolute value of R_{ii} is 1.6×10^{-8} ($R^+_{ii} = 2.2\times10^{-5}$) for the Newtonian flow, and 9.2×10^{-8} ($R^+_{ii} = 4.0\times10^{-6}$) for the drag-reduced flow. These small numbers confirm the small divergence of the computed velocity field, i.e. the convergence of the Poisson iterative solver at each time step.

First we explain the Newtonian flow, and then compare it with the drag-reduced flow. The R_{11} component is negative across the channel and thus, acts as a sink of energy for $\langle uu\rangle$, especially in the near-wall region. R_{22} is positive across the channel and acts as a source of energy for $\langle vv\rangle$. R_{33} is negative in the vicinity of the wall, say $z^+ < 11$, and is positive elsewhere. This means that R_{33} is a sink of energy for $\langle ww\rangle$ in the vicinity of the wall and a

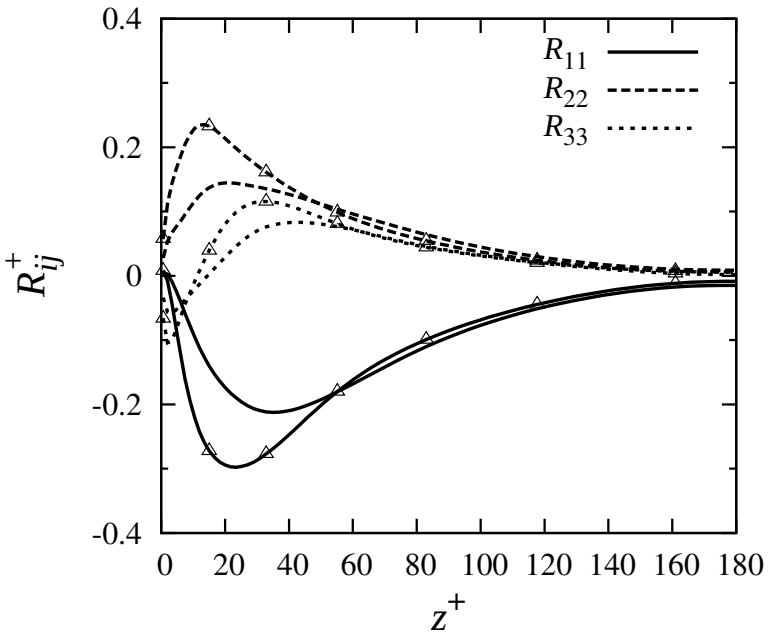

Figure 5.28: Diagonal components of the pressure-strain correlation for the Newtonian and fibrous flows versus the wall distance z^+, Newtonian with $\triangle$ and fibrous without symbol.

source of energy for $\langle ww \rangle$ elsewhere.

In the drag-reduced flow, the behavior of R_{11}, R_{22} and R_{33}, as explained above, remains unchanged, while the magnitude of sources and sinks changes. R_{11}'s sink is weaker, which explains the increase in $\langle uu \rangle$. R_{22}'s source is also weaker. This is consistent with the reduction in $\langle vv \rangle$. Weakening of the energy source due to R_{33} is also in line with the decrease in $\langle ww \rangle$. All the peaks of the diagonal components of the pressure-strain correlation are moved away from the wall, which is consistent with the thickening of the viscous sublayer. Also, $R_{33} = 0$ takes place at $z^+ \approx 15$. Generally, the diagonal components of R_{ij} in the drag-reduced flow are scaled down up to a wall distance $z^+ \approx 60$ as compared to those of the Newtonian flow.

The aforementioned modifications in the pressure-strain correlation $R_{\{ii\}} = \langle\, p' s'_{\{ii\}} \,\rangle$ can be due to one or a combination of the following reasons:

1. Change in p'_{rms}
2. Change in $s'_{\{ii\},\text{rms}}$
3. Change in the correlation coefficient between p' and $s'_{\{ii\}}$

$$R\left\{p', s'_{\{ii\}}\right\} = \frac{R_{\{ii\}}}{p'_{\text{rms}}\, s'_{\{ii\},\text{rms}}}, \tag{5.13}$$

where the subscript $\{ii\}$ means that the Einstein's summation convention does not hold. In the following, we study the above possibilities for the three diagonal components of the pressure-strain correlation tensor.

Figure 5.29 presents the r.m.s. pressure fluctuations for the Newtonian and fibrous flows. The fluctuating pressure is normalized by the wall shear stress:

$$p'^{+}_{\text{rms}} = \frac{p'_{\text{rms}}}{\tau_w} = \frac{p'_{\text{rms}}}{\rho u_\tau^2}. \tag{5.14}$$

It is observed that pressure fluctuations are decreased in the near-wall region, and are slightly increased in the channel center. This behavior is consistent with the reduction in the pressure-strain correlation in the near-wall region. A similar trend was observed by Foysi *et al.* [32] in compressible turbulent channel flow at Ma = 1.5, with Ma being the Mach number. In order to assess the reduction in r.m.s pressure fluctuations, we plot the PDF of the fluctuating pressure in figure 5.30. We observe that the PDF is narrower, meaning that strong pressure fluctuations are attenuated in the drag-reduced flow, as compared to the Newtonian flow. To verify that this attenuation explains the reduction in the r.m.s. pressure fluctuations, we perform the following analysis. The ratio of the r.m.s pressure fluctuations of the Newtonian flow to that of the non-Newtonian flow can be computed from the PDF via

$$\left(p'^{+}_{\text{rms}}\right)^2 = \langle p'p' \rangle^{+} = \int_{-\infty}^{+\infty} p'^{+} p'^{+}\, \text{PDF}\left(p'^{+}\right) \mathrm{d}p'^{+}. \tag{5.15}$$

At $z^+ = 20$, equation (5.15) yields $\left(p'^+_{\mathrm{rms}}\right)_{\mathrm{N}} / \left(p'^+_{\mathrm{rms}}\right)_{\mathrm{NN}} = 1.1615$ which is in good agreement with the actual value 1.1758 obtained by the DNS statistics (see figure 5.29) within 1.2% relative error. The integrand $p'^+ p'^+ \mathrm{PDF}\left(p'^+\right)$ is plotted in figure 5.31. The fractional contributions show that the area under the integrand is decreased in the drag-reduced flow which is indicative of the reduction in p'_{rms}.

The root-mean-square strain fluctuations $(\partial u/\partial x)_{\mathrm{rms}}$, $\left(\partial v/\partial y\right)_{\mathrm{rms}}$ and $(\partial w/\partial z)_{\mathrm{rms}}$ are plotted in figures 5.32, 5.33 and 5.34. They are normalized by the wall shear stress and the viscosity of the carrier fluid via

$$\left(\frac{\partial u_i}{\partial x_j}\right)^+_{\mathrm{rms}} = \frac{\mu}{\tau_w}\left(\frac{\partial u_i}{\partial x_j}\right)_{\mathrm{rms}} = \frac{\nu}{u_\tau^2}\left(\frac{\partial u_i}{\partial x_j}\right)_{\mathrm{rms}}. \tag{5.16}$$

It is observed that all r.m.s. strain fluctuations are considerably reduced in the fibrous flow, as compared to the Newtonian flow, which is consistent with the reduction in the pressure-strain correlation. This is not similar to what is observed in compressible flows [31, 32], where the reduction in the pressure-strain correlation is mainly due to the reduction in pressure fluctuations. We conclude that the modification in the energy redistribution process in mainly a result of the reduction in r.m.s. strain fluctuations. In the near-wall region additionally, the reduction in r.m.s. pressure fluctuations also reduces the energy redistribution via the pressure-strain term.

This analysis shows that the change in anisotropy is due to a change in structure of the strain-rate tensor, and cannot be explained by pressure alone.

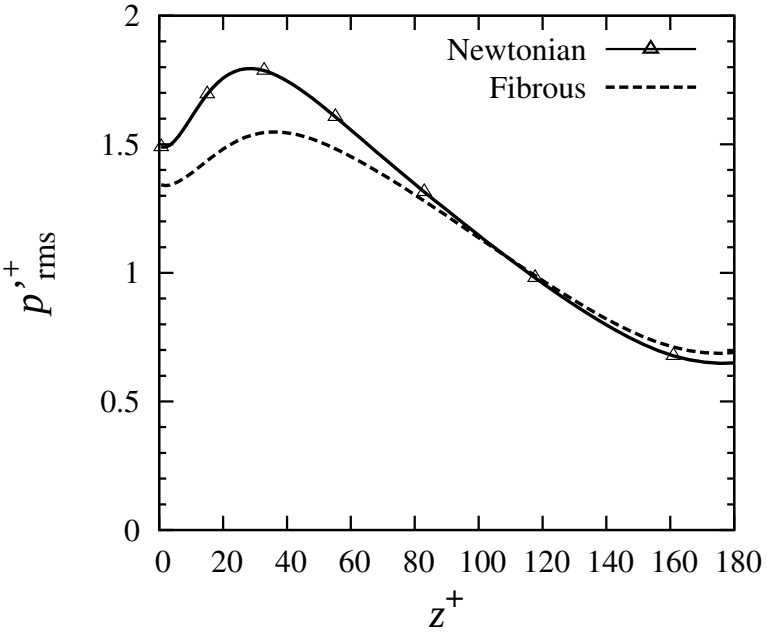

Figure 5.29: Root-mean-square pressure fluctuations in inner scaling for the Newtonian and fibrous flows versus the wall distance z^+.

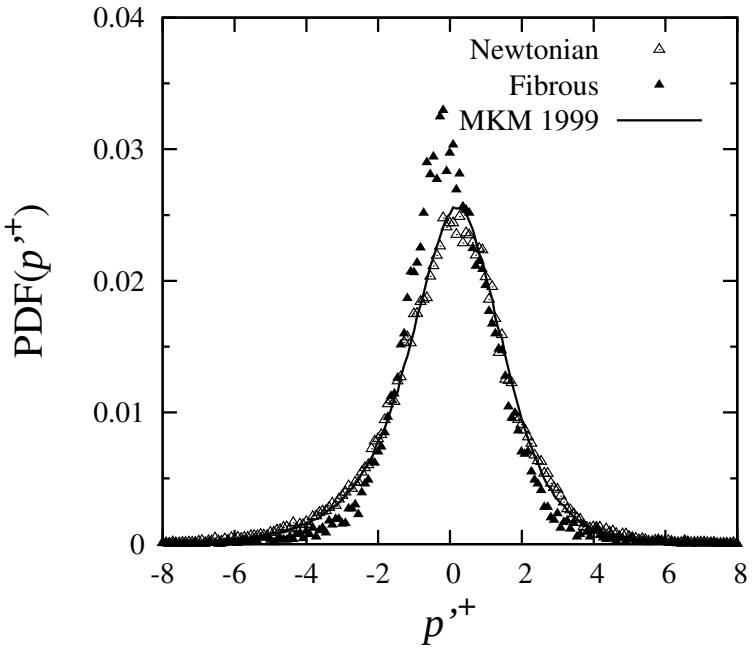

Figure 5.30: Probability distribution function (PDF) of the fluctuating pressure at $z^+ = 20$ (MKM 1999 data at $z^+ = 19$).

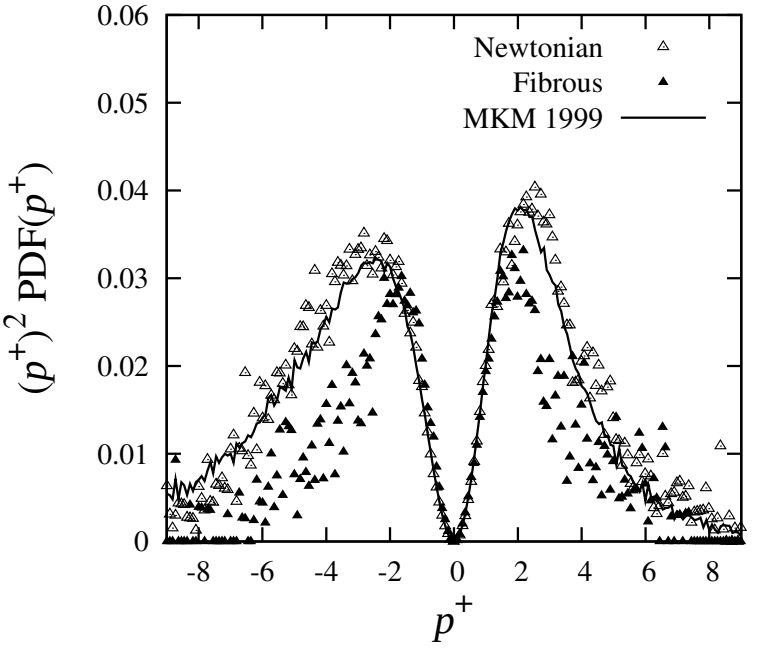

Figure 5.31: Fractional contributions to r.m.s. pressure fluctuations at $z^+ = 20$ (MKM 1999 data at $z^+ = 19$).

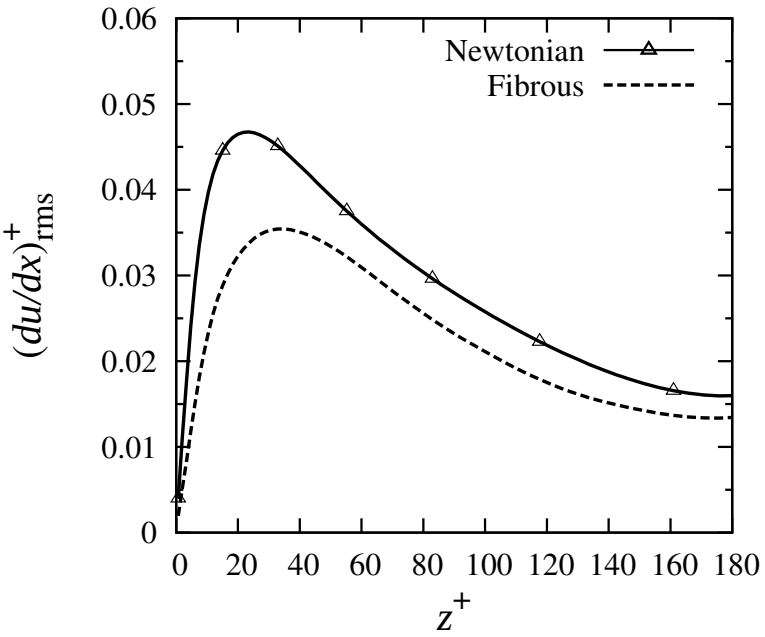

Figure 5.32: Root-mean-square strain fluctuations $(\partial u/\partial x)_{\mathrm{rms}}$ in inner scaling for the Newtonian and fibrous flows versus the wall distance z^+.

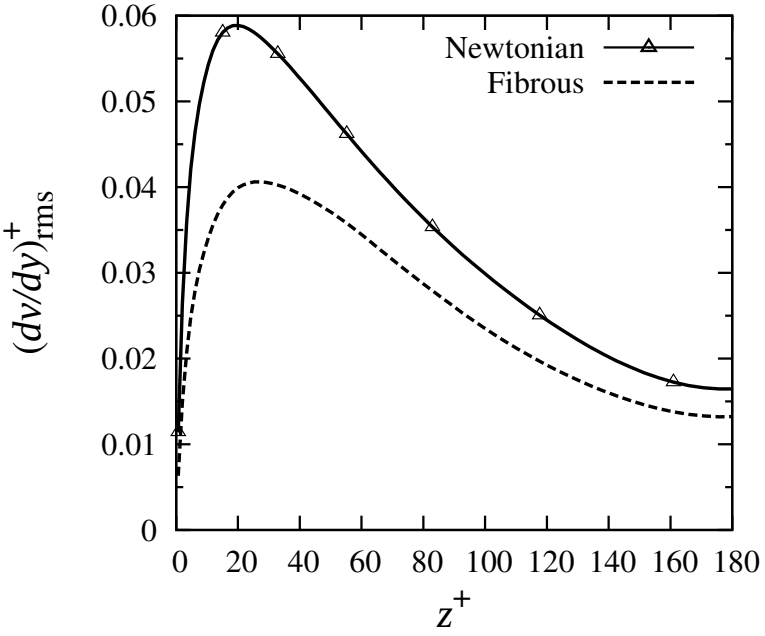

Figure 5.33: Root-mean-square strain fluctuations $(\partial v/\partial y)_{\mathrm{rms}}$ in inner scaling for the Newtonian and fibrous flows versus the wall distance z^+.

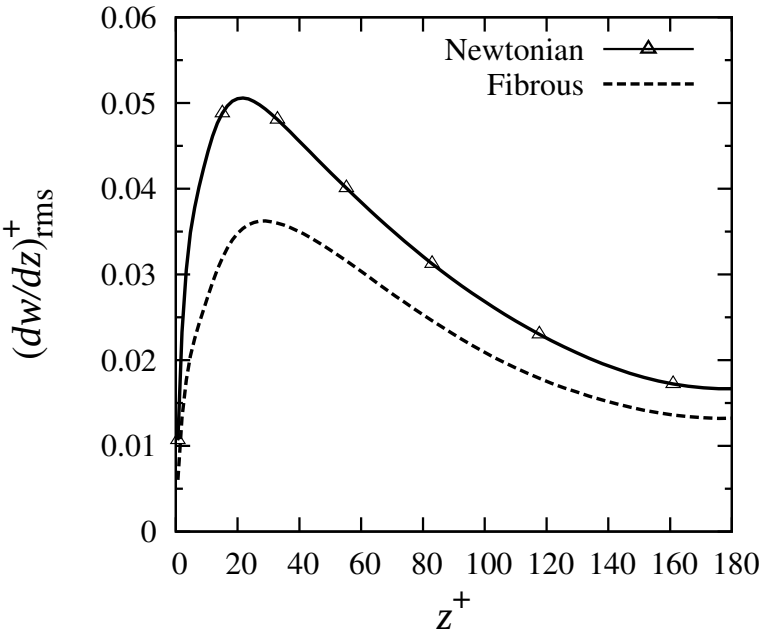

Figure 5.34: Root-mean-square strain fluctuations $(\partial w/\partial z)_{\mathrm{rms}}$ in inner scaling for the Newtonian and fibrous flows versus the wall distance z^+.

5.2.9. Analysis of Pressure-Strain Correlation

We further analyze the pressure-strain correlation by using the following Poisson equation for pressure fluctuations, written here for a turbulent channel flow:

$$\frac{1}{\rho}\frac{\partial^2 p'}{\partial x_j \partial x_j} = -2\frac{\partial \langle U\rangle}{\partial z}\frac{\partial w}{\partial x} - \frac{\partial}{\partial x_i \partial x_j}\left(u_i u_j - \left\langle u_i u_j\right\rangle\right) + \frac{\partial^2 \tau_{ij}^{'\mathrm{NN}}}{\partial x_i \partial x_j}, \tag{5.17}$$

as derived in appendix C. This analysis will hopefully lead to a better understanding of the redistribution process of the Reynolds stresses. Kim [56] have investigated the pressure-strain term using a Green's function solution of the Poisson equation in a Newtonian incompressible turbulent channel flow. Foysi *et al.* [32] have analyzed the pressure-strain term in a compressible turbulent channel flow using a similar approach.

For convenience, the Poisson equation (5.17) can be written as

$$\frac{1}{\rho}\left(\frac{\partial^2 p'}{\partial x^2} + \frac{\partial^2 p'}{\partial y^2} + \frac{\partial^2 p'}{\partial z^2}\right) = f\left(x,y,z\right) = f^{\mathrm{N}}\left(x,y,z\right) + f^{\mathrm{NN}}\left(x,y,z\right), \tag{5.18}$$

in which

$$f^{\mathrm{N}}(x,y,z) = \underbrace{-2\frac{\partial\langle U\rangle}{\partial z}\frac{\partial w}{\partial x}}_{f_1} - \underbrace{\frac{\partial}{\partial x_i \partial x_j}\left(u_i u_j - \left\langle u_i u_j\right\rangle\right)}_{f_2}, \tag{5.19}$$

$$f^{\mathrm{NN}}(x,y,z) = \frac{\partial^2 \tau_{ij}^{'\mathrm{NN}}}{\partial x_i \partial x_j}, \tag{5.20}$$

are the Newtonian and non-Newtonian source terms, respectively. One can take advantage of the periodicity of the channel flow in streamwise and spanwise directions, and take the Fourier transform of the Poisson equation (5.18):

$$\frac{1}{\rho}\left[\frac{\mathrm{d}^2}{\mathrm{d}z^2} - \left(k_x^2 + k_y^2\right)\right]\hat{p}'\left(k_x,k_y,z\right) = \hat{f}\left(k_x,k_y,z\right), \tag{5.21}$$

where $\hat{p}'\left(k_x,k_y,z\right)$ and $\hat{f}\left(k_x,k_y,z\right)$ are the Fourier transforms of $p'(x,y,z)$ and $f(x,y,z)$, respectively. k_x and k_y are the wavenumbers in streamwise and spanwise directions, respectively. We define $k = \sqrt{k_x^2 + k_y^2}$ for future use. The exact boundary condition of equation (5.21) at the wall can be obtained from the Navier-Stokes equation:

$$\left.\frac{\mathrm{d}\hat{p}'}{\mathrm{d}z}\right|_w = \mu\frac{\mathrm{d}^2 w}{\mathrm{d}z^2}. \tag{5.22}$$

According to Kim [56], this boundary condition can be included in a so-called Stokes pressure which is the solution of a Laplace equation. By doing so, the Poisson equation (5.21) is subjected to the following homogenous boundary condition at the wall

$$\left.\frac{\mathrm{d}\hat{p}'}{\mathrm{d}z}\right|_w = 0. \tag{5.23}$$

However, we adopt the boundary condition (5.22) in the following analysis.

For each k_x and k_y, the ordinary differential equation (5.21) can be solved. The inverse Fourier transform of the results will yield the pressure fluctuations. The solution of the linear differential equation (5.21) can be obtained by using the Green's function approach. The Green's function of a differential operator is the solution of the corresponding differential equation under the action of a Dirac delta function as the source term. The Green's function of the differential operator in equation (5.21) is given by Kim [56]. A detailed derivation of the Green's function can be found in [31]. For $k \neq 0$, the Green's function reads

$$\hat{G}\left(k,z,z'\right) = -\frac{\cosh\left[k\left(z'-1\right)\right]\cosh\left[k\left(z+1\right)\right]}{2k\cosh\left(k\right)\sinh\left(k\right)}, \quad \text{for } z < z', \tag{5.24}$$

$$\hat{G}\left(k,z,z'\right) = -\frac{\cosh\left[k\left(z'+1\right)\right]\cosh\left[k\left(z-1\right)\right]}{2k\cosh\left(k\right)\sinh\left(k\right)}, \quad \text{for } z > z'. \tag{5.25}$$

For $k = 0$, the Green's function is defined as

$$\hat{G}\left(z,z'\right) = \frac{1}{2}\left(z'-z\right), \quad \text{for } z < z', \tag{5.26}$$

$$\hat{G}\left(z,z'\right) = \frac{1}{2}\left(z-z'\right), \quad \text{for } z > z'. \tag{5.27}$$

From the theory of Green's functions, the solution of the Poisson equation (5.21) is given by the following convolution integral:

$$p'\left(x,y,z\right) = \int_{L_z} G * f\,\left(x,y,z,z'\right) \mathrm{d}z', \tag{5.28}$$

where the integral is performed over the channel width L_z and the convolution $G * f$ is the inverse Fourier transform of $\hat{G}\left(k,z,z'\right)\hat{f}\left(k_x,k_y,z'\right)$. The Fourier transform and its inverse can be efficiently done using the fast Fourier transform (FFT) algorithm. Similarly, the pressure-strain correlation is computed via [56]

$$R_{ij}\left(z\right) = \frac{1}{\rho}\left\langle p's'_{ij}\right\rangle\left(z\right) = \frac{1}{\rho}\int_{L_z}\left\langle G * f\, s'_{ij}\right\rangle\left(z,z'\right)\mathrm{d}z', \tag{5.29}$$

The above-mentioned solver has been implemented in `FORTRAN`. In order to check that it is implemented properly, another iterative Poisson solver has been developed. The comparison between the two solvers verifies the implementation. In the following, we present the results obtained by the Green's function solver.

Figure 5.35 shows the R_{11} component of the pressure-strain correlation as obtained by equation (5.29). It agrees well with DNS statistics. We observe that the influence of the non-Newtonian source term f^{NN} is to reduce R_{11}. However, its magnitude is small and does not explain the reduction in R_{11}. Actually, the pressure-strain computed by only considering f^{N} is very close to the one obtained by DNS statistics. We observe a similar situation for R_{22} and R_{33} components and therefore, they are not presented here.

We now consider the contributions to f^{N}, namely f_1 and f_2 (equation (5.18)) in the Newtonian and drag-reduced flows, as shown in figure 5.36. As can be seen, both f_1 and f_2 contributions are generally less in the fibrous flow in comparison with the Newtonian counterpart. Therefore, the reduction in f^{N} contribution is a result of the reduction in f_1 and f_2 contributions.

This analysis shows that the reduction of the pressure-strain correlation cannot be attributed to the direct action of the non-Newtonian stresses.

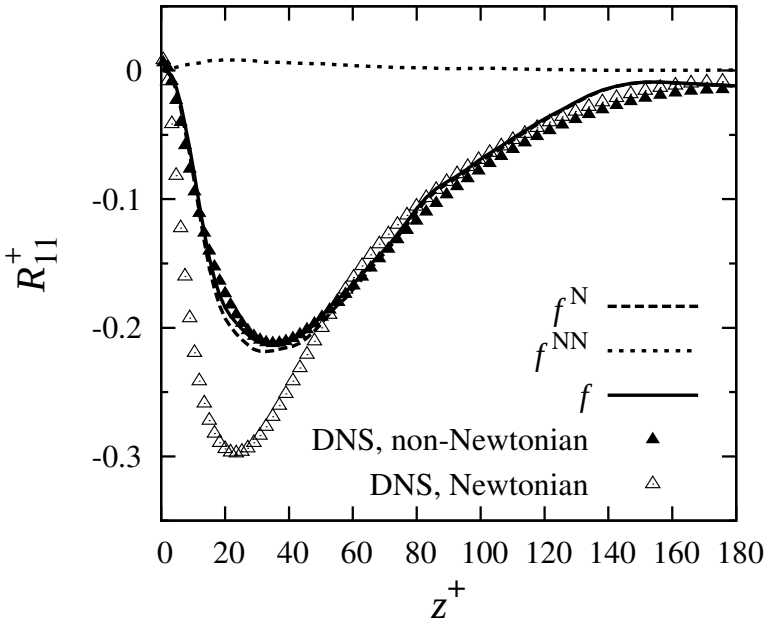

Figure 5.35: Diagonal components of the pressure-strain correlation for the Newtonian and fibrous flows versus the wall distance z^+, Newtonian with $\triangle$ and fibrous without symbol.

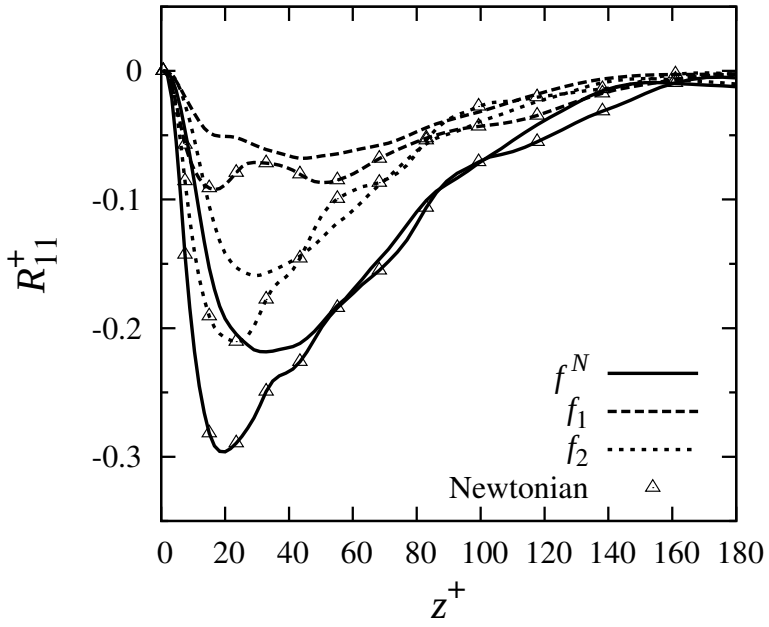

Figure 5.36: Diagonal components of the pressure-strain correlation for the Newtonian and fibrous flows versus the wall distance z^+, Newtonian with $\triangle$ and fibrous without symbol.

5.2.10. Strain-Rate Fluctuations

We have seen that the reduction in the pressure-strain correlation R_{11} is mainly due to the reduction in strain-rate fluctuations $(\partial u/\partial x)_{\mathrm{rms}}$. In this subsection, we analyze the budget of $\left\langle (\partial u/\partial x)^2 \right\rangle = (\partial u/\partial x)^2_{\mathrm{rms}}$. Moreover, we know that $\partial u/\partial x = \partial U/\partial x$ in a fully-developed channel flow due to homogeneity in the streamwise direction. A transport equation for the strain-rate tensor can be derived from the Navier-Stokes equations, for example see equation (2.2) of [97] for an incompressible Newtonian flow. For an incompressible non-Newtonian flow, this equation reads

$$\frac{\mathrm{D}D_{ij}}{\mathrm{D}t} = \underbrace{-D_{ik}D_{kj}}_{A_1} \underbrace{-\frac{1}{4}\left(\omega_i\omega_j - \delta_{ij}\omega_k\omega_k\right)}_{A_2} \underbrace{-\frac{1}{\rho}\frac{\partial^2 p}{\partial x_i \partial x_j}}_{A_3} + \underbrace{\nu\frac{\partial^2 D_{ij}}{\partial x_k \partial x_k}}_{A_4} + \underbrace{\frac{1}{\rho}\frac{\partial^2 \tau^{\mathrm{NN}}_{ik}}{\partial x_j \partial x_k}}_{A_5}, \tag{5.30}$$

where A_1 to A_5 are the self-interaction, effect of local vorticity, local and non-local action through the pressure field, viscous dissipation [97] and the non-Newtonian effects, respectively. From equation (5.30), one can derive the following transport equation for the average fluctuation level of the strain rate, here in streamwise direction $\langle f^2 \rangle = \left\langle (\partial U/\partial x)^2 \right\rangle$, using a procedure similar to that of the Reynolds stress transport equation (see for example [106]).

$$\begin{aligned}\frac{\overline{\mathrm{D}}\langle f^2\rangle}{\overline{\mathrm{D}}t} = &\underbrace{-\left\langle u_k \frac{\partial f^2}{\partial x_k}\right\rangle}_{B_0} \underbrace{-\left\langle 2f\left(f^2 + D_{12}^2 + D_{13}^2\right)\right\rangle}_{B_1} + \underbrace{\frac{1}{4}\left(\left\langle 2f\left(\omega_y^2 + \omega_z^2\right)\right\rangle\right)}_{B_2} \\ &\underbrace{-\frac{1}{\rho}\left\langle 2f\frac{\partial^2 p}{\partial x^2}\right\rangle}_{B_3} + \underbrace{\nu\left\langle 2f\frac{\partial^2 f}{\partial x_k \partial x_k}\right\rangle}_{B_4} + \underbrace{\frac{1}{\rho}\left\langle 2f\frac{\partial^2 \tau^{\mathrm{NN}}_{1k}}{\partial x \partial x_k}\right\rangle}_{B_5},\end{aligned} \tag{5.31}$$

in which B_1 to B_5 correspond to A_1 to A_5 in equation (5.30), respectively. B_0 is the transport of $\langle f^2 \rangle$ by velocity fluctuations u_k. These contributions are plotted in figure 5.37 versus the wall distance z^+. We observe that main contributions are due to the self-interaction (B_1) and the local vorticity (B_2) terms. The self-interaction term contributes positively while the vorticity term contributes negatively to the budget of $\left\langle (\partial U/\partial x)^2 \right\rangle$. The contributions of other terms are small as compared to those of B_1 and B_2. Figure 5.38 shows the contributions of B_3, B_4 and B_5 terms. Like other budgets, the non-Newtonian contribution B_5 is very small and negligible. All other contributions are smaller in the drag-reduced flow in comparison with the Newtonian flow. The most pronounced effect is the reduction in B_1 and B_2 contributions by a factor of about 2.

Again, we can observe that the direct interaction of the non-Newtonian stresses on the strain-rate fluctuations is very weak and cannot be used to explain drag reduction.

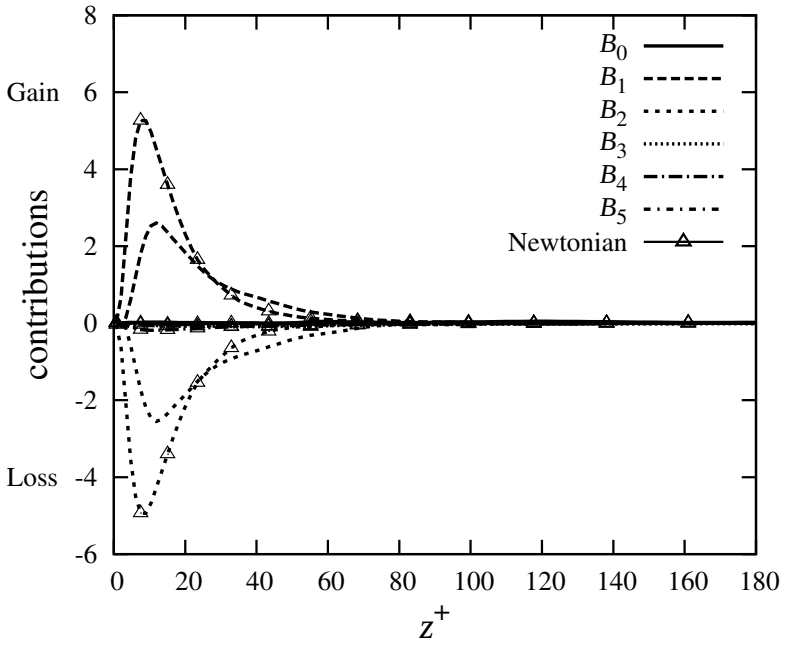

Figure 5.37: Budget of $\left\langle (\partial U/\partial x)^2 \right\rangle$ for the Newtonian and fibrous flows versus the wall distance z^+.

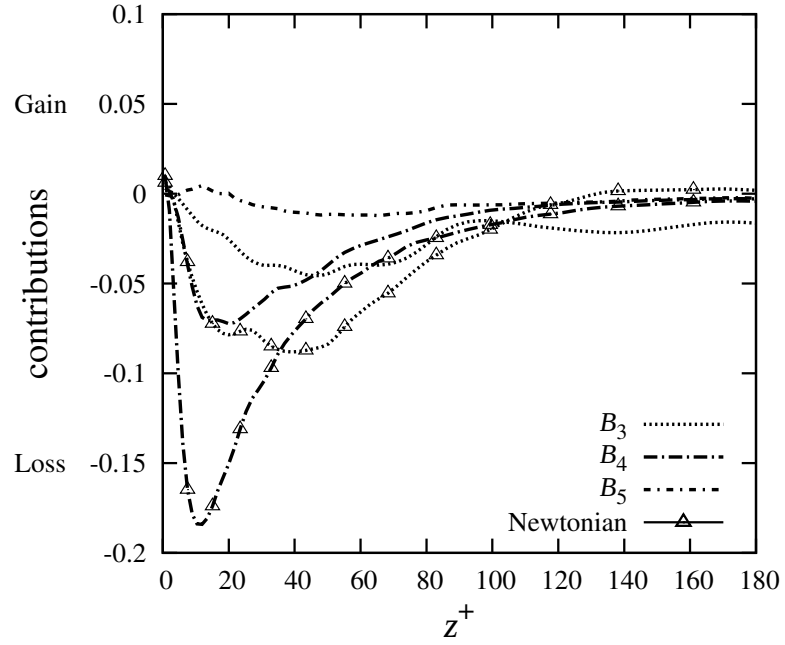

Figure 5.38: Budget of $\left\langle (\partial U/\partial x)^2 \right\rangle$ for the Newtonian and fibrous flows versus the wall distance z^+. B_3, B_4 and B_5 contributions are shown.

5.2.11. Vorticity Field

We investigate in detail the vorticity field of the drag-reduced flow compared with that of the Newtonian flow. The vorticity vector is defined as $\boldsymbol{\omega} = \boldsymbol{\nabla} \times \mathbf{U}$ with the following Cartesian components:

$$\omega_x = \frac{\partial W}{\partial y} - \frac{\partial V}{\partial z}, \tag{5.32}$$

$$\omega_y = \frac{\partial U}{\partial z} - \frac{\partial W}{\partial x}, \tag{5.33}$$

$$\omega_z = \frac{\partial V}{\partial x} - \frac{\partial U}{\partial y}. \tag{5.34}$$

Due to the statistical homogeneity of the turbulent channel flow, we have $\langle \omega_x \rangle = 0$, $\langle \omega_z \rangle = 0$ and $\langle \omega_y \rangle = \mathrm{d}\langle U \rangle / \mathrm{d}z$. Therefore, the mean spanwise vorticity $\langle \omega_y \rangle$ has the same behavior as the viscous shear stress shown in figure 5.13, and is not explained here. It is well known from previous experimental and numerical studies on polymer-induced drag reduction that the root-mean-square of the fluctuations in streamwise vorticity decreases in a drag-reduced flow as compared to its Newtonian counterpart. This is shown in figure 5.39, in which the r.m.s. streamwise vorticity fluctuations is normalized via $\omega'^{+}_{x,\mathrm{rms}} = \omega'_{x,\mathrm{rms}} \nu / u_\tau^2$. Although the shapes of the profiles are generally similar, the fluctuation level is lower in the drag-reduced flow. This is confirmed by the simulation of Paschkewitz *et al.* [102, 104]. The r.m.s. of the spanwise and wall-normal vorticity components are presented in figures 5.40

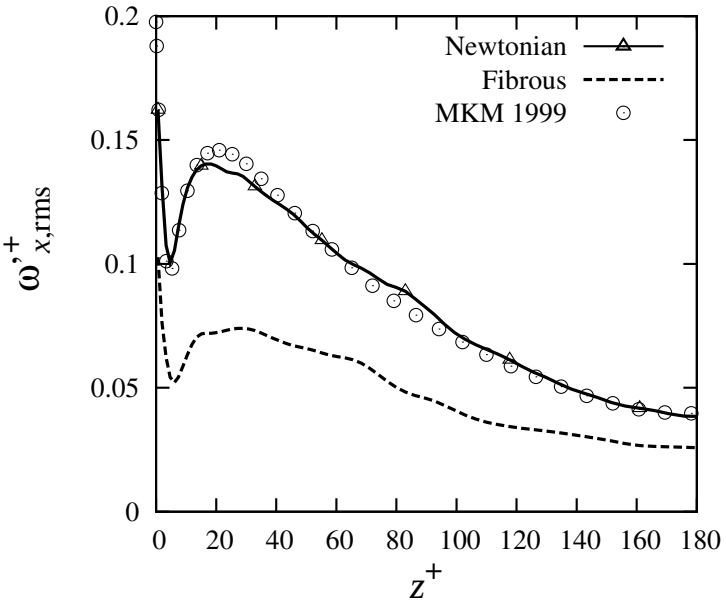

Figure 5.39: Root-mean-square of streamwise vorticity fluctuations of the Newtonian and fibrous flows in inner scaling versus the wall distance z^+, $\omega'^{+}_{x,\mathrm{rms}} = \omega'_{x,\mathrm{rms}} \nu / u_\tau^2$.

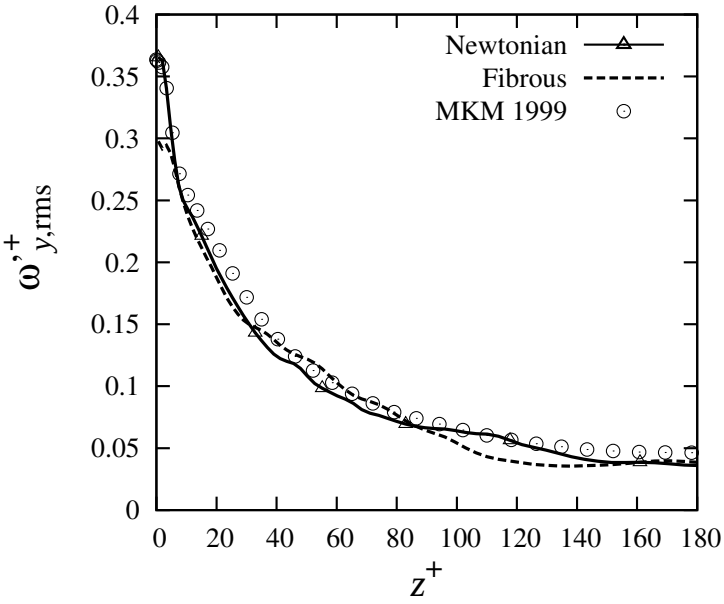

Figure 5.40: Root-mean-square of spanwise vorticity fluctuations of the Newtonian and fibrous flows in inner scaling versus the wall distance z^+, $\omega'^{+}_{y,\mathrm{rms}} = \omega'_{y,\mathrm{rms}}\nu/u_\tau^2$.

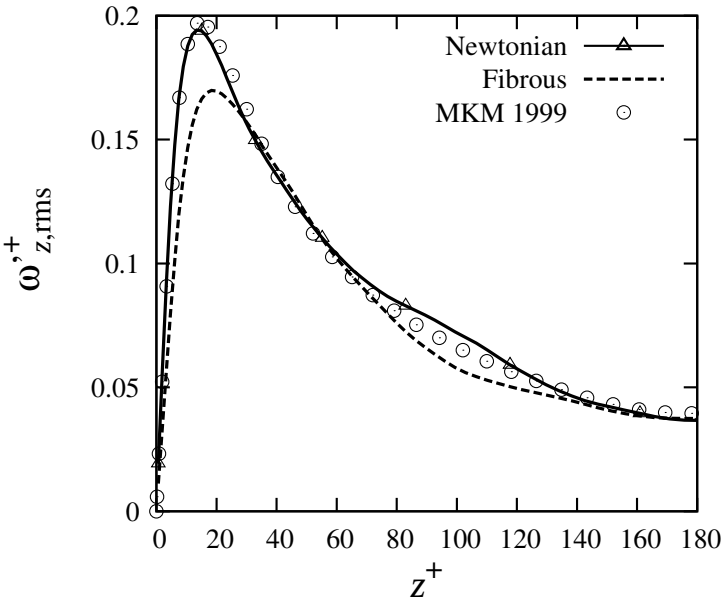

Figure 5.41: Root-mean-square of wall-normal vorticity fluctuations of the Newtonian and fibrous flows in inner scaling versus the wall distance z^+, $\omega'^{+}_{z,\mathrm{rms}} = \omega'_{z,\mathrm{rms}}\nu/u_\tau^2$.

and 5.41, respectively. The profiles of the spanwise vorticity fluctuations in Newtonian and drag-reduced flows are similar with the exception of the value at the wall. The fluctuation level of the wall-normal component is lower than that of the Newtonian flow in the wall region ($z^+ < 30$). Further away from the wall, the two profiles nearly show the same level of

fluctuations.

The reduction in streamwise vorticity fluctuations is known as one of the main features of polymer-induced drag-reduced turbulent wall flows. In the following, we investigate this reduction in more detail. To this aim, we derive an equation for the r.m.s. of streamwise vorticity fluctuations from equation (5.32):

$$\left(\omega'_{x,\mathrm{rms}}\right)^2 = \left\langle \omega'_x \omega'_x \right\rangle = \left\langle \left(\frac{\partial W}{\partial y}\right)^2 \right\rangle + \left\langle \left(\frac{\partial V}{\partial z}\right)^2 \right\rangle - 2\left\langle \frac{\partial W}{\partial y}\frac{\partial V}{\partial z} \right\rangle . \tag{5.35}$$

These three contributions are plotted in figures 5.42, 5.43 and 5.44, respectively.

All three contributions are in favor of reducing the streamwise vorticity fluctuations. This means that the reduction in the streamwise vorticity fluctuations can be attributed to the reduction in the second moments of the strain rates $\langle \partial W/\partial y \, \partial W/\partial y \rangle$, $\langle \partial V/\partial z \, \partial V/\partial z \rangle$ and $\langle \partial W/\partial y \, \partial V/\partial z \rangle$. Furthermore, the reduction in $\langle \partial W/\partial y \, \partial V/\partial z \rangle$ can be a result of reduction in $\left(\partial W/\partial y\right)_{\mathrm{rms}}$, $\left(\partial V/\partial z\right)_{\mathrm{rms}}$ and/or reduction in the correlation coefficient between them:

$$R\left\{\frac{\partial W}{\partial y}, \frac{\partial V}{\partial z}\right\} = \frac{-\left\langle \frac{\partial W}{\partial y}\frac{\partial V}{\partial z} \right\rangle}{\left(\frac{\partial W}{\partial y}\right)_{\mathrm{rms}} \left(\frac{\partial V}{\partial z}\right)_{\mathrm{rms}}}. \tag{5.36}$$

The correlation coefficient across the channel width is shown in figure 5.45 for both Newtonian and drag-reduced flows. It is observed that the modification in the correlation coefficient

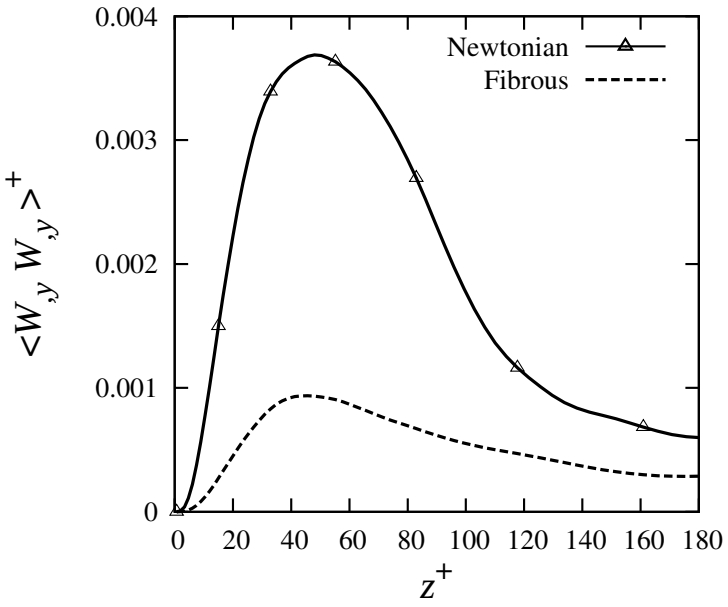

Figure 5.42: $\left\langle \left(\partial W/\partial y\right)^2 \right\rangle$ contribution to streamwise vorticity fluctuations for the Newtonian and fibrous flows in inner scaling versus the wall distance z^+, $\left\langle \left(\partial W/\partial y\right)^2 \right\rangle^+ = \left\langle \left(\partial W/\partial y\right)^2 \right\rangle \nu^2/u_\tau^4$.

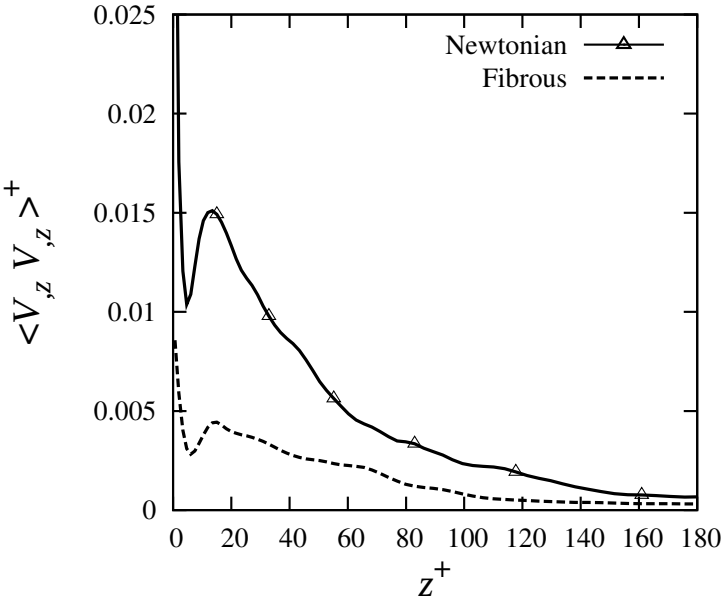

Figure 5.43: $\left\langle (\partial V/\partial z)^2 \right\rangle$ contribution to streamwise vorticity fluctuations for the Newtonian and fibrous flows in inner scaling versus the wall distance z^+, $\left\langle (\partial V/\partial z)^2 \right\rangle^+ = \left\langle (\partial V/\partial z)^2 \right\rangle \nu^2/u_\tau^4$.

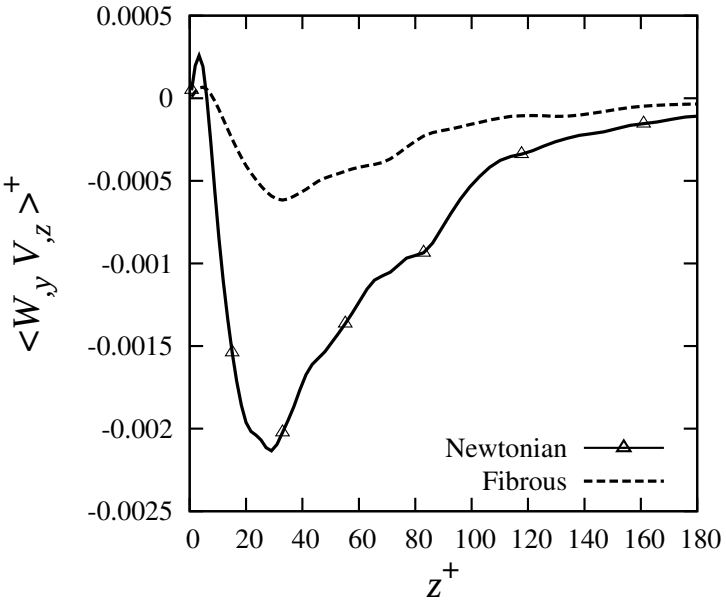

Figure 5.44: $\langle \partial W/\partial y\ \partial V/\partial z \rangle$ contribution to streamwise vorticity fluctuations for the Newtonian and fibrous flows in inner scaling versus the wall distance z^+, $\langle \partial W/\partial y\ \partial V/\partial z \rangle^+ = \langle \partial W/\partial y\ \partial V/\partial z \rangle \nu^2/u_\tau^4$.

due to the fibers is modest. Therefore, the reduction in $\langle \partial W/\partial y\ \partial V/\partial z \rangle$ is mainly due to the reduction in $(\partial W/\partial y)_{\text{rms}}$ and $(\partial V/\partial z)_{\text{rms}}$.

We conclude that the reduction in r.m.s. streamwise vorticity fluctuations is mainly due to the reduction in r.m.s. velocity gradient fluctuations, i.e. $(\partial W/\partial y)_{\text{rms}}$ and $(\partial V/\partial z)_{\text{rms}}$.

Finally, we consider the inclination angle associated with the tilting of vorticity vector in the x-z plane. The definition of the inclination angle and its measurement is schematically depicted in figure 5.46. The main observations are as follows. In the wall region, the tilting angles are more populated about 0° and the compliment angles, −180° and 180°, in the drag-reduced flow compared to the Newtonian flow. In the fibrous flow, the distributions possess stronger peaks further away from the wall. In the Newtonian flow, above $z^+ = 25$, the tilting angles are more populated about 45° and −135°. This is a well-known result in the Newtonian turbulent channel flow [84]. We observe that the drag-reduced flow reveals such behavior at a

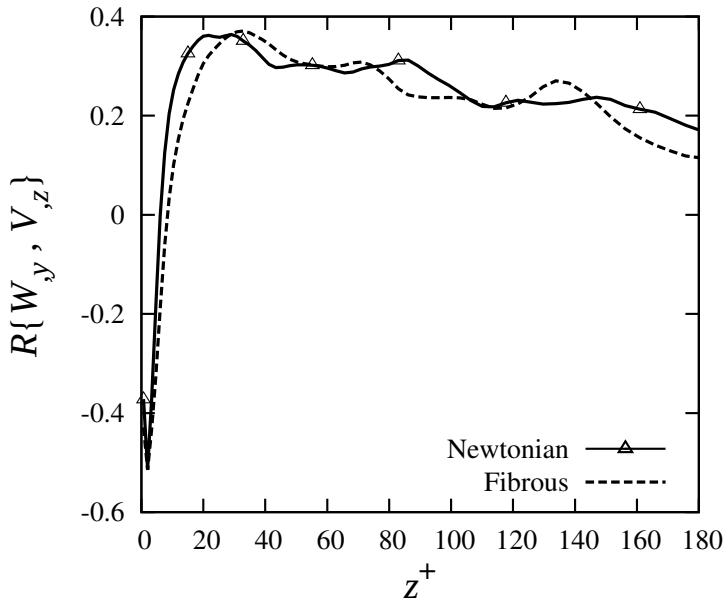

Figure 5.45: Correlation coefficient $R\{\partial W/\partial y, \partial V/\partial z\}$ for the Newtonian and fibrous flows versus the wall distance z^+.

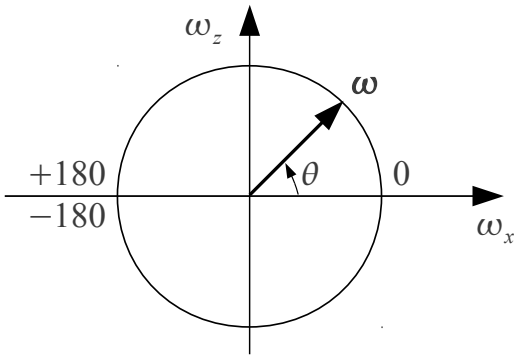

Figure 5.46: Convention for the vorticity tilting angle in $x - z$ plane.

wall distance of about $z^+ = 90$. Ultimately, the tilting angle reaches at an almost uniform distribution at the channel centerline in both flows. However, the distribution in the fibrous flow is less uniform. This is conjectured to be a consequence of the fibrous flow being less isotropic at the centerline, see the Lumley anisotropy map in figure 5.27.

It seems that up to the buffer layer, the fibrous flow is more organized and it has higher peaks. However, these peaks are more away from $45°/-135°$ than in the Newtonian flow. This indicates that less effective vortices (45°) are there.

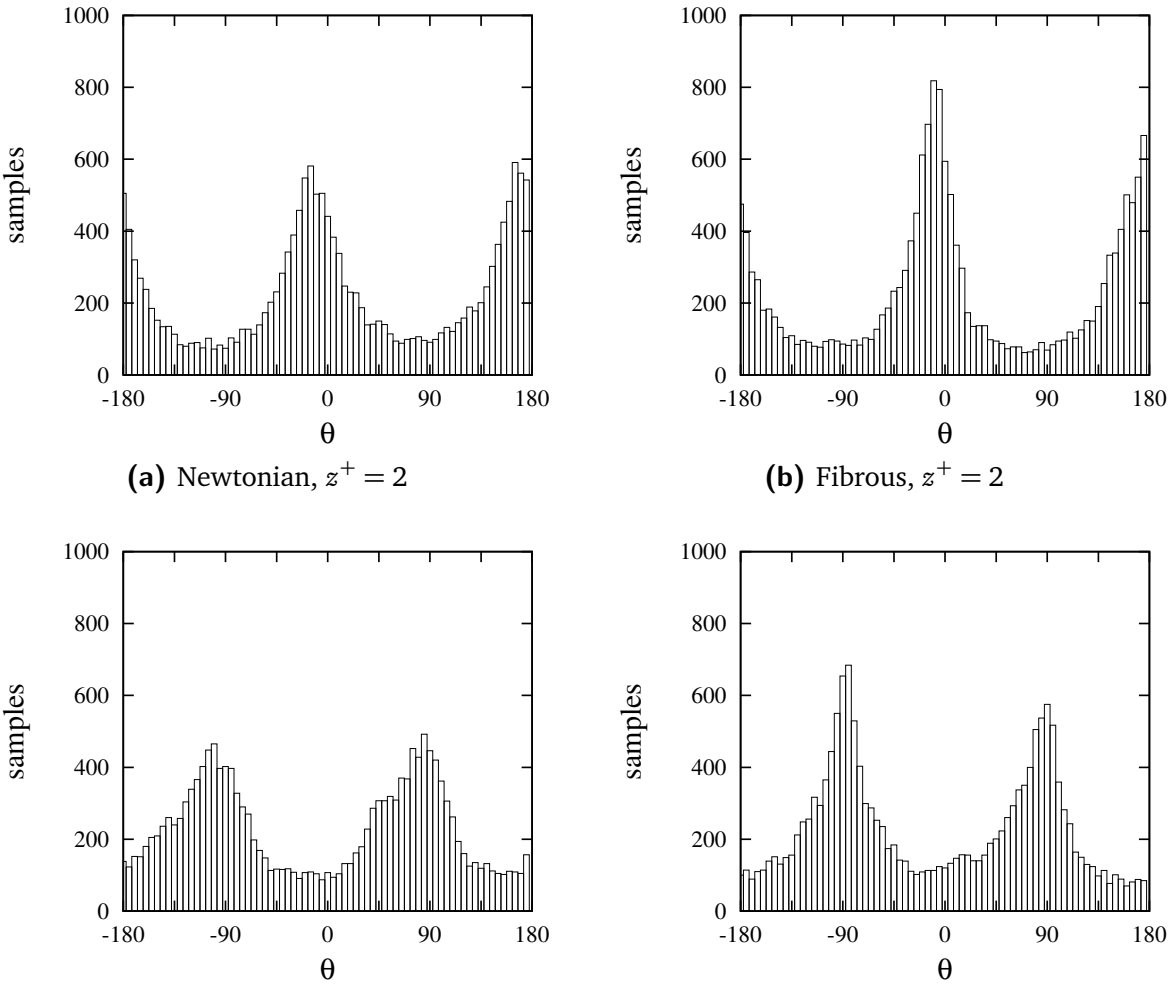

(a) Newtonian, $z^+ = 2$ **(b)** Fibrous, $z^+ = 2$

(c) Newtonian, $z^+ = 8.9$ **(d)** Fibrous, $z^+ = 8.9$

Figure 5.47: Distribution of the inclination angle of the vorticity vector in x-z plane.

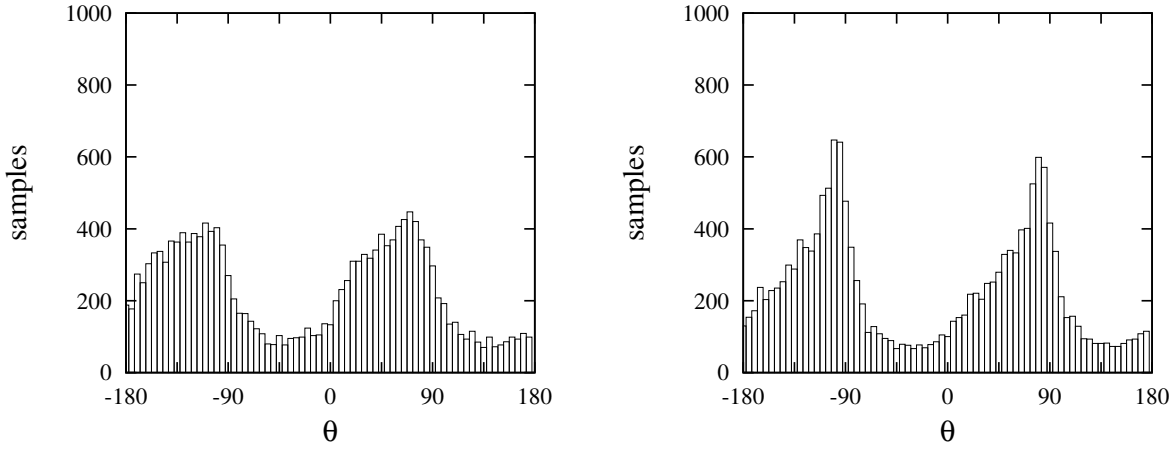

(e) Newtonian, $z^+ = 25$ **(f)** Fibrous, $z^+ = 25$

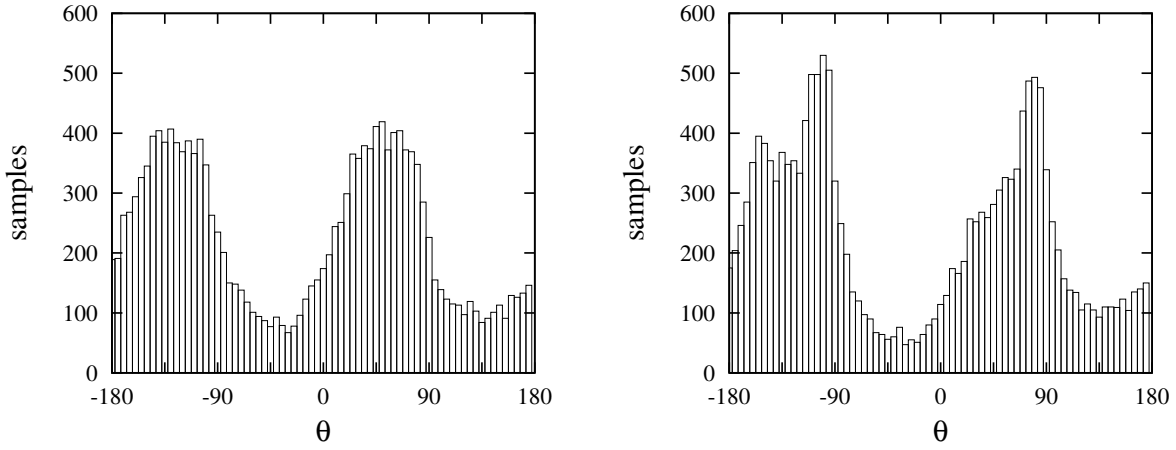

(g) Newtonian, $z^+ = 34.9$ **(h)** Fibrous, $z^+ = 34.9$

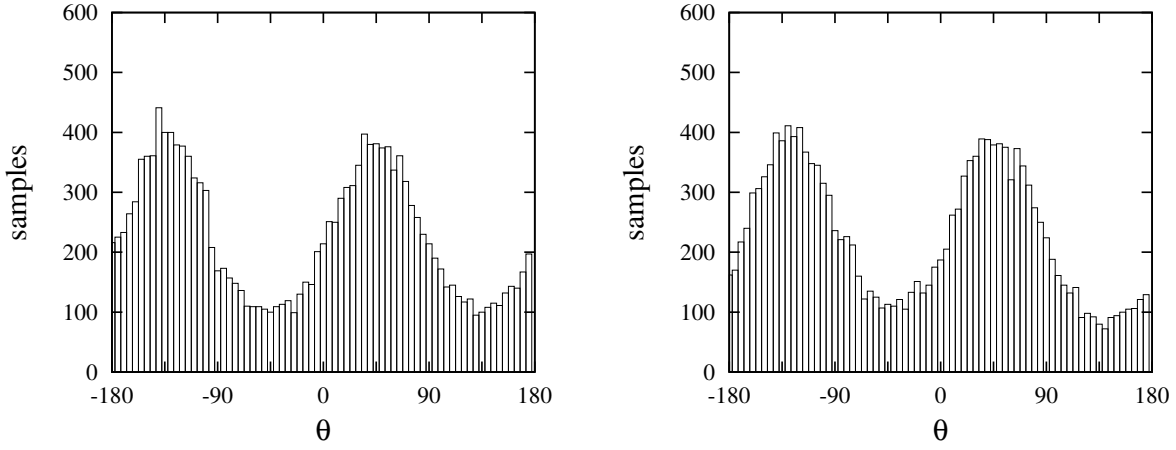

(i) Newtonian, $z^+ = 89.3$ **(j)** Fibrous, $z^+ = 89.3$

Figure 5.47: Distribution of the inclination angle of the vorticity vector in x-z plane (continued).

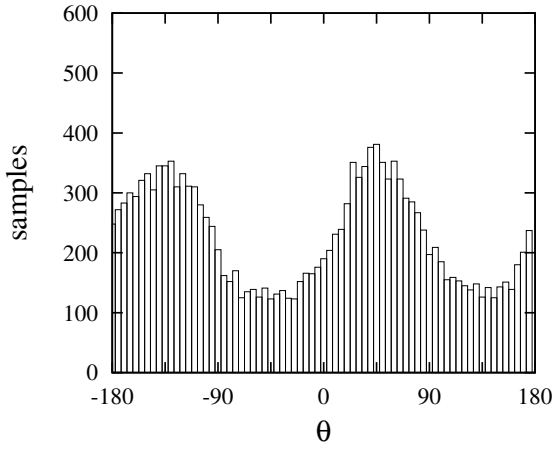

(k) Newtonian, $z^+ = 138$

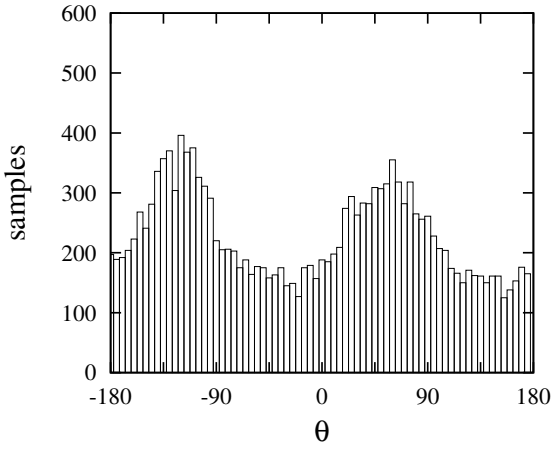

(l) Fibrous, $z^+ = 138$

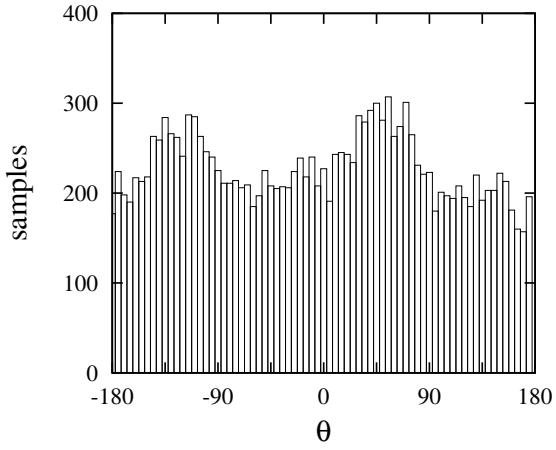

(m) Newtonian, $z^+ = 165.9$

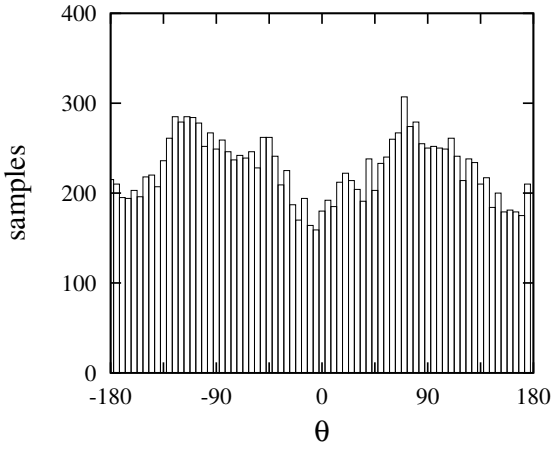

(n) Fibrous, $z^+ = 165.9$

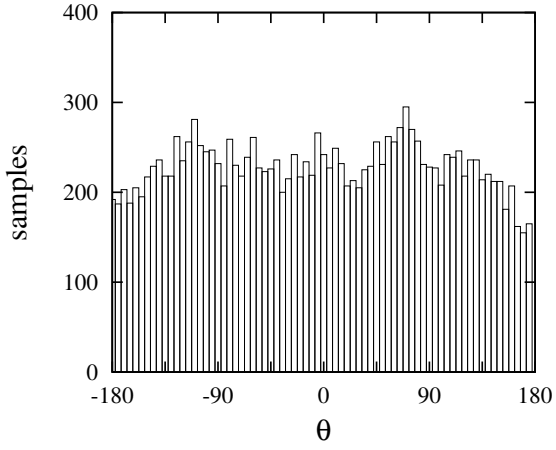

(o) Newtonian, centerline

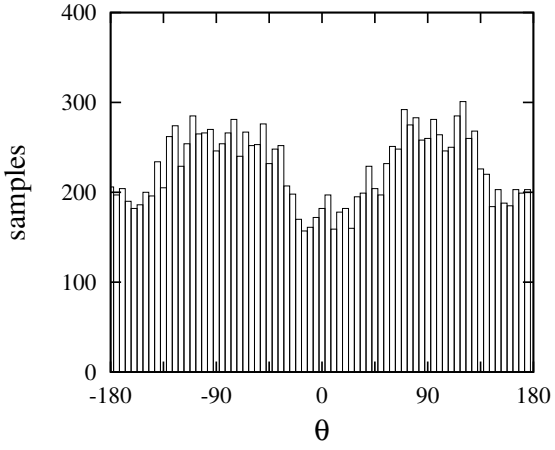

(p) Fibrous, centerline

Figure 5.47: Distribution of the inclination angle of the vorticity vector in x-z plane (continued).

5.2.12. Near-Wall Partial Enstrophy

We now consider the dynamics of near-wall vorticity. Similar to the work of Lee and Kim [64], our approach is to investigate the near-wall partial enstrophy. To this aim, we consider the vorticity transport equation

$$\frac{\partial \boldsymbol{\omega}}{\partial t} = -\mathbf{U}\cdot\boldsymbol{\nabla}\boldsymbol{\omega} + \boldsymbol{\omega}\cdot\boldsymbol{\nabla}\mathbf{U} + \nu\,\boldsymbol{\nabla}^2\boldsymbol{\omega} + \frac{1}{\rho}\,\boldsymbol{\nabla}\times\boldsymbol{\nabla}\cdot\boldsymbol{\tau}^{\mathrm{NN}}, \tag{5.37}$$

which is obtained by taking the curl of the Navier-Stokes equation, and noting that $\boldsymbol{\omega} = \boldsymbol{\nabla}\times\mathbf{U}$. The advective term $\mathbf{U}\cdot\boldsymbol{\nabla}\boldsymbol{\omega}$ transports the vorticity by the velocity field. It does not contribute to the production and dissipation of vorticity, and is disregarded in the following analysis. The term $\boldsymbol{\omega}\cdot\boldsymbol{\nabla}\mathbf{U}$ describes the tilting and stretching of vorticity. The third term in the right-hand side of equation (5.37) is the viscous dissipation of vorticity. The above-mentioned terms exist in a Newtonian flow. The last term is additionally present in a fibrous flow. Here, we consider the streamwise and wall-normal vorticity components. Because, the spanwise vorticity of the fibrous flow does not considerably differ from that of the Newtonian flow. In a fully-developed channel flow, ω_x and ω_z have only fluctuating components.

In the streamwise vorticity equation, the tilting term $\boldsymbol{\omega}\cdot\boldsymbol{\nabla}\mathbf{U}$ in the near-wall region reduces to [116, 64]

$$\omega_x\frac{\partial U}{\partial x} + \omega_y\frac{\partial U}{\partial y} + \omega_z\frac{\partial U}{\partial z} = -\frac{\partial V}{\partial x}\frac{\partial U}{\partial z}. \tag{5.38}$$

Similarly, the tilting term of the wall-normal vorticity equation in the near-wall region can be written as [64]

$$\omega_x\frac{\partial W}{\partial x} + \omega_y\frac{\partial W}{\partial y} + \omega_z\frac{\partial W}{\partial z} = -\frac{\partial W}{\partial y}\frac{\partial U}{\partial z}. \tag{5.39}$$

Therefore, the streamwise and wall-normal vorticity equations can be written as (by neglecting the advective term):

$$\frac{\partial \omega_x}{\partial t} \approx -\frac{\partial V}{\partial x}\frac{\partial U}{\partial z} + \nu\,\frac{\partial^2\omega_x}{\partial x_j\partial x_j} + \frac{1}{\rho}\,\varepsilon_{1ik}\,\frac{\partial^2\tau^{\mathrm{NN}}_{jk}}{\partial x_i\partial x_j}, \tag{5.40}$$

$$\frac{\partial \omega_z}{\partial t} \approx -\frac{\partial W}{\partial y}\frac{\partial U}{\partial z} + \nu\,\frac{\partial^2\omega_z}{\partial x_j\partial x_j} + \frac{1}{\rho}\,\varepsilon_{3ik}\,\frac{\partial^2\tau^{\mathrm{NN}}_{jk}}{\partial x_i\partial x_j}, \tag{5.41}$$

where ε_{ijk} is the Levi-Civita permutation symbol [128]. By multiplying equations (5.40) and (5.41) by ω_x and ω_z, respectively, and then adding them together, we obtain an equation for $\omega_x^2 + \omega_z^2$. Averaging over the homogenous streamwise and spanwise directions yields an equation for the near-wall partial enstrophy $\left\langle\omega_x^2\right\rangle + \left\langle\omega_z^2\right\rangle$:

$$\frac{\partial\left(\left\langle\omega_x^2\right\rangle + \left\langle\omega_z^2\right\rangle\right)}{\partial t} \approx P_{\omega_x} + P_{\omega_z} + \epsilon_\omega + f_x + f_z, \tag{5.42}$$

in which

$$P_{\omega_x} = -\left\langle \omega_x \frac{\partial V}{\partial x} \right\rangle \frac{\mathrm{d}\langle U \rangle}{\mathrm{d}z}, \tag{5.43}$$

$$P_{\omega_z} = -\left\langle \omega_z \frac{\partial W}{\partial y} \right\rangle \frac{\mathrm{d}\langle U \rangle}{\mathrm{d}z}, \tag{5.44}$$

$$\begin{aligned} \epsilon_\omega = -\nu \Bigg[&\left\langle \left(\frac{\partial \omega_x}{\partial x} \right)^2 \right\rangle + \left\langle \left(\frac{\partial \omega_x}{\partial y} \right)^2 \right\rangle + \left\langle \left(\frac{\partial \omega_x}{\partial z} \right)^2 \right\rangle \\ &+ \left\langle \left(\frac{\partial \omega_z}{\partial x} \right)^2 \right\rangle + \left\langle \left(\frac{\partial \omega_z}{\partial y} \right)^2 \right\rangle + \left\langle \left(\frac{\partial \omega_z}{\partial z} \right)^2 \right\rangle \Bigg], \end{aligned} \tag{5.45}$$

$$\begin{aligned} f_x = \frac{1}{\rho} \Bigg(&\left\langle \omega_x \frac{\partial^2 \tau_{13}^{\mathrm{NN}}}{\partial x \partial y} \right\rangle + \left\langle \omega_x \frac{\partial^2 \tau_{23}^{\mathrm{NN}}}{\partial y^2} \right\rangle + \left\langle \omega_x \frac{\partial^2 \tau_{33}^{\mathrm{NN}}}{\partial y \partial z} \right\rangle \\ &- \left\langle \omega_x \frac{\partial^2 \tau_{12}^{\mathrm{NN}}}{\partial x \partial z} \right\rangle - \left\langle \omega_x \frac{\partial^2 \tau_{22}^{\mathrm{NN}}}{\partial y \partial z} \right\rangle - \left\langle \omega_x \frac{\partial^2 \tau_{23}^{\mathrm{NN}}}{\partial z^2} \right\rangle \Bigg), \end{aligned} \tag{5.46}$$

$$\begin{aligned} f_z = \frac{1}{\rho} \Bigg(&\left\langle \omega_z \frac{\partial^2 \tau_{12}^{\mathrm{NN}}}{\partial x^2} \right\rangle + \left\langle \omega_z \frac{\partial^2 \tau_{22}^{\mathrm{NN}}}{\partial x \partial y} \right\rangle + \left\langle \omega_z \frac{\partial^2 \tau_{23}^{\mathrm{NN}}}{\partial x \partial z} \right\rangle \\ &- \left\langle \omega_z \frac{\partial^2 \tau_{11}^{\mathrm{NN}}}{\partial x \partial y} \right\rangle - \left\langle \omega_z \frac{\partial^2 \tau_{12}^{\mathrm{NN}}}{\partial y^2} \right\rangle - \left\langle \omega_z \frac{\partial^2 \tau_{13}^{\mathrm{NN}}}{\partial y \partial z} \right\rangle \Bigg). \end{aligned} \tag{5.47}$$

P_{ω_x} and P_{ω_z} are the production terms, ϵ_ω is the viscous dissipation, and f_x and f_z are the non-Newtonian contributions. All these contributions are shown in figures 5.48 and 5.49 for the Newtonian and drag-reduced flows. The enstrophy production of the Newtonian flow is positive everywhere except for P_{ω_x} in the region adjacent to the wall ($z^+ < 2$ for the Newtonian and $z^+ < 3.2$ for the drag-reduced flows). The extended negative zone of P_{ω_x} in the drag-reduced flow can be explained by the thickened viscous sublayer . The wall-normal enstrophy production P_{ω_z} is almost twice as large as the streamwise enstrophy production P_{ω_x}. These are in agreement with the findings of Lee and Kim [64] for a Newtonian channel flow at $\mathrm{Re}_\tau = 110$. Both production terms are decreased in the drag-reduced flow as compared to the Newtonian flow. The amount of dissipation has been also reduced. The direct non-Newtonian contribution is very small and can be neglected.

The partial enstrophy production terms P_{ω_x} and P_{ω_z} are proportional to $\langle \omega_x \omega_z \rangle \, \mathrm{d}\langle U \rangle / \mathrm{d}z$ [64]. Therefore, the one-point correlation $\langle \omega_x \omega_z \rangle^+ = \langle \omega_x \omega_z \rangle h^2 / u_\tau^2$ is plotted in figure 5.50 for the Newtonian and drag-reduced flows versus the wall distance z^+. $\langle \omega_x \omega_z \rangle$ is negative in the vicinity of the wall ($z^+ < 5$ for Newtonian and $z^+ < 6.7$ for the fibrous flows) and is positive elsewhere. Streamwise and wall-normal vorticities decay where $\langle \omega_x \omega_z \rangle$ is negative and grow where $\langle \omega_x \omega_z \rangle$ is positive [64]. Our simulation shows that, in the drag-reduced flow, the structures with opposite signs of ω_x and ω_z exist in a thicker region near the wall as compared

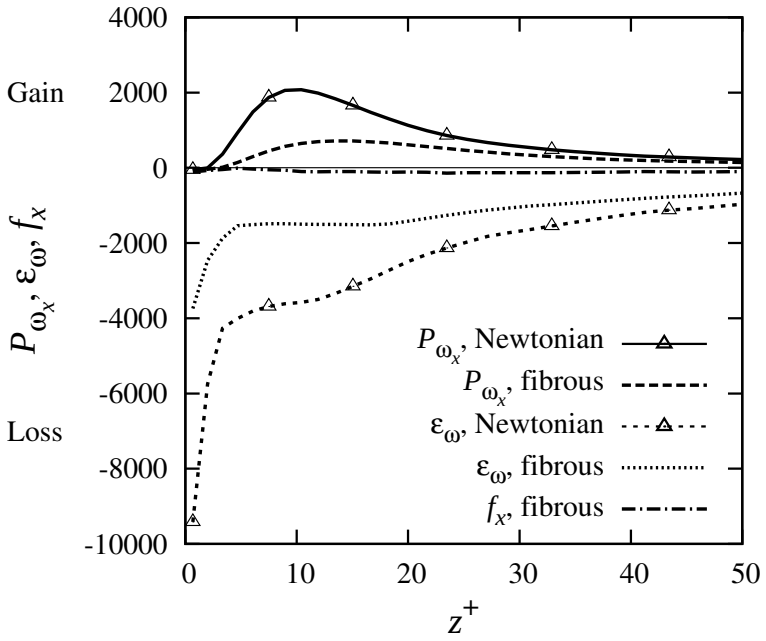

Figure 5.48: Budget of near-wall partial enstrophy for the Newtonian and fibrous flows versus the wall distance z^+. Contributions are normalized by h and u_τ. The balance does not hold because the turbulent transport is neglected.

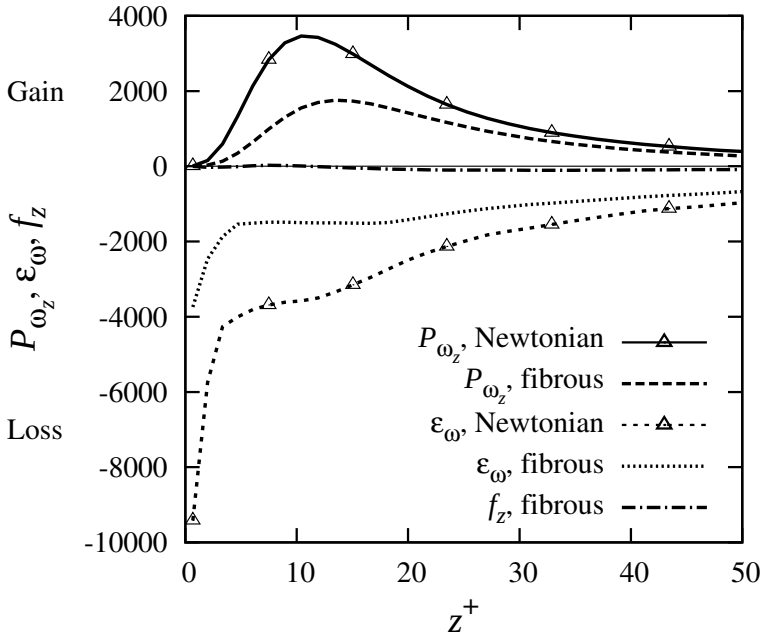

Figure 5.49: Budget of near-wall partial enstrophy for the Newtonian and fibrous flows versus the wall distance z^+. Contributions are normalized by h and u_τ. The balance does not hold because the turbulent transport is neglected.

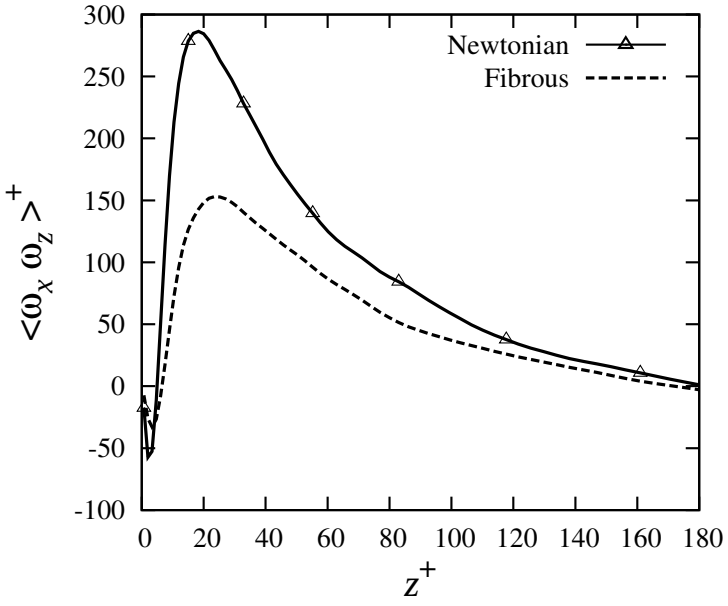

Figure 5.50: One-point correlation $\langle \omega_x \omega_z \rangle^+$ in inner scaling for the Newtonian and fibrous flows versus the wall distance z^+.

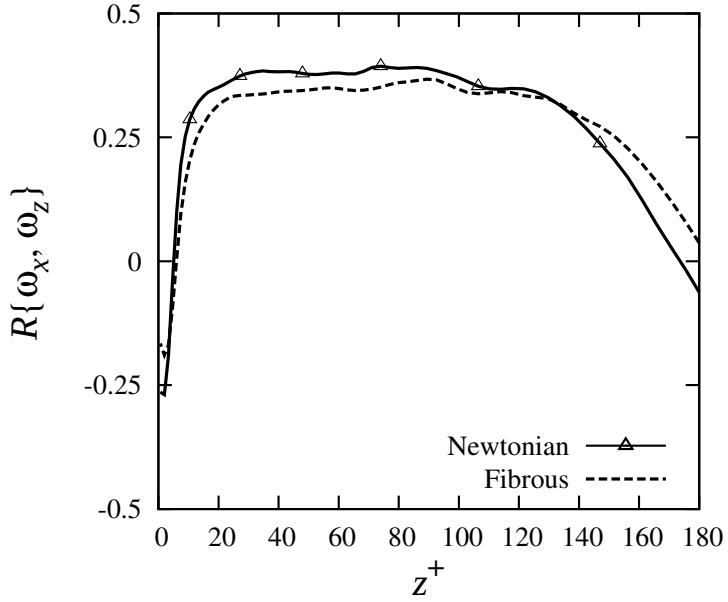

Figure 5.51: Correlation coefficient between ω_x and ω_z of the Newtonian and fibrous flows versus the wall distance z^+.

to the Newtonian counterpart, i.e. vortical structures are decayed in a thicker wall layer. This is consistent with the thickening of the viscous sublayer, and also indicates the movement of the streaky structures away from the wall. Note that the wall-normal vorticity is a representative of the streamwise streaks observed in the near-wall region.

The reduction in $\langle \omega_x \omega_z \rangle$ can be a result of reduction in $\omega_{x,\mathrm{rms}}$, $\omega_{z,\mathrm{rms}}$ and/or reduction in the correlation coefficient between them:

$$R\{\omega_x, \omega_z\} = \frac{\langle \omega_x \omega_z \rangle}{\omega_{x,\mathrm{rms}}\, \omega_{z,\mathrm{rms}}}. \tag{5.48}$$

We have observed in subsection 5.2.11 that, in the drag-reduced flow, $\omega_{x,\mathrm{rms}}$ is substantially decreased while the change in $\omega_{z,\mathrm{rms}}$ is modest, as compared to the Newtonian counterpart. The correlation coefficient $R\{\omega_x, \omega_z\}$ is plotted in figure 5.51. We see that the correlation coefficient is decreased up to a wall distance of $z^+ = 140$. Above this wall distance, $R\{\omega_x, \omega_z\}$ is increased. This can be explained by the distribution of the vorticity inclination angle θ presented in figures 5.47a to 5.47p. In the Newtonian flow, most of the vorticity inclination angles are populated about $\theta = 45°/-135°$, from the buffer layer up to about $z^+ = 140$. On the contrary, in the fibrous flow, the population around $\theta = 45°/-135°$ happens above about $z^+ = 90$. That is why the correlation coefficient of the Newtonian flow is higher than that of the fibrous flow in the region between the buffer layer up to about $z^+ = 90$. Above $z^+ = 90$, the correlation coefficients of both flows are close to each other up to about $z^+ = 140$. Above this wall distance, the correlation coefficient of the fibrous flow is greater than that of the Newtonian flow. This is because the inclination angles in the Newtonian flow tend to an isotropic state, while they are still, to some extent, anisotropic in the fibrous flow.

Considering both figures 5.39 and 5.51, we conclude that the reduction in $\langle \omega_x \omega_z \rangle$, in $z^+ < 140$ region, is due to reduction in both $\omega_{x,\mathrm{rms}}$ and the correlation coefficient $R\{\omega_x, \omega_z\}$. Above $z^+ = 140$, we observe that the $\langle \omega_x \omega_z \rangle$ curves of both flows are close to each other. This means that, in the fibrous flow, the reduction in $\omega_{x,\mathrm{rms}}$ is compensated by the increase in $R\{\omega_x, \omega_z\}$.

5.3. Summary

In this chapter, we have presented the results of the direct Monte-Carlo simulation of turbulent drag reduction by rigid fibers in a channel flow at a nominal shear Reynolds number $\mathrm{Re}_\tau = 180$. The suspended fibers have an aspect ratio $r = 100$ and a rotary Péclet number $\mathrm{Pe}_r = 1000$. We have studied the turbulence statistics. The classical features of a polymeric drag-reduced flow were observed. Especially, we look at the pressure-strain correlation which explains the change in the anisotropy of the drag-reduced flow. It turns out that the reduction in $\langle p' s'_{11} \rangle$ is mainly due to the reduction in $\langle (\partial U/\partial x)^2 \rangle$. We have analyzed the budget of $\langle (\partial U/\partial x)^2 \rangle$. Finally, we have investigated the vorticity field of the fibrous flow in comparison with the Newtonian flow.

6. Conclusions and Outlook

A two-way coupled solver for the simulation of fiber suspension flows has been developed. The incompressible non-Newtonian Navier-Stokes equations are solved using an existing finite-volume-based DNS solver. The suspended microstructure is treated in a Lagrangian manner using a particle tracking scheme. On each Lagrangian path, a cluster of sampling fibers are followed. The conformation of each cluster is computed using a direct Monte-Carlo method, i.e. a stochastic simulation of the Fokker-Planck equation. This direct solver is in contrast to the moment approximation simulation approach which requires a closure model. The numerical methods have been presented in detail. A benchmark with an analytical solution has been developed and used to validate the two-way coupled solver.

The developed numerical method has been employed to study the turbulent drag reduction caused by rigid fibers in a channel flow at a nominal shear Reynolds number $\mathrm{Re}_\tau = 180$. To the best of the author's knowledge, this is the first two-way coupled direct simulation of turbulent drag reduction by rigid fibers at a high Péclet number regime. This is achieved by using 128^3 Eulerian grid cells and 6 553 600 000 suspended fibers. The simulation demands a tremendous amount of computational resources. The code is parallelized over the Lagrangian particles, similar to the approach used by Manhart [74]. We have used 128 processing elements for the reported simulation.

Turbulence statistics of the drag-reduced flow are presented. All known features of a fibrous drag-reduced channel flow have been reproduced. The main results are as follows. Two-point correlations of velocity components in streamwise and spanwise directions are presented. Based on the two-point correlation of the streamwise velocity in the spanwise direction, the mean streak spacing is computed as a function of the wall distance. This shows about 50 wall units increase in the mean streak spacing. The power spectra of the velocity and the non-Newtonian stress components in streamwise and spanwise directions are also presented. The least decay among the velocity power spectra belongs to the wall-normal component in the spanwise direction, in the near-wall region. The decay of the stress spectra is not as fast as those of velocities.

The mean velocity profile has a slightly increased slope in the logarithmic-law region. Streamwise turbulence intensity is increased while the spanwise and wall-normal ones are decreased. The Reynolds shear stress is also reduced. Our quadrant analysis showed that the fibers mainly modify the contribution of the ejection and sweep events; ejections contribute more and sweeps contribute less. The probability density function (PDF) of the fluctuating velocities are shown. We have found out that the PDF of the streamwise velocity fluctuations is wider and those of the spanwise and wall-normal velocity fluctuations are narrower. This is consistent with the increased u_{rms} and the decreased v_{rms} and w_{rms}.

The Lumley anisotropy map has been presented and we have observed that the fibrous flow is more anisotropic. This is in line with the findings of Paschkewitz [102] and Frohnapfel *et al.* [35]. In order to explain the modification in the anisotropy map, we have considered the pressure-strain correlation which is responsible for the redistribution of the turbulent kinetic energy among different components. We have demonstrated that, in the drag-reduced flow, the sink term for u_{rms} and the source terms for v_{rms} and w_{rms} are weaker. This means that the redistribution process is less effective and hence, the turbulence is more anisotropic. We have found that the reduction in the streamwise component of the pressure-strain term is mainly due to the reduction in the strain fluctuations and partly due to the reduction in the pressure fluctuations. The pressure-strain correlation has been further analyzed by means of a Green's function solution of the Poisson equation for pressure fluctuations. We deduce that the direct effect of the non-Newtonian stresses is very small. This is similar to the direct contribution of the non-Newtonian stresses to the budget of the turbulent kinetic energy as described by Paschkewitz *et al.* [104]. The modification of the pressure-strain correlation, which is responsible for the most pronounced modification of the anisotropy comes from the modified terms in the budget that are present in the Newtonian flow budget as well.

We have also investigated the vorticity field of the turbulent drag-reduced flow. The streamwise vorticity fluctuations are reduced, similar to the result of Paschkewitz *et al.* [104]. The reduction in the root-mean-square streamwise vorticity fluctuations is mainly due to the reduction in the strain fluctuations, similar to the reduction in the pressure-strain correlation. The distribution of the vorticity tilting angle at different distances from the wall have been presented. It has been observed that the peaks in the distribution of the tilting angle are stronger in the fibrous flow. Another observation is that the tilting angle of the drag-reduced flow tends to 45° at a considerably higher distance from the wall as compared with the Newtonian flow.

Possible extentions to this thesis are suggested in the following directions. So far, only one-way coupled simulations of inertial fibers in turbulent flows have been available. Two-way coupled simulation of fibers in turbulent flows is an interesting extention to this work, which allows us to study the effect of the fiber inertia on the drag reduction. To this aim, one needs a rheological theory for suspension of inertial fibers. Another extention would be the direct simulation of a mixture of fibers and flexible polymers. This has been done by Paschkewitz [102] using the moment approximation model for fibers and the FENE-P model for flexible polymers. One can perform a direct simulation using the Monte-Carlo simulation of fibers and the FENE simulation of polymers. The simulation of turbulent fibrous flows in complex geometries would be another interesting extention to this work. Richter *et al.* [112] have pioneered a work in this direction using the FENE-P model for flexible polymers in viscoelatic flow around a circular cylinder at $\mathrm{Re} = 100$ and 300.

A. Fitting Coefficients of IBOF Closure

In this appendix, the $3 \times 21 = 63$ fitting coefficients of the IBOF closure model, i.e. $a\left(i,j\right)$ with $i = 3,4,6$ and $j = 1,\ldots,21$, are presented. These values are obtained by Chung and Kwon [16].

$i=3$		
$a(3,\ 1)$	$=$	$+0.249409081657860E02$
$a(3,\ 2)$	$=$	$-0.435101153160329E03$
$a(3,\ 3)$	$=$	$+0.372389335663877E04$
$a(3,\ 4)$	$=$	$+0.703443657916476E04$
$a(3,\ 5)$	$=$	$+0.823995187366106E06$
$a(3,\ 6)$	$=$	$-0.133931929894245E06$
$a(3,\ 7)$	$=$	$+0.880683515327916E06$
$a(3,\ 8)$	$=$	$-0.991630690741981E07$
$a(3,\ 9)$	$=$	$-0.159392396237307E05$
$a(3,10)$	$=$	$+0.800970026849796E07$
$a(3,11)$	$=$	$-0.237010458689252E07$
$a(3,12)$	$=$	$+0.379010599355267E08$
$a(3,13)$	$=$	$-0.337010820273821E08$
$a(3,14)$	$=$	$+0.322219416256417E05$
$a(3,15)$	$=$	$-0.257258805870567E09$
$a(3,16)$	$=$	$+0.214419090344474E07$
$a(3,17)$	$=$	$-0.449275591851490E08$
$a(3,18)$	$=$	$-0.213133920223355E08$
$a(3,19)$	$=$	$+0.157076702372204E10$
$a(3,20)$	$=$	$-0.232153488525298E05$
$a(3,21)$	$=$	$-0.395769398304473E10$

$i = 4$

$a(4,\ 1)$	$=$	$-0.497217790110754E00$
$a(4,\ 2)$	$=$	$+0.234980797511405E02$
$a(4,\ 3)$	$=$	$-0.391044251397838E03$
$a(4,\ 4)$	$=$	$+0.153965820593506E03$
$a(4,\ 5)$	$=$	$+0.152772950743819E06$
$a(4,\ 6)$	$=$	$-0.213755248785646E04$
$a(4,\ 7)$	$=$	$-0.400138947092812E04$
$a(4,\ 8)$	$=$	$-0.185949305922308E07$
$a(4,\ 9)$	$=$	$+0.296004865275814E04$
$a(4,10)$	$=$	$+0.247717810054366E07$
$a(4,11)$	$=$	$+0.101013983339062E06$
$a(4,12)$	$=$	$+0.732341494213578E07$
$a(4,13)$	$=$	$-0.147919027644202E08$
$a(4,14)$	$=$	$-0.104092072189767E05$
$a(4,15)$	$=$	$-0.635149929624336E08$
$a(4,16)$	$=$	$-0.247435106210237E06$
$a(4,17)$	$=$	$-0.902980378929272E07$
$a(4,18)$	$=$	$+0.724969796807399E07$
$a(4,19)$	$=$	$+0.487093452892595E09$
$a(4,20)$	$=$	$+0.138088690964946E05$
$a(4,21)$	$=$	$-0.160162178614234E10$

$i = 6$

$a(6,\ 1)$	$=$	$+0.2341462915709 99E02$
$a(6,\ 2)$	$=$	$-0.4120480433725 34E03$
$a(6,\ 3)$	$=$	$+0.3195532003920 89E04$
$a(6,\ 4)$	$=$	$+0.5732595943310 15E04$
$a(6,\ 5)$	$=$	$-0.4852128030648 13E05$
$a(6,\ 6)$	$=$	$-0.6050061135155 92E05$
$a(6,\ 7)$	$=$	$-0.4771737400175 67E05$
$a(6,\ 8)$	$=$	$+0.5990664866898 36E07$
$a(6,\ 9)$	$=$	$-0.1106569351765 69E05$
$a(6,10)$	$=$	$-0.4605435806806 96E08$
$a(6,11)$	$=$	$+0.2030429603228 74E07$
$a(6,12)$	$=$	$-0.5566061567348 35E08$
$a(6,13)$	$=$	$+0.5674249110078 37E09$
$a(6,14)$	$=$	$+0.1289670586862 04E05$
$a(6,15)$	$=$	$-0.1527528549565 14E10$
$a(6,16)$	$=$	$-0.4993217460925 34E07$
$a(6,17)$	$=$	$+0.1321248281433 33E09$
$a(6,18)$	$=$	$-0.1623599946209 83E10$
$a(6,19)$	$=$	$+0.7925268498822 18E10$
$a(6,20)$	$=$	$+0.4667675812929 85E04$
$a(6,21)$	$=$	$-0.1280507782794 59E11$

B. Evolution of Reynolds Stress Tensor and Turbulent Kinetic Energy

In this appendix, we derive differential equations governing the evolution of the Reynolds stress tensor and turbulent kinetic energy in non-Newtonian turbulent flows. These equations are derived from the incompressible non-Newtonian Navier-Stokes equations. The derivation for Newtonian flows can be found in [106].

First, we turn to the evolution of Reynolds stresses. A transport equation in the following form is sought:

$$\frac{\overline{\mathrm{D}}\left\langle u_i u_j \right\rangle}{\overline{\mathrm{D}}t} = \cdots, \tag{B.1}$$

in which

$$\frac{\overline{\mathrm{D}}}{\overline{\mathrm{D}}t} = \frac{\partial}{\partial t} + \left\langle U_i \right\rangle \frac{\partial}{\partial x_i}, \tag{B.2}$$

is the mean material derivative. From the definition of the material derivative, one can readily derive

$$\left\langle u_i \frac{\mathrm{D}u_j}{\mathrm{D}t} + u_j \frac{\mathrm{D}u_i}{\mathrm{D}t} \right\rangle = \frac{\overline{\mathrm{D}}\left\langle u_i u_j \right\rangle}{\overline{\mathrm{D}}t} + \frac{\partial}{\partial x_k}\left\langle u_i u_j u_k \right\rangle. \tag{B.3}$$

The following transport equation for fluctuating velocities is obtained by subtracting the mean flow (Reynolds) equation from the Navier-Stokes equation:

$$\frac{\mathrm{D}u_j}{\mathrm{D}t} = -u_k \frac{\partial \left\langle U_j \right\rangle}{\partial x_k} + \frac{\partial \left\langle u_k u_j \right\rangle}{\partial x_k} + \nu \frac{\partial^2 u_j}{\partial x_k \partial x_k} - \frac{1}{\rho}\frac{\partial p'}{\partial x_j} + \frac{\partial \tau_{kj}^{'\mathrm{NN}}}{\partial x_k}, \tag{B.4}$$

where $\tau_{kj}^{'\mathrm{NN}}$ is the fluctuating non-Newtonian stress. Substituting equation (B.4) into equation (B.3) yields

$$\frac{\overline{\mathrm{D}}\left\langle u_i u_j \right\rangle}{\overline{\mathrm{D}}t} + \frac{\partial T_{kij}}{\partial x_k} = P_{ij} + R_{ij} - \epsilon_{ij} + F_{ij}, \tag{B.5}$$

where

$$T_{kij} = \left\langle u_i u_j u_k \right\rangle - \nu \frac{\partial \left\langle u_i u_j \right\rangle}{\partial x_k} + \frac{1}{\rho}\left\langle u_i p' \right\rangle \delta_{jk} + \frac{1}{\rho}\left\langle u_j p' \right\rangle \delta_{ik}, \tag{B.6}$$

is the Reynolds stress flux,

$$P_{ij} = -\left\langle u_i u_k \right\rangle \frac{\partial \left\langle U_j \right\rangle}{\partial x_k} - \left\langle u_j u_k \right\rangle \frac{\partial \left\langle U_i \right\rangle}{\partial x_k}, \tag{B.7}$$

is the production term,

$$R_{ij} = \frac{1}{\rho} \left\langle p' \left(\frac{\partial u_i}{\partial x_j} + \frac{\partial u_j}{\partial x_i} \right) \right\rangle = \frac{1}{\rho} \left\langle p' s'_{ij} \right\rangle, \tag{B.8}$$

is the pressure-strain correlation,

$$\epsilon_{ij} = 2\nu \left\langle \frac{\partial u_i}{\partial x_j} \frac{\partial u_j}{\partial x_i} \right\rangle, \tag{B.9}$$

is the dissipation term, and

$$F_{ij} = \left\langle u_i \frac{\partial \tau'^{\mathrm{NN}}_{kj}}{\partial x_k} + u_j \frac{\partial \tau'^{\mathrm{NN}}_{ki}}{\partial x_k} \right\rangle, \tag{B.10}$$

is the non-Newtonian term. s'_{ij} in the pressure-strain term (B.8) is the fluctuating strain-rate tensor

$$s'_{ij} = \frac{\partial u_i}{\partial x_j} + \frac{\partial u_j}{\partial x_i}, \quad s'_{ii} = \partial i v \; u_i = 0. \tag{B.11}$$

A transport equation for the turbulent kinetic energy can be derived by simply changing u_j to u_i in equation (B.5):

$$\frac{\overline{\mathrm{D}} \left\langle u_i u_i \right\rangle}{\overline{\mathrm{D}} t} + \frac{\partial T_{kii}}{\partial x_k} = P_{ii} - \epsilon_{ii} + F_{ii}. \tag{B.12}$$

Note that R_{ii} vanishes due to the continuity of the fluctuating velocity field:

$$R_{ii} = \frac{1}{\rho} \left\langle p' \left(\frac{\partial u_i}{\partial x_i} + \frac{\partial u_i}{\partial x_i} \right) \right\rangle = \frac{1}{\rho} \left\langle p' s'_{ii} \right\rangle = 0. \tag{B.13}$$

The pressure-strain correlation R_{ij} appears in the transport of the Reynolds stresses (B.5), but does not appear in the transport of the turbulent kinetic energy (B.12). This means that R_{ij} does not act as a source or sink of the turbulent kinetic energy, but rather as a redistribution term for the Reynolds stresses. Redistribution is referred to the exchange of energy among different components of the Reynolds stress tensor.

C. Poisson Equation for Fluctuating Pressure

In this appendix, we derive a Poisson equation for the fluctuating pressure p' from the non-Newtonian Navier-Stokes equations. The derivation for the Newtonian case can be found in [106]. The non-Newtonian Navier-Stokes equations for incompressible flow in indicial notation read

$$\frac{\partial U_i}{\partial x_i} = 0, \tag{C.1}$$

$$\rho\left(\frac{\partial U_i}{\partial t} + U_j\frac{\partial U_i}{\partial x_j}\right) = -\frac{\partial p}{\partial x_i} + \mu\frac{\partial^2 U_i}{\partial x_j \partial x_j} + \frac{\partial \tau_{ij}^{\mathrm{NN}}}{\partial x_j}. \tag{C.2}$$

Taking the divergence of the momentum equation (C.2), one has the following Poisson equation for pressure:

$$\frac{1}{\rho}\frac{\partial^2 p}{\partial x_j \partial x_j} = -\frac{\partial U_i}{\partial x_j}\frac{\partial U_j}{\partial x_i} + \frac{\partial^2 \tau_{ij}^{\mathrm{NN}}}{\partial x_i \partial x_j}. \tag{C.3}$$

The mean flow (Reynolds) equations are obtained by Reynolds averaging the above Navier-Stokes equations:

$$\frac{\partial \langle U_i \rangle}{\partial x_i} = 0, \tag{C.4}$$

$$\rho\left(\frac{\partial \langle U_i \rangle}{\partial t} + \langle U_j \rangle \frac{\partial \langle U_i \rangle}{\partial x_j}\right) = -\frac{\partial \langle p \rangle}{\partial x_i} + \mu\frac{\partial^2 \langle U_i \rangle}{\partial x_j \partial x_j} - \rho\frac{\partial \langle u_i u_j \rangle}{\partial x_j} + \frac{\partial \langle \tau_{ij}^{\mathrm{NN}} \rangle}{\partial x_j}. \tag{C.5}$$

A detailed analysis of the Reynolds-averaged equations applied to polymeric flows can be found in [53]. By taking the divergence of the mean momentum equation (C.5) we obtain a Poisson equation for the mean pressure:

$$\frac{1}{\rho}\frac{\partial^2 \langle p \rangle}{\partial x_j \partial x_j} = -\frac{\partial \langle U_i \rangle}{\partial x_j}\frac{\partial \langle U_j \rangle}{\partial x_i} - \frac{\partial^2 \langle u_i u_j \rangle}{\partial x_i \partial x_j} + \frac{\partial^2 \langle \tau_{ij}^{\mathrm{NN}} \rangle}{\partial x_i \partial x_j}. \tag{C.6}$$

Finally, subtracting equation (C.6) for $\langle p \rangle$ from equation (C.3) for p and noting that $p' =$

$p - \langle p \rangle$, we obtain

$$\frac{1}{\rho}\frac{\partial^2 p'}{\partial x_j \partial x_j} = -2\frac{\partial \langle U_i \rangle}{\partial x_j}\frac{\partial u_j}{\partial x_i} - \frac{\partial^2}{\partial x_i \partial x_j}\left(u_i u_j - \langle u_i u_j \rangle\right) + \frac{\partial^2 \tau_{ij}^{'\mathrm{NN}}}{\partial x_i \partial x_j}, \tag{C.7}$$

which is a Poisson equation for the fluctuating pressure. Considering the statistical homogeneity, equation (C.7) can be written in the following form for a fully-developed turbulent channel flow:

$$\frac{1}{\rho}\frac{\partial^2 p'}{\partial x_j \partial x_j} = -2\frac{\partial \langle U \rangle}{\partial z}\frac{\partial w}{\partial x} - \frac{\partial^2 u_i u_j}{\partial x_i \partial x_j} + \frac{\partial^2 \langle ww \rangle}{\partial z^2} + \frac{\partial^2 \tau_{ij}^{'\mathrm{NN}}}{\partial x_i \partial x_j}. \tag{C.8}$$

Equation (C.8) can be alternatively written as

$$\frac{1}{\rho}\frac{\partial^2 p'}{\partial x_j \partial x_j} = -2\frac{\partial \langle U \rangle}{\partial z}\frac{\partial w}{\partial x} - \frac{\partial u_i}{\partial x_j}\frac{\partial u_j}{\partial x_i} + \frac{\partial^2 \langle ww \rangle}{\partial z^2} + \frac{\partial^2 \tau_{ij}^{'\mathrm{NN}}}{\partial x_i \partial x_j}, \tag{C.9}$$

by taking into account the continuity of the fluctuating velocity field:

$$\frac{\partial u_i}{\partial x_i} = 0. \tag{C.10}$$

Bibliography

[1] S. G. Advani and C. L. Tucker. The use of tensors to describe and predict fiber orientation in short fiber composites. *J. Rheol.*, 31:751–784, 1987.

[2] S. G. Advani and C. L. Tucker. Closure approximations for three-dimensional structure tensors. *J. Rheol.*, 34:367–386, 1990.

[3] M. P. Allen and D. J. Tildesley. *Computer Simulation of Liquids*. Oxford University Press, New York, 1987.

[4] Y. Amarouchene, D. Bonn, H. Kellay, T.-S. Lo, V. S. L'vov, and I. Procaccia. Reynolds number dependence of drag reduction by rodlike polymers. *Phys. Fluids*, 20:065108, 2008.

[5] S. Balachandar and M. R. Maxey. Methods for evaluating fluid velocities in spectral simulations of turbulence. *J. Comput. Phys.*, 83:96–125, 1989.

[6] G. I. Barenblatt, A. J. Chorin, and V. M. Prostokishin. Scaling laws for fully developed turbulent flow in pipes. *Appl. Mech. Rev.*, 50:413–429, 1997.

[7] G. Batchelor. The stress system in a suspension of force-free particles. *J. Fluid Mech.*, 41:545–570, 1970.

[8] R. Benzi, E. S. C. Ching, E. De Angelis, and I. Procaccia. Comparison of theory and direct numerical simulations of drag reduction by rodlike polymers in turbulent channel flows. *Phys. Rev. E*, 77:046309, 2008.

[9] R. Benzi, E. De Angelis, V. S. L'vov, I. Procaccia, and V. Tiberkevich. Maximum drag reduction asymptotes and the cross-over to the Newtonian plug. *J. Fluid Mech.*, 551:185–195, 2006.

[10] A. N. Beris and C. D. Dimitropoulos. Pseudospectral simulation of turbulent viscoelastic channel flow. *Comput. Meth. Appl. Mech. Eng.*, 180:365–392, 1999.

[11] H. Brenner. Rheology of a dilute suspension of axisymmetric Brownian particles. *Int. J. Multiphase Flow*, 1:195–341, 1974.

[12] C. Brun, D. Juvé, M. Manhart, and C.-D. Munz. *Numerical Simulation of Turbulent Flows and Noise Generation. Vol. 104 of Notes on Numerical Fluid Mechanics and Multidisciplinary Design*. Springer-Verlag, Berlin, 2009.

[13] H. Choi, P. Moin, and J. Kim. Direct numerical simulation of turbulent flow over riblets. *J. Fluid Mech.*, 255:503–539, 1993.

[14] H. Choi, P. Moin, and J. Kim. Active turbulence control for drag reduction in wall-bounded flows. *J. Fluid Mech.*, 262:75–110, 1994.

[15] A. J. Chorin. Numerical solution of the Navier-Stokes equations. *Math. Comp.*, 22:745–762, 1968.

[16] D. Chung and T. Kwon. Invariant-based optimal fitting closure approximation for the numerical prediction of flow-induced fiber orientation. *J. Rheol.*, 46:169–194, 2002.

[17] C. J. Cyron and W. A. Wall. Finite-element approach to Brownian dynamics of polymers. *Phys. Rev. E*, 80:066704, 2009.

[18] E. De Angelis, C. M. Casciola, and R. Piva. DNS of wall turbulence: dilute polymers and self-sustaining mechanisms. *Comput. Fluids*, 31:495–507, 2002.

[19] R. B. Dean. Reynolds number dependence of skin friction and other bulk flow variables in two-dimensional rectangular duct flow. *Trans. ASME J. Fluids Engng.*, 100:215–223, 1978.

[20] J. M. J. den Toonder, M. A. Hulsen, G. D. C. Kuiken, and F. T. M. Nieuwstadt. Drag reduction by polymer additives in a turbulent pipe flow: numerical and laboratory experiments. *J. Fluid Mech.*, 337:193–231, 1997.

[21] C. D. Dimitropoulos, Y. Dubief, E. S. G. Shaqfeh, and P. Moin. Direct numerical simulation of polymer-induced drag reduction in turbulent boundary layer flow of inhomogeneous polymer solutions. *J. Fluid Mech.*, 566:153–162, 2006.

[22] C. D. Dimitropoulos, R. Sureshkumar, and A. N. Beris. Direct numerical simulation of viscoelastic turbulent channel flow exhibiting drag reduction: effect of the variation of rheological parameters. *J. Non-Newtonian Fluid Mech.*, 79:433–468, 1998.

[23] M. Doi and S. F. Edwards. *The Theory of Polymer Dynamics*. Clarendon, Oxford, 1986.

[24] F. W. Dorr. The direct solution of the discrete Poisson equation on a rectangle. *SIAM Rev.*, 12:248–263, 1970.

[25] Y. Dubief, C. M. White, V. E. Terrapon, E. S. G. Shaqfeh, P. Moin, and S. K. Lele. On the coherent drag-reducing and turbulence-enhancing behaviour of polymers in wall flows. *J. Fluid Mech.*, 514:271–280, 2004.

[26] A. Einstein. Über die von der molekularkinetischen Theorie der Wärme geforderte Bewegung von in ruhenden Flüssigkeiten suspendierten Teilchen. *Ann. Physik*, 322:549–560, 1905.

[27] A. Einstein. Eine neue Bestimmung der Moleküldimensionen. *Ann. Physik*, 324:289–306, 1906.

[28] A. Einstein. Berichtigung zu meiner Arbeit: Eine neue Bestimmung der Moleküldimensionen. *Ann. Physik*, 339:591–592, 1911.

[29] F.-G. Fan and G. Ahmadi. Wall deposition of small ellipsoids from turbulent air flows - a Brownian dynamics simulation. *J. Aerosol Sci.*, 31:1205–1229, 2000.

[30] J. H. Ferziger and M. Perić. *Computational Methods for Fluid Dynamics*. Springer-Verlag, Berlin, 2001.

[31] H. Foysi. *Transport passiver Skalare in wandgebundener und isotrope kompressibler Turbulenz*. PhD Dissertation, Technische Universität München, 2005.

[32] H. Foysi, S. Sarkar, and R. Friedrich. Compressibility effects and turbulence scalings in supersonic channel flow. *J. Fluid Mech.*, 509:207–216, 2004.

[33] P. L. Frattini and G. G. Fuller. Rheo-optical studies of the effect of weak Brownian rotations in sheared suspensions. *J. Fluid Mech.*, 168:119–150, 1986.

[34] R. Friedrich, T. J. Hüttl, M. Manhart, and C. Wagner. Direct numerical simulation of incompressible flows. *Comput. Fluids*, 30:555–579, 2001.

[35] B. Frohnapfel, P. Lammers, J. Jovanović, and F. Durst. Interpretation of the mechanism associated with turbulent drag reduction in terms of anisotropy invariants. *J. Fluid Mech.*, 577:457–466, 2007.

[36] W. K. George and L. Castillo. Zero-pressure-gradient turbulent boundary layer. *Appl. Mech. Rev.*, 50:689–729, 1997.

[37] J. J. J. Gillissen. Polymer flexibility and turbulent drag reduction. *Phys. Rev. E*, 78:046311, 2008.

[38] J. J. J. Gillissen, B. J. Boersma, P. H. Mortensen, and H. I. Andersson. On the performance of the moment approximation for the numerical computation of fiber stress in turbulent channel flow. *Phys. Fluids*, 19:035102, 2007.

[39] J. J. J. Gillissen, B. J. Boersma, P. H. Mortensen, and H. I. Andersson. The stress generated by non-Brownian fibers in turbulent channel flow simulations. *Phys. Fluids*, 19:115107, 2007.

[40] J. J. J. Gillissen, B. J. Boersma, P. H. Mortensen, and H. I. Andersson. Fibre-induced drag reduction. *J. Fluid Mech.*, 602:209–218, 2008.

[41] C. Gobert. *Large Eddy Simulation of Particle-Laden Flow*. PhD Dissertation, Technische Universität München, 2010.

[42] J. Haile. *Molecular Dynamics Simulations: Elementary Methods*. John Wiley & Sons, New York, 1997.

[43] F. E. Ham, F. S. Lien, and A. B. Strong. A fully conservative second-order finite difference scheme for incompressible flow on nonuniform grids. *J. Comput. Phys.*, 177:117–133, 2002.

[44] G. L. Hand. A theory of anisotropic fluids. *J. Fluid Mech.*, 13:33–46, 1962.

[45] F. H. Harlow and J. E. Welch. Numerical calculation of time-dependent viscous incompressible flow of fluid with free surface. *Phys. Fluids.*, 8:2182, 1965.

[46] E. J. Hinch and L. G. Leal. The effect of Brownian motion on the rheological properties of a suspension of non-spherical particles. *J. Fluid Mech.*, 52:683–712, 1972.

[47] E. J. Hinch and L. G. Leal. Time-dependent shear flows of a suspension of particles with weak Brownian rotations. *J. Fluid Mech.*, 57:753–767, 1973.

[48] E. J. Hinch and L. G. Leal. Constitutive equations in suspension mechanics. Part 1: General formulation. *J. Fluid Mech.*, 71:481–495, 1975.

[49] E. J. Hinch and L. G. Leal. Constitutive equations in suspension mechanics. Part 2: Approximate forms for a suspension of rigid particles affected by Brownian rotations. *J. Fluid Mech.*, 76:187–208, 1976.

[50] A. Hokpunna. *Compact Fourth-Order Scheme for Numerical Simulations of Navier-Stokes Equations*. PhD Dissertation, Technische Universität München, 2010.

[51] A. Hokpunna and M. Manhart. Compact fourth-order finite volume method for numerical solutions of Navier-Stokes equations on staggered grids. *J. Comput. Phys.*, 229:7545–7570, 2010.

[52] Y. X. Hou, V. S. R. Somandepalli, and M. G. Mungal. Streamwise development of turbulent boundary-layer drag reduction with polymer injection. *J. Fluid Mech.*, 567:31–66, 2008.

[53] G. Iaccarino, E. S. G. Shaqfeh, and Y. Dubief. Reynolds-averaged modeling of polymer drag reduction in turbulent flows. *J. Non-Newtonian Fluid Mech.*, 165:376–384, 2010.

[54] G. Jeffery. The motion of ellipsoidal particles immersed in a viscous fluid. *Proc. R. Soc. Lond. A*, 102:161–179, 1922.

[55] J. Jiménez and P. Moin. The minimal flow unit in near-wall turbulence. *J. Fluid Mech.*, 225:213–240, 1991.

[56] J. Kim. On the structure of pressure fluctuations in simulated turbulent channel flow. *J. Fluid Mech.*, 205:421–451, 1989.

[57] J. Kim and P. Moin. Application of a fractional-step method to incompressible Navier-Stokes equations. *J. Comput. Phys.*, 59:308–323, 1985.

[58] J. Kim, P. Moin, and R. D. Moser. Turbulence statistics in fully developed channel flow at low Reynolds number. *J. Fluid Mech.*, 177:133–166, 1987.

[59] S. Kim and S. Karrila. *Microhydrodynamics: Principles and Selected Applications*. Butterworth-Heinemann Ltd, Oxford, 1991.

[60] A. N. Kolmogorov. The local structure of turbulence in incompressible viscous fluid for very large Reynolds numbers (in Russian). *Dokl. Akad. Nauk. SSSR*, 30:299–303, 1941.

[61] A. N. Kolmogorov. The local structure of turbulence in incompressible viscous fluid for very large Reynolds numbers (translated by V. Levin). *Proc. R. Soc. London A*, 434:9–13, 1991.

[62] K. Kontomaris, T. Hanratty, and J. McLaughlin. An algorithm for tracking fluid particles in a spectral simulation of turbulent channel flow. *J. Comput. Phys.*, 103:231–242, 1992.

[63] N. V. Krylov. *Introduction to the Theory of Diffusion Processes*. American Mathematical Society, Providence, 1995.

[64] C. Lee and J. Kim. Control of the viscous sublayer drag reduction. *Phys. Fluids*, 14:2523–2529, 2002.

[65] S. K. Lele. Compact finite difference schemes with spectral-like resolution. *J. Comput. Phys.*, 103:16–42, 1992.

[66] S. K. Lele. Compressibility effects on turbulence. *Annu. Rev. Fluid Mech.*, 26:211–254, 1994.

[67] J. L. Lumley. Drag reduction by additives. *Annu. Rev. Fluid Mech.*, 1:367–384, 1969.

[68] J. L. Lumley and G. Newman. The return to isotropy of homogeneous turbulence. *J. Fluid Mech.*, 82:161–178, 1977.

[69] M. Manhart. *Umströmung einer Halbkugel in turbulenter Grenzschicht*. PhD Dissertation, Universität der Bundeswehr München, 1995.

[70] M. Manhart. Rheology of suspensions of small fibres in turbulent channel flow. Part 1: Simple steady flows. *Sonderforschungsbereich 438: TU-München, Universität Augsburg*, SFB-438-0203, 2002.

[71] M. Manhart. Rheology of suspensions of rigid-rod like particles in turbulent channel flow. *J. Non-Newtonian Fluid Mech.*, 112:269–293, 2003.

[72] M. Manhart. Visco-elastic behaviour of suspensions of rigid-rod like particles in turbulent channel flow. *Eur. J. Mech. B-Fluids*, 23:461–474, 2004.

[73] M. Manhart. A zonal grid algorithm for DNS of turbulent boundary layers. *Comput. Fluids*, 33:435–461, 2004.

[74] M. Manhart. A coupled DNS/Monte-Carlo solver for dilute suspensions of Brownian fibres in turbulent channel flow. In S. Wagner, W. Hanke, A. Bode, and F. Durst, editors, *High Performance Computing in Science and Engineering, Munich 2004*, pages 119–131. Springer-Verlag, Berlin, 2005.

[75] M. Manhart and R. Friedrich. DNS of a turbulent boundary layer with separation. *Int. J. Heat Fluid Flow*, 23:572–581, 2002.

[76] M. Manhart, F. Tremblay, and R. Friedrich. MGLET: A parallel code for efficient DNS and LES of complex geometries. In *Parallel Computational Fluid Dynamics 2000*, pages 449–456, 2001.

[77] C. Marchioli, M. Fantoni, and A. Soldati. Orientation, distribution, and deposition of elongated, inertial fibers in turbulent channel flow. *Phys. Fluids*, 22:033301, 2010.

[78] W. D. McComb and K. T. J. Chan. Drag reduction in fibre suspension. *Nature*, 292:520–522, 1981.

[79] D. W. Meyer and P. Jenny. Conservative velocity interpolation for PDF methods. *Proc. Appl. Math. Mech.*, 4:466–467, 2004.

[80] C. M. Millikan. A critical discussion of turbulent flows in channel and circular pipes. In *Proceedings of the 5th International Congress of Applied Mechanics*, pages 386–392, 1938.

[81] P. Moin. *Fundamentals of Engineering Numerical Analysis*. Cambridge University Press, Cambridge, 2001.

[82] P. Moin and J. Kim. On the numerical solution of time-dependent viscous incompressible fluid flows involving solid boundaries. *J. Comput. Phys.*, 35:381–392, 1980.

[83] P. Moin and J. Kim. Numerical investigation of turbulent channel flow. *J. Fluid Mech.*, 118:341–377, 1982.

[84] P. Moin and J. Kim. The structure of the vorticity field in turbulent channel flow. Part 1. Analysis of instantaneous fields and statistical correlations. *J. Fluid Mech.*, 155:441–464, 1985.

[85] P. Moin and J. Kim. Tackling turbulence with supercomputers. *Scientific American Magazine*, January 1997.

[86] P. Moin and K. Mahesh. Direct numerical simulation: a tool in turbulence research. *Annu. Rev. Fluid Mech.*, 30:539–578, 1998.

[87] A. Moosaie, A. Le Duc, and M. Manhart. A comparative study on the performance of various moment closures in flows of fiber suspensions. *Proc. Appl. Math. Mech.*, 10:447–448, 2010.

[88] A. Moosaie, A. Le Duc, and M. Manhart. Numerical simulation of flow-induced fiber orientation using normalization of second moment. *J. Non-Newtonian Fluid Mech.*, 165:551–554, 2010.

[89] A. Moosaie, A. Le Duc, and M. Manhart. On the performance of various moment closure models for dilute fiber suspensions. In *GAMM*, Karlsruhe, March 22-26 2010.

[90] Y. Morinishi, T. S. Lund, O. V. Vasilyev, and P. Moin. Fully conservative higher order finite difference schemes for incompressible flow. *J. Comput. Phys.*, 143:90–124, 1998.

[91] P. H. Mortensen, H. I. Andersson, J. J. J. Gillissen, and B. J. Boersma. Particle spin in a turbulent shear flow. *Phys. Fluids*, 19:078109, 2007.

[92] P. H. Mortensen, H. I. Andersson, J. J. J. Gillissen, and B. J. Boersma. Dynamics of prolate ellipsoidal particles in a turbulent channel flow. *Phys. Fluids*, 20:093302, 2008.

[93] P. H. Mortensen, H. I. Andersson, J. J. J. Gillissen, and B. J. Boersma. On the orientation of ellipsoidal particles in a turbulent shear flow. *Int. J. Multiphase Flow*, 34:678–683, 2008.

[94] R. D. Moser, J. Kim, and N. N. Mansour. Direct numerical simulation of turbulent channel flow up to $\mathrm{Re}_\tau = 590$. *Phys. Fluids*, 11:943–945, 1999.

[95] R. D. Moser, J. Kim, and N. N. Mansour. Direct numerical simulation of turbulent channel flow up to $\mathrm{Re}_\tau = 590$. `http://turbulence.ices.utexas.edu/MKM_1999.html`, 1999. [Online; accessed 18-October-2010].

[96] R. D. Moser and P. Moin. The effects of curvature in wall-bounded turbulent flows. *J. Fluid Mech.*, 175:479–510, 1987.

[97] K. K. Nomura and G. K. Post. The structure and dynamics of vorticity and rate of strain in incompressible homogeneous turbulence. *J. Fluid Mech.*, 377:65–97, 1998.

[98] A. Okagawa, R. Cox, and S. Mason. The kinetics of flowing dispersions. VI. Transient orientation and rheological phenomena of rods and discs in shear flow. *J. Colloid Interface Sci.*, 45:303–329, 1973.

[99] S. A. Orszag and G. S. Patterson. Numerical simulation of three-dimensional homogeneous isotropic turbulence. *Phys. Rev. Lett.*, 28:76–79, 1972.

[100] H. Öttinger. *Stochastic Processes in Polymeric Fluids. Tools and Examples for Developing Simulation Algorithms*. Springer-Verlag, Berlin, 1996.

[101] H. C. Öttinger. On the stupendous beauty of closure. *J. Rheol.*, 53:1285–1304, 2009.

[102] J. S. Paschkewitz. *Turbulent Drag Reduction Using Microfibers*. PhD Dissertation, Stanford University, 2004.

[103] J. S. Paschkewitz, C. D. Dimitropoulos, Y. X. Hou, V. S. R. Somandepalli, M. G. Mungal, E. S. G. Shaqfeh, and P. Moin. An experimental and numerical investigation of drag reduction in a turbulent boundary layer using a rigid rodlike polymer. *Phys. Fluids*, 17:085101, 2005.

[104] J. S. Paschkewitz, Y. Dubief, C. D. Dimitropoulos, E. S. G. Shaqfeh, and P. Moin. Numerical simulation of turbulent drag reduction using rigid fibres. *J. Fluid Mech.*, 518:281–317, 2004.

[105] J. S. Paschkewitz, Y. Dubief, and E. S. G. Shaqfeh. The dynamic mechanism for turbulent drag reduction using rigid fibers based on Lagrangian conditional statistics. *Phys. Fluids*, 17:063102, 2005.

[106] S. B. Pope. *Turbulent Flows*. Cambridge University Press, Cambridge, 2000.

[107] I. Procaccia, V. S. L'vov, and R. Benzi. Theory of drag reduction by polymers in wall-bounded turbulence. *Rev. Mod. Phys.*, 80:225–247, 2008.

[108] I. Radin, J. Zakin, and G. Patterson. Drag reduction in solid-fluid systems. *AIChE J.*, 21:358–371, 1975.

[109] O. Reynolds. An experimental investigation of the circumstances which determine whether the motion of water shall be direct or sinuous, and of the law of resistance in parallel channels. *Philos. Trans.*, 174:935–982, 1883.

[110] C. M. Rhie and W. L. Chow. Numerical study of the turbulent flow past an airfoil with trailing edge separation. *AIAA J.*, 21:1525–1532, 1983.

[111] L. F. Richardson. *Weather Prediction by Numerical Process*. Cambridge University Press, Cambridge, 1922.

[112] D. Richter, G. Iaccarino, and E. S. G. Shaqfeh. Simulations of three-dimensional viscoelastic flows past a circular cylinder at moderate Reynolds numbers. *J. Fluid Mech.*, 651:415–442, 2010.

[113] R. S. Rogallo and P. Moin. Numerical simulation of turbulent flows. *Annu. Rev. Fluid Mech.*, 16:99–137, 1984.

[114] S. Sasaki. Drag reduction effect of rod-like polymer solutions. I. Influences of polymer concentration and rigidity of skeletal back bone. *J. Phys. Soc. Jpn.*, 60:868–878, 1991.

[115] S. Sasaki. Drag reduction effect of rod-like polymer solutions. II. Comparison between microgel and linear type polyions. *J. Phys. Soc. Jpn.*, 60:2613–2618, 1991.

[116] O. Sendstad and P. Moin. The near wall mechanics of three-dimensional turbulent boundary layers. *Report No. TF-57, Department of Mechanical Engineering, Stanford University*, 1992.

[117] E. S. G. Shaqfeh and G. H. Fredrickson. The hydrodynamic stress in a suspension of rods. *Phys. Fluids A*, 2:7–24, 1990.

[118] J. Smagorinsky. General circulation experiments with the primitive equations. *Mon. Weather Rev.*, 91:99–164, 1963.

[119] V. S. R. Somandepalli, Y. X. Hou, and M. G. Mungal. Concentration flux measurements in a polymer drag-reduced turbulent boundary layer. *J. Fluid Mech.*, 644:281–319, 2010.

[120] M. Somasi, B. Khomami, N. J. Woo, J. S. Hur, and E. S. G. Shaqfeh. Brownian dynamics simulations of bead-rod and bead-spring chains: numerical algorithms and coarse-graining issues. *J. Non-Newtonian Fluid Mech.*, 108:227–255, 2002.

[121] H. L. Stone. Iterative solution of implicit approximations of multidimensional partial differential equations. *SIAM J. Numer. Anal.*, 5:530–558, 1968.

[122] G. Subramanian and D. L. Koch. Inertial effects on fibre motion in simple shear flow. *J. Fluid Mech.*, 535:383–414, 2005.

[123] R. Sureshkumar, A. N. Beris, and R. A. Handler. Direct numerical simulation of the turbulent channel flow of a polymer solution. *Phys. Fluids*, 9:743, 1997.

[124] R. Temam. Sur l'approximation de la solution des équations de Navier-Stokes par la méthode des pas fractionnaires (ii). *Arch. Ration. Mech. Anal.*, 33:377–385, 1969.

[125] V. Terrapon. *Lagrangian Simulations of Turbulent Drag Reduction by a Dilute Solution of Polymers in a Channel Flow*. PhD Dissertation, Stanford University, 2005.

[126] V. E. Terrapon, Y. Dubief, P. Moin, E. S. G. Shaqfeh, and S. K. Lele. Simulated polymer stretch in a turbulent flow using Brownian dynamics. *J. Fluid Mech.*, 504:61–71, 2004.

[127] B. A. Toms. Some observations on the flow of linear polymer solutions through straight tubes at large Reynolds numbers. In *Proc. 1st Int. Congr. Rheol.*, volume 2, pages 135–141, Amsterdam, 1948.

[128] R. Trostel. *Mathematische Grundlagen der Technischen Mechanik I: Vektor- und Tensoralgebra*. Vieweg-Verlag, Braunschweig, 1993.

[129] L. Vervisch and T. Poinsot. Direct numerical simulation of non-premixed turbulent flames. *Annu. Rev. Fluid Mech.*, 30:655–691, 1998.

[130] P. S. Virk. An elastic sublayer model for drag reduction by dilute solutions of linear macromolecules. *J. Fluid Mech.*, 45:417–440, 1971.

[131] C. M. White and M. G. Mungal. Mechanics and prediction of turbulent drag reduction with polymer additives. *Annu. Rev. Fluid Mech.*, 40:235–256, 2008.

[132] J. H. Williamson. Low-storage Runge-Kutta schemes. *J. Comput. Phys.*, 35:48–56, 1980.

[133] J. Xu, M. R. Maxey, and G. E. Karniadakis. Numerical simulation of turbulent drag reduction using micro-bubbles. *J. Fluid Mech.*, 468:271–281, 2002.

[134] P. Yeung and S. Pope. An algorithm for tracking fluid particles in numerical simulations of homogeneous turbulence. *J. Comput. Phys.*, 79:373–416, 1988.

[135] J. L. Zakin, B. Lu, and H. W. Bewersdorff. Surfactants drag reduction. *Rev. Chem. Eng.*, 14:253–320, 1988.

[136] H. Zhang, G. Ahmadi, F.-G. Fan, and J. B. McLaughlin. Ellipsoidal particles transport and deposition in turbulent channel flows. *Int. J. Multiphase Flow*, 27:971–1009, 2001.

[137] L. H. Zhao, H. I. Andersson, and J. J. J. Gillissen. Turbulence modulation and drag reduction by spherical particles. *Phys. Fluids*, 22:081702, 2010.

[138] Q. Zhou and R. Akhavan. A comparison of FENE and FENE-P dumbbell and chain models in turbulent flow. *J. Non-Newtonian Fluid Mech.*, 109:115–155, 2003.